Bending the Rules: Magnetically-Actuated Surgical Continuum Manipulators

Theodosia Lourdes Thomas

Bending the Rules

Magnetically-Actuated Surgical Continuum Manipulators

Theodosia Lourdes Thomas

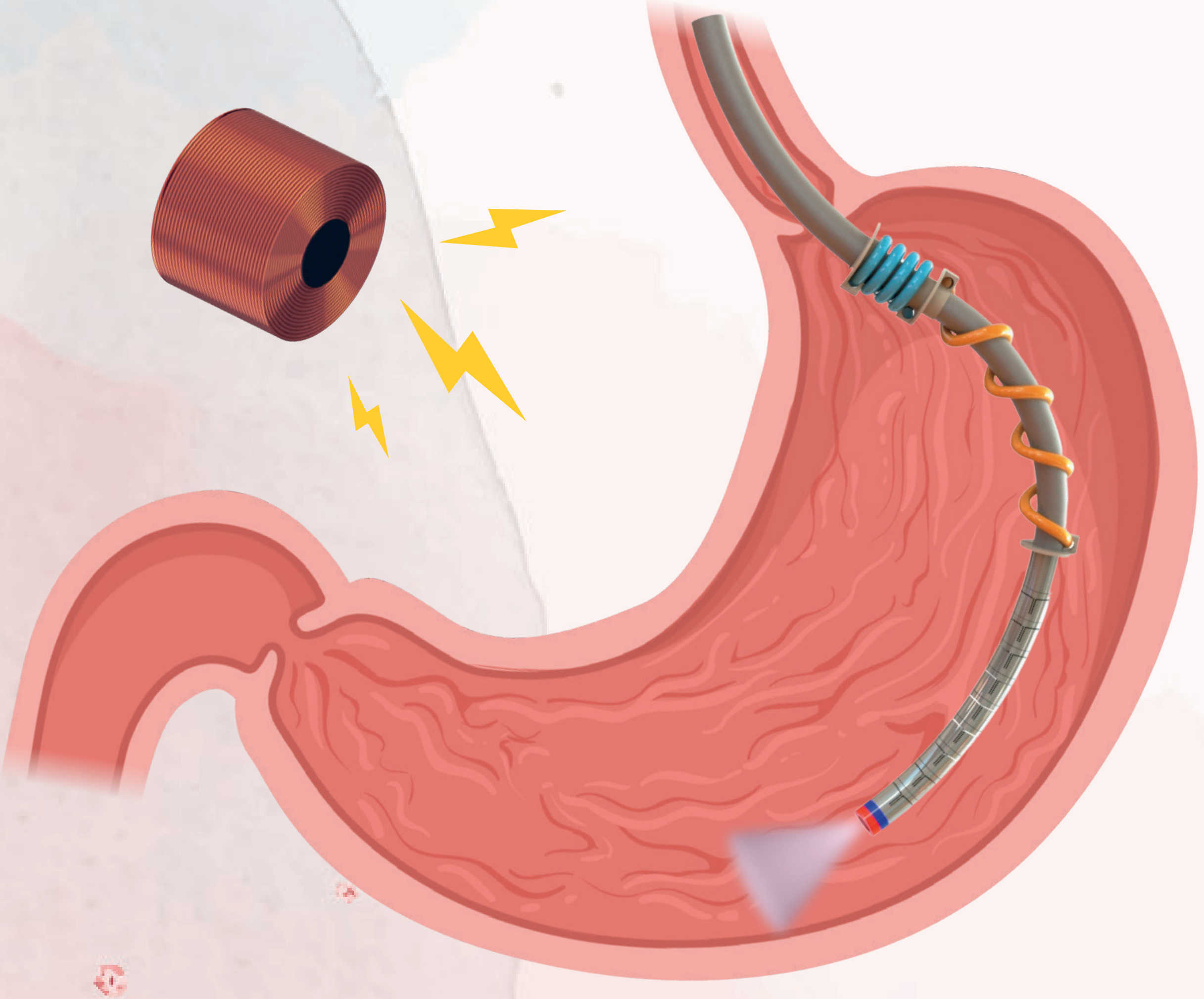

INVITATION

I cordially invite you to attend
the public defence
of my doctoral dissertation
titled

Bending the Rules
Magnetically-Actuated
Surgical Continuum
Manipulators

On the 6th of April 2023
at 16:30
in the Prof. dr. G. Berkhoff
room, the Waaier,
University of Twente

Theodosia Lourdes Thomas
t.l.thomas@utwente.nl

Paranymphs
Juan J. Huaroto
Yu-Hsiang Lin

BENDING THE RULES

MAGNETICALLY-ACTUATED SURGICAL CONTINUUM MANIPULATORS

Theodosia Lourdes Thomas

BENDING THE RULES
MAGNETICALLY-ACTUATED SURGICAL CONTINUUM MANIPULATORS

DISSERTATION

to obtain
the degree of doctor at the University of Twente,
on the authority of the rector magnificus,
Prof. Dr. Ir. A. Veldkamp,
on account of the decision of the Doctorate Board,
to be publicly defended
on Thursday the 6th of April 2023 at 16.45 hours

by

Theodosia Lourdes Thomas

born on the 11th of February 1996
in Gobichettipalayam, India

This dissertation has been approved by:

Prof. Dr. S. Misra
Dr. V. Kalpathy Venkiteswaran

Cover design: Theodosia Lourdes Thomas. Background watercolor art by Artnizu - stock.adobe.com. Illustration of the stomach created with BioRender.com
Lay-out: Sumit Mohanty
Printed by: Proefschriften.nl
ISBN (print): 978-90-365-5590-6
ISBN (digital): 978-90-365-5591-3
DOI: 10.3990/1.9789036555913

GRADUATION COMMITTEE:

Chairman/Secretary:

Prof. Dr. Ir. H.F.J.M. Koopman	*University of Twente*

Supervisor/Promoter:

Prof. Dr. S. Misra	*University of Twente,* *University of Groningen, and* *University Medical Center Groningen*

Co-supervisor:

Dr. V. Kalpathy Venkiteswaran	*University of Twente*

Committee Members:

Prof. Dr. G.K. Ananthasuresh	*Indian Institute of Science, Bengaluru*
Prof. Dr. Ir. J.L. Herder	*Delft University of Technology*
Prof. Dr. P.C. Jutte	*University Medical Center Groningen*
Prof. Dr. Ir. G.J.M. Tuijthof	*University of Twente*
Dr. Ir. M. Mehrpouya	*University of Twente*

This work is part of the research projects **INSPIRE** and **SAMURAI**.

The reported research has received funding from the European Research Council (ERC) under the European Union's Horizon 2020 Research and Innovation programme (ERC Proof of Concept Grant Agreement #790088 — project INSPIRE: Instrument Shape Sensing for Minimally Invasive Interventions) and the Netherlands Organization for Scientific Research (*Nederlands Organisatie voor Wetenschappelijk Onderzoek*) under the Innovational Research Incentives Scheme (Grant Agreement #14855 — project SAMURAI: Steering Actuated Probes under Magnetic- and Ultrasound-Guidance for Targeted Interventions).

To my loving parents, Thomas and Lilly Pushpam,
and my dear brother, Theophilus

Summary

Continuum manipulators have revolutionized the field of minimally invasive surgery (MIS) in the past few decades. Major advances in fiber optics, imaging technologies, teleoperation, and haptics have accelerated the development of robot-assisted surgeries. The continuum manipulators used in robot-assisted surgery are equipped with laparoscopic tools as end effectors to augment the hand movements of the surgeon with precision. With robot assistance, surgeons can perform complex procedures inside the human body with high dexterity. However, the continuum robotics research community has challenged the lack of intuitive and effective operation of the surgical tools. Much uncertainty still exists about the tool-tissue interactions which have associated risks of tissue damage caused by unreliable control and articulation of the tool. This problem is further exacerbated by the limited visualization resolution of internal organs of the human body for safe operation. There is a pressing need to develop continuum manipulators with improved maneuverability and control to reach difficult-to-access surgical sites accurately.

The aforementioned challenges of MIS play a critical role in the design and development of surgical continuum manipulators. The concept of compliant mechanisms (CMs) has been central to the design of various surgical devices. CMs are flexible mechanisms that use elastic deformation to transfer or transform force, motion, or energy. Devices made of CMs are generally monolithic in nature which leads to simplified fabrication, no wear, no friction, therefore, beneficial in high precision applications. CMs and their sub-components are increasingly used to enhance the range of motion and articulation of surgical continuum manipulators. Recently, magnetic actuation has emerged as a powerful means to execute several surgical functions such as instrument positioning, navigation, grasping, resection, and retraction. Magnetic actuation coupled with CMs has considerable impact in the design of miniaturized manipulators that eliminates the need for any cables tethered for control. Furthermore, accurate modeling of the continuum manipulators and integration of embedded sensing have been effective in the localization of manipulators. Real-time three-dimensional (3D) shape sensing of manipulators in tandem with medical imaging modalities aids in

the safe control of the manipulators.

Another significant area of research for surgical continuum manipulators is stiffness controllability. Evidence suggests that variable stiffness mechanisms can be leveraged to achieve specific functions like grasping, exerting forces, and locomotion. Continuum manipulators designed using variable stiffness mechanisms make the best use of flexibility and rigidity when it comes to surgical applications. While softness promotes high flexibility, rigidity is important for precision and load bearing. These attributes promote soft yet stable interactions of the manipulator with the tissue.

The main objective of this doctoral research is the development of magnetically-actuated multi-functional surgical continuum manipulators with embedded sensing. The manipulators are designed to address the following key challenges: (1) Design and fabrication of miniaturized flexible manipulators with a working channel, (2) accurate modeling and shape sensing of continuum manipulators, (3) actuation and control strategies to enhance the maneuverability and manipulation capabilities. The overall structure of this dissertation takes the form of three parts and includes seven chapters. **Chapter 1** begins by introducing the field of MIS, the use of continuum manipulators for surgical interventions and discusses the challenges in the surgical applications. It then proceeds to describe the research objectives and the list of publications resulting from this research.

Part I of this dissertation is a rigorous investigation on CMs for surgical applications. **Chapter 2** is a survey reviewing the surgical devices that use CMs for broadly five functions: (i) Grasping and cutting, (ii) reachability and steerability, (iii) transmission, (iv) sensing, and (v) implants and deployable devices. The design of CMs are assessed focusing on five key aspects: (i) Conceptual design and synthesis, (ii) analysis, (iii) materials, (iv) manufacturing, and (v) actuation. **Chapter 3** presents a new design of a flexure-based compliant continuum manipulator which is magnetically-actuated. The design is based on the idea of mechanical motion constraints to limit the stresses in the flexures. The steerability of the manipulator is demonstrated using a 2D Helmholtz coil magnetic actuation setup in a gelatin phantom under the guidance of ultrasound imaging. **Chapter 4** follows on to study the motion characteristics of the spatial bending of the manipulator using a 3D magnetic actuation setup (PaCMag). An intra-operative shape sensing method combining a quasi-static model based on rigid-link modeling and fiber Bragg grating (FBG) sensors is proposed. A closed-loop control strategy to trace different trajectories with the tip of the manipulator is demonstrated. Clinical feasibility of the manipulator as a steerable catheter is shown in phantoms of a bifurcating artery and a heart with the guidance of a miniature camera.

Part II explores the concept of variable stiffness mechanisms for surgical applications focusing on grasping and shape locking. **Chapter 5** presents a magnetically-actuated variable stiffness robot (VSR). It is made of a soft magnetic elastomer with a sliding nitinol backbone. The synchronised retraction of the backbone with magnetic actuation leads to high deformation coiling action of the VSR. The grasping of objects of varying diameters in closed-loop using visual feedback is demonstrated. **Chapter 6** presents a novel design of a magnetically-actuated variable stiffness manipulator (VSM) based on shape memory polymers (SMPs). The VSM is composed of two nested concentric silicone tubes enclosed within two SMP springs, and a permanent magnet at its tip. The VSM exhibits variable stiffness and variable bending curvatures at variable working lengths. Potential applications of the VSM capable of shape locking are demonstrated in endoscopy, biopsy and laser surgery using robotic magnetic actuation.

Part III concludes the dissertation by discussing the results of the five studies (**Chapters 2-6**) conducted in this research. **Chapter 7** begins by laying out the conclusions focusing on three key themes: 1) Design and fabrication, 2) modeling and sensing, 3) actuation and control. It concludes by providing directions on future research and an outlook. While the scope of this doctoral research was limited to laboratory experiments, it paves the way towards the design of the next generation of surgical continuum manipulators with embedded sensing and stiffening to strengthen the competence of the state of the art surgical interventions.

Contents

1

Introduction

Technological advances in minimally invasive surgery (MIS) have paved the way for widespread use of continuum manipulators in robot-assisted surgical interventions. MIS comprises a set of surgical procedures that requires only small cuts to be made on the human body and slender instruments are inserted to perform the surgery. Natural orifice transluminal endoscopic surgery (NOTES) is a surgical technique in which abdominal operations are performed by inserting an endoscope through a natural orifice (oral, rectal, vaginal, vesical), thus leaving no scar. Surgical procedures have evolved over the years to work in tandem with continuum manipulators due to their inherent compliance, high dexterity and precision in carrying out the surgery. The goal of this doctoral research is to develop continuum manipulators which are controlled using magnetic fields for surgical applications. Compliant mechanisms and variable stiffness mechanisms are explored to design these manipulators to facilitate insertion, navigation, and perform different surgical tasks. Furthermore, closed-loop control strategies with the integration of optical sensors are investigated for improved localization and precision in steering and manipulation. This chapter begins with a brief history of MIS, followed by the introduction of continuum manipulators for MIS and the associated challenges. Thereafter, it continues on with the research objectives and concludes with the list of publications that resulted as part of this doctoral study.

1.1 Evolution of Minimally Invasive Surgery

The origins of MIS can be traced back to as early as 5000 years ago in ancient civilizations of Egypt, Mesopotamia, Greece and Rome [1]. Around 3000 BC, the Sumerians devised small copper knives to perform surgery, and are known to have even developed soft malleable catheters using gold. Around 600 BC, Sushruta who was an ancient Indian surgeon classified several types of surgical instruments including the early endoscopes used for inspecting ear, nose, and mouth [2]. He also detailed different sizes of rectal specula having two apertures which were used for inspection, cautery and treatment of haemorrhoids (Fig. 1.1). Hippocrates, an ancient Greek physician of circa 460 BC, now credited with the historic Hippocratic Oath, reported the use of a variety of surgical instruments and catheters [3]. Around 1000 AD, Albucasis, who was an Arab surgeon, wrote a thirty-volume medical encyclopedia describing over 200 surgical instruments including different kinds of probes, surgical knives, scalpels, and hooks (Fig. 1.1) [4].

The different approaches for MIS to access and inspect the internal body organs were investigated extensively in the first two millennia AD. It was not until 1806 that Phillipp Bozzini of Germany invented the original endoscope with lighting for urological views, made from a vase-shaped leather-lined box that held a candle [6]. In the following decades, different forms of illumination using alcohol-turpentine flame and paraffin lamp were investigated to extend the usage of the endoscopes to examine auditory canal, pharynx, and larynx. The rigid scopes posed challenges as their use steered towards gastrointestinal tract, raising the need for designing flexible scopes with illumination [7]. The advent of the fiber optic technology in the 1950s made it possible to transmit light through thin, long strands of flexible glass fibers. With glass-encased fiberscope as a successful visualizing technology, colonoscopy was officially recognized in 1967 [8]. Technological innovations progressed the development of more laparoscopic tools like uterine manipulator, knot-tying instruments for performing tubal ligation and appendectomy in the late 1970s [9]. The first high-resolution video camera for laparoscopy was developed in 1982 enabling the projection of magnified images of the surgical site on a monitor. There was a steady rise in designing innovative surgical tools like endoloops, harmonic scalpel, and ultrasound shears [10].

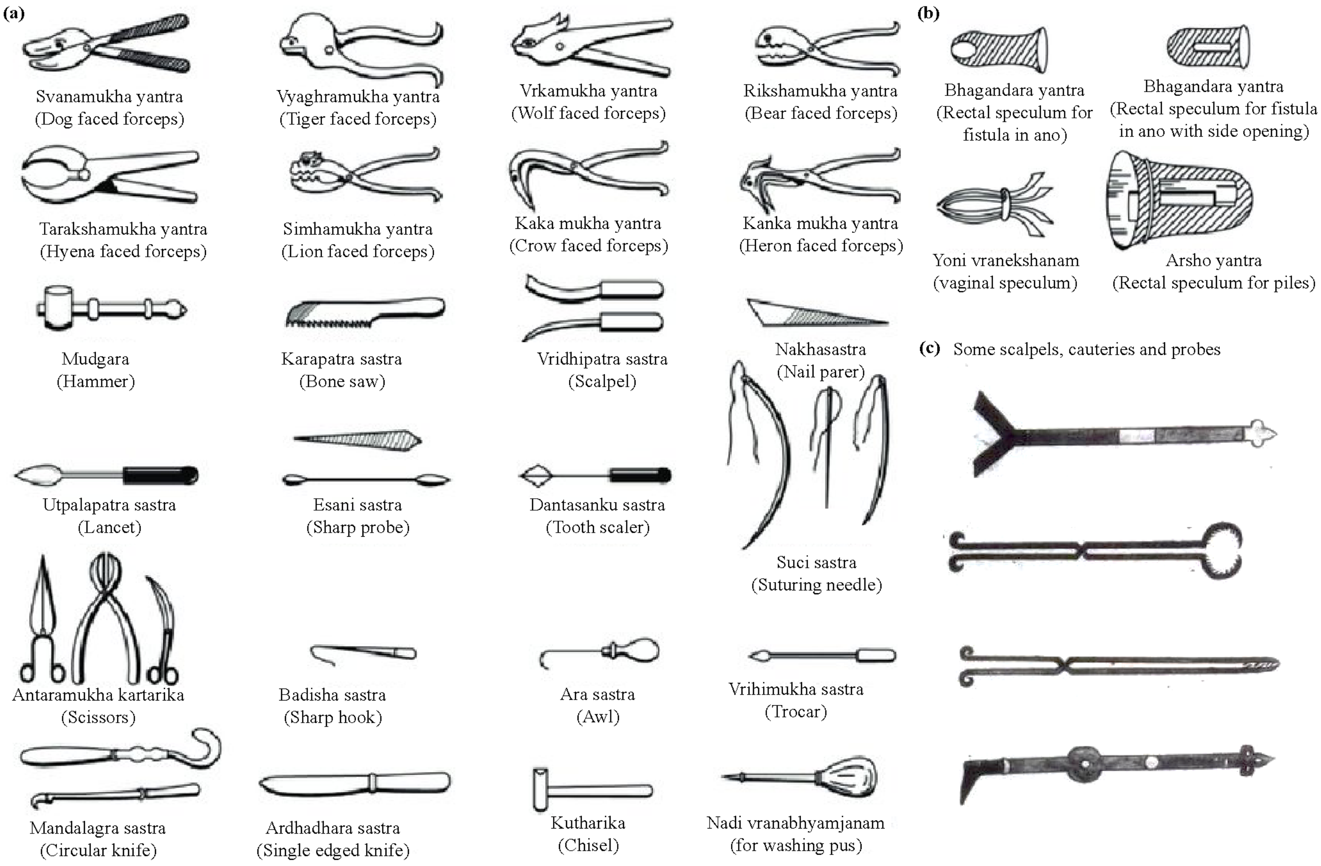

Figure 1.1: (a) Ancient surgical instruments from the Sushruta Samhita [2]. (b) Endoscopes from the Sushruta Samhita [2]. (c) Medieval surgical instruments from Albucasis's Kitab al-Tasrif [5].

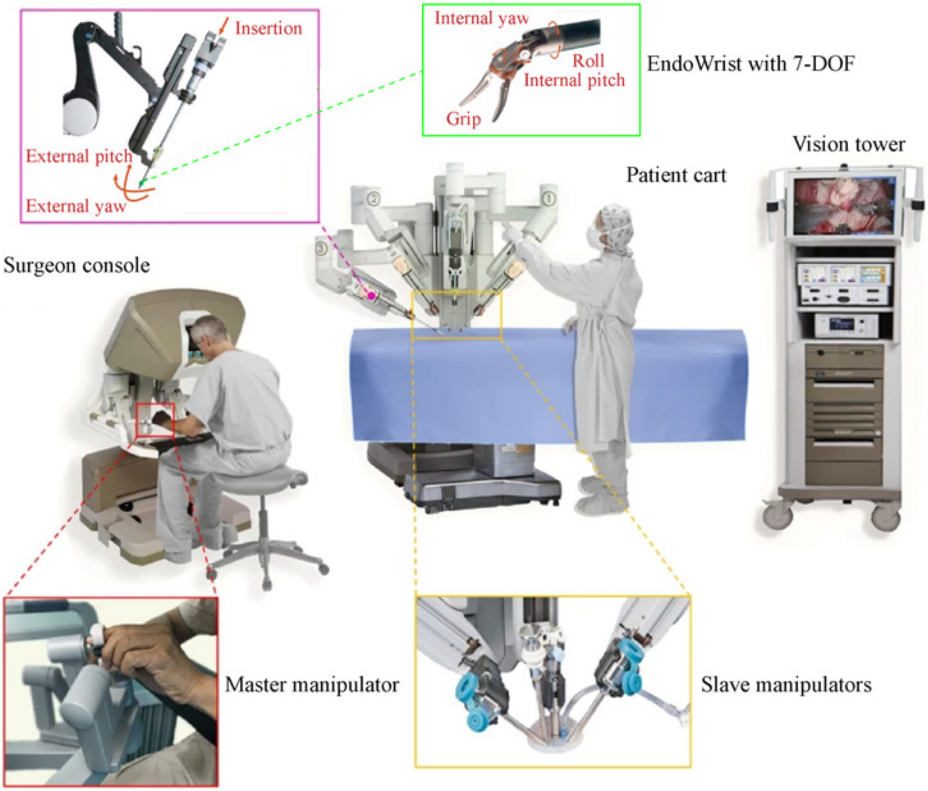

Figure 1.2: The da Vinci Robotic Surgical System, adapted from [11].

MIS became the preferred choice over open surgery with the explosion of novel laparoscopic techniques as it involves small incisions to be made on patients resulting in faster recovery and shorter hospital stays. However, concerns remained about the limited dexterity in articulation of laparoscopic instruments and the lack of tactile feedback, opening the avenue for robotic surgeries [3]. In 1985, the first known surgical robot, PUMA 360 was used to perform neurosurgical biopsies accurately. Subsequently in 1988, PROBOT was developed for the transurethral resection of the prostate. In 1992, ROBODOC became the first active robotic system approved by the federal Food and Drug Administration (FDA) for hip replacement surgery. By the late 1990s, the da Vinci Surgical System, and the

Automated Endoscopic System for Optimal Positioning (AESOP) which was later relaunched as the ZEUS operating system were developed. These systems enabled surgeons to precisely control various surgical instruments using voice commands, and robotic arms that mimic the hand movements of the surgeon who is situated in a distant console from the patient and equipped with a 3D laparoscopic view (Fig. 1.2) [12]. The modern era of MIS has embraced robot-assisted surgeries with proven competence in supplementing the surgeon's skills.

1.2 Continuum Manipulators for Surgical Interventions

Continuum manipulators are used in robot-assisted surgical interventions to maneuver in tortuous pathways of human vasculature, manipulate instruments, and perform surgical functions with high dexterity. A continuum manipulator is a long, tubular robotic device that can change its shape similar to an elephant's trunk or an octopus's tentacles. Such manipulators are increasingly being used for diverse surgical applications including but not limited to laparoscopy, ablation, otolaryngology surgery, cardiac surgery, and urologic surgery as shown in Fig. 1.3 [13].

Continuum manipulators can be classified based on their actuation method into three groups: extrinsic, intrinsic, and hybrid [24]. The actuation takes place outside the structure of the manipulator through mechanical linkage in extrinsic actuation, whereas, the actuation occurs within the main structure of the manipulator in intrinsic actuation. Hybrid actuation uses a combination of both extrinsic and intrinsic actuations. Extrinsic actuation methods include cable-driven actuation, multi-backbone structures and concentric-tube transmission. Extrinsically-actuated manipulators can often be miniaturized because of the remotely located actuators. Intrinsic actuation methods include pneumatic and hydraulic actuation, and smart materials. Pneumatic/hydraulic actuated manipulators tend to be lightweight and have fast reaction speed. Smart materials used in actuation include shape memory alloy (SMA), shape memory polymer (SMP), and electro active polymer (EAP). They are lightweight, have high energy density, and operate without noise [25].

Variable stiffness manipulators are an emerging class of continuum ma-

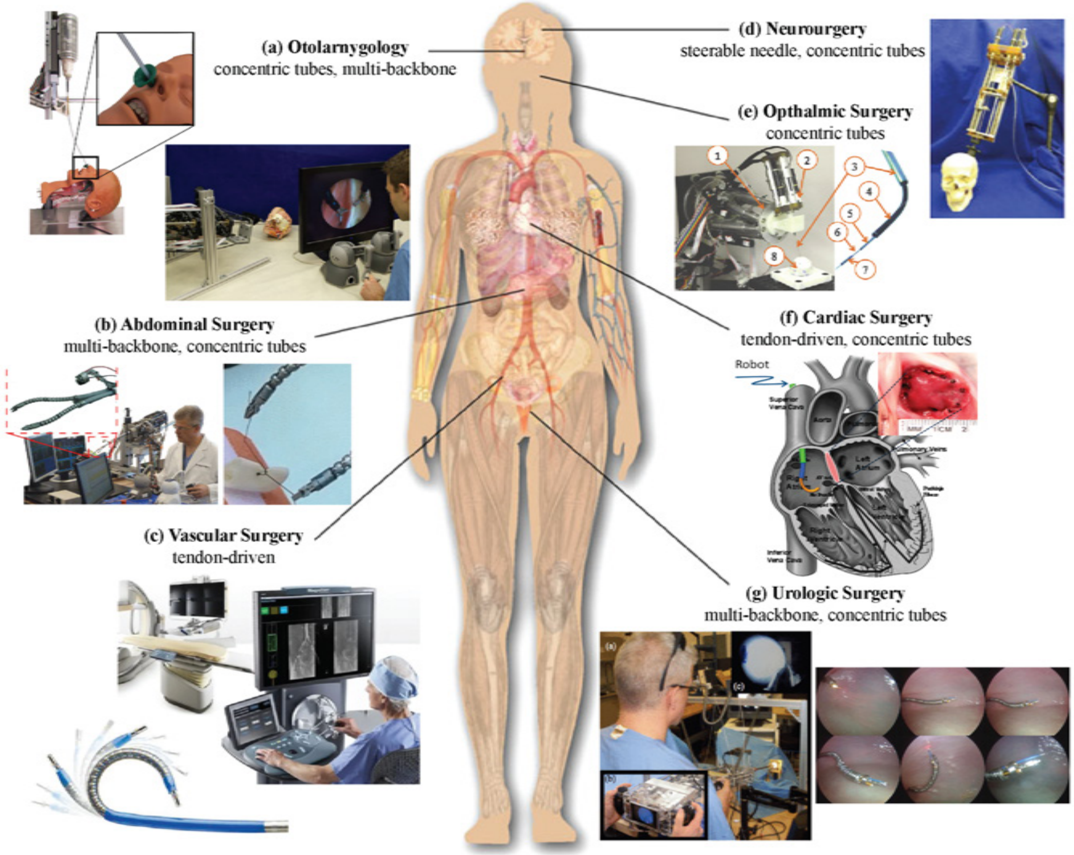

Figure 1.3: Various surgical applications of continuum manipulators, adapted from [13]. (a) Otolaryngology [14], [15], (b) abdominal surgery [16], (c) vascular surgery [17], [18], (d) neurosurgery [19], (e) opthalmic surgery [20], (f) cardiac surgery [21], (g) urologic surgery [22], [23].

nipulators with tunable stiffness properties, embodying the characteristics of both soft and rigid body elements [26]. Although rigidity is crucial for high motion accuracy and exerting high forces, softness is advantageous because it imparts high flexibility. Variable stiffness methods for continuum manipulators can be classified into three categories: mechanism-based, materials-based and acoustic-based [27]. Mechanism-based methods include antagonistic actuation, drive-rod-locking mechanism, central-cable-tensioning mechanism, and layer/granular jamming [28], [29]. Materials-based methods use materials like electro-rheological fluid (ERF), magneto-rheological fluid (MRF), low melting point alloy (LMPA), SMP, and EAP, which exhibit variable stiffness when triggered by an external stimulus [30]–[33]. Acoustic-based method is a new potential way to alter stiffness using acoustic waves that change particle arrangement [34]. There is an ongoing investigation on novel stiffness modulation methods for surgical applications requiring soft interactions in unstructured environments and steady movement [35].

In recent years, there has been an increasing interest in the use of magnetic actuation for endovascular interventions [36]. Continuum manipulators embedded with permanent magnets and/or magnetic particles dispersed in a soft polymer matrix can be actuated using external magnetic fields [37]. Magnetic actuation facilitates development of miniaturized manipulators that result in a wireless system for control. For example, a 4 mm flexible catheter (NaviStar-RMT, Biosense Webster, Inc., California, USA) integrated with small permanent magnets was developed for cardiovascular interventions [38]. Commercial systems based on remote magnetic navigation like the Niobe magnetic navigation system (Stereotaxis, Inc., Missouri, USA) are available to control such magnetic catheters for ablation procedures (Fig. 1.4) [39]. In other work, a submillimeter-scale ferromagnetic soft continuum robot with a hydrogel skin grown on its surface was proposed for steering and navigation in narrow and complex human vasculature [40]. There is a growing trend towards designing advanced magnetically-actuated continuum manipulators which are modular and multi-functional to cater to various surgical applications.

Figure 1.4: Commercially available magnetic actuation systems: (a) Stereotaxis Niobe Robotic Magnetic Navigation System [41] (b) Aeon Phocus, interventional robotic system [42] (c) Catheter Guidance Control and Imaging (CGCI) system [43]

1.3 Challenges in Surgical Applications

Despite the advantages of continuum manipulators for surgical applications, there is still some uncertainty in bringing them closer to clinical practice. Extrinsically actuated continuum manipulators having cables or pre-curved tubes for navigation to the surgical site suffer from friction, hysteresis and require bulky actuation units. Compliant continuum manipulators with notched-tube designs made of different shapes and patterns of notches that offer flexibility have been investigated [44]. Such manipulators enhance the steerability and range of reach of the surgical tools [45], [46]. However, they are prone to mechanical failure due to stress concentrations and fatigue. To date, only a few studies have examined the virtues of variable stiffness manipulators which exhibit both rigid and soft behaviour [47]. The mechanisms that underpin the stiffness characterization of such manipulators to achieve specific surgical tasks like grasping and navigation are not fully understood.

The growing body of literature on continuum designs has investigated the accurate modeling and control of the continuum manipulators [48]. Constant curvature approximation is a classical modeling approach which has limitations when the actual deflection of the manipulator does not comply with the circular arc approximation [49]. Cosserat-rod theory is a geometrically-exact model commonly used for soft manipulators. This model can become computationally expensive when closed-form solutions are necessary [50]. Rigid-link model is a simplified approach based on well-established kinematic and dynamic models which can be efficiently adopted for control and sensing purposes [51]. However, it becomes difficult to determine the exact location and stiffness approximation of the joints of a continuum structure.

Closed-loop control strategies are necessary for safe means of operation of manipulators to negate the inaccuracies in modelling. Sensory feedback can provide measurement of the internal state of the manipulator as well as the external disturbances [52]. However, this poses challenges in sensor integration, especially for surgical applications owing to the decreased size of the manipulator, and compatibility with the human anatomy and imaging modalities [53]. The most widely used clinical imaging modalities are computed tomography (CT), magnetic resonance imaging (MRI), and ultrasound (US) imaging. Although these techniques are reasonably accurate in imaging the inside of the human body, there are some limitations. CT uses a series of X-rays which can be harmful with excess exposure. MRI uses very strong magnetic fields and makes noise. It requires the patient to stay still for a prolonged period of time which can be uncomfortable. It is difficult to acquire real-time image sequence from both CT and MRI. US imaging is portable in design, uses high-frequency sound waves, and does not use radiation. But it has limited spatial imaging resolution and is susceptible to imaging artefacts.

There is a growing trend towards investigating real-time 3D shape

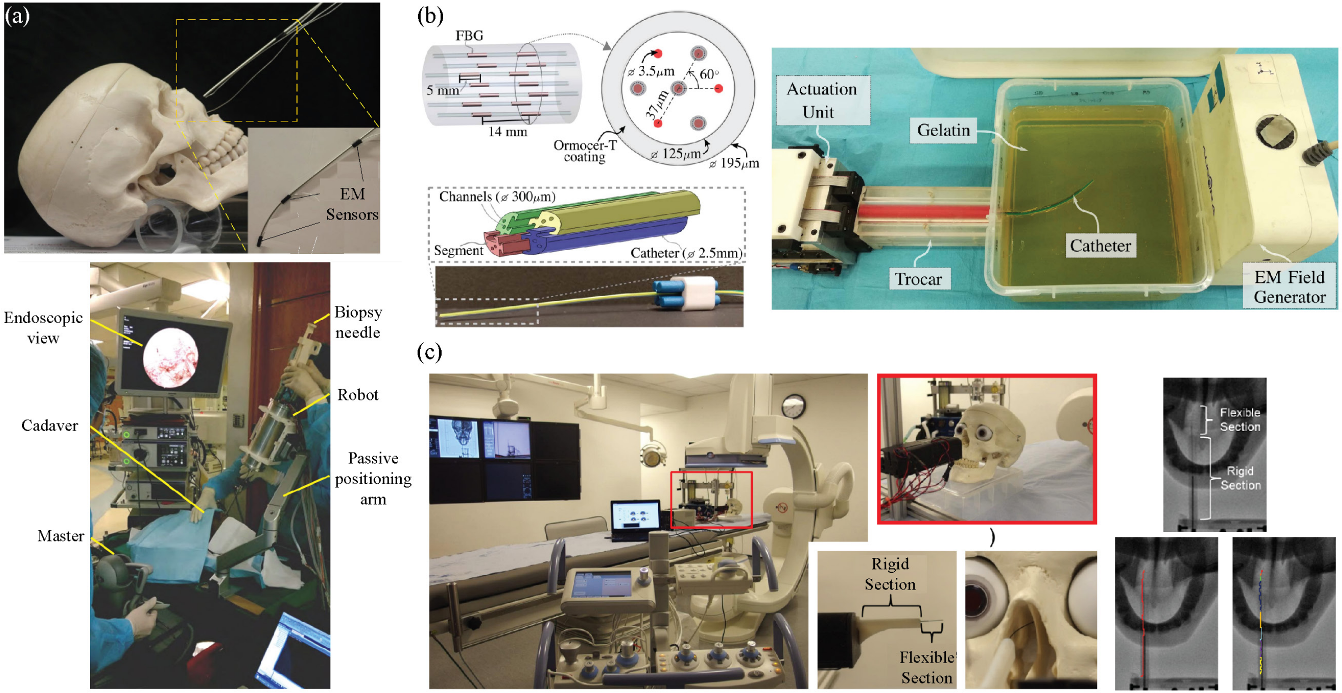

Figure 1.5: Shape sensing techniques for continuum manipulators in minimally invasives surgery: (a) Electromagnetic (EM)-based tracking of a continuum tubular robot for nasopharyngeal biopsy [54]. (b) Fiber Bragg gratings (FBG) sensors used for shape reconstruction of a catheter [55]. (c) Shape-sensing technique fusing X-ray fluoroscopy with the kinematics model of a concentric tube robot [56].

sensing technologies for surgical manipulators which are based on: fiber-optic-sensor, electromagnetic-tracking, and intraoperative imaging modality shape reconstruction methods (Fig. 1.5) [57]. Shape sensing using fiber Bragg gratings (FBG) sensors has great potential, as the sensors are very flexible, easy to integrate with the manipulator and are known to be biocompatible [58]. However, the careful placement and distribution of the fragile sensors along the length of the manipulator is essential to minimize error accumulation in strain measurements. In the case of electromagnetic-tracking, the accuracy is affected by the presence of ferromagnetic and conductive metal components like electric motors and magnets in its vicinity [59]. There has been extensive research on fusion of intraoperative imaging modalities like fluoroscopy and US imaging with kinematic models of the manipulators to improve the accuracy of shape tracking [56], [60]. Thus, there is an ongoing quest for an accurate real-time shape sensing technique that can be seamlessly integrated in the design of surgical manipulators and is suitable with the surgical workflow.

1.4 Research Objectives

The challenges in MIS have been the primary driving factor in the development of the continuum manipulators presented in this work. The following research questions (RQs) are identified in the areas of design, sensing and control of surgical continuum manipulators.

RQ.1

How are compliant mechanisms used in the design of surgical devices to achieve various functions like grasping and enhancing range of motion?

Compliant mechanisms (CMs) can be found all around us in paper clips, bottle lids, and mouse buttons. Over the years, the applications of CMs have grown remarkably in a variety of fields such as aerospace, transportation, microelectromechanical systems (MEMS), robotics, and medical devices [61]. CMs tend to be monolithic or jointless structures leading to easy fabrication without any assembly. CMs are mechanically efficient without incurring any losses due to wear, friction or backlash and can be used to attain high precision. The multitude of advantages of CMs can be capitalized to perform surgical tasks like grasping and cutting. Literature search revealed several studies which use CMs for surgical applications ranging from laparoscopy to robot-assisted surgeries. Surprisingly, there is a lack of a detailed account of CM design approach that can be categorically applied by researchers with little to no experience in the MIS field. The aim is to contribute to this growing area of research by reviewing all the applications of CMs in surgical interventions and providing a comprehensive analysis of the different design aspects.

RQ.2

Can a miniaturized monolithic continuum manipulator which is magnetically actuated, be designed for precise motion in surgical applications?

Compliant continuum manipulators can be classified based on their basic transmission units into several types such as concentric tube manipulators, origami-based manipulators, and compliant joint manipulators [62]. A wide range of compliant joints like blade flexures, contact-aided joints and rolling contact joint have been used in the design of the compliant manipulators to enhance steerability and range of motion [63]. Compliant joints can increase precision in motion due to the absence of relative motion and can be easily miniaturized by using external means of actuation. However, such joints are impaired by stress concentrations due to geometric irregularities, fatigue, and buckling. These challenges have been addressed in previous work by making geometric changes like rounding corners and gradually increasing the depth of cut from proximal to distal end of the manipulator [44]. This thesis examines the way in which a miniaturized manipulator composed of compliant joints can be designed with mechanical constraints to limit the stresses. It determines whether such a compliant design of manipulator can be precisely controlled and maneuvered using external magnetic fields.

RQ.3

Can the compliant design of continuum manipulators complement fiber optic sensing modalities in improving the localization of surgical continuum manipulators?

Real-time 3D shape sensing is a major research challenge within the field of continuum manipulators for MIS [13]. Of particular concern is the difficulty in incorporating shape sensors in the small size of the surgical manipulators. FBG sensing is one of the more feasible ways of shape sensing among other methods like electromagnetic-tracking, as FBG sensors are very thin, flexible, and compatible with magnetic actuation. But they are prone to errors caused by the positioning, orientation, and distribution of the sensors on the manipulator. While seeking the advantages of a compliant design of surgical manipulators for steering, the extent to which kinematic modeling can boost the shape sensing of such a manipulator integrated with FBG sensors is investigated. An attempt to develop a shape sensing methodology for surgical manipulators that works concurrently with existing intraoperative imaging is made to enhance the steering accuracy of the targeted surgical intervention [57].

RQ.4

Can variable stiffness mechanisms be used in the design of surgical continuum manipulators to perform functions of grasping and surgical tool insertion?

Soft continuum manipulators can adapt, operate safely in complex environment and less likely to cause damage [64]. However, existing soft manipulators are not adequately capable of tasks requiring high load capacity and precision. Recently, variable stiffness mechanisms for manipulators have piqued the attention of researchers in this regard. Previous research has suggested granular/particle jamming methods, electrostatic and pneumatic forces for tuning the stiffness. Lightweight actuator designs in the form of snake-like manipulators and grippers are possible using layer jamming mechanisms [65], [66]. An octopus arm-like manipulator based on a pneumatic extending actuator connected by tendons was developed which can squeeze through narrow openings in soft state and used for high force applications in rigid state [67]. LMPA and SMP which exhibit variable stiffness with temperature change have been used in the design of variable stiffness catheters [68], [69]. The high temperature requirements and slow response time of these phase-change materials limit their clinical feasibility. This dissertation seeks to examine the emerging role of variable stiffness manipulators in the context of performing surgical tasks like grasping and surgical tool insertion with a focus on mechanism-based and materials-based stiffening.

1.5 Thesis Outline

This doctoral thesis is organized into three parts with seven chapters to address the aforementioned research questions. The five chapters in **Part I** and **Part II** form part of the research studies either published or under review in international peer-reviewed journals.

Part I makes major contributions to the research on compliant mechanisms. **Chapter 2** addresses **RQ. 1** and is the first study to undertake an in-depth analysis of CMs for surgical interventions in the form of a survey. It provides a comprehensive assessment of design methodologies, material selection and failure prevention, fabrication and actuation methods. The surgical applications of CMs are reviewed in an interpretative manner to provide new insights into the integration of CMs in the development of surgical devices. **Chapter 3** presents a novel miniaturized monolithic compliant manipulator design combined with magnetic actuation. A distributed compliant design with built-in mechanical motion constraints that can limit the stress is proposed. A proof-of-concept study attempts to answer **RQ. 2** and demonstrate the accurate maneuvering of the manipulator as a steerable surgical manipulator by examining its motion characteristics and guiding it in a gelatin phantom through water medium with US imaging. **Chapter 4** proposes an intraoperative localization alternative for the compliant manipulator answering **RQ. 3,** and analyses its efficacy in closed-loop control path planning experiments. Furthermore, clinical feasibility of the manipulator is shown in phantoms of a bifurcating artery and a heart with integration of a miniature camera.

Part II illuminates the concept of variable stiffness mechanisms for surgical applications focusing on **RQ. 4**. **Chapter 5** introduces a variable stiffness robot (VSR) made of soft magnetic elastomer with nitinol backbone for grasping purposes. Closed-loop control experiments are conducted to demonstrate the high deformation coiling ability of the robot to grasp objects of varying sizes. **Chapter 6** presents a magnetically-actuated variable stiffness manipulator (VSM) based on SMP springs. This study describes the design and implementation of a deployable VSM with shape locking ability that can facilitate the surgical tool insertion and manipulation. Potential clinical applications in endoscopy, biopsy, and laser surgery are demonstrated using robotic magnetic actuation. Throughout this thesis, the terms 'VSR' and 'VSM' refer to the manipulators developed in **Chapter 5** and **Chapter 6**, respectively.

Part III presents the main findings of the doctoral research, focusing on the design, modeling, sensing and control themes of surgical manipulators. **Chapter 7** begins by reporting the important contributions and concludes by offering valuable insights for future research.

1.6 Research Framework

All the research studies that constitute this doctoral thesis have been supported by the funds from the European Research Council (ERC) under the European Union's Horizon 2020 Research and Innovation Programme (ERC Proof of Concept) under Grant #790088: Project INSPIRE, and the Netherlands Organization for Scientific Research (Innovational Research Incentives Scheme - VIDI: SAMURAI (Steering Actuated Probes under Magnetic- and Ultrasound-Guidance for Targeted Interventions) project #14855). All the studies presented in this thesis have been performed with the experimental setups at the Surgical Robotics Laboratory (SRL), in the Department of Biomechanical Engineering of the University of Twente, Enschede, the Netherlands.

1.7 Scientific Output

The studies presented in this doctoral thesis have been a part of the following articles that have been published or under review in the following international peer-reviewed journals:

1. **T. L. Thomas**, V. Kalpathy Venkiteswaran, G. K. Ananthasuresh, and S. Misra, "A Monolithic Compliant Continuum Manipulator: A

Proof-of-Concept Study," *Journal of Mechanisms and Robotics*, vol. 12, pp. 061006, December 2020.

2. **T. L. Thomas**, V. Kalpathy Venkiteswaran, G. K. Ananthasuresh, and S. Misra, "Surgical Applications of Compliant Mechanisms: A Review," *Journal of Mechanisms and Robotics*, vol. 13, pp. 020801, April 2021.
3. **T. L. Thomas**, J. Sikorski, G. K. Ananthasuresh, V. Kalpathy Venkiteswaran, and S. Misra, "Design, Sensing, and Control of a Magnetic Compliant Continuum Manipulator," *IEEE Transactions on Medical Robotics and Bionics*, vol. 4, no. 4, pp. 910-921, November 2022.
4. P. Lloyd, **T. L. Thomas**, V. Kalpathy Venkiteswaran, G. Pittiglio, J. H. Chandler, P. Valdastri and S. Misra, "A Magnetically-Actuated Coiling Soft Robot with Variable Stiffness," *IEEE Robotics and Automation Letters*, special issue on *Small-Scale Robots in the Medical Context, From Modeling and Fabrication to Clinical Applications*, October 2022 (Under Review).
5. **T. L. Thomas**, J. Bos, J. J. Huaroto, V. Kalpathy Venkiteswaran, and S. Misra, "A Magnetically-actuated Variable Stiffness Manipulator based on Deployable Shape Memory Polymer Springs," *Advanced Intelligent Systems*, special issue of *Soft Robotics Across Scales: Fundamentals and Applications*, February 2023 (In Press).

The following abstract submission was presented at a national symposium:

- **T. L. Thomas**, V. Kalpathy Venkiteswaran, and S. Misra, "A magnetically controllable variable stiffness surgical manipulator based on shape memory polymers," in *Proceedings of the Summer School and Symposium on Soft Robotics in Healthcare*, TU Delft, Netherlands, September 2022.

I

Compliant Mechanisms

Preface

Compliant mechanisms (CMs) have become an integral part of a wide range of technologies in the field of robotics, microelectromechanical systems (MEMS) and biomedical devices, among others. CMs play an emerging role in diverse applications due to their several advantages over traditional rigid-body mechanisms. CMs reduce part count, streamline fabrication process, increase precision by reducing or eliminating friction, backlash and wear. However, CMs are affected by stress concentrations and fatigue. Energy storage in the elastic members of CMs has a profound effect on the input-output efficiency and mechanical advantage. This part of the dissertation seeks to expand our understanding of how CMs can be used to their full potential in the context of surgical interventions.

Chapter 2 begins by systematically reviewing the literature on CMs to examine the changing nature of CMs in a broad range of surgical devices. The pivotal role of CMs in the state of the art is identified based on their functions and classified into five major groups: (i) Grasping and cutting, (ii) reachability and steerability, (iii) transmission, (iv) sensing, and (v) implants and deployable devices. The challenges and future research directions for integration of CMs in the development of safe and dexterous surgical devices are discussed. Chapter 3 presents a new design of a compliant continuum manipulator which is magnetically actuated for precise motion. A flexure-based design with mechanical stops to limit the stress concentrations is fabricated, and actuated using a 2D magnetic actuation setup based on Helmholtz coils. The steerability of the manipulator is demonstrated in a simulated arterial system and a gelatin phantom using ultrasound imaging. Chapter 4 investigates the spatial bending of the manipulator and an intraoperative shape sensing scheme combining quasi-static model with FBG sensor-based shape reconstruction. A closed-loop control strategy to trace different trajectories with the manipulator in a 3D electromagnetic setup (PaCMag) is demonstrated. The maneuverability of the manipulator is validated in phantoms of a bifurcating artery and a heart using a miniature camera.

2

Surgical Applications of Compliant Mechanisms: A Review

Note: *The following chapter is adapted from the article "Surgical Applications of Compliant Mechanisms: A Review" by* ***T. L. Thomas****, V. Kalpathy Venkiteswaran, G. K. Ananthasuresh, and S. Misra, published in "Journal of Mechanisms and Robotics", vol. 13, pp. 020801, April 2021. The chapter has been reformatted in terms of figures and tables to fit this doctoral thesis. No changes to the technical contents of this peer-reviewed manuscript have been made.*

Authors' Contributions: *S. Misra and T. L. Thomas conceived the study. T. L. Thomas collected the papers, conducted the analysis and interpretation, and prepared the manuscript. V. Kalpathy Venkiteswaran contributed to the analysis and interpretation, and supervised the manuscript preparation. G. K. Ananthasuresh verified the analysis and interpretation, and supplemented the papers collected for review. S. Misra supervised the overall manuscript preparation.*

Abstract

Current surgical devices are mostly rigid and are made of stiff materials, even though their predominant use is on soft and wet tissues. With the emergence of compliant mechanisms (CMs), surgical tools can be designed to be flexible and made using soft materials. CMs offer many advantages like monolithic fabrication, high precision, no wear, no friction and no need

for lubrication. It is therefore beneficial to consolidate the developments in this field and point to challenges ahead. With this objective, in this chapter, we review the application of CMs to surgical interventions. The scope of the review covers five aspects that are important in the development of surgical devices: (i) Conceptual design and synthesis, (ii) analysis, (iii) materials, (iv) manufacturing, and (v) actuation. Furthermore, the surgical applications of CMs are assessed by classification into five major groups, namely, (i) Grasping and cutting, (ii) reachability and steerability, (iii) transmission, (iv) sensing, (v) implants and deployable devices. The scope and prospects of surgical devices using CMs are also discussed.

2.1 Introduction

Compliant mechanisms (CMs) are designed to achieve transfer or transformation of motion, force, or energy through elastic deformation of flexible elements. Devices that implement CMs can be traced back to as early as 8000 BC in the form of bows, which were the primary hunting tools [70]. While reviewing the history of urethral catheterization, Bloom *et al.* [71] noted that ancient Chinese medical texts used lacquer-coated compliant tubular leaves of allium fistulosum (bunched onion) as catheters. They also mention that Sushruta, the author of ancient Indian surgical text, described tubes of gold and silver coated with ghee (clarified butter) used for catheterization. Ancient Greek and Roman surgeons too are known to have used flexible silver tubes in surgery. Over the years, CMs have seen several applications in surgical procedures. Furthermore, the applications of CMs have been extended to aerospace and automotive industries, microelectromechanical systems (MEMS), actuators and sensors, high precision instruments, and robots [72], [73].

CMs have gained significant attention in the last few decades as they offer many advantages over traditional rigid-body mechanisms. A CM has monolithic structure, which reduces the number of assembly steps, thus simplifying the fabrication process and requiring reduced maintenance [74]. High precision is attained and the need for lubrication is eliminated due to absence of contact among members that causes wear, friction, backlash, and noise [75].

The merits of CMs have led to a proliferation of studies that implement CM, especially in the medical field [76]. Many variants of CMs have been designed as surgical devices to perform various functions. The structural compliance integrated in the main body of a device is exploited to perform object manipulation tasks such as grasping, cutting, retracting and suturing for surgical procedures in the form of ablation, laproscopy, endoscopy, and biopsy, to mention a few. Additionally, easy miniaturization of CMs enables the device to reach remote difficult-to-access surgical sites as seen in the design of several continuum manipulators [13]. CMs also serve a secondary function in the device to transmit force/motion, as observed in some surgical robots [77], [78]. Applications of CMs are found in microactuators, MEMS and micro-scale surgical devices as well [79]–[82]. Force sensing using CMs to monitor tool-tissue interaction has also been demonstrated, which serves as a feedback for safe operation of the device inside the human body [83], [84]. The potential of CMs made using biocompatible materials has been realized in the development of biomedical implants, stents and deployable devices [85]–[87].

There is a growing body of literature that provides a useful account of the design process of CMs [75], [88]. However, there is no detailed investigation into the different aspects to be considered while designing surgical devices using CMs. It poses a problem for those with little to no experience in the medical field on what approach to follow, to go from initial concept to final prototype. This chapter aims to provide an overview of this process which involves five major aspects: (i) CM conceptual design and synthesis, (ii) analysis, (iii) material selection, (iv) fabrication methods, and (v) actuation methods. Furthermore, this chapter also reviews the existing literature on surgical devices that use CMs by classification into five major groups: (i) grasping and cutting, (ii) reachability and steerability, (iii) transmission, (iv) sensing, (v) implants and deployable devices. We conclude this chapter by addressing the associated challenges and provide an outlook on future scope.

2.2 Design Aspects

This section presents the various methods used during the design process of surgical devices that use CMs. The process begins with synthesis of the CM, followed by optimization to satisfy the intended functional requirements and constraints are identified. Various methods of generating or synthesizing CMs have been explored by researchers. Howell [73] describes four techniques used in the synthesis of CMs: Freedom and Constraint Topologies (FACT); Building Blocks; Topology Optimization; and Rigid-Body-Replacement. Hegde and Ananthasuresh [89], [90] introduced a Selection Maps method for conceptual design and synthesis of CMs. The five aforementioned synthesis methods are explained briefly in Table 2.1. However, many compliant surgical devices are designed without explicit use of these conventional synthesis methods. This may be because the synthesis methods developed for CMs mostly apply to input-output transmission characteristics rather than guiding and maneuvering. The scope of the expected functions of surgical devices, described later in the chapter, offers a huge opportunity for designers. Therefore, the synthesis methods and subsequent classification of devices is not discussed in detail in this review.

During synthesis of CM, selection of suitable material is crucial to ensure failure prevention. It is generally desirable to have large deformation of a CM, while ensuring the strain is small and the stress stays within limits. This depends on the Young's modulus and the failure strength of the material. From a clinical standpoint, other criteria that need to be considered are the biocompatibility, chemical resistance, elasticity, transparency, strength, temperature resistance, and most importantly, sterilizability of the chosen material [91]. Table 2.2 describes the materials and different fabrication methods that are suitable for making surgical devices. The four commonly used 3D printing technologies for rapid prototyping compliant surgical devices are also described in Table 2.2. While punching and blanking technique is used in meso-scale compliant grippers, electrical discharge machining (EDM) is most widely used for micro-scale fabrication of flexure-based continuum manipulators and grippers. Pop-up book MEMS fabrication is an emerging multi-material technique of fabricating MEMS and micro-scale surgical devices. Milling and laser cutting are conventional subtractive manufacturing methods used for surgical manipulators and their constituent parts like wrist and end effector. Although injection molding was not typically used in the making of surgical devices reviewed in this chapter, it is an economical way of mass manufacturing implants and medical plastics.

The method of actuation is an important aspect to be considered in the design of a CM. Based on the specific function that the CM serves in the design, various actuation methods have been demonstrated in literature. Table 2.3 presents commonly-used actuation methods of CMs which are suited to surgical applications, along with their advantages and limitations. Cable-driven actuation is the most widely used method among continuum manipulators and steerable instruments. Shape memory alloys (SMAs) and piezoelectric materials are seen more in high precision devices and for micro/nano manipulation. While fluidic actuation is used in few flexible surgical instruments, there is a gradual increase towards the use of magnetic actuation in designing surgical devices for precise contactless control.

2.3 Surgical Applications

This section presents a review of the different surgical applications of CMs. The applications of CMs in surgical devices can be broadly classified into five major groups: (i) grasping and cutting, (ii) reachability and steerability, (iii) transmission, (iv) sensing, and (v) implants and deployable devices. Fig. 2.1 is an overview of this classification showing examples of surgical devices designed for each of these groups of applications, while Fig. 2.2 depicts the distribution of the number of surgical devices in each group. These are explored in detail in the remainder of this section.

2.3.1 Grasping and Cutting

CMs have been used to develop forceps, scissors, graspers, and needle holders for performing different surgical tasks such as grasping, cutting, suturing, and holding tissue. For instance, Frecker *et al.* [181], [188] designed a multifunctional compliant instrument with forceps and scissors using topology optimization and fabricated a 5.0 mm diameter stainless steel prototype. Subsequently, a miniaturized prototype was developed by applying size and shape optimization [180], [189]. Recently, a compliant forceps with serpentine flexures was designed to overcome the problem of parallel motion found in traditional forceps with 'U' shaped flexure [190]. Cronin *et al.* [179] demonstrated an endoscopic suturing instrument by optimizing a compliant design that provides sufficient puncture force with maximum distal opening of the suture arms.

Several forms of grasping tools have been investigated which utilize the flexibility and stiffness that a CM can offer with different geometry, materials and fabrication techniques. For example, an underactuated compliant gripper made of five phalanges was designed to have large shape-adaptation

Table 2.1: Description of synthesis methods for Compliant Mechanisms (CMs), stating their applications and limitations. References of work relevant to each method are provided in square brackets. Numbers in **bold** refer to the papers that describe the general approach of the method and numbers in *italics* refer to the surgical devices reviewed in this chapter which are designed using the particular method.

Synthesis Method	Description	Applications and Limitations
Topology Optimization [**92**]–[**94**]*[86], [95]–[98]*	Uses optimization algorithms to search for best CM topology to realize the design objective, subject to desired requirements and constraints generally through finite element methods.	• Most widely-used CM synthesizing method within surgical devices, with its ability to generate solutions from a wide design space. • Difficult to account for localized stresses and buckling. Resulting topologies are sometimes difficult to manufacture, warranting 3D printing or post-processing for manufacturing.
Building Blocks [**99**], [**100**]*[101], [102]*	Two main approaches based on: (i) instant centers and compliance ellipsoids, and (ii) flexible building blocks and optimization.	• Synthesizing CMs with intermediate to large deflections. • Infeasible geometry may result depending on the chosen basic building block.
Freedom and Constraint Topologies (FACT) [**103**]–[**105**] *[none]*	Provides topological solution for known freedom space and constraint space based on screw theory, in which twists and wrenches are used to represent constraints and degree-of-freedoms of compliant elements.	• Synthesizing CMs with small to intermediate deflections. • Research on large deformation analysis and representation of elastomechanics, dynamics characteristics and parasitic errors is limited.

Synthesis Method	Description	Applications and Limitations
Rigid-Body-Replacement [70], [106]–[108]*[102]*, *[109]*, *[110]*	Utilizes the pseudo-rigid-body model to replace compliant members and joints with equivalent rigid links and movable joints, with springs for capturing elastic deformation energy.	• Reduced-order method that relies on established rigid-body kinematics methods, providing more intuitive analysis. • Accuracy of analysis suffers with increase in the complexity of CM.
Selection Maps [89], [90], [111]–[113] *[none]*	Uses a catalog of CMs whose inherent stiffness and inertia characteristics are captured in two-port spring-lever and spring-mass-lever models for matching the user-specifications for the purpose of selection.	• Can incorporate practical considerations of material selection, manufacturability, strength, and scaling. • Limited to single-input-single-output CMs at present.

Table 2.2: Description of fabrication methods and materials suitable for compliant mechanisms (CMs) in surgical applications. The pros (+) and cons (–) of each method are described, along with examples of surgical devices made using the given method. Numbers of references are given in square brackets.

	Fabrication Method	Materials	Surgical Devices	Pros and Cons
Subtractive Manufacturing	**Milling** [114]–[120]	Metals like stainless steel, aluminium and titanium. Plastics like nylon, acrylonitrile butadiene styrene (ABS), polyether ether ketone (PEEK), polyvinyl chloride (PVC).	Surgical manipulators and associated supports like wrist, fixtures and end-effector.	+ Accurate, precise and repeatable machining applicable on a wide variety of materials. – High initial machinery and tooling costs. – Difficult to model complex 3D parts.
	Laser Cutting [121]–[124]	Plastics like acrylic, ABS and delrin. And metals like stainless steel, aluminium and titanium.	Endoscopic manipulators and surgical tooltips with intricate patterned cuts.	+ Contactless cutting with accuracy and speed. – Not suitable for cutting parts with very wide thickness. – Releases toxic fumes that needs good ventilation provision.
Mass Manufacturing	**Injection Molding** [91], [125]–[127]	Plastics like polyvinyl chloride (PVC), styrene acrylonitrile copolymer (SAN), polycarbonate (PC), and polyester. Metals like titanium alloys.	Surgical implants and medical plastics.	+ Efficient and economic manufacturing method that is automated to produce high output in one step. – High inital tooling costs and long lead times. – For high fatigue resistance and increased lifetime, mold designs for CMs should orient the polymer chain in specific directions.

	Fabrication Method	Materials	Surgical Devices	Pros and Cons
Micro-scale Fabrication	**Electrical Discharge Machining (EDM)** [110], [119], [120], [128]–[138]	Conductive materials like titanium, inconel and kovar.	Miniature components like coronary stents, implants, grippers and micro-scale flexures for compliant manipulators.	+ Suitable to fabricate biocompatible surfaces as it can create an oxide layer on the surface to enhance biological attachment. – Expensive. – Fabricating parts with complex shapes require specially designed fixtures and takes more time.
	Pop-up Book MEMS Fabrication [81], [82], [139]	3D multi-material fabrication using a flexible polyimide layer (Kapton®, by DuPont de Nemours, Inc.) and structural layers (304 Stainless Steel), with adhesive (Dupont FR1500 acrylic adhesive).	MEMS and micro-surgical devices.	+ Monolithic meso- and micro-structures made can be inserted through small incisions and 'pop-up' to perform their function. + Soft fluidic micro-actuators can also be integrated in the fabrication process. – Risk of peel failure. – Castellated hinge failure due to stress concentrations.
	Punching and Blanking [140]	Sheet form of metals like steel, aluminium and plastics. like PEEK, nylon and delrin.	Meso-scale compliant grippers.	+ Low cost and fast process. – Cutting complex geometry is difficult. – Negatively affects the quality of edges of cut-out part.

Fabrication Method		Materials	Surgical Devices	Pros and Cons
Rapid Prototyping	**PolyJet** [141]–[147]	Biocompatible materials like MED625FLX, MED610 and MED620.	Flexible surgical manipulators, tooltips and catheters.	+ Suitable for small parts with intricate details and printed with high precision. – Vulnerable to heat and light degradation. – Provides limited mechanical strength.
	Stereolithography (SL) [148]–[150]	Photopolymer resins.	Flexible surgical instruments and surgical robot joints.	
	Selective Laser Sintering (SLS) [77], [98], [151]–[153]	Biocompatible polymers such as polyetheretherketone (PEEK), poly(vinyl alcohol) (PVA), polycaprolactone (PCL) and poly(L-lactic acid) (PLLA).	Surgical robot joints.	+ Uses a wide-variety of materials that provide good mechanical performance. – Expensive. – Produces rough surface finish.
	Selective Laser Melting (SLM) [115], [154], [155]	Biocompatible metals like steel, titanium alloys and cobalt-chrome.	Surgical continuum manipulators with flexure hinges and bone implants.	

Table 2.3: Description of actuation methods for surgical devices, stating their advantages (+) and limitations (–) in surgical applications and integration with CMs. Numbers of references are given in square brackets.

Actuation Method	Surgical Applications	Integration with Compliant Mechanisms
Cable-driven actuation [78], [137], [138], [153], [156]–[160]	Surgical robotic systems and flexible surgical instruments. + Uses lightweight and flexible cables for deformation of the structure. – Miniaturization is challenging due to the associated cables and moment arms.	+ Ability to transmit force/motion to remote joints and application points enables convenient location of the actuation unit away from the workspace of the device. – High pretension in cable is necessary to reduce backlash and hysteresis.
Shape memory alloys (SMAs) [161]–[167]	Internal actuators for instruments like biopsy forceps, hingeless graspers, endoscopic and laparoscopic instruments, among others. Also used in stents, stent grafts and in orthopaedics as correction rods and fracture fixators. + Similar hysteresis behaviour with bone and tendons and low sensitivity to MRI. + Shape memory effect provides a collapsible form during insertion and expands after deployment. – Limited by rise in temperature caused by heating.	+ Reliable control on actuating CM by training the SMA to fine-tune the performance. + Offers high power-to-weight ratio. + Easy to embed in complex structures. – Generally activated by Joule heating while deactivation takes place via convection heat transfer, which leads to a slow response time.

Actuation Method	Surgical Applications	Integration with Compliant Mechanisms
Piezoelectric materials [131], [147], [168]–[171]	Actuators for micro/nano manipulation. + Delivers sub-nanometer positioning accuracy and is compact in size. – Expensive to fabricate.	+ Offers high response speed. + Large force-to-weight ratio. – Limited by low strain range. – Transmission of forces to remote location is challenging.
Magnetic actuation [?], [110], [143], [172]–[174]	Endoscopic devices and surgical instruments with inherent compliance. + Precise positioning and control.	+ Enables contactless actuation of CM. – Adversely affected upon scaling to large surgical workspace.
Flexible fluidic actuators [82], [120], [175]	Flexible surgical instruments. + Safe to operate under radiation and magnetic fields. + Ability of the inflatable membranes to lose and regain their shape facilitates the insertion of instrument inside a patient's body.	+ Causes no relative motion between parts, no wear and there is no need for lubrication. – Risk of leakages, and controlling pressure is more complex when compared to electrical signals used in motors and other conventional actuators.

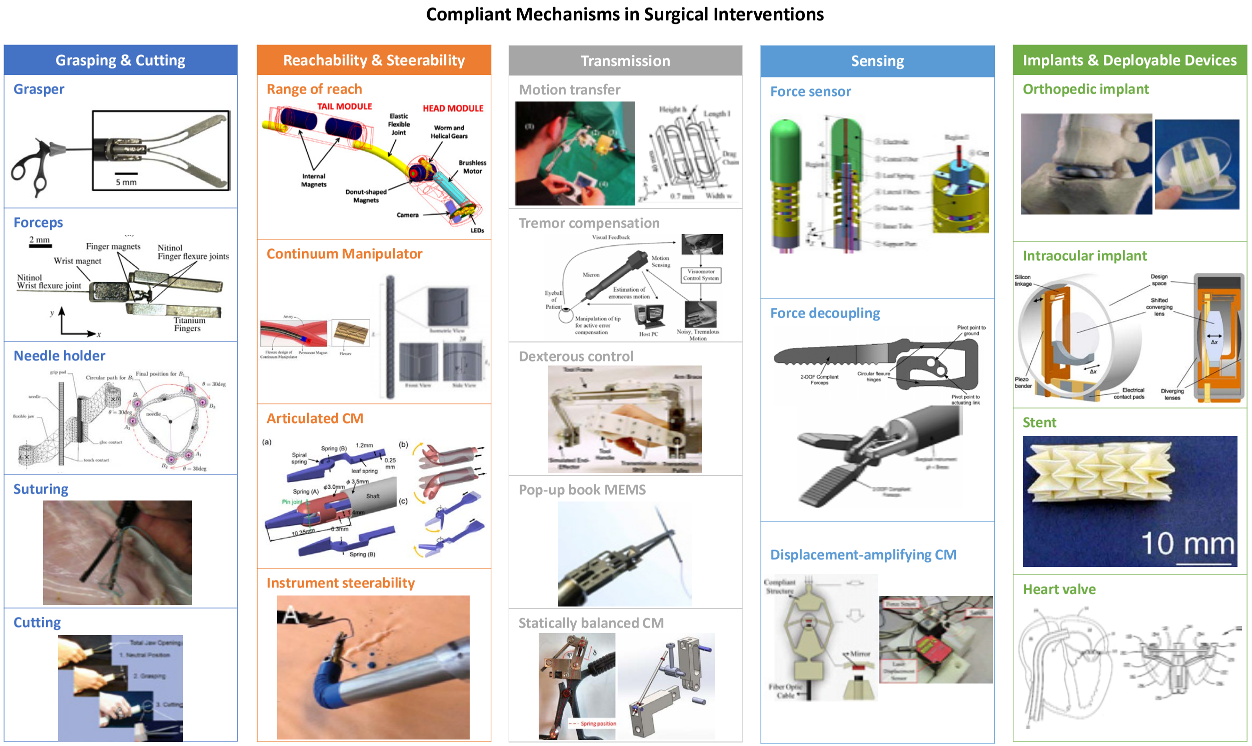

Figure 2.1: An overview of different surgical applications of compliant mechanisms (CMs). Courtesy of images: Grasper [176], [177]; Forceps [174]; Needle holder [178]; Suturing [179]; Cutting [180], [181]); Range of reach [173]; Continuum Manipulator [110]; Articulated CM [182]; Instrument steerability [122]; Motion transfer [77]; Tremor compensation [149]; Dexterous control [183]; Pop-up book MEMS [139]; Statically balanced CM [177]; Force sensor [184]; Force decoupling [84]; Displacement-amplifying CM [185]; Orthopedic implant [85]; Intraocular implant [186]; Stent [164]; Heart valve [187].

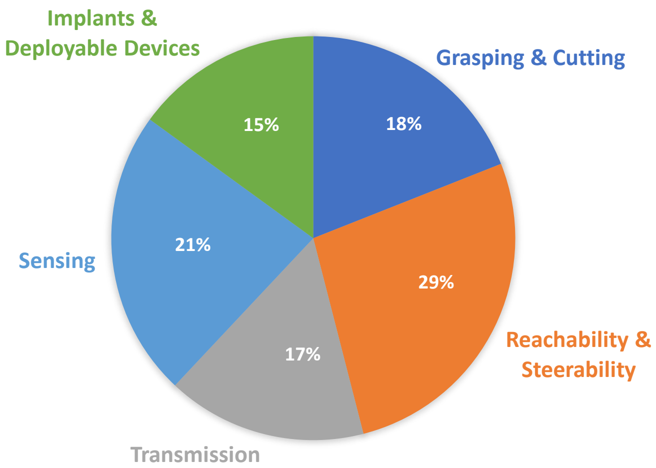

Figure 2.2: Contribution of different surgical applications of compliant mechanisms, showing the distribution of the number of surgical devices reviewed in this chapter in each application group.

capability and the deformation was shared by many joints so as to increase the lifetime of the device [133]. A polymer-based MIS shaft instrument was developed using a hybrid effector mechanism combining compliant joints and conventional pin joints [120]. A three-fingered laparoscopic grasper for finger articulation was designed using flexures, leading to distribution of the grasping force, and thereby minimizing tissue perforation [191]. A multi-material design was utilized for a compliant narrow-gauge surgical forceps for laparoscopic and endoscopic procedures [192]. Large grasping forces were realized through a hybrid design approach by having some regions with high stiffness and other regions with greater flexibility to provide larger jaw openings. In subsequent work, a design optimization routine was carried out to maximize the tool performance, validating the grasping potential of a meso-scale contact-aided compliant forceps [193], [194]. Recently, the grasping performance of a compliant surgical grasper was enhanced by functional grading which introduces material with elastic nonlinearity at certain segments of the grasper, while reducing the maximum overall stress [176].

The introduction of robot-assisted surgery has led to many designs of CM-based grasping end effectors, in order to deliver efficient manipulation with high dexterity. Piccin *et al.* [178] showed that a flexible needle grasping device for medical robots has a higher threshold force and stiffness before slipping, compared to a rigid-body needle grasping device. In another work by Forbrigger *et al.* [174], the distal dexterity of a brain tissue resection robot was enhanced by a magnetically-driven forceps made with flexible beams and eliminating the need for an external mechanical or electrical transmission to actuate the end effector.

The monolithic nature of CMs makes them easier to fabricate when compared to the pivoted jaw configurations of current grasping tools [195]. Hence, CM was used in developing a disposable compliant forceps for HIV patients in which, the Q-joints methods was employed to replace a conventional pin-joint [196]. Later, Sun *et al.* [98] synthesized the shape of a disposable compliant forceps for traditional open surgical applications using topology optimization. Subsequently, an adaptive grasping function of the forceps to overcome damaging sensitive organs during both open surgery and robot-assisted minimally invasive surgery (MIS) was devised using topology optimization [160].

At micrometer scale, CM-based microgrippers and micromanipulators have been developed based on flexure hinges and cantilever beam structures. A microgripper made up of piezoelectric bending unimorphs was demonstrated by Haddab *et al.*[169]. Accurate manipulation of a hybrid compliant gripper was achieved using a combination of flexure hinges and a bias spring [131]. Ease in grasping and accurate tool positioning of a micro-forceps was provided by optimizing the jaw design to minimize actuation force, internal stresses, and size [197]. Yang *et al.* [198] demonstrated the opening and closing of the jaws of a compliant micrograsper and micro-cutter for ophthalmic surgery, by using a cylindrical package tube pulled through the device. While the use of CMs contributes to the elimination of Coulomb friction and backlash, they have some inherent drawbacks. As noted in the design of a low cost flexure-based handheld mechanism for micromanipulation, a drift in the major axis is caused by the imperfect rotation of most compliant joints [147]. Flexure hinges have limited range of angular motion depending on the geometry and material properties of the hinge, and cantilever structures fail to produce perfect parallel motion [131], [199]. However, topology optimization aided by intuition has been used to design CM grippers with parallel-jaw motion.

2.3.2 Reachability and Steerability

This section describes applications of CMs to increase range of motion and enhance steerability of the surgical instruments to reach difficult to reach surgical sites inside the body. Single-port laproscopic and endoscopic procedures are adversely affected by limited maneuverability of surgical instruments through confined spaces and narrow visual view inside the human body. Therefore, a steerable endoscopic instrument was developed using three coaxial tubes that slide together concentrically to form a single tube [122]. The design offers additional flexibility due to narrow cuts in the tube and more room in the lumen as the steering mechanism resides in the tubular wall. A review on the different joint types used in the steerable tips of MIS instruments is described by Jelínek *et al.* [63]. To maximize the span of an endoscopic camera, Simi *et al.* [173] modelled a compliant joint in a magnetic levitation system and potential to reduce instrument collision inside the body was shown. Similarly, a flexure-based foldable and steerable CM was reported for providing stereo vision capture in laparoscopic surgery with a pair of miniature cameras [200].

Continuum manipulators are devices that can be precisely steered inside the body to reach difficult-to-access surgical sites. CMs have been used to design flexible miniaturized continuum manipulators for robot-assisted surgery. For example, a 2 degree-of-freedom (DoF) flexible distal tip for enhanced dexterity of endoscopic robot surgery was constructed with a flexible tube cut into a structure consisting of a series of rings connected by thin elastic joints [137], [201]. A similar design was used in a flexible micro manipulator for neurosurgery [138], [202]. A two-section tendon-driven continuum robot with a backbone cut into flexures from a pipe was designed to enhance tip positioning and offer large viewing angles in endoscopic surgery [45], [203]. A multi-arm snake-like robot for MIS was developed using flexible overtube structure as a spine which guides endoscope and other instruments, and two manipulator arms at its tip made of three separate flexure hinge sections [153]. Since beam flexure structures suffer from stress concentrations in the corners, as well as fatigue, a snake-like surgical robot composed of flexible joints based on helical spring was designed [155]. Furthermore, to prevent axial compression, circular rolling contacts were introduced at each turn of the helix. Recently, a contactless mode of actuation and steering of a monolithic metallic compliant continuum manipulator with flexures using magnetic fields was demonstrated [110].

Notched-tube compliant joint mechanisms are variants of aforementioned continuum manipulators, where different shapes, sizes and patterns of notches made on tubes can enable different DoFs and range of motion [44]. For instance, a flexible manipulator arm for single port access abdominal surgery was made from a superelastic nitinol tube with triangular notches [204]–[207]. A needle-sized wrist made from a nitinol tube with rectangular cutouts was developed to increase the DoF and dexterity of needle laparoscopic surgery (needlescopy) surgical tools [116], [208]. Eastwood *et al.* [209] designed asymmetric notch joints for surgical robots and noted that decreasing the joint's tube diameter and increasing notch depth favours compact bending of the manipulator, but leads to significant reduction in stiffness. Hence, a contact-aided compliant notched-tube joint for surgical manipulation was introduced to improve the stiffness and bending compactness, while operating in confined workspaces [44]. In another work, a cable-driven dexterous continuum manipulator (DCM) comprising two nested superelastic nitinol tubes with notches was designed for removing osteolytic lesions with enhanced volumetric exploration [46], [132], [210]–[216]. In subsequent work, a flexible ring currette made of thin and long pre-curved ring nitinol strips was designed to pass through the open lumen of the DCM [217]. The integration of DCM to a da Vinci actuation box (Intuitive Surgical, Inc., USA) as a hand-held actuator was also shown [136], [218]. In related work, a flexible cutter and an actuation unit to control the DCM were designed to study its buckling behavior during the cutting procedure [219]. The designs of a debriding tool that passes through the lumen of DCM and a steerable drill following a curved-drilling approach to remove lesions were also investigated [220], [221]. Subsequently, by using the curved drilling technique, a bendable medical screw made of two arrays of orthogonal notches along its shaft was devised for internal fixation of bone fractures [135], [222].

Concentric tube robots (CTRs) are a special type of continuum manipulators that are made of multiple precurved elastic tubes that are concentrically nested within one another [223]. CTRs have been deployed for "follow-the-leader" insertion and their steering is not affected by the tissue interaction forces [224]. Thus, they have found several applications as steerable needles and miniaturized surgical manipulators [225].

Some surgical manipulators rely on CMs to enhance articulation. For instance, a compliant articulation structure for surgical tool tips using nitinol was designed to increase the functional workspace and deliver a large blocked force [226]. Other work studied the use of corner-filleted flexure hinge-based compliant joints in a compliant grasper integrated to a 2-DoF surgical tooltip, and circular guide members were added to strengthen the load carrying capacity of the slender compliant joints [142]. Later, a 3-DoF surgical tooltip with modified serpentine flexures and magnetic coupling was developed [143]. Arata *et al.* [227] designed a prototype of 2-DoF articulated laparoscopic surgical instrument using a CM to move two spring blades at the tip. Thereafter, a 4-DoF compliant manipulator was proposed consisting of springs designed to deform locally, reducing the bending radius [182]. A subsequent study on the variation of range of motion and rigidity of elastic moments revealed that to achieve a higher range of motion, there will be a trade-off with the lower values of output force and the precision, and vice versa [228].

The flexibility provided by CMs can be extended to positively affect some specific surgical applications. For instance, a compliant endoscopic ablation probe composed of an array of compliant tines was designed to generate target spherical heating zones, and improve the distribution of heat in the ablation zone [229], [230]. A 3 DoF microrobotic wrist for needlescopy was fabricated using MEMS technology [130], [167]. It was based on a CM derived from a reference parallel kinematics mechanism architecture with three legs, which offered increased instantaneous mobility. A compliant instrument for preparing the subtalar joint for arthroscopic joint fusion was developed, having a shaft design which was compliant in only one direction and stiff in the other two directions to resist and transmit machining forces [231]. In subsequent work, a sideways-steerable instrument joint was designed for meniscectomy that increases range of motion and reachability within the knee joint while operating through small portal of the body [232], [233]. It consisted of a compliant rolling-contact element (CORE) which was rotated by flexural steering beams configured in a parallelogram mechanism. Steerability of kinked bevel-tip needles was improved through the use of a flexure-based needle tip design while minimizing tissue damage, as the flexure keeps the needle in place during insertion [234].

2.3.3 Transmission

Transmission refers to the use of CMs in augmenting an actuator in the transfer of force, displacement or energy. In some surgical devices, CMs made for force or displacement transmission serve as an input or feedback for the principal function of the device. For example, the translation motion of a medical robot for ENT (ear, nose and throat) surgery was provided using compliant linear joints fabricated by 3D printing [77]. Yim *et al.* [172] showed passive deformation and recovery of a magnetically actuated compliant capsule endoscopic robot, by having its structure based on a Sarrus linkage and circular flexure hinges.

The traditional compliant rolling-contact element (CORE) joint involves joining two half cylinders with flexures. Derived from CORE, the Split CORE was integrated to a wrist design provided by Intuitive Surgical Inc. to create a 3 DoF gripping mechanism [150]. Lan *et al.* [78] developed an adjustable constant-force forceps for robot-assisted surgical manipulation to aid in grasping soft tissues. It employs a compliant constant-torque mechanism made using flexible arms to transmit the required force to forceps tips. The motion of a flexure-based parallel manipulator for an active handheld microsurgical instrument was tracked in order to cancel the hand tremors using piezo-actuators [149]. Awtar *et al.* [183] developed FlexDex™, a minimally invasive surgical tool frame that is attached to the surgeon's forearm to enhance dexterity and provide intuitive control. The design projects a two-DoF virtual center of rotation for the tool handle at the surgeon's wrist using transmission strips, making it stiff about one axis and compliant in the orthogonal axis.

In microsurgery applications, the concept of pop-up book MEMS has found a few applications. For example, pop-up components made of flexible hinges were designed to realize an articulating microsurgical gripper and a flexural return spring to passively open the gripper [81]. A multi-articulated robotic arm was fabricated by introducing soft elastomeric materials into the pop-up book MEMS process, and mounted on top of an endoscope model demonstrating potential surgical applications such as tissue retraction [82].

A drawback of CMs is that energy efficiency is challenged due to energy storage in the flexible members of the mechanism [235]. Herder and Van Den Berg [236] introduced the principle of a statically balanced compliant mechanism (SBCM) to circumvent this problem for a partially compliant statically balanced laparoscopic grasper (SBLG), in which a negative stiffness mechanism negates the elastic forces of the CM. Drent and Herder [237] developed a numerical optimization model for total range of motion of a SBLG with normal springs (with non-zero free length) and a constant force transfer function. Powell and Frecker [238] designed a compensation mechanism of a compliant forceps for ophthalmic surgery using a rigid link slider-crank mechanism with a nonlinear spring, which balances the potential energy of the CM. de Lange *et al.* [95] used topology optimization for a SBCM, which resulted in reduced actuation force of a SBLG. Tolou and Herder [109] modelled a partially compliant SBLG using pairs of pre-stressed initially-curved pinned-pinned beams made of linear elastic material that resulted in reduced Von Mises stress and balancing error. Hoetmer *et al.* [101] investigated a building block approach in designing SBCM, since the pseudo-rigid-body method and the topology optimization did not consider an optimization process and the stress constraints, respectively. Subsequently, the first physical demonstration of SBCM with fully compliant elements was shown by taking into account stiffness, range of motion, and stress [239]. Lassooij *et al.* [240] used pre-curved straight-guided beams that are preloaded collinear with the direction of actuation of a fully compliant SBLG with a near zero stiffness, also demonstrating its bi-stable behaviour. Earlier, Stapel and Herder [241] had carried out a feasibility study of a fully compliant SBLG using the pseudo-rigid-body method. In subsequent work, Lamers *et al.* [102] developed a fully compliant SBLG with zero stiffness and zero operation force.

2.3.4 Sensing

Sensing application refers to the use of CMs in detecting or measuring physical quantities. Several kinds of sensors rely on the change in deflection or stiffness of CMs in conjunction with other transducers like optical sensors and strain gauges to measure physical parameters. Alternatively, vision-based force sensing integrated with miniature grippers was reported by Reddy *et al.* [242]. Subsequently, a compliant end-effector to passively limit the force in tele-operated tissue-cutting using the vision-based force sensing for haptic feedback was demonstrated [114].

Force sensing forms an integral part of different surgical applications that involve tissue palpation, pulling and pushing of tissue during biopsy, to name a few. A miniature microsurgical instrument tip force sensor during robot-assisted manipulation was developed using a double-cross flexure beam configuration [243]. It can provide uniform force sensitivity in all directions at the instrument tip by altering the vertical separation between the beam crosses. A force-torque transducer based on flexural-jointed Stewart platform was integrated to an MIS instrument's tip to enable 6-axis force sensing capability [244].

Magnetic resonance imaging (MRI)-compatible force sensors, in particular, benefit from a CM-based design as the metallic and electric elements can be placed outside MRI. The force sensing element typically consists of an elastic body which deforms under the influence of an applied force, which in turn is measured by a transducer like optical fiber. For example, high accuracy and high sensitivity to displacement was demonstrated using optical micrometry by supporting the force detector with thin annular plates which convert applied force into minute displacement [245]. Later, a parallel plate structure was chosen to design a uniaxial force sensor due to its directionality and simplicity, offering better accuracy including hysteresis characteristics and axial interference than the previous design [246].

Different types of flexible elements can be adapted in the design of force sensors. Analysing the mechanical design of sensing elements, a polymer torsion beam guided in rotation by a ball bearing and supported by compliant linkages was proposed in the development of an MRI-compatible torque sensor [118]. The sensor design was further improved for a 2-DoF haptic interface by using a sensing body made of two blades fixed between the optical head and the reflective target [124]. The blade causes a displacement of the optical head upon application of force by the subject and prevents deformation in other directions, thereby minimizing cross-sensitivity. Later, an ultrasonic motor torque sensor using flexible hinges was also developed [119]. A 3-axis optical fiber force sensor for MRI applications was designed using a 3-DoF compliant platform made of 3 identical cantilever beams with their supports, offering flexibility in response to axial forces and bending moments and high stiffness to withstand axial torque [247]. A 3-axis optical force sensor made of two parallelogram-like segments of helical circular engravings that can provide intrinsic axial/ lateral overload protection during prostate needle placement was developed [248]. Similarly, a triaxial catheter tip force sensor having flexures and integrated reflector was developed for cardiac procedures [144]. The flexures are designed so that the axial and lateral forces cause different deformation of the flexures which leads to different amounts of light getting reflected and detected by the photo detectors.

A challenge with multi-axial force sensors lies in the decoupling of forces along the axes as observed in the study by Gao *et al.* [184]. Linear decoupling methods proved to be inaccurate since local deformation of flexures affects the strains measured. A method to decouple pulling and grasping forces of a 2-DOF compliant forceps was derived using the serial connections of two torsional springs which was realized by optimizing the shape of two circular-type flexure hinges [84]. However, rotational perturbation of forceps, sideway forces acting at the forceps, and fabrication errors introduced disturbances in the force measurement. Gonenc *et al.* [197] demonstrated axial-transverse force decoupling in their flexure design of micro-forceps for robot-assisted vitreoretinal surgery. Peirs *et al.* [134] decoupled the deformations caused by axial and radial forces of a micro optical force sensor for minimally invasive robotic surgery, using four identical parallelograms placed in an axisymmetric arrangement. Fifanski *et al.* [249] developed a flexure-based in-vivo force sensor that can measure forces in 3D using individual optical fibers. As flexure-based force sensors cause undesirable transverse moments, twists and lateral deflections, making it difficult to measure forces along the different axes, Tan *et al.* [96] presented a potential solution of decoupling the force measurements using topology optimization to design the elastic frame structure.

Other factors to be considered while designing force sensors include thermal sensitivity, hysteresis, plastic deformation and friction due to contact between internal components that can alter the elastic behaviour of flexures [145]. Kumar *et al.* [250] developed a force sensor using a compliant version of the Sarrus mechanism and strain gauges. Their elastic model could not address the hysteresis, viscoelastic effects, and non-linearities in the prototype caused by fabrication process. To increase the sensitivity of force sensors, Krishnan and Ananthasuresh [251] evaluated several displacement-amplifying compliant mechanisms (DaCMs) and proposed a general design methodology using application-specific topology optimization. Furthermore, a study by Turkseven and Ueda [185], [252] showed that a DaCM-based force sensor with lower sensitivity can enhance the performance of the sensor by reducing hysteresis and improving signal-to-noise ratio. CMs can also be used to passively sense force and respond in surgical situations. An instance of this was discussed in the context of endoscopy simulation [253], which could also be used in virtual surgical trials. In this work, a CM was designed to convert radial force experienced by the inner rim of a ring into circumferential motion of the ring that can be measured using an encoder.

2.3.5 Implants and Deployable Devices

Implants are medical devices embedded inside the body via surgery to replace or enhance damaged biological tissue. Within this review, different applications of implants designed using CMs are discussed. FlexSuRe™, a spinal implant based on the geometry of Lamina Emergent Torsional (LET) joint was developed to restore normal motion to the degenerate spine [254]. The LET joint is made from a lamina, and torsion of beams results in flexibility in multiple directions similar to the intervertebral disc. An intraocular implant with CM-based silicon linkages was designed to amplify the displacement of a piezoelectric bender and provide an almost tilt-free translational displacement of the lens for optical imaging quality [186]. Krucinski *et al.* [171] showed that the flexural stresses of bioprosthetic heart valves can be reduced by incorporating a flexible or expansile supporting stent into the valve design.

Within the context of this chapter, deployable devices refer to CMs designed to change in shape and size that facilitate insertion of the surgical device in a compact form to reduce invasiveness of the procedure. For example, Chen *et al.* [255] designed an intra-cardiac magnetic resonance imaging (ICMRI) catheter consisting of folded imaging coil during vascular navigation (4.5 mm in diameter). Upon deployment, it forms a circular loop (40 mm in diameter) to image a 40mm field of view. Herrmann *et al.* [187] developed a bistable heart valve prosthesis that can be folded inside a catheter and percutaneously inserted for delivery to the patient's heart for implantation. In designing cardicovascular stents, topology optimization was used to generate optimal geometry of stent cells and maximize the stiffness of the point of application of forces, thereby maintaining structural integrity [97]. However, plastic strains can cause non-uniformity in the expanded portion of the stent. Hence, James *et al.* [86] used topology optimization to design a bi-stable stent that snaps-through to a stable expanded configuration, relying on the geometric non-linearity of the structure.

Origami-based designs have emerged as a powerful tool in developing deployable devices for MIS [87]. According to Edmondson *et al.* [256], "Origami can be viewed as a compliant mechanism when folds are treated as joints and panels as links." A pair of origami-inspired surgical forceps was developed to ease the fabrication and sterilization process of robotic forceps. Increase in flexibility while maintaining rigidity was achieved by ultilizing multi-layer lamina emergent mechanisms (MLEMs) in the design process. (MLEMs are a type of CM made from multiple sheets (lamina) of material with motion out of plane of fabrication, to achieve specific design objectives [257]). Subsequently, small grippers (3 mm in diameter) were developed for the Intuitive Surgical's da Vinci robotic surgical systems which can be deployed inside the body during surgery [258]. Salerno *et al.* [163] integrated an origami parallel module to generate rotations and translation of a compliant gripper. Recently, Kuribayashi *et al.* [164] designed a self-deployable origami stent graft using hill and valley folds. Bobbert *et al.* [259] fused the origami, kirigami, and multi-stability principles to fabricate deployable meta-implants. It was also shown that the mechanical properties of the implant can gradually increase, depending on the design of kirigami cut patterns that determine the porous structures allowing bone regeneration. Halverson *et al.* [85] developed a disc implant based on CORE to mimic the biomechanics of human spine. Later, Nelson *et al.* [260] demonstrated a deployable CORE joint (D-CORE) using curved-folding origami techniques to enable transition from a flat state to a deployed functioning state. Origami works well with flexible non-metallic materials, thus making them ideal for MRI-guided procedures which is hazardous in the presence of magnetic materials. Recently, an MR-conditional SMA-based origami joint using CORE for potential applications in endoscopy was demonstrated [165].

2.4 Discussion

This study set out with the aim of assessing the utility of CMs in designing surgical devices. There are some challenges that hinder the further development and implementation of these devices in clinical practice. A drawback concerning CMs is the adverse effect of stress concentrations and fatigue, especially in flexure-based designs under cyclic loading. This is a major challenge in the medical field where device failure is not acceptable. To tackle this issue, there is a growing interest towards developing multi-material CMs [127], [261]–[263] and functional grading of CMs [176], [264], to enhance structural integrity. The emerging concept of the so-called 4D printing ushers in many more possibilities for using CMs in surgical applications [265]. This technology can strengthen mechanical properties and create multi-material programmable structures made of elastomers and soft active materials like shape memory polymers which react to environment stimuli such as temperature, moisture and magnetic field. Soft robotics is another emerging field of interest which utilizes flexibility to function but is not classified under CMs. Inspired by the softness and body compliance of biological systems, continuum devices based on soft robotics systems are designed using compliant materials [266].

The behaviour of CMs with geometric nonlinearity caused by large deflections is disregarded in many studies described in Section 2.3. Researchers have investigated this behaviour of CMs using topology synthesis and other non-linear modelling methods. It is beyond the scope of this chapter to discuss these approaches, and readers are advised to refer to the following works: [267]–[271]. An interesting finding of this study is the pivotal role of CMs in developing a new class of force sensors for surgical procedures. However, much uncertainty still exists on the underlying convoluted issues of hysteresis, plastic deformation, among others as discussed in Section 2.3.4. There is scope for improvement by analysing and understanding the deformation of flexible members of CMs under these complex conditions.

This review highlights the merits of CMs over conventional rigid body mechanisms due to elimination of joint friction, backlash, wear, and need for lubrication. This aspect is leveraged by integration of CMs with modern actuators such as magnets, SMAs, and piezoelectric materials [272]. However, a major challenge lies in analysing an overall system of CM consisting of multiple flexible members. While the monolithic nature of most of the CMs simplifies the fabrication and assembly processes, the flip side is that the whole design may fail if even one part of the mechanism breaks. It is infeasible to restore and modify CM-based designs for quick testing and improvement. Since the key functioning of CMs depends on the stiffness and the resulting deformation, accurate fabrication is critical, which can lead to higher production costs and lead time.

From a clinical standpoint, the protection of instruments from contamination due to contact with fluids is important. As a potential solution, some researchers have suggested soft elastic coating of the instrument [110], [144], [273]. However, further analysis of the implications of *in-vivo* operating conditions on the instrument's performance, while maintaining sterilization, is necessary.

2.5 Conclusions

An overview of the design aspects of CMs in surgical interventions is presented in this chapter, discussing design methodology, material selection and failure prevention, fabrication, and actuation methods. CMs provide many advantages such as reduction of assembly steps, high precision, accurancy and repeatability with the elimination of backlash, friction and wear. This study has identified the virtues of elastic deformation of compliant members in achieving desired functions tailored for diverse surgical applications including but not limited to laparoscopy, endoscopy, ablation, ENT surgery, vitreoretinal surgery, to robot-assisted surgical interventions. The challenges associated with these applications related to biocompatibility of surgical instrument, fatigue, stress concentration, energy efficiency, fabrication and complex modelling methods of CMs are discussed. The domain of CMs is a niche area of research that has seen tremendous growth in the last few decades and has raised many questions in need of further investigation. The analysis undertaken here extends our existing knowledge of CMs and offers valuable insights for future research. This would help in paving the way towards seamless integration of CMs in designing safe, dexterous, efficient and cutting-edge surgical devices.

Acknowledgment

The authors would like to thank Ms. Jyoti Sonawane for her assistance in the literature review.

3

A Monolithic Compliant Continuum Manipulator: A Proof-of-Concept Study

Note: *The following chapter is adapted from the article "A Monolithic Compliant Continuum Manipulator: A Proof-of-Concept Study" by* ***T. L. Thomas****, V. Kalpathy Venkiteswaran, G. K. Ananthasuresh, and S. Misra, published in "Journal of Mechanisms and Robotics", vol. 12, pp. 061006, December 2020.*
The chapter has been reformatted in terms of figures and tables to fit this doctoral thesis. No changes to the technical contents of this peer-reviewed manuscript have been made.

Authors' Contributions: *G. K. Ananthasuresh conceived the manipulator design. V. Kalpathy Venkiteswaran performed the design analysis for fabrication of the manipulator, designed the Helmholtz coil setup, and planned the experiments. T. L. Thomas carried out the experiments, performed the analysis and interpreted the results. V. Kalpathy Venkiteswaran contributed to the experiments, analysis and results. S. Misra supervised the project. T. L. Thomas wrote the manuscript with inputs from all the authors.*

Abstract

Continuum robots have the potential to form an effective interface between the patient and surgeon in minimally invasive procedures. Magnetic actuation has the potential for accurate catheter steering, reducing tissue trauma and decreasing radiation exposure. In this chapter, a new design of a monolithic metallic compliant continuum manipulator is presented, with flexures for precise motion. Contactless actuation is achieved using time-varying magnetic fields generated by an array of electromagnetic coils. The motion of the manipulator under magnetic actuation for planar deflection is studied. The mean errors of the theoretical model compared to experiments over three designs are found as 1.9 mm and 5.1° in estimating the in-plane position and orientation of the tip of the manipulator, respectively and 1.2 mm for the whole shape of the manipulator. Maneuverability of the manipulator is demonstrated by steering it along a path of known curvature and through a gelatin phantom which is visualized in real-time using ultrasound imaging, validating its application as a steerable surgical manipulator.

3.1 Introduction

The field of continuum robots has seen significant growth in the last few decades. The designs of snakes, elephant trunks, and octopus tentacles have encouraged researchers to devise bio-inspired hyper-reduntant robots for dexterous manipulation of objects [274]. Continuum robots have great potential within medical applications, and in particular for robot-assisted minimally invasive surgery (MIS). In current literature, the focus is on designing miniaturized manipulators which are sufficiently flexible to be steered inside the body and reach difficult-to-access surgical sites with high dexterity. Such devices find applications in neurosurgery, endoscopy, laparoscopy, biopsy and other surgical procedures in which these devices enter the body through small incisions [275], [276].

There is a growing body of literature that demonstrates many applications of continuum manipulators in MIS with different designs [13]. For example, concentric-tube robots having multiple tubes of different predetermined curvature and stiffness can cover wide geometry that enables surgical dexterity [49]. Burgner *et al.* [19] showed that an interchangeable inner tube enables easy sterilization. However, tackling snapping behavior of concentric-tube robots during manipulation remains a challenge [224]. A teleoperated multibackbone continuum manipulator with multiple instrumentation channels has been demonstrated by Goldman *et al.* [23], and Yang *et al.* [277] developed a snake-inspired robot for performing complex endoscopic tasks. Nonetheless, piston-lead screw actuation units have inherent backlash which reduces positioning accuracy and tendon-driven systems are difficult to miniaturize. Other commercially available systems such as the Sensei X by Hansen Medical, Inc. (California, U.S.), have demonstrated significant advantage in reduction of X-ray exposure [278], [279]. As the radiation exposure time of patients and physicians depends on the complexity of the procedure, such remote navigation systems have the potential to assist surgeons perform their task quickly without direct intervention [280], [281].

Over the years, surgical instruments based on compliant mechanisms have gained significant attention [76]. The use of monolithic mechanism designs reduce the number of assembly steps, thereby simplifying the fabrication process and reducing maintenance [73]. Relative motion between members is eliminated, leading to high precision, reduction in wear, friction, backlash, noise, while rendering lubrication non-essential [282]. A number of compliant mechanisms utilize flexure hinges, which are flexible members that enable relative limited rotation between two adjacent rigid members [283]. Yin and Anathasuresh have previously demonstrated the virtues of distributed compliance in flexure-based mechanisms, reducing peak stresses in the system and achieving restrained uniform local deformation [284]. Thus, flexure-based designs with reduced stress and limited local deformation, have potential for application in design of surgical devices. For instance, Swaney *et al.* [234] have designed a flexure-based steerable needle that minimizes tissue damage and Chandrasekaran *et al.* [142], [143] have developed flexure-based designs of surgical tooltip combined with magnetic coupling and tether-driven power transmission. Previously, Kim et al. have designed a continuum manipulator using creative slotting patterns of narrow necked flexures resulting in discrete compliance [285]. Flexure-based designs are also found in the backbone structures of endoscopic continuum robot designed by Kato *et al.* [45] and the Artisan Extend Control Catheter by Hansen Medical, Inc. (California, U.S.) [278], which are tendon-driven devices.

Recently, several studies have proposed magnetic actuation of surgical devices due to the advantages offered by contactless actuation, leading to compact designs [37], [286]. Static or low-frequency magnetic fields are also suitable for surgical environments because they are not harmful to humans. Commercial systems using remote magnetic navigation (RMN) are available, such as the Niobe magnetic navigation system (Stereotaxis, Inc., U.S.)

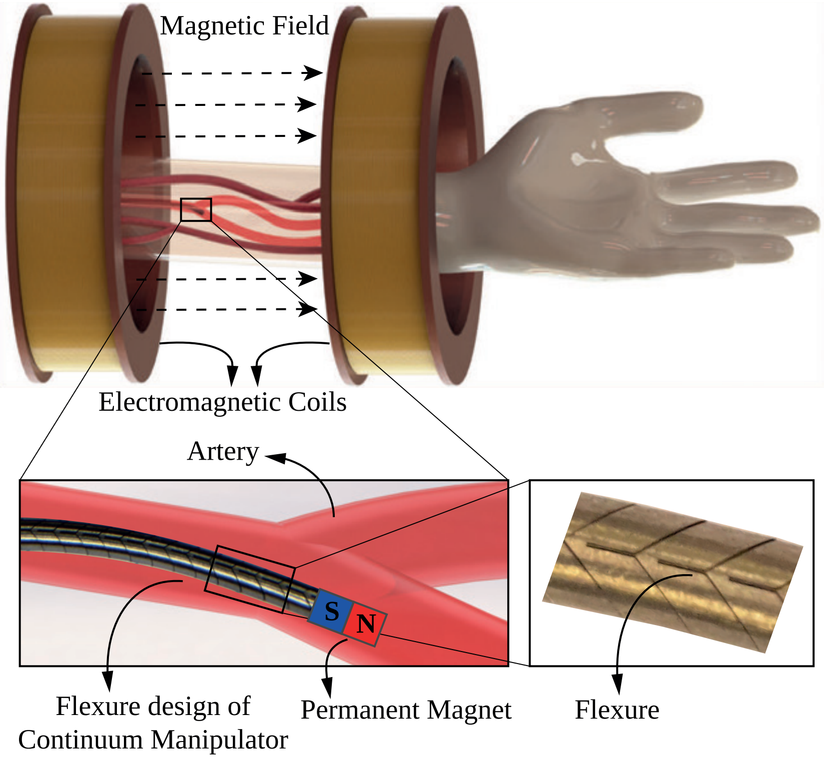

Figure 3.1: An illustration of the continuum manipulator being guided inside the arterial system of forearm by a pair of electromagnetic coils. The inset shows the continuum manipulator with a magnet at its end. The inset of the manipulator shows the flexures.

for ablation procedures with catheters equipped with small permanent magnets [287]–[289]. Multiple studies have been conducted on the use of RMN and magnetic control strategies for surgical manipulators [290]–[293]. This has heightened the need for versatile designs of magnetic catheters which are dexterous and multifunctional to perform complex surgical procedures [26], [294], [295].

This chapter describes a new design of a metallic compliant continuum manipulator capable of planar and spatial bending. The design entails a novel slotting pattern to make a segmented continuum manipulator that is capable of bending about two axes and is cut out of a monolithic tube without using assembly. The objective of this research is to demonstrate the use of a monolithic flexure-based continuum manipulator capable of precise motion using contactless actuation, thereby eliminating undesired backlash and friction, with the potential for further miniaturization. The monolithic compliant design of manipulator enables easy modeling due to linear load-deformation characteristics at individual segments of the manipulator. In contrast to other designs in literature, the manipulator described here has built-in mechanical motion constraints which restrict the maximum stress in the flexure, thereby maintaining the strength of the manipulator and leading to distributed compliance. In this work, three designs of the planar bending manipulator design are fabricated. Each of them is actuated using controlled magnetic fields by attaching a permanent magnet at its tip. Experiments are conducted to examine the motion characteristics of the manipulator under the influence of actuation loads. The potential of the manipulator as a flexible surgical manipulator which can be steered inside the body is also demonstrated. A conceptual schematic of the continuum manipulator in a surgical application actuated by electromagnetic coils is shown in Fig. 3.1.

3.2 Design of the Continuum Manipulator

In this section, the design of the metallic continuum manipulator is described. The concept of the flexures with limited range of motion is presented, followed by the details for single-axis bending, two-axis bending, and the fabrication method.

The body of the manipulator is made from a hollow metallic tube with a series of flexures created by cuts along its length, with each flexure forming an elastic rotational pair. Fig. 2(a) shows a schematic of the design, with the inset showing a cut-section. The range of motion of each flexure is physically constrained by the nature of the cut, thereby limiting the maximum stress in the flexure and preventing failure. The flexures enable bending of the manipulator about the axis perpendicular to the plane of section.

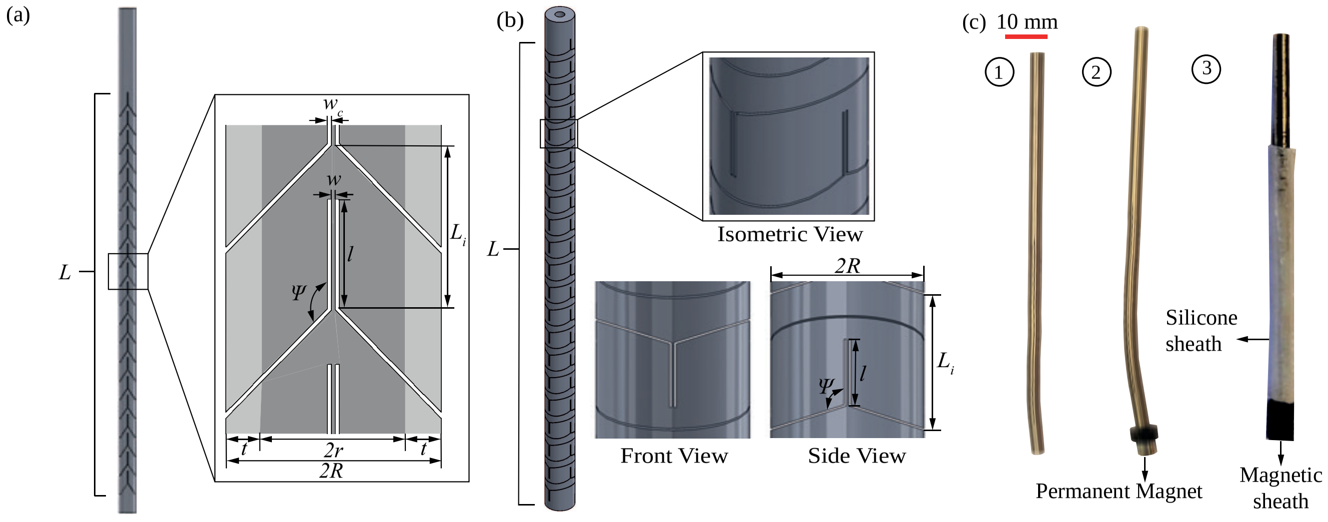

Figure 3.2: (a) Front view and section view of cross-section of single-axis bending design of manipulator. (b) The isometric, front and side views of two-axis bending design of manipulator. (c) ① Fabricated Design A of manipulator ② Design A with permanent magnet at the tip ③ Design A with silicone sheath and magnetic sheath.

3.2.1 Single-axis bending design

For achieving rotation about one axis, all flexures are aligned to bend in the same plane. Consider the design shown in Fig. 2(a): it consists of N flexures along the manipulator of length (L). The hollow tube has inner radius (r) and outer radius (R). Each flexure is a thin plate having length (l), width (w) and thickness ($t = R - r$). The thin plate can be approximately modeled as a cantilever beam. Each beam (i) is restricted to bend such that its tip displacement (δ_i) is limited to the width of the cut (w_c). The cut into the tube is made at an angle (ψ) to the length of the flexure. Since the flexures are designed such that $w_c << l$, linear load-displacement relationships are applicable. For the purpose of design, the flexures are assumed to undergo pure bending (no shear loads) due to the actuation method used in this chapter. Thus, the maximum tip displacement of the flexure (i) is

$$\delta_i^{max} = \frac{M_i l^2}{2EI} = w_c \ , \tag{3.1}$$

where M_i is the internal bending moment in flexure i and E is the elastic modulus of the material. The second moment of area of the flexure's cross-section (I) is given by $I = \frac{w^3 t}{12}$.

Each flexure (i) rotates by an angle (θ_i) with respect to the preceding beam ($i-1$). The maximum deflection angle of each flexure (θ_i^{max}) is given by,

$$\theta_i^{max} = \frac{M_i l}{EI} \ , \tag{3.2}$$

Substituting (3.1) into (3.2) delivers,

$$\theta_i^{max} = \frac{2w_c}{l} \ , \tag{3.3}$$

Since each segment of length (L_i) rotates by a maximum angle (θ_i^{max}), the manipulator of length (L) can undergo a total maximum rotation (θ^{max}) expressed as,

$$\theta^{max} = \frac{L}{L_i}\theta_i^{max} \ , \tag{3.4}$$

Additionally, to ensure that the manipulator does not fail, the stress in each flexure must be limited to well below the yield stress (σ_y) of the material.

The maximum stress in the manipulator (σ_{max}) and factor of safety (FoS) are calculated as follows:

$$\sigma_{max} = \frac{M_i w}{2I} = E\frac{w_c w}{l^2} \ , \tag{3.5}$$

$$FoS = \frac{\sigma_y}{\sigma_{max}} \ , \tag{3.6}$$

For planar bending, we assume $L_i = 1.5l$ between two consecutive beams for sufficient spacing, and the angle (ψ) is set to 135°. Therefore,

$$\theta^{max} = \frac{L}{1.5l}\left(\frac{2w_c}{l}\right) = \frac{4}{3}\frac{Lw_c}{l^2} \ , \tag{3.7}$$

Therefore, for a required maximum deflection (θ^{max}), the length of each flexure is given by

$$l = \sqrt{\frac{4}{3}\frac{Lw_c}{\theta^{max}}} \ , \tag{3.8}$$

This implies that the size of the flexure depends on the total length of the manipulator and the desired deflection of manipulator. These parameters can be fine-tuned to achieve a suitable design. Additionally, the critical load for buckling (P_{cr}) is calculated using Euler's formula as follows:

$$P_{cr} = \frac{\pi^2 EI}{l^2} \ . \tag{3.9}$$

3.2.2 Two-axis bending design

In order to achieve spatial bending, the flexures must be cut in two planes orthogonal to each other so as to permit rotation about two axes perpendicular to the longitudinal axis of the tube. The isometric, front, and side views of such a design are shown in Fig. 2(b). The directions of the cuts into the tube for each axis are reversed to make the design more compact, and the angle of cut (ψ) is reduced to 110°. In order to accommodate the orthogonal cuts, the length of each segment is set to $L_i = l - 3R\cos(\psi)$.

The equations for each flexure (3.1-4.4) also hold for the spatial design. It is inferred from (3.3) that with increase in width of cut (w_c), the maximum angular deflection (θ^{max}) increases. However, the factor of safety (FoS) decreases with increasing w_c, as observed in (4.3) and (4.4). This is

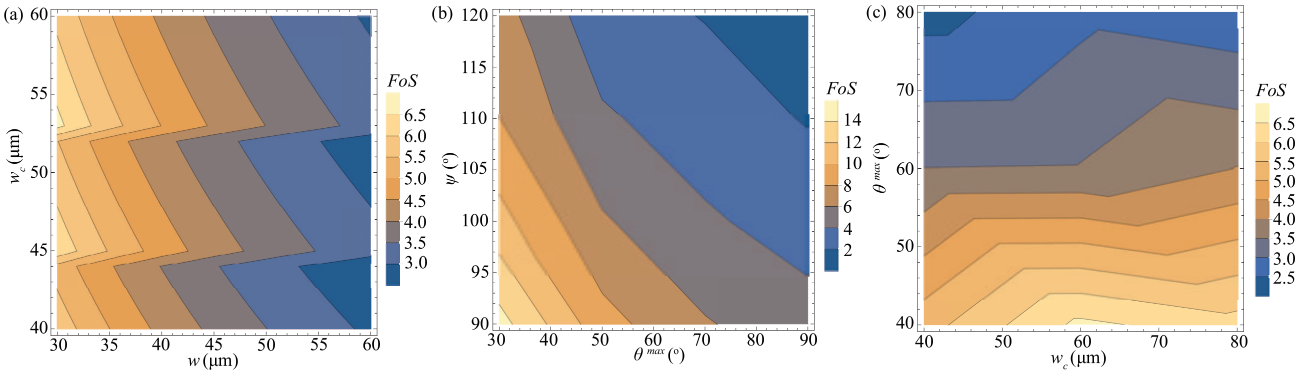

Figure 3.3: Contour plots showing the effect on factor of safety (FoS) over a varying range of (a) width of flexure (w) and width of cut (w_c), for maximum angular deflection (θ^{max}) $= 60°$ and angle of cut (ψ) $= 110°$ (b) θ^{max} and ψ, for $w = 50$ μm and $w_c = 40$ μm (c) w_c and θ^{max}, for $w = 50$ μm and $\psi = 110°$.

Table 3.1: Design parameters for two-axis bending design as shown in Fig. 3.2. N, FoS and P_{cr} are the number of flexures, factor of safety, and critical load for buckling respectively.

l (mm)	L (mm)	w (μm)	w_c (μm)	N	FoS	$P_{cr}(N)$
1.46	60	50	40	20	3.51	10.11

evident in the contour plots showing the effect of different design parameters on factor of safety in Fig. 3.3. In Fig. 3.3(a), sharp changes in FoS are observed over a range of w and w_c. This is because the number of flexures (N) can only take whole integer values. The final design parameters are determined through a trade-off between FoS and θ^{max}. Titanium grade-2 ($E = 105$ GPa, $\sigma_y = 345$ MPa) is chosen as the material. The resultant parameters are listed in Table 3.1. It has $N = 20$ flexures for bending along each orthogonal plane, and is designed for a deflection of $\theta^{max} = 60°$.

To validate the concept, one segment of the two-axis design is analyzed using Finite Element software (Workbench 16.2, Ansys Inc., Canonsburg, PA, USA). The model is meshed using SOLID187 3-D 10-node elements with a minimum edge length of 0.01 mm. The bottom end is constrained and a rotational displacement is applied at the top. The combined bending case is tested by a tip rotation of 3° (θ^{max}/N) to both flexures. The results are shown in Fig. 3.4. The maximum stress when both flexures are at maximum deflection is 101.16 MPa, while the stress calculated using (4.3) is 99.82 MPa with $FoS = 3.51$. Therefore, the proposed design is considered safe and the theoretical stress prediction using the beam model is tenable.

3.2.3 Fabrication

For demonstrating a proof-of-concept, the design of single-axis bending manipulator is adopted as it involves a relatively less complex fabrication process, compared to the two-axis design. Titanium (grade-2) is chosen for fabrication, due to its high ratio of yield strength to elastic modulus ($\sigma_y = 345$ MPa, $E = 105$ GPa) and low weight ratio [70]. Furthermore, it can be used in medical applications due to its non-toxic nature. A hollow titanium tube of outer diameter 3 mm and wall thickness 0.5 mm is used here. The flexures are cut along the tube using the technique of wire

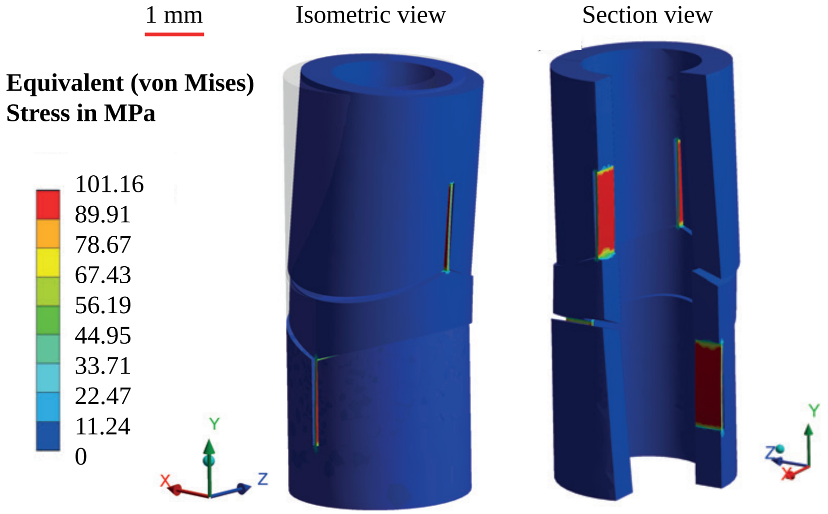

Figure 3.4: Stress analysis of a single segment of the two-axis bending design using finite element software. Isometric view shows spatial deflection of the tube under combined loading, while the section view demonstrates that the bending stresses are limited to the flexures.

electrical discharge machining (EDM). The diameter of the wire used in EDM determines the width of cut (w_c). Three single-axis (planar) bending designs are demonstrated in this chapter: their dimensions and properties as listed in Table 3.2. The flexures are made along a length of 47.5 mm for Designs A, leaving 7.5 mm without flexures at the end. For Design B and Design C, flexures are made along a length of 45 mm and 42 mm, respectively. The three fabricated designs have $FoS > 3$ as determined using (4.4).

In addition, a protective sheath is designed for the manipulator to prevent environmental debris from limiting its function during operation. An outer lumen of thickness 0.5 mm is made from silicone rubber (Ecoflex$^{\mathrm{TM}}$00-10, Smooth-On, Inc., USA), having a low elastic modulus (E_s = 55 kPa). The silicone rubber sheath is cured in molds made from 3D printed Acrylonitrile Butadiene Styrene (ABS) parts. The fabricated manipulator with

Table 3.2: Fabricated design parameters for single-axis bending design as shown in Fig. 3.2.

Manipulator	l (mm)	w (μm)	w_c (μm)	N	θ_{max} ($^\circ$)	FoS	P_{cr} (N)
Design A	1.5	40	55	21	53.58	3.03	2.45
Design B	1.5	65	40	20	36.09	3.12	10.54
Design C	1.1	30	40	23	39.83	3.36	1.92

the sheath is shown in Fig. 3.2(c).

3.3 Magnetic Actuation and Test Setup

In this section, a theoretical model is derived to calculate the deflection of the manipulator under the influence of an actuating magnetic field. This is followed by the description of the test setup.

3.3.1 Magnetic Actuation of the Manipulator

A controlled magnetic field is used to actuate the manipulator. To predict the deflection of the manipulator, a theoretical model based on principle of minimum potential energy is used. Consider a manipulator fixed at one end and suspended vertically with a permanent magnet of magnetic dipole moment (μ) at its tip (Fig. 3.5(a)). When a magnetic field (B) is applied at an angle (ϕ) to the vertical plane ($x - z$ plane), the permanent magnet experiences a torque (τ) that tries to align it to the direction of external field. This causes the flexures to bend resulting in the deflection of manipulator.

The deflection of the manipulator is calculated using a pseudo-rigid-body model. Each segment is approximated by a rigid link of length (L_i), with an associated bending stiffness (K_i). When the manipulator is covered by the polymer sheath, the overall stiffness of each segment is the sum of stiffnesses of the flexure (K_i^f) and the sheath (K_i^s).

$$K_i = 2K_i^f + K_i^s, \tag{3.10}$$

$$K_i^f = \frac{EI}{l}, \qquad K_i^s = \frac{E_s I_s}{L_i}. \tag{3.11}$$

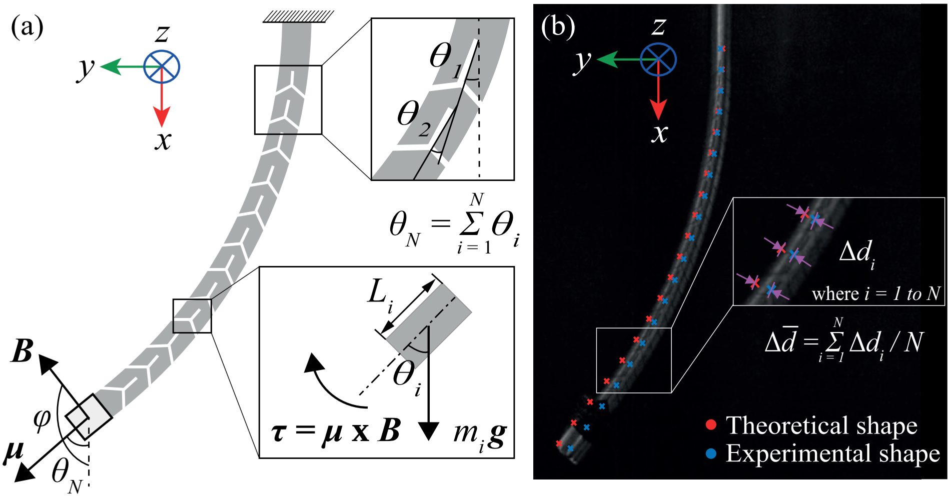

Figure 3.5: The manipulator is fixed at top and a permanent magnet having dipole moment (μ) is attached to its tip. (a) Free body diagram: under the influence of magnetic field B acting at an angle (ϕ), the manipulator deflects by an angle (θ_N). Top inset shows the deflection (θ_i) of each flexure. Bottom inset shows a rigid link with gravitation force ($m_i g$) acting at its center of mass and torque due to magnetic field (τ). (b) Camera image of Design C taken during static experiments: The red and blue markers indicate the theoretical and experimental shape estimate of the manipulator, respectively. The inset shows the calculation of whole shape estimation errors (Δd_i) for i points on the manipulator. Mean whole shape estimation error ($\Delta\bar{d}$) is calculated as the average of Δd_i for N points on the manipulator.

Here E, I, and l are the elastic modulus of Titanium (grade-2), second moment of area of the flexure's cross-section, and length of flexure respectively. E_s and I_s are the approximate linear elastic modulus of the polymer sheath and the second moment of area of its cross section respectively. Note that there are two flexures in each segment, one on either side of the manipulator.

The principle of minimum potential energy is used to analyze the deflection of the manipulator. The manipulator has N segments, each with a mass (m_i) that deflects by an angle (θ_i). Since the manipulator is held vertically, we consider the effect of gravity in this model. The total potential energy of the system is given by, $\Pi = U - W_{ext}$. Here, U is the elastic energy of the system that is, the strain energy in the flexures. And, W_{ext} is the work done by the external forces, which is equal to the sum of work done by gravity (W_g) and work done by magnetic field (W_μ). This results in

$$\Pi = U - W_g - W_\mu, \tag{3.12}$$

where

$$U = \sum_{i=1}^{N} \frac{1}{2} K_i \theta_i^2, \tag{3.13}$$

$$W_g = \sum_{i=1}^{N} m_i g x_i + m_\mu g x_\mu, \tag{3.14}$$

$$\begin{aligned} W_\mu = \int_0^{\theta_N} \tau d\theta &= \int_0^{\theta_N} \mu B \sin(\phi - \theta) d\theta \\ &= \mu B \left[\cos\left(\sum_{i=1}^{N} \theta_i - \phi \right) - \cos(\phi) \right], \end{aligned} \tag{3.15}$$

where location of center of mass of each segment (x_i,y_i) is computed using forward kinematics as follows:

$$\begin{aligned} x_i &= x_{i-1} + L_i \left[\cos(\theta_1) + \cos(\theta_1 + \theta_2) + ... + \cos\left(\sum_1^i \theta_i \right) \right], \\ y_i &= y_{i-1} + L_i \left[\sin(\theta_1) + \sin(\theta_1 + \theta_2) + ... + \sin\left(\sum_1^i \theta_i \right) \right]. \end{aligned} \tag{3.16}$$

Similarly the weight of last segment and the magnet (m_μ) acts at its center of mass distance (L_{CoM}), whose x-coordinate is given by,

$$x_\mu = x_N + L_{CoM} \cos\left(\sum_{i=1}^{N} \theta_i \right), \tag{3.17}$$

Variation of (3.15-3.17) with respect to θ_j (where j = 1,2,...,N) results in

$$\frac{\partial W_\mu}{\partial \theta_j} = \mu B \left[\sin\left(\phi - \sum_{i=1}^{N} \theta_i \right) \right], \tag{3.18}$$

$$\frac{\partial x_i}{\partial \theta_j} = \begin{cases} 0 & \text{if } i < j \\ -L_i \sum_{k=i}^{j} \sin\left(\sum_1^k \theta_k\right) & \text{if } j \le i \le N \end{cases}, \tag{3.19}$$

$$\frac{\partial x_\mu}{\partial \theta_j} = -L_i \sum_{k=i}^{N} \sin\left(\sum_1^k \theta_k\right) - L_{CoM} \sin\left(\sum_{k=1}^{N} \theta_k\right), \tag{3.20}$$

The principle of minimum potential energy states that the variation of total potential energy is zero that is, $\partial\Pi = 0$. Substituting (3.18-3.20) in variation of (3.12) with respect to θ_j gives N equations as follows:

$$K_i\theta_i = m_i g \sum_{i=1}^{N} \frac{\partial x_i}{\partial \theta_j} + m_\mu g \frac{\partial x_\mu}{\partial \theta_j} + \mu B \sin\left(\phi - \sum_{i=1}^{N} \theta_i\right). \tag{3.21}$$

This forms a system of equations in θ_j (where $j = 1, 2,...,N$) with the constraint: $-\frac{\theta^{max}}{N} \le \theta_j \le \frac{\theta^{max}}{N}$, where θ_{max} is the total rotation angle observed at maximum deflection of the manipulator (mechanical rotational limit of each segment). If the actuation magnetic field is known (B and ϕ), we can solve the preceding system of equations to obtain the position and orientation of the manipulator by this model.

3.3.2 Test Setup

For magnetic actuation, two methods of incorporating magnetic properties on the manipulator are tested. In the first method, a permanent magnet (radius = 2 mm, height = 5 mm, $\mu = 0.06$ Am^2) is fit at the tip of the manipulator. In the other method, a magnetic sheath of thickness 0.5 mm and length 5 mm is made to cover the manipulator's tip. It is made by fusing ferromagnetic particles (praseodymium-iron-boron: PrFeB, with a mean particle size of 5 μm, Magnequench GmbH, Germany) into the silicone rubber in 1:1 ratio. The cured polymer is subjected to an external magnetic field of 1 T (B-E 25 electromagnet, Bruker Corp., USA) to align the magnetic dipoles, forming a soft polymer magnet [296]. These two designs are shown in Fig. 3.2(c).

The setup used here consists of two pairs of Helmholtz coils to generate uniform magnetic fields. Each pair consists of two identical electromagnetic coils as shown in Fig. 3.6. The first pair of coils generates a uniform magnetic field along the y-axis. The second pair of smaller coils is placed

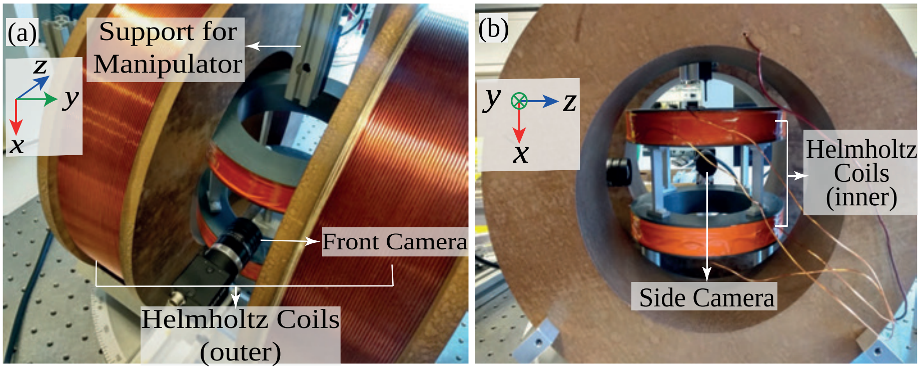

Figure 3.6: Experimental setup of two-axis Helmholtz coil setup used for generating magnetic fields. (a) Front view (b) Side view.

inside the first pair to produce a field along the x-axis. Two cameras are placed in the setup to monitor the front and side view of the workspace.

3.4 Experiments and Results

The deformation characteristics of the three designs of manipulator under magnetic actuation are evaluated using experiments. The theoretical and experimental results are compared to substantiate the open-loop actuation of manipulator under the influence of magnetic field. Section 3.4.1 presents the static experiments carried out to analyse the motion of manipulator. Sections 3.4.2 and 3.4.3 are part of a feasibility study of the manipulator which demonstrates the steering of manipulator along a path of known curvature and through gelatin phantom with ultrasound visualization respectively.

3.4.1 Static Experiments

The manipulator with a permanent magnet at its tip is suspended vertically at the center of magnetic setup. It is subjected to a magnetic field (B) of constant magnitude. The angle of the magnetic field to the vertical plane (ϕ) is varied to control the tip angle of the manipulator. The theoretical deformation of the manipulator is calculated using (3.21), with

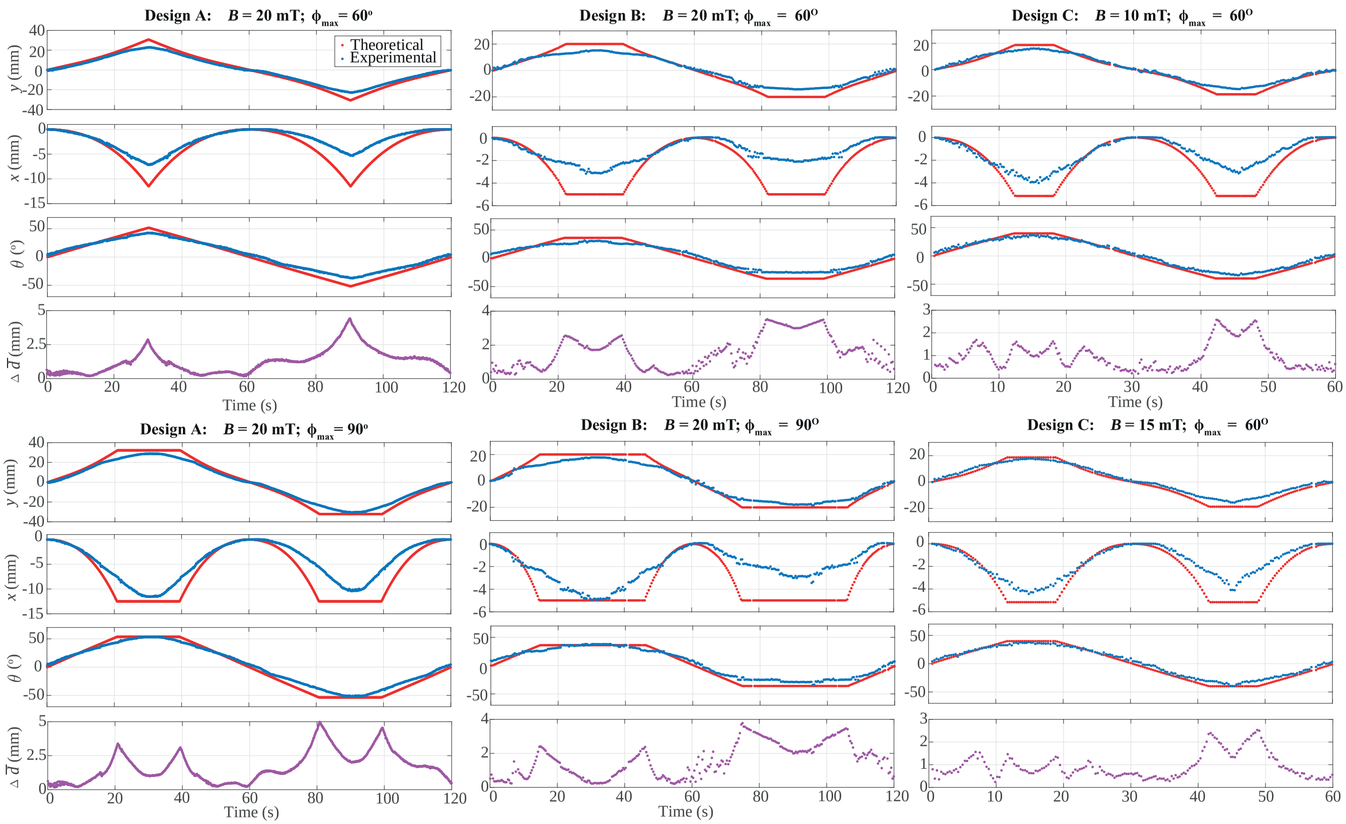

Figure 3.7: Plots of x-coordinate, y-coordinate, deflection θ, and mean whole shape error $\Delta\bar{d}$ of the three designs of manipulator for the experimental cases of Design A: ($B = 20$ mT, $\phi_{max} = 60°$ and $90°$), Designs B: ($B = 20$ mT, $\phi_{max} = 60°$ and $90°$) and Design C: ($B = 10$ mT and 15 mT, $\phi_{max} = 60°$).

x and y coordinates determined using (3.16). The experiments were carried out without the polymer sheath, hence from (3.10) we use $K_i = 2K_i^f$. The experimental deflected shape of manipulator is obtained using camera images acquired at various instants of its motion (Fig. 3.5(a)). An image processing algorithm tracks several points along the length of the manipulator based on a threshold set on pixel intensity. A cubic polynomial curve is fit using these points which forms the shape of manipulator. The experimental values of position (x, y) of the manipulator are obtained from the cubic curve equation and its slope gives the orientation (θ). Fig. 3.5(b) is a camera image acquired during the experiment showing the theoretical and experimental shape estimate of the manipulator.

The plots of x, y-coordinates, deflection θ of the tip of manipulator, and mean whole shape estimation error $(\Delta\bar{d})$ for the three designs are shown in Fig. 3.7. The mean and standard deviation of errors between the two sets of data are presented in Table 4.2. Designs A, B and C permit a maximum deflection of 54°, 36° and 40° respectively.

Table 3.3: Details of experiments: For strength of magnetic field (B) at maximum angle (ϕ_{max}), maximum angular deflection of manipulator (θ_{max}), error between theoretical and experimental models for: position (Δx and Δy), orientation $(\Delta\theta)$ of manipulator tip, and mean whole shape $(\Delta\bar{d})$ are shown in terms of mean values and standard deviation (in brackets).

B (mT)	ϕ_{max} (°)	θ_{max} (°)	$\Delta\ x$ (mm)	$\Delta\ y$ (mm)	$\Delta\theta$ (°)	$\Delta\ \bar{d}$ (mm)
Design A						
20	60	42.85	1.2 (1.4)	2.2(2.3)	5.12 (3.38)	1.1 (0.83)
20	90	53.58	1.8 (1.7)	3.0(2.5)	5.01 (3.53)	1.5 (1.10)
Design B						
20	60	31.52	1.4 (1.2)	3.4 (2.2)	6.20 (3.19)	1.5 (0.92)
20	90	38.06	1.4 (1.1)	3.0 (2.2)	5.21 (3.59)	1.3 (0.91)
Design C						
10	60	37.31	0.77 (0.66)	2.2 (1.6)	4.76 (2.59)	0.98 (0.60)
15	60	39.83	0.72 (0.59)	2.1 (1.5)	4.48 (2.44)	0.94 (0.56)

3.4.2 Manipulator Steering

In this section, the steerability of the manipualtor under open-loop actuation is demonstrated. The length of the manipulator within the workspace is controlled using a linear slide (LX20, Misumi Group Inc., Tokyo, Japan) which is fixed vertically at the top support. The linear slide is powered by a brushless DC motor (maxon EC-max, Maxon Motor, Switzerland) connected to a 24 V power supply. The manipulator with a permanent magnet at its tip is deflected by the magnetic field to control its direction. To follow the path of particular curvature, the manipulator is turned by an angle (θ_N) by applying an actuation field of B = 20 mT at an angle (ϕ), calculated using (3.21). The manipulator is steered with a polymer sheath covering its body to show clinical feasibility, hence from (3.10) we use $K_i = K_i^s + 2K_i^f$. Figure 3.8 illustrates the snippets of the video recorded of controlled steering motion of the manipulator.

3.4.3 Ultrasound Visualization

In this section, steering of the manipulator using real-time ultrasound visualization is demonstrated. A channel of width 10 mm and curvature 45° is created inside a phantom made by mixing 8% (by weight) gelatin powder (Technical grade, Boom B.V., The Netherlands) with distilled water. The channel is filled with water and the manipulator with the permanent magnet at its tip is inserted through it using the linear slide. The direction of manipulator is controlled by changing the orientation of magnetic field which is provided by user input. The phantom is imaged using a 14 MHz multi-D matrix probe (14L5 transducer) connected to a 2D medical ultrasound machine (SIEMENS AG, Erlangen, Germany). Fig. 3.8 shows the snapshots from the ultrasound imaging of manipulator insertion.

3.4.4 Discussion

From the results of static experiments (Table 4.2), it is seen that Design B has the highest error. This maybe due to its greater width of beam (w) than the width of cut, which restricts the motion of the flexure. Design A has a greater width of cut (w_c) compared to the other two designs, which allows it to achieve larger deflections. Design C has smaller width of beam, which makes it more susceptible to deformation. These factors have to be

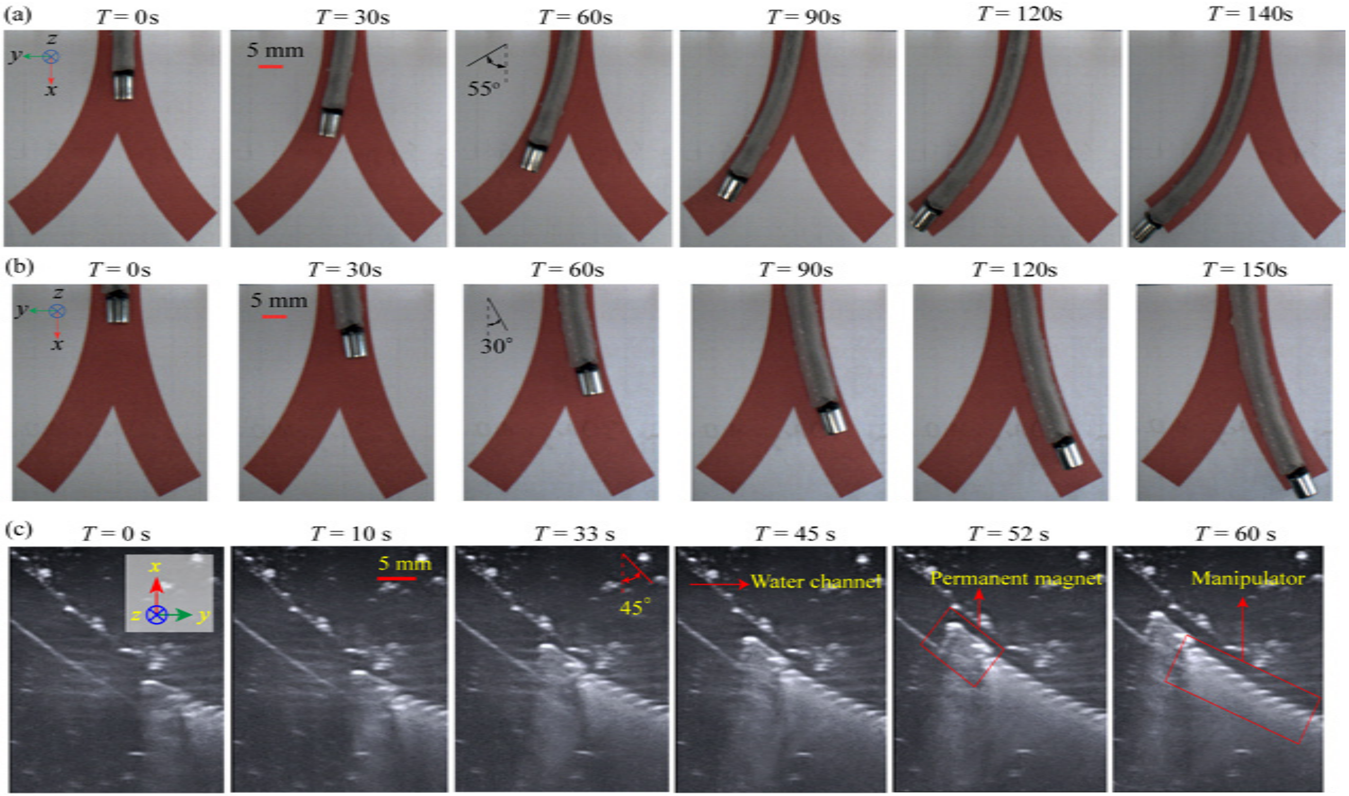

Figure 3.8: Illustration of manipulator steering with a polymer sheath around the flexures, six frames for experiment time (T) are shown for:(a) Design A following a curvature angle of 55° (b) Design B following a curvature angle of 30°. (c) Ultrasound images acquired during insertion of manipulator through a channel of water in a gelatin phantom.

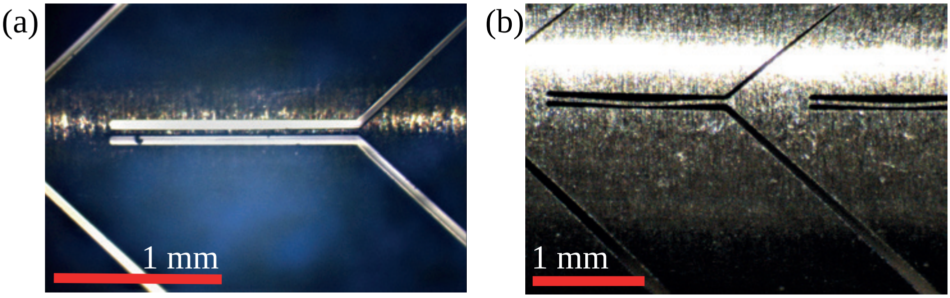

Figure 3.9: Microscopic images of metallic tubes showing (a) accurately machined flexures and (b) inaccurately machined deformed flexures.

taken into account for developing an optimized design.

It is also observed that there is a difference in bending curvature between the two half cycles of motion of manipulator that is, the deflection in the $+y$ direction is different from that in the $-y$ direction. This may be attributed to the manipulator not being exactly straight in the neutral position, due to errors in fabrication. When observed under a microscope, it is noticeable that some of the flexures have buckled slightly, suggesting potential plastic deformation (Fig. 3.9). This can be avoided by using a tube with a thicker wall (increased t), so that the critical buckling load is higher. It is also noticed that the tubes are bent out of the plane of motion, possibly due to stresses during machining. These inaccuracies affect the expected motion of the manipulator.

For magnetic actuation of the manipulator, the use of a permanent magnet and magnetic sheath at its tip is tested (Fig. 3.2(c)). It is observed that the deflection when using permanent magnet is higher than when using magnetic sheath (Fig. 3.10). This is because of the low magnetic dipole moment (μ) of the magnetic sheath. Therefore, the magnetic sheath is incapable of producing large bends, and is restricted to angles below 30°. This can be improved by using a magnetic polymer sheath with a greater magnetic dipole moment — using a magnetic powder with a higher residual magnetic field or a higher ratio of powder to polymer. The polymer sheath protects the flexures from the environment without restricting the motion of the manipulator. For medical applications, the replaceable sheath can potentially reduce tissue trauma during steering and can also simplify the

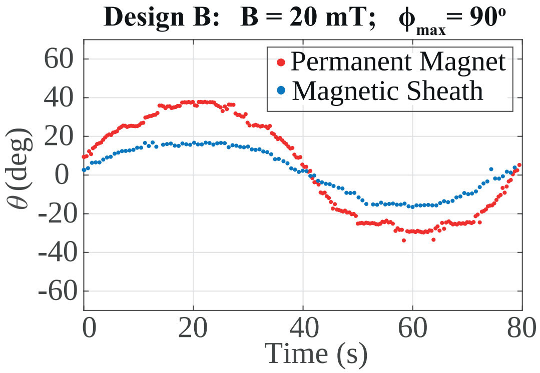

Figure 3.10: Plot showing deflection (θ) of Design B with a permanent magnet and a magnetic sheath for the experimental case of B = 20 mT, $\phi_{max} = 90°$.

sterilization process.

The distal force bearing capacity of the manipulator is also estimated for potential applications in minimally invasive surgery (Appendix A.1). Three loading conditions of bending, extension and compression are considered to obtain the following values respectively for Design A: 151.67 N, 13.8 N, 2.45 N, Design B: 151.67 N, 22.42 N, 10.54 N, Design C: 206.83 N, 10.35 N, 1.92 N. It is found that the bending load is highest of the three, as failure occurs only when the cylindrical wall of the manipulator breaks. The buckling load is the leading potential cause of failure, and can be improved by increasing the thickness of the tube. Another potential cause of failure caused by cyclic loading on the flexures is fatigue. Titanium grade-2 has a fatigue strength of 300 MPa at 10^7 cycles unnotched [297]. This stress value is well above the maximum stresses calculated using (4.3) for our designs, which are within 120 MPa. Note, it is difficult to estimate the lifetime of the flexure. Besides material properties, fatigue failure also depends on the machining process, surface quality and operating environment. However, the steering of the manipulator is not expected to generate alternating stresses with large amplitude, suggesting that fatigue failure will not be a significant factor in the design process.

3.5 Conclusions and Future Work

In this chapter, the design of a monolithic metallic compliant continuum manipulator of diameter 3 mm is presented. The performance of the manipulator is evaluated by actuating with a magnetic field up to 20 mT using Helmholtz coils. The three designs, Design A with highest width of cut (55 μm), Design B with highest width of beam (65 μm), and Design C with lowest length of beam (1.1 mm) are tested. The maximum deflection observed is 54° for Design A, while Design B and Design C achieved 36° and 40° bends, respectively. The mean error over three designs in modeling the in-plane position and orientation of the manipulator tip are (1.2 mm, 2.6 mm) and 5.1°, respectively and for whole shape of the manipulator is 1.2 mm. The manipulator steering experiment proves accurate guidance of a manipulator along a path of known curvature using open-loop actuation. The real-time ultrasound visualization of the manipulator inside a gelatin phantom through a water medium shows its clinical feasibility as a steerable surgical manipulator. Contactless actuation of the manipulator is demonstrated by using magnetic field, eliminating the need for a force transmission mechanism. The monolithic design with a small permanent magnet enables easy miniaturization for application as a steerable manipulator in minimally invasive surgical procedures.

In future work, we plan to improve the fabrication process of the manipulator and improve the accuracies in machining. A two-axis bending design of manipulator will be fabricated to validate the concept of spatial bending. The upgraded design will be tested for higher deflection ($> 90°$). Potential applications in endocopsy, biopsy, and ablation will be explored by enhancing the functionality of manipulator. This will be done by embedding additional surgical tools (such as scalpel, retractor, curette, forceps, or scissors) and related sensors (like camera, laser cautery fiber, light, or optical fibers) within its hollow interior. The manipulator steering process will be improved by enabling rotation of the manipulator during insertion. This will be demonstrated in a clinically-relevant scenarios such as animal tissue or human cadaver studies.

4

Design, Sensing, and Control of a Magnetic Compliant Continuum Manipulator

Note: *The following chapter is adapted from the article "Design, Sensing, and Control of a Magnetic Compliant Continuum Manipulator" by* ***T. L. Thomas****, J. Sikorski, G. K. Ananthasuresh, V. Kalpathy Venkiteswaran, and S. Misra, published in "IEEE Transactions on Medical Robotics and Bionics", vol. 4, no. 4, pp. 910-921, November 2022.*
The chapter has been reformatted in terms of figures and tables to fit this doctoral thesis. No changes to the technical contents of this peer-reviewed manuscript have been made.

Authors' Contributions: *T. L. Thomas performed the analysis for fabrication of the manipulator, designed and assembled PaCMag - electromagnetic setup, carried out the experiments, derived quasi-static model, performed the closed-loop control analysis, and interpreted the results. J. Sikorski contributed to the hardware and software integration of PaCMag and developed the FBG shape reconstruction model and observer-based fusion method. V. Kalpathy Venkiteswaran contributed to the design of the manipulator and PaCMag, helped with analysis and supervised the project. G. K. Ananthasuresh conceived the original design of manipulator and contributed to the analysis. S. Misra helped shape the research and supervise the overall project. T. L. Thomas wrote the manuscript in consultation with all the authors.*

4. Design, Sensing, and Control of a Magnetic Compliant Continuum Manipulator

Abstract

Continuum manipulators coupled with magnetic actuation have great potential as steerable instruments for diverse surgical applications. They can be maneuvered inside the human body to reach difficult-to-access surgical sites with contactless actuation. This chapter presents a new design of a compliant continuum manipulator of diameter 3 mm and length 70 mm, capable of spatial bending under magnetic actuation. A quasi-static model is developed to estimate the 3D motion of the manipulator. Experiments report an overall mean error in whole shape estimation of the manipulator between the model and the ground truth of 1.7 mm and 4.8 mm, when suspended vertically and horizontally from its base, respectively. Furthermore, fiber Bragg grating (FBG) sensors are integrated with the manipulator to enable shape sensing. Closed-loop control is demonstrated to trace different trajectories with the tip of the manipulator. A square trajectory and a straight line trajectory are generated with an average error in tip position of 4.1 mm between the desired and estimated positions. The potential of the manipulator as a steerable instrument is validated by maneuvering it inside phantoms of a bifurcating arterial system and a heart with visual guidance from a miniature camera.

4.1 Introduction

Continuum manipulators have seen tremendous growth over the last few decades in various surgical applications such as laparoscopy, colonoscopy, neurosurgery and robot-assisted surgery among others [13]. A continuum manipulator is a continuously curving robotic device with several degrees of freedom (DoF). Miniaturized continuum manipulators can be designed to control their shape in 3D space and precisely steer inside the human body to reach difficult-to-access surgical sites. Recent advancements in the design of compliant mechanisms have resulted in various miniaturized flexible continuum manipulators with a wide range of motion [298]. Notched-tube compliant joint mechanisms in particular have gained significance in enhancing DoF and dexterity. Flexible manipulators having different patterns of triangular, rectangular and asymmetric notches have been explored to operate in single-port access surgeries [116], [206]. Such manipulators are known to have reduced stiffness and require careful optimization of the notch pattern to operate in confined spaces [44].

Accurate modelling of continuum manipulators is important in precisely maneuvering the manipulator to the surgical site. Constant curvature approximation is a commonly applied framework for continuum robots, but it can be challenging due to the error propagating from variable curvature robot shapes [49]. Cosserat-rod is a geometrically-exact model more generally used for soft manipulators, however it can be difficult to implement as it involves solving partial differential equations [299]. By contrast, rigid-link modelling is a simplified approach for approximating continuum manipulators with multiple DoFs as concatenated rigid links and flexible joints using well-established kinematic and dynamic models [300].

A common method of controlling continuum manipulators is using cable-driven actuation. Examples include commercially available systems like the Sensei X Robotic Catheter System by Hansen Medical Inc. (California, U.S.) and ViaCath system by BIOTRONIK (Berlin, Germany) [301]. Such systems require energy transfer through tendon coupling and can suffer from backlash and hysteresis. Recently, magnetic actuation is gaining interest in creating miniaturized manipulator designs as it enables manipulator control without the need for cables or tendons [37]. For instance, a 4 mm flexible catheter (NaviStar-RMT, Biosense Webster, Inc., California, USA) integrated with small permanent magnets, controlled using the Niobe magnetic navigation system (Stereotaxis Inc., Missouri, USA) and a motor drive (Cardiodrive, Stereotaxis, Inc., USA) is a leading technology for cardiovascular interventions [38]. Kratchman *et al.* demonstrated 3D tip trajectory planning of a magnet-tipped rod using Kirchoff elastic rod model in open-loop [302]. Model-based closed-loop control has been studied by many researchers using feedback of actuating wrenches [48], [52]. For instance, the first 3D closed loop control of a magnetic catheter was demonstrated by Edelmann *et al.* using Cosserat-rod model, however an external camera-based localization was implemented which is not clinically feasible [290].

Sensing the 3D shape of the manipulator in real-time while operating inside the body is quite challenging. Computed tomography (CT), magnetic resonance imaging (MRI) and ultrasound (US) imaging are widely used clinical imaging modalities for catheter tracking. However, these techniques have some limitations: CT leads to excessive X-ray exposure, MRI is not compatible with magnetic actuation and US has limited resolution inside the body [57]. Several studies have shown the virtues of using fiber Bragg grating (FBG) sensors in shape reconstruction of flexible medical instruments [303]–[305]. Optical fibers inscribed with FBG sensors are free from electromagnetic interference, thin, highly flexible and can be seamlessly integrated with medical instruments [58].

A new design of a monolithic metallic compliant manipulator capable of planar bending was presented in our previous proof-of-concept study [110]. This chapter presents a novel design capable of spatial bending of the manipulator under magnetic actuation. This work validates the efficacy of the manipulator as a steerable surgical instrument with improved shape sensing and visualization capabilities over the previous study. The monolithic manipulator has a notched pattern of flexures with built-in mechanical motion constraints that limit the maximum stress in the flexures. A quasi-static model that uses rigid-link modelling is proposed to study the 3D motion of the manipulator when subjected to magnetic fields. Static experiments are conducted with the manipulator in an electromagnet setup (PaCMag), to analyse the proposed model. The shape sensing of the manipulator is improved by integrating an optical fiber inscribed with FBG sensors within the manipulator. A closed-loop control strategy is demonstrated in PaCMag to trace different trajectories with the tip of the manipulator. An observer-based fusion algorithm that fuses the tip pose information from the model and FBG sensors serves as feedback for the controller. The sensor fusion algorithm does not require external imaging like cameras or US imaging to estimate the tip pose of the manipulator [306], [307]. It has potential to offer a real-time visualization alternative to CT using X-rays.

The miniaturized manipulator presented is fabricated using a single tube of titanium, unlike most other manipulator designs reported in the literature that require assembly. The mechanical motion constraints in the design leads to distributed compliance, resulting in a safe manipulator by preventing the flexures from failing under stress. A comprehensive quasi-static model of the manipulator is developed which accounts for multiple DoFs, motion constraints, gravity and torsion. The 1 mm working channel of the manipulator enables integration of additional tools and sensors. The clinical feasibility of the manipulator is studied by carrying out experiments using a miniature camera (0.91 mm diameter) in phantom models of a bifurcating arterial system and a heart. Magnetic steering of the manipulator integrated with a miniature camera as feedback shows potential as a steerable catheter for endoscopy and ablation.

The rest of the chapter is structured as follows: Section 4.2 begins with the description of the design and fabrication process of the manipulator. Section 4.3 introduces the quasi-static model developed to study the motion characteristics of the manipulator under magnetic actuation and is followed by the description of the test setup. Section 4.4 details the three set of experiments with the manipulators comprising of static experiments, closed-loop control, and phantom study. The inference and discussion on the results of the experiments are given in Section 4.5. Finally, Section 4.6 concludes the chapter with a summary of this study and provides recommendations for future work.

4.2 The Compliant Continuum Manipulator

The compliant continuum manipulator is made by making cuts on a metallic tube to form two series of flexure pairs along the length of the tube. The two flexure pair series are oriented at 90° circumferential separation. The direction of cuts of one flexure pair series is reversed with respect to the other to make a compact design as shown in the isometric view of the manipulator in Fig. 4.1(a). Each flexure pair forms an elastic rotational joint that enables bending of the manipulator about the axis perpendicular to the longitudinal axis and the width of the flexure. A combination of the two series of flexure pairs oriented orthogonal with respect to each other results in the two-axis bending design. The range of motion of each flexure is physically constrained by the design geometry which also limits the maximum stress in the flexure to prevent failure.

4.2.1 Design

The design of the manipulator is shown in Fig. 4.1(a). It consists of two series of N flexure pairs distributed with 90° circumferential separation along the length (L) of the manipulator. The tube of the manipulator has inner radius (r) and outer radius (R). Each flexure is a thin plate of length (l), width (w) and thickness ($t = R - r$).

For design purposes, only the primary bending direction of the flexure is considered in the stress analysis as it is the predominant contributor to the stress. The total deflection of the manipulator is determined from the

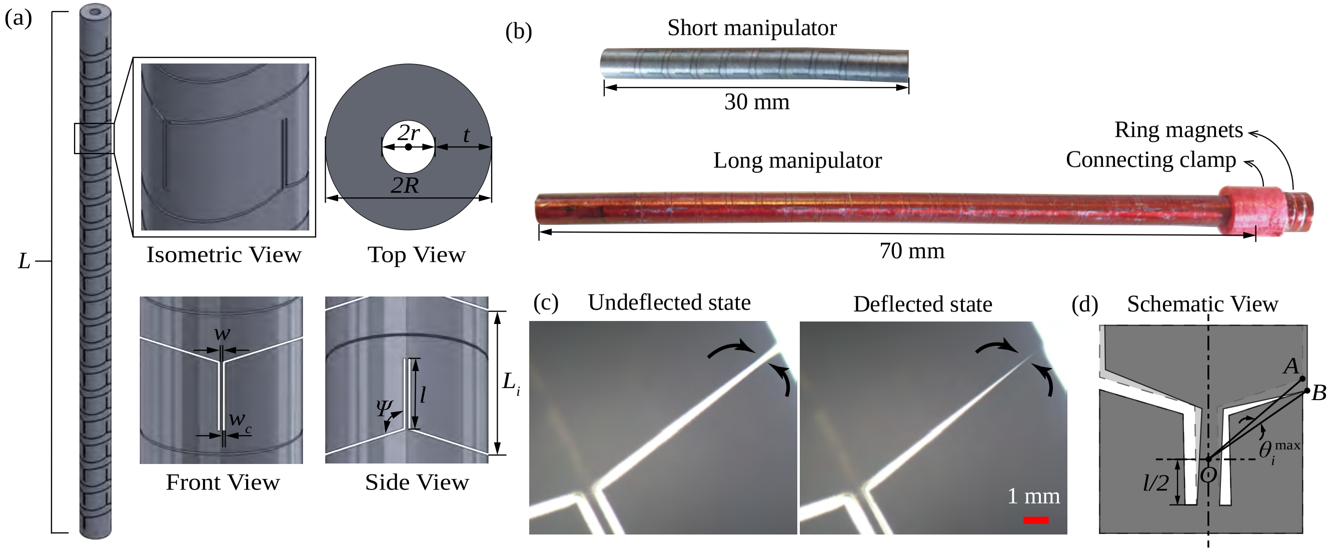

Figure 4.1: (a) The isometric, top, front and side views of two-axis bending design of manipulator with variables to define the design parameters. (b) Short and long versions of the manipulators fabricated using wire EDM. Three Neodymium ring magnets are connected to the long manipulator which is colored red for stereo vision tracking purposes. (c) Microscopic images of one flexure joint of the manipulator undergoing maximum deflection. (d) A schematic view of a flexure pair undergoing maximum deflection.

resultant sum of the deflections of each flexure pair ($\theta_i^{\max}$) while bending. In this design, $\theta_i^{\max}$ is limited by the width of the cut. It can be computed from geometry by assuming the axis of rotation is at the centre of the flexure. As shown in Fig. 4.1(d), point A in the wall of the manipulator makes first contact with the adjacent wall at point B. $\theta_i^{\max}$ is computed geometrically by the angle subtended by $\overline{AB}$ at the axis of rotation passing through O. Thus, the maximum deflection of the manipulator is calculated as follows

$$\theta^{\max} = N\theta_i^{\max}. \tag{4.1}$$

For safe operation of the manipulator without failure, the manipulator is designed such that the stress in each flexure does not exceed the yield stress of the chosen material (σ_y). Each flexure (i) experiences a maximum moment ($M_i^{\max}$) at a maximum deflection ($\theta_i^{\max}$) with respect to the preceding flexure ($i-1$) using Euler-Bernoulli beam theory [308] given by

$$M_i^{\max} = \frac{EI}{l}\theta_i^{\max}, \tag{4.2}$$

where E is the elastic modulus of the material and the second moment of area of the flexure's cross section (I) given by $I = w^3t/12$. The maximum stress in the flexure ($\sigma_{\max}$) and the factor of safety (FoS) is expressed as follows

$$\sigma_{\max} = \frac{M_i^{\max}w}{2I} = \frac{E\theta_i^{\max}w}{2l}\ , \tag{4.3}$$

$$FoS = \frac{\sigma_y}{\sigma_{\max}}\ . \tag{4.4}$$

Furthermore, the critical load for buckling (P_{cr}) is calculated using Euler's formula as follows:

$$P_{cr} = \frac{\pi^2 EI}{l^2}\ . \tag{4.5}$$

This is the maximum axial load that the manipulator can safely carry without buckling. Similarly, the load capacities for bending and extension can also be calculated based on our previous work [110]. Bending will be the dominant effect and failure due to bending will only occur with fracture of the wall of the manipulator.

Table 4.1: Design parameters for two-axis bending designs of short manipulator ($N = 9$) and long manipulator ($N = 21$) as shown in Fig. 4.1(a), where N is the the number of flexures. Load capacity for bending (F_{bend}), extension (F_{ext}), compression (P_{cr}), and factor of safety (FoS) are also given.

Design Parameters		Load Capacity	
L	30 mm	F_{bend}	171.71 N
l	1.55 mm	F_{ext}	41.4 N
w	60 μm	P_{cr}	15.52 N
w_c	40 μm	FoS	7.13
ψ	100°		

4.2.2 Fabrication

The manipulator is fabricated using a Titanium (grade-2) tube of outer and inner diameters of 3 mm and 1 mm, respectively. Titanium (grade-2) is chosen as the material as it has high ratio of yield strength to elastic modulus ($\sigma_y = 345$ MPa and $E = 105$ GPa) and low weight ratio. It is biocompatible and magnetically transparent. A series of flexure pairs is created along the length of the manipulator by making cuts using wire electrical discharge machining (EDM). Two manipulators of length 70 mm and 30 mm, henceforth known as the "long manipulator" and "short manipulator", respectively are fabricated as shown in Fig. 4.1(b) with design parameters and load capacities given in Table 4.1. Prior to fabrication, a segment of the manipulator was analysed using finite element software (COMSOL Multiphysics 5.4). It was modelled using tetrahedral elements with minimum and maximum element size of 0.024 mm and 0.33 mm, respectively, in a stationary solid mechanics study. As shown in Fig. 4.2, the top end was constrained and the moment ($2M_i^{\max} = 5.8$ x 10^{-5} Nm, because of two flexures) was applied to the bottom end about the two axes perpendicular to the longitudinal axis of the segment. This resulted in a maximum stress in the flexure of 50.9 MPa, which was validated with the stress calculated from the modelling approach Eqn. (4.3) giving 48.3 MPa with a factor of safety of 7.13.

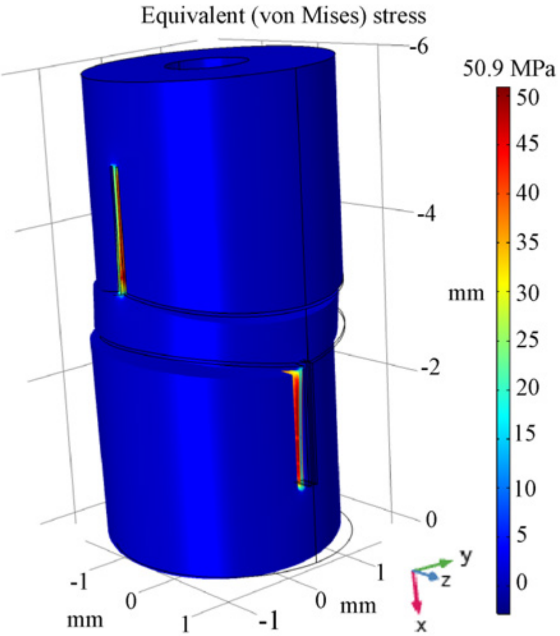

Figure 4.2: Stress analysis of a single segment of the two-axis bending design using finite element software (COMSOL Multiphysics 5.4).

4.3 Magnetic Actuation and Test Setup

The manipulator is actuated using magnetic fields by means of a permanent magnet attached to its tip (Fig. 4.1(b)). The manipulator is modelled using a rigid-body model to determine its configuration under the influence of external magnetic fields [293].

4.3.1 Quasi-Static Model

For the purposes of analysis, it is assumed that the manipulator undergoes quasi-static motion. The rigid-body model of the manipulator consists of N segments (Fig. 4.3). Each segment (S_k) taken in isolation is in static equilibrium with a load ($\mathbf{W}_k \in \mathbb{R}^6$) at its end. Each segment is composed of two orthogonally oriented flexure pairs. Each flexure pair is modelled as a spherical joint having three DoFs, with the axis of rotation located at the center of the flexure pair. Two DoFs correspond to the primary and auxiliary bending directions of flexure which are about the two axes perpendicular to the longitudinal axis, and the third DoF is due to the torsion about the longitudinal axis. Therefore, each segment consists of two spherical joints ($i \in \{2,3\}$) at two points ($\mathbf{r}_i \in \mathbb{R}^3$) connecting three rigid links of given length ($l_i \in \mathbb{R}^+$, where $i \in \{1,2,3\}$). The three DoFs of the spherical joint (i) are the three rotational angles about x, y and z axes ($\alpha_i, \beta_i, \gamma_i \in \mathbb{S}$). The corresponding rotational stiffnesses ($K_{\alpha_i}, K_{\beta_i}, K_{\gamma_i} \in \mathbb{R}^+$) are calculated by approximating the flexure pair as two thin plates in parallel configuration, which gives

$$K_{\beta_i} = \frac{2EI_i^y}{l}\, , K_{\gamma_i} = \frac{2EI_i^z}{l}\, , K_{\alpha_i} = \frac{2GJ_i^x}{l}\ , \tag{4.6}$$

where E and G are the Young's modulus and shear modulus of the material. The second moment of area (I_i^*) and the polar moment of inertia (J_i^*) of the flexure pair (i) with the respective axes ($*$) are $I_2^y = I_3^z = \frac{w^3t}{12}$, $I_2^z = I_3^y = \frac{wt^3}{12}$ and $J_i^x = I_i^y + I_i^z$, where l, w and t are the length, width and thickness of the flexure, respectively.

The internal joint torque ($\boldsymbol{\tau} \in \mathbb{R}^6$) of the rigid-body model is given by

$$\boldsymbol{\tau} = \begin{bmatrix} K_{\beta_2}\beta_2 & K_{\gamma_2}\gamma_2 & K_{\alpha_2}\alpha_2 & K_{\beta_3}\beta_3 & K_{\gamma_3}\gamma_3 & K_{\alpha_3}\alpha_3 \end{bmatrix}^T\ . \tag{4.7}$$

The load wrench ($\mathbf{W} \in \mathbb{R}^6$) acting at the end of the segment ($\mathbf{r}_4 \in \mathbb{R}^3$) in the spatial reference frame is defined as

$$\mathbf{W} = \begin{bmatrix} \mathbf{F} \\ \mathbf{M} \end{bmatrix} + \begin{bmatrix} 0_{3\times 1} \\ \mathbf{r}_4 \times \mathbf{F} \end{bmatrix}\ , \tag{4.8}$$

where force ($\mathbf{F} \in \mathbb{R}^3$) and moment ($\mathbf{M} \in \mathbb{R}^3$) are associated with internal load (gravity) and external load (actuation). For static equilibrium, the following equation holds

$$\boldsymbol{\tau} = (\mathbf{J}_{\boldsymbol{\Theta}})^T \mathbf{W}\ , \tag{4.9}$$

where $\mathbf{J}_{\boldsymbol{\Theta}} \in \mathbb{R}^{6\times 6}$ is the spatial manipulator Jacobian. Please refer to Appendix A.2 for the detailed derivation. The above equation is a set of six nonlinear algebraic equations which can be solved to obtain the six DoFs ($\alpha_i, \beta_i, \gamma_i$, where $i \in \{2,3\}$) of a segment of the manipulator. This formulation can be extended for the entire manipulator having N 6-DoF

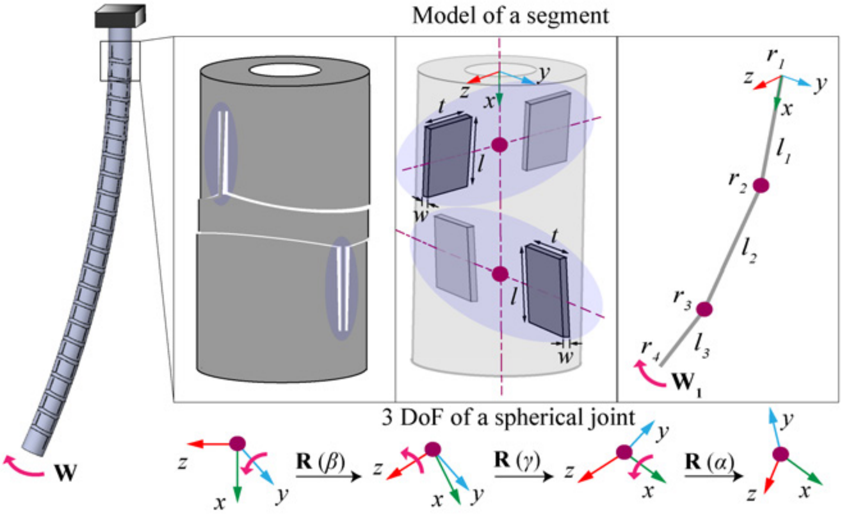

Figure 4.3: A schematic of the quasi-static model of the manipulator made of N segments. Each segment is made of two flexure pairs, which are modelled as thin plates forming two spherical joints. Each spherical joint has three degrees of freedom (3-DoF) with three successive rotations $\mathbf{R}(\beta)$, $\mathbf{R}(\gamma)$ and $\mathbf{R}(\alpha)$, about x, y and z axes, respectively. The manipulator is fixed at one end and subjected to a load ($\mathbf{W}$) at its end. Each segment (i) is in static equilibrium with a load ($\mathbf{W}_i$) at its end.

segments with N loads acting at the respective ends. The static equilibrium equations for the entire manipulator using the rigid-body model are given by

$$\begin{bmatrix} \boldsymbol{\tau}_1 \\ \boldsymbol{\tau}_2 \\ \vdots \\ \boldsymbol{\tau}_N \end{bmatrix} = \begin{bmatrix} (\mathbf{J}_{\boldsymbol{\Theta}_1})^T & (\mathbf{J}_{\boldsymbol{\Theta}_1})^T & \dots & (\mathbf{J}_{\boldsymbol{\Theta}_1})^T \\ 0 & (\mathbf{J}_{\boldsymbol{\Theta}_2})^T & \dots & (\mathbf{J}_{\boldsymbol{\Theta}_2})^T \\ \vdots & \vdots & \ddots & \vdots \\ 0 & 0 & \dots & (\mathbf{J}_{\boldsymbol{\Theta}_N})^T \end{bmatrix} \begin{bmatrix} \mathbf{W}_1 \\ \mathbf{W}_2 \\ \vdots \\ \mathbf{W}_N \end{bmatrix}, \qquad (4.10)$$

where $\boldsymbol{\tau}_k$, $\mathbf{J}_{\boldsymbol{\Theta}_k}$, and $\mathbf{W}_k$ are the internal torques, Jacobian matrix and wrench associated with segment (S_k), respectively. Solving the above $N \times 6$ system of equations gives the displacement of each flexure pair of the manipulator, and the position and orientation of the manipulator can be calculated using forward kinematics (Appendix A.2).

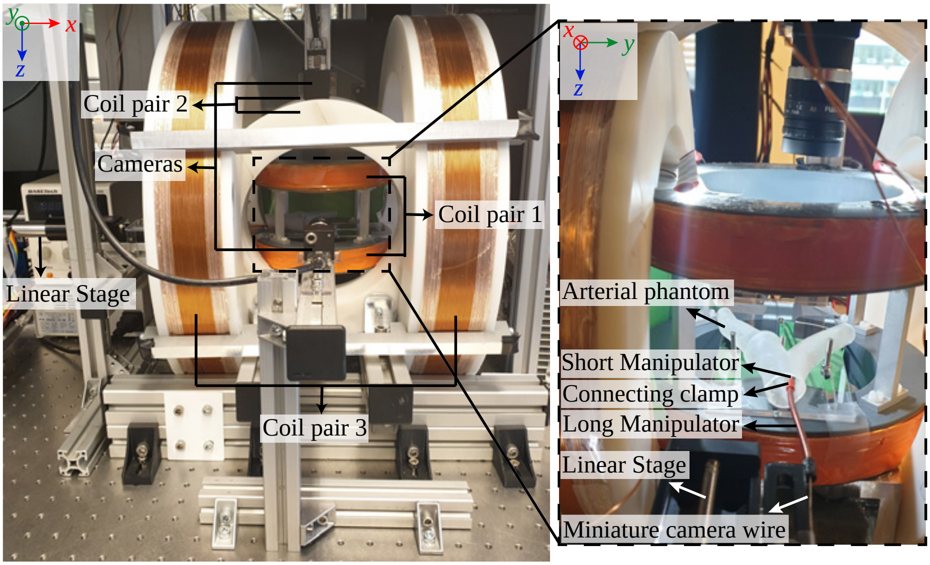

Figure 4.4: PaCMag — an electromagnetic setup used for generating magnetic fields. The inset shows the insertion of the manipulator into a bifurcating arterial phantom using a linear stage.

4.3.2 Test Setup

The actuation of the manipulator is achieved using a magnetic actuation setup (PaCMag) as shown in Fig. 4.4. PaCMag consists of three pairs of electromagnetic coils which are situated orthogonal to each other to generate magnetic fields in 3D space. The two coil pairs except for the coil pair 1 do not conform to the configuration of a Helmholtz coil pair. A magnetic field model for PaCMag is formulated based on Cartesian multipole expansion of a scalar potential that uses measurement-informed least squares optimization [309]. The current ($\mathbf{I} \in \mathbb{R}^3$) to field ($\mathbf{B}^{\mathbf{m}} \in \mathbb{R}^3$) mapping is given by

$$\mathbf{B}^{\mathbf{m}}(\mathbf{p},\mathbf{I}) = \boldsymbol{\beta}(\mathbf{p})\mathbf{I} \ , \tag{4.11}$$

where $\beta(\mathbf{p}) \in \mathbb{R}^{3\times 3}$ is the unit-current field for position ($\mathbf{p} \in \mathbb{R}^3$) in PaCMag's reference frame. The inverse field map calculates the required currents to generate the magnetic field at any given position. The current in each coil pair is controlled by Xenus XE2-230-20 amplifiers (Copley Controls, Canton, USA). Each coil pair can independently generate a maximum magnetic field of 55 mT along its axis at the center of the workspace. PaCMag offers a cylindrical workspace of equal radius and height (65 mm). PaCMag is also equipped with two cameras placed orthogonal to each other, thus forming a stereo vision system to monitor the workspace.

Experiments with the long manipulator are performed by suspending it in the workspace of PaCMag. The base of the manipulator is fixed to a 3D printed support. N48 neodymium ring magnets (outer diameter = 4 mm, inner diameter = 1.5 mm, thickness = 1 mm, mass = 0.08 g and magnetic dipole moment = 0.012 Am^2) are attached to the end of the manipulator. Closed-loop control of the manipulator is performed with the integration of FBG sensors. A multi-core fiber inscribed with FBG sensors is used for this study [55] (Fig. 4.7). The multi-core fiber enclosed within a Hytrel furcation tubing (0.9 mm) is inserted into the 1 mm hole of the long manipulator. Additionally, an FBG-Scan 804D interrogator is installed to record the FBG sensor data.

To show clinical feasibility, experiments are conducted in 3D printed phantoms of a bifurcating arterial system and a heart. The manipulator is inserted using a linear slide (LX20, Misumi Group Inc., Tokyo, Japan), which is fixed horizontally at the base support. A miniature camera of 0.91 mm diameter (Misumi Electronic Corporation, Taiwan) integrated into the 1 mm hole of the manipulator, is used as guidance to steer the manipulator.

4.4 Experiments and Results

This section presents the details of the different experiments carried out with the long and short manipulators. The first set of experiments is conducted to study the motion characteristics of the long manipulator under magnetic actuation. The second set of experiments demonstrates the closed-loop steering of the manipulator using tip pose feedback obtained from a sensor fusion algorithm. The final phase of the study comprises two experiments to show clinical feasibility. The combination of long and short manipulators is tested in 3D phantoms of a bifurcating arterial system and a heart guided by a miniature camera within the manipulators' working channel.

4.4.1 Static Experiments

Static experiments are performed inside PaCMag by suspending the long manipulator in two configurations: horizontally and vertically from its base. Two and three ring magnets are attached to the tip of the manipulator for the experiments in vertical and horizontal configurations, respectively. Time-varying magnetic fields are applied to generate different trajectories with the tip. A stereo vision setup is implemented to capture the shape of the manipulator based on 3D point cloud information followed by a fourth order 3D polynomial fitting along the length of the captured voxels of the manipulator [306]. Furthermore, the quasi-static model detailed in Section III-A is used to estimate the shape of the manipulator. The mean and standard deviation of errors between the quasi-static model and stereo vision data are presented in Table 4.2. It shows the error in position of the tip of the manipulator and the mean whole shape estimation error which is calculated as the average of error in the position of N segments of the manipulator. The plots of the mean whole shape estimation error and the position of the manipulator tip are shown in Fig. 4.5. The overall mean error in whole shape estimation between the model and stereo vision in vertical and horizontal configurations are 2 mm and 4.8 mm, respectively.

4.4.2 Closed-Loop Control

This study presents the closed loop control of the tip of the manipulator integrated with FBG sensors to trace different trajectories. The manipulator with two ring magnets at its tip is suspended horizontally in PaCMag and is subjected to magnetic torques. A proportional-integral (PI) controller is implemented to trace a desired trajectory with the tip of the manipulator as follows. Firstly, the pose of the manipulator tip is calculated using the quasi-static model. Additionally, the shape reconstruction technique with FBGs based on Bishop frames is used to calculate the pose of the manipulator tip [55]. Secondly, an observer-based fusion algorithm using Kalman state estimators fuses the aforementioned calculated poses from the quasi-static model and FBG model to obtain the estimated pose of the manipulator tip [307]. Thirdly, the torque necessary to correct the error between the estimated pose and desired pose of the manipulator tip is determined using a PI controller. The corresponding magnetic field is calculated using the torque and the estimated pose of the manipulator tip, that is, the ring

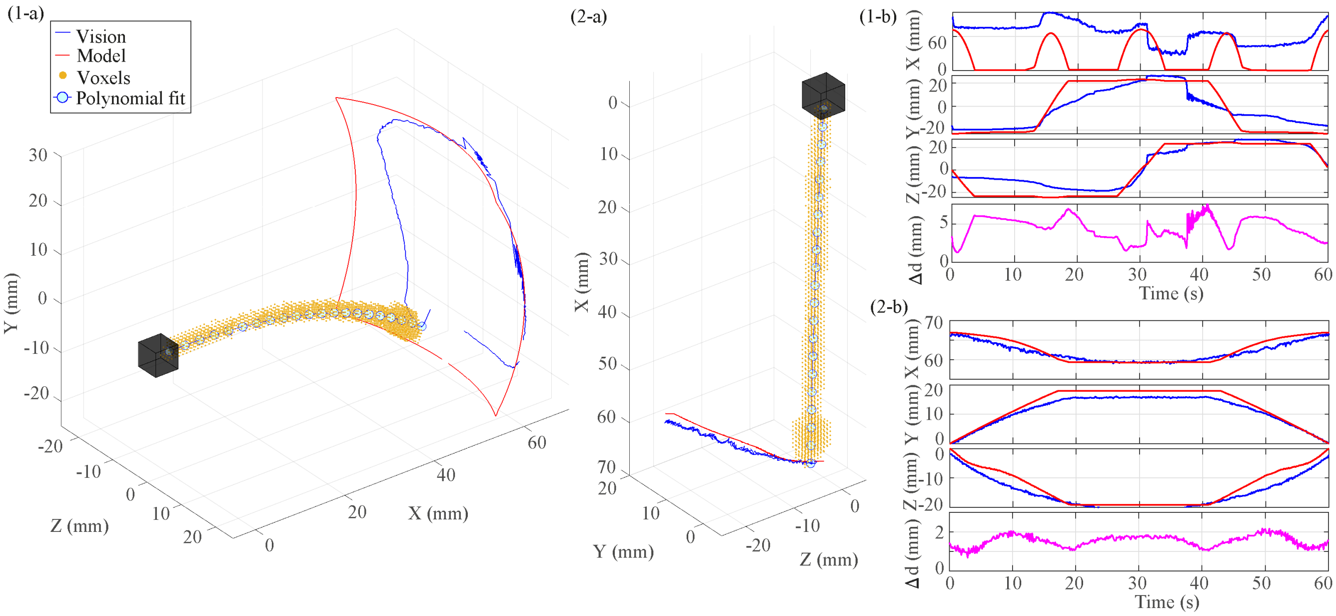

Figure 4.5: Plots showing the captured voxels of the shape of the long manipulator, traced manipulator tip trajectory in x, y and z-coordinates, and the mean whole shape error ($\Delta\bar{d}$) of the manipulator for the following experimental cases: (1) Square tip trajectory at B_{max} = 40 mT in horizontal configuration, (2) Line (m = -1) tip trajectory at B_{max} = 20 mT in vertical configuration.

Table 4.2: Results of static experiments in vertical and horizontal configurations for different tip trajectories: square and line with slope in yz-plane (m) of the long manipulator with maximum strength of magnetic field (B_{max}), the error between quasi-static model and stereo vision models for position (Δx,Δy,Δz) of the manipulator tip, and mean whole shape error ($\Delta\bar{d}$) are shown in terms of mean values and standard deviation (in brackets).

Tip trajectory	B_{max} (mT)	Δx (mm)	Δy (mm)	Δz (mm)	$\Delta\bar{d}$ (mm)
Vertical Configuration					
Square	15	0.8 (0.6)	2.1 (1.4)	2.9 (1.4)	2.0 (0.5)
Square	10	0.7 (0.5)	2.0 (0.9)	2.3 (1.5)	1.8 (0.4)
Line: $m = \infty$	20	1.1 (0.5)	2.3 (1.1)	2.5 (1.2)	1.9 (0.3)
Line: $m = 0$	20	0.6 (0.4)	1.9 (1.3)	2.3 (1.1)	1.6 (0.2)
Line: m = -1	20	0.7 (0.6)	1.7 (0.8)	1.9 (1.2)	1.6 (0.3)
Line: m = -1	15	0.8 (0.6)	1.5 (0.9)	1.9 (1.3)	1.5 (0.3)
Horizontal Configuration					
Square	40	3.9 (2.1)	8.5 (5.8)	5.4 (4.6)	4.5 (1.6)
Square	25	4.0 (2.8)	10.5 (5.7)	5.8 (5.8)	5.4 (1.8)
Square	20	3.8 (2.5)	12.7 (5.3)	7.1 (5.6)	5.8 (1.6)
Line: $m = 0$	30	1.6 (1.5)	6.9 (5.7)	5.5 (4.8)	4.6 (1.2)
Line: $m = 0$	20	1.2 (0.9)	4.8 (1.9)	7.3 (4.2)	4 (1.1)

magnets. Lastly, the inverse field map of PaCMag computes the required current which is supplied to the coils. The actuated manipulator is tracked by the stereo vision setup during the whole process. The pose measured by the stereo vision setup serves as the ground truth for the study. Fig. 4.6 is a block diagram summarizing the closed-loop control system.

4.4.2.1 FBG Shape Reconstruction

This section outlines the shape reconstruction technique using the multi-core fiber with FBG sensors integrated into the manipulator. Fig. 4.7 shows a schematic of the fiber. Four cores of the fiber, each with four FBG sensors are used for shape reconstruction of the manipulator. The fiber is modelled as a regular unit-speed space curve in 3D space defined by curvature vectors and Bishop frame equations. The curvature vectors

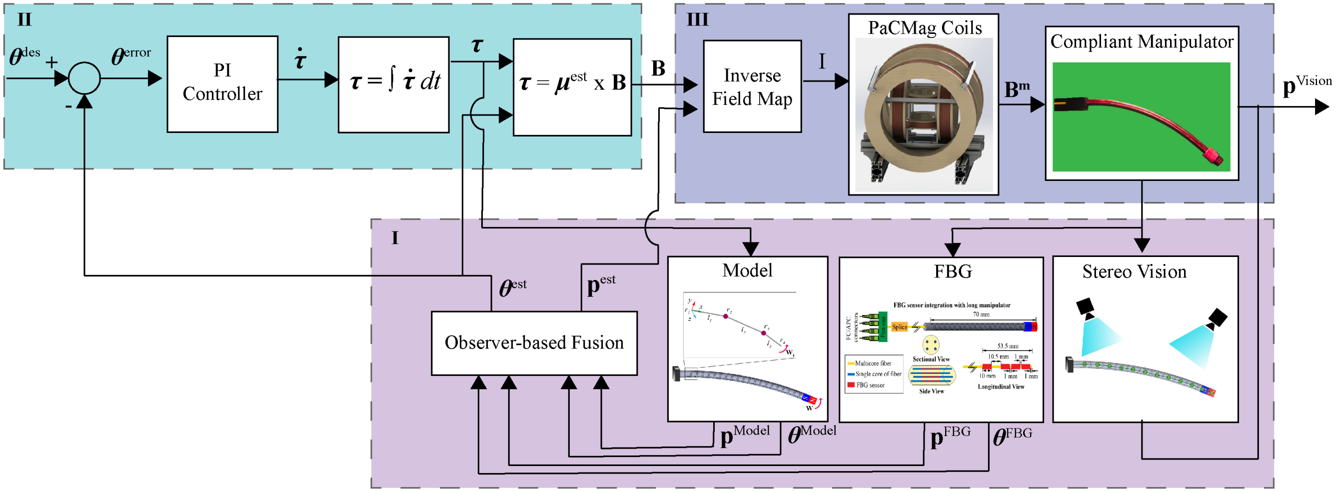

Figure 4.6: Closed-loop control system of the manipulator to trace different trajectories summarized in three blocks: (I) The pose of the manipulator tip is calculated by the quasi-static model ($\mathbf{p}^{\text{Model}}$,$\boldsymbol{\theta}^{\text{Model}}$) and the FBG sensors ($\mathbf{p}^{\text{FBG}}$,$\boldsymbol{\theta}^{\text{FBG}}$). An observer-based fusion algorithm fuses the two sets of data to calculate the estimated pose of the manipulator tip ($\mathbf{p}^{\text{est}}$, $\boldsymbol{\theta}^{\text{est}}$). The stereo vision system records the position of the manipulator tip ($\mathbf{p}^{\text{Vision}}$), which serves as the ground truth. (II) A proportional-integral (PI) controller computes the torque rate ($\dot{\boldsymbol{\tau}}$) necessary to minimize the error ($\boldsymbol{\theta}^{\text{error}}$) between the desired ($\boldsymbol{\theta}^{\text{des}}$) and estimated ($\boldsymbol{\theta}^{\text{est}}$) tip orientation. The associated magnetic torque (τ) is obtained by numerical integration of $\dot{\boldsymbol{\tau}}$. The corresponding magnetic field ($\mathbf{B}$) is obtained using the estimated magnet orientation ($\boldsymbol{\mu}^{\text{est}}$). (III) The inverse field map of PaCMag determines the required current (I) for the coils to generate the reference magnetic field ($\mathbf{B}^{\mathbf{m}}$) and control the tip of the manipulator.

are calculated at the four FBG sensor sets using the strains computed from FBG wavelength measurements. Subsequently, the Bishop frame is used to derive the curve. Consequently, the pose of the manipulator tip is determined using the reconstructed shape of the manipulator. More details on this derivation can be found in the previous work [55].

Following the reconstruction technique, the fiber enclosed inside the manipulator is calibrated for this study by using data points obtained from open-loop experiments. The FBG shape reconstruction is registered with the ground truth shape obtained from the stereo vision. Fig. 4.7(b) shows the reconstructed tip position of the FBG sensors, quasi-static model and stereo vision. The overall mean error in tip position estimation between the FBG sensors and stereo vision is 4.86 mm and that between the quasi-static model and stereo vision is 6.86 mm.

4.4.2.2 Observer-based Fusion

To improve the accuracy of the estimated pose of the manipulator tip, the pose data from the quasi-static model and FBG sensors are fused. The fusion of position and orientation of the manipulator tip are done separately using an observer-based sensor fusion algorithm in conjunction with Kalman state estimators. The estimated pose of the manipulator is obtained from the fused position ($\mathbf{p}^{\text{est}} \in \mathbb{R}^3$) and orientation ($\boldsymbol{\theta}^{\text{est}} \in \mathbb{S}^3$) computed as follows

$$\hat{\mathbf{x}}_{k+1|k+1} = \hat{\mathbf{x}}_{k+1|k} + \mathbf{K}_{k+1}\left[\mathbf{y}(k) - \mathbf{C}_d\hat{\mathbf{x}}_{k+1|k}\right] \ , \tag{4.12}$$

where $\hat{\mathbf{x}}_{k|k}$ is the estimate of $\hat{\mathbf{x}}$ at time instant k given observations up to and including at time k, $\mathbf{K}_{k+1}$ is the optimal Kalman gain, $\mathbf{y}(k)$ is the measurement data from the model ($\mathbf{p}^{\text{Model}} \in \mathbb{R}^3$ and $\boldsymbol{\theta}^{\text{Model}} \in \mathbb{S}^3$) and FBG sensors ($\mathbf{p}^{\text{FBG}} \in \mathbb{R}^3$ and $\boldsymbol{\theta}^{\text{FBG}} \in \mathbb{S}^3$) at time k, and $\mathbf{C}_d$ belongs to the disturbance dynamics measurement. More information on the above formulation is detailed in Appendix A.3 and can be found in the previous work [307].

4.4.2.3 Proportional-Integral Control

The manipulator is actuated to follow a desired tip trajectory by implementing a PI controller. The controller is designed to control the orientation of the manipulator about two axes (θ_y and θ_z), since no torque can

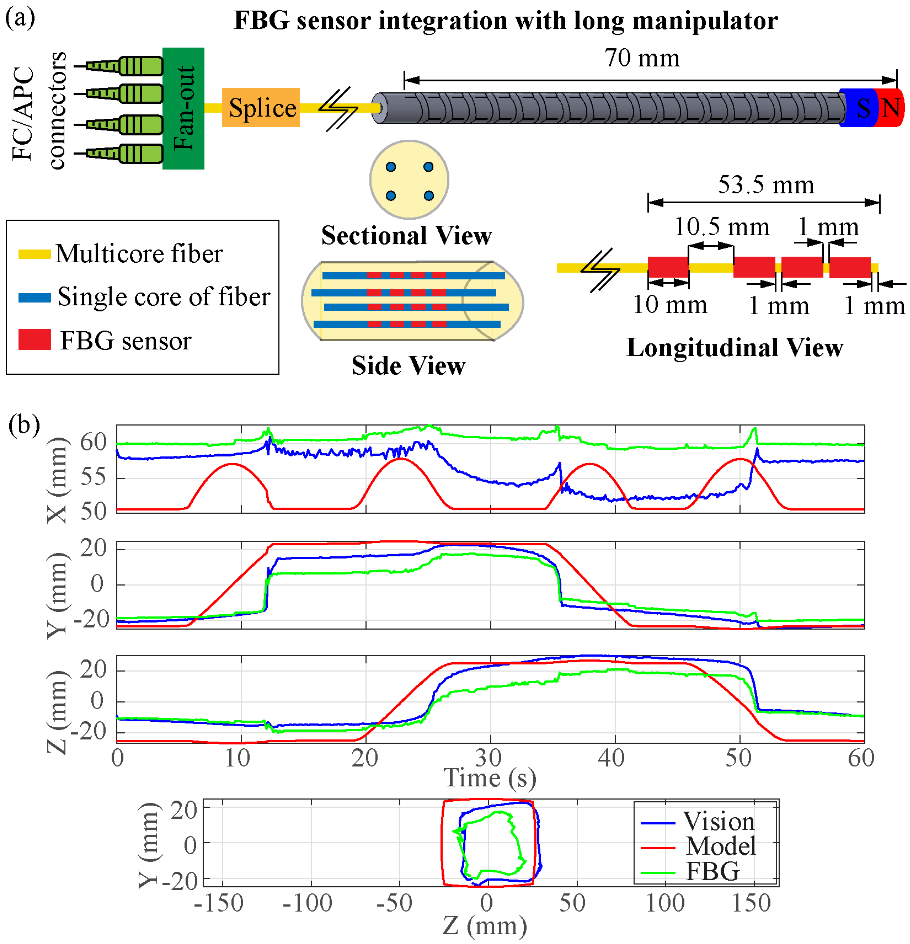

Figure 4.7: (a) A schematic of the multicore fiber with fiber Bragg grating (FBG) sensors integrated with the long manipulator. The side view depicts the four cores in blue, each with four FBG sensors in red. The section view depicts the orientation of the cores and the longitudinal view outlines the the spacing of the FBG sensors in the fiber. (b) Plots of manipulator tip position obtained from FBG shape reconstruction (FBG), quasi-static model (Model) and stereo vision (Vision) after calibration.

be produced about the axis parallel to the direction of the magnetic dipole ($\boldsymbol{\mu}^{\text{est}}$). The torque ($\boldsymbol{\tau} \in \mathbb{R}^3$) necessary to minimize the error ($\mathbf{e} \in \mathbb{S}^3$) between the desired tip orientation ($\boldsymbol{\theta}^{\text{des}} \in \mathbb{S}^3$) and estimated tip orientation ($\boldsymbol{\theta}^{\text{est}} \in \mathbb{S}^3$) is calculated as follows

$$\dot{\boldsymbol{\tau}} = K_P\,\mathbf{e} + \int K_I\,\mathbf{e}dt \ , \tag{4.13}$$

where $\mathbf{e} = \boldsymbol{\theta}^{\text{des}} - \boldsymbol{\theta}^{\text{est}}$, K_P and K_I are the PI gains. The corresponding magnetic control torque ($\boldsymbol{\tau}$) is obtained by the numerical integration of $\dot{\boldsymbol{\tau}}$. The associated magnetic field ($\mathbf{B}$) is determined for the current estimated magnet orientation ($\boldsymbol{\theta}^{\text{est}}$) using the inverse of the equation below

$$\boldsymbol{\tau} = \boldsymbol{\mu}^{\text{est}} \times \mathbf{B} \ , \tag{4.14}$$

where $\boldsymbol{\mu}^{\text{est}}$ is the estimated magnetic dipole moment. The obtained magnetic field ($\mathbf{B} \in \mathbb{R}^3$) is transformed to the reference frame of PaCMag ($\mathbf{B}^{\mathbf{m}} \in \mathbb{R}^3$) in order to find the necessary current to be supplied by the coils. In this way, the inverse field map using Eqn. 4.11 calculates the required currents to generate the magnetic field ($\mathbf{B}^{\mathbf{m}}$) at the current estimated position ($\mathbf{p}^{\text{est}}$) of the manipulator tip.

4.4.2.4 Results

Closed-loop control of the manipulator tip traces two trajectories: square and straight line. The poses of the manipulator tip calculated by the FBG sensors, quasi-static model, fusion and the stereo vision, and the applied magnetic torques are recorded during the experiment as plotted in Fig. 4.8. For the square and straight line trajectories, results show the average errors between the desired and estimated positions from fusion of 5.3 mm and 2.9 mm, respectively and that between the desired and stereo vision measured positions of 6.8 mm and 6.7 mm, respectively in position. The average error between the desired and estimated orientations from fusion of the square and straight line trajectories are 11.1° and 4.8°, respectively. The tip orientation control implemented has a control frequency of 6.5 Hz.

4.4.3 Phantom Study

These experiments demonstrate the maneuverability of the manipulator suspended in horizontal configuration inside two clinically relevant phan-

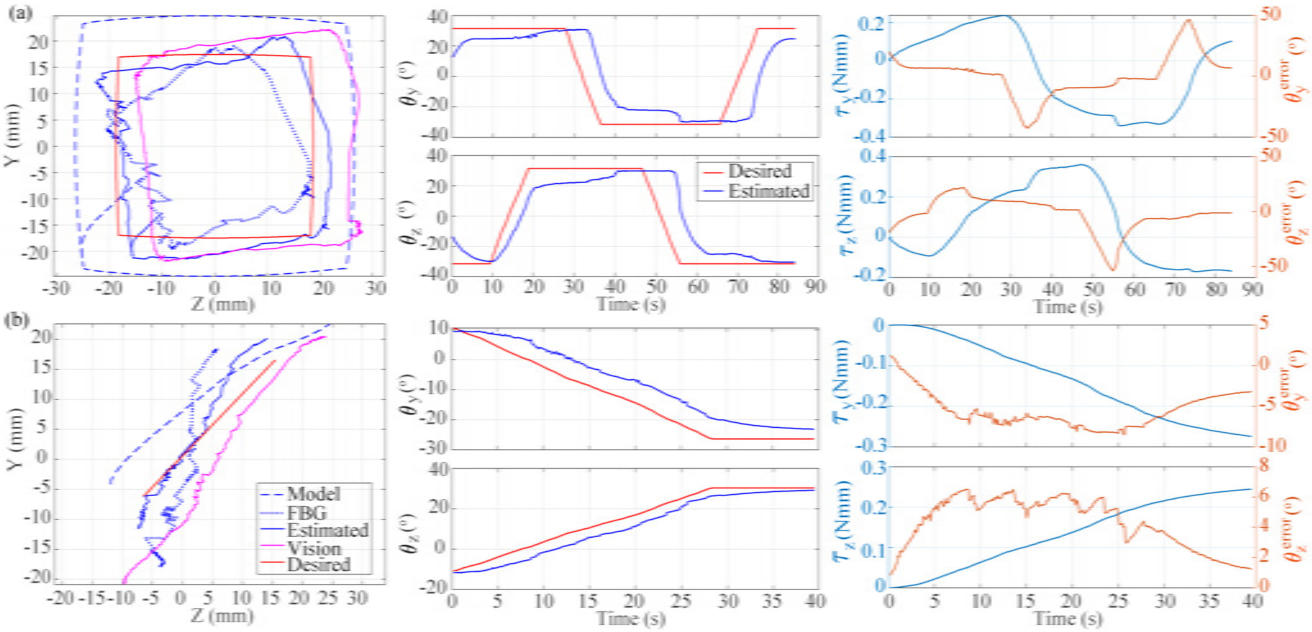

Figure 4.8: Plots of closed-loop control experiments showing the position (y,z-coordinates) and orientation (θ_y, θ_z) of the manipulator tip, and magnetic torque (τ_y,τ_z) generated to correct the error in orientation (θ_y^{error},θ_z^{error}), for two trajectories: (a) Square (b) Straight line.

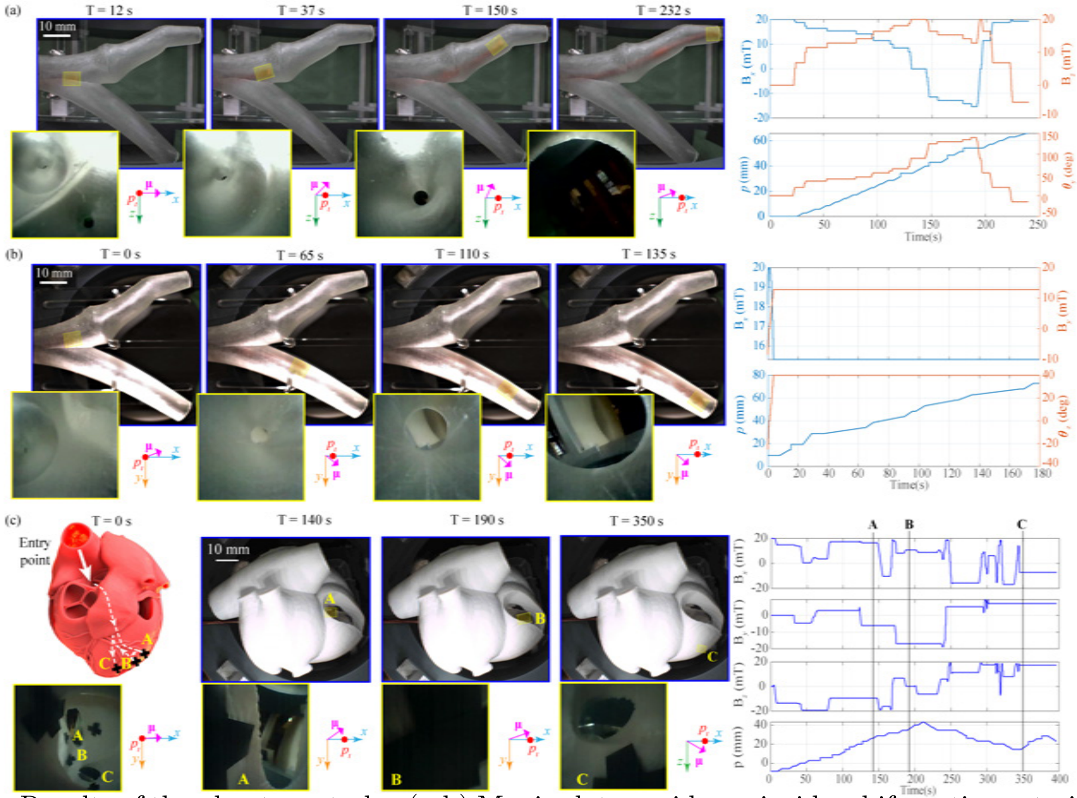

Figure 4.9: Results of the phantom study: (a-b) Manipulator guidance inside a bifurcating arterial phantom suspended vertically and horizontally in the workspace of PaCMag. (c) Manipulator guidance inside a heart model placed in PaCMag. The dotted white lines show the traced trajectory starting at the aortic valve to reach three target locations A, B and C in the left ventricle. For all the experiments, the views of the miniature camera at the tip of the manipulator (highlighted in yellow) are shown at different time instants. Plots show generated magnetic field (B_x,B_y,B_z), its direction (θ_y,θ_z), and position of the linear stage (p). Please refer to the supplementary video for the complete demonstration.

toms. A combination of the long and short manipulators forming a total length of 100 mm is used to cover a larger workspace. Two ring magnets are attached to its tip. The manipulator is inserted using a linear stage and steered in 3D by rotating the magnetic field to create different shapes and maneuver to target locations. A miniature camera integrated into the manipulator provides the visualization of the environment to navigate the manipulator in a clinically-relevant manner.

In the first experiment, the manipulator is accurately guided inside the undulating tapered channels of a bifurcating arterial phantom. The experiment is performed by positioning the phantom in vertical and horizontal orientations as shown in Fig. 4.9 (a-b). In the second experiment, the maneuverability of the manipulator is tested inside a heart model. The manipulator is inserted through the aortic valve and is guided to reach three targets locations in the left ventricle (Fig. 4.9(c)). By incorporating the miniature camera and increasing the length of the manipulator, these experiments demonstrate the steerability of the manipulator without relying on an external imaging system. Please refer to the supplementary video for demonstration of the experiment results.

4.5 Discussion

The monolithic design of the manipulator makes it easy to fabricate from a single tube of titanium without requiring assembly. The 1 mm hollow interior channel offers room for embedding sensors to enhance its functionality. The flexure pair deflection is limited by the contact between the adjacent walls. The stress experienced by the flexures is below the designed threshold. This has led to a reliable and safe design without any noticeable plastic deformation even after repeated testing, as compared to the single-axis bending designs previously fabricated [110]. However, the maximum deflection of the long manipulator is observed to be 40°. The deflection can be increased by eliminating the contact between adjacent walls and enabling deflection until the flexures make contact with the adjoining wall. This redesign will require further optimization of the associated design parameters (l,w,w_c,ψ) of the manipulator.

Results of the static experiments with the long manipulator show that the quasi-static model is more accurate in the vertical configuration than the horizontal configuration experiments. This could be due to the difference in the effect of gravity. In vertical configuration, all the flexures experience gravity in the same direction, while in horizontal configuration the two sets of flexure pairs in the orthogonal planes experience gravity in different (local) bending directions. Therefore, in the subsequent closed-loop control demonstration, the manipulator was fixed at the base such that the flexure pairs are oriented 45° with respect to the direction of gravity for uniformity.

FBG sensors are introduced into the long manipulator to improve shape estimation of the manipulator. The accuracy of the FBG shape reconstruction is limited by the small curvature of the manipulator measured by only four sets of FBG sensors. The twisting of the fiber relative to the manipulator could also be a cause of error, since the fiber is only secured at its base and inserted in the hollow channel of the manipulator. The stereo vision system used as ground truth is also prone to calibration error. Owing to the large length to diameter ratio of the manipulator, some distortion is observed in the images captured by the cameras.

The calibration results for shape sensing indicate that the tip position estimation using either the FBG sensors or the quasi-static model have errors greater than 3 mm (diameter of the manipulator) as shown in Fig. 4.7(b). It is observed that the FBG shape reconstruction underestimates the curvature and the quasi-static model overestimates the curvature. Therefore, an observer-based sensor fusion algorithm is implemented to improve the sensing results. This approach has been found to be the best among other multi-sensor fusion algorithms of unscented Kalman filter, Luenberger and Kalman state estimators investigated in our previous work [307], [310], [311].

For closed-loop control, orientation control of the manipulator tip (θ_y, θ_z) is chosen over position control, since position control becomes computationally expensive using the Jacobian of the manipulator. This can be simplified by reducing the DoFs per segment in the quasi-static model, as the deflection due to torsion and auxiliary bending are not significant compared to primary bending deflection. Although the shape reconstruction using FBG sensors works reasonably well in open-loop (Fig. 4.7(b)), noise is observed during closed-loop (Fig. 4.8). This could be attributed to the low stiffness of the flexures which influences the dynamics of the manipulator during closed-loop motion, which in turn affects the performance of the sensor fusion algorithm. However, the controller follows the desired trajectory for the most part as inferred from the orientation plot of tip (Fig. 4.8). Higher error is seen during the periods of motion with rapid transitions, like in square trajectory when transitioning from one edge to another. Straight line trajectory has relatively lower error due to the lower rate of changing angles. Though all the experiments are conducted assuming constant room temperature, temperature feedback can be added to the control system by incorporating a temperature sensor. For example, an additional FBG sensor can be embedded in the manipulator which does not experience any strain and measures the temperature.

The phantom study is carried out by combining the long and short manipulators in order to reach more locations in the workspace. The ability of the manipulator to be precisely steered through a bifurcating artery phantom and reach specific target locations inside a heart phantom with the guidance of a miniature camera demonstrates potential applications in angioplasty, endoscopy and catheter ablation. The size of the manipulator is comparable to the 6 – 10 Fr Magellan robotic catheters which are of outer diameters 2 – 3.33 mm [312]. The maximum deflection of the combined manipulator is limited to 57°, whereas the bending angle of steerable catheters can be between 45 – 180°, up to 270° or even 360° depending on the application. There is a definite need to improve the positioning accuracy of the manipulator which is crucial in surgical procedures like ventricular tachycardia, where multiple lesions can be found at adjacent distances of the order of 5-10 mm [313].

4.6 Conclusions and Future Work

This chapter presents a new design of a monolithic compliant continuum manipulator with a novel notched-tube pattern of flexures that ensures the stresses experienced are within design limits. Two versions of manipulator of lengths 70 mm and 30 mm capable of spatial bending up to 40° and 17°, respectively, are fabricated using a single titanium tube of diameter 3 mm. The combination of the two can bend up to 57°. A quasi-static model is developed to study the 3D motion of the manipulator under magnetic actuation. Static experiments show overall mean errors between whole shape estimated by the model and the ground truth of 1.7 mm and 4.8 mm, in horizontal and vertical configurations respectively. In order to improve the accuracy of shape estimation, an observer-based sensor fusion algorithm using Kalman state estimators is implemented with the integration of FBG sensors. The fusion algorithm has potential in offering a real-time visualization alternative to X-ray exposure during operation. Thereafter, a closed-loop control strategy to trace a square and a straight line tip trajectories is demonstrated, resulting in an average error between the desired and estimated tip positions of 4.1 mm. The feasibility of the continuum manipulator as a steerable catheter is studied by incorporating a miniature camera within its working channel, to show potential applications in endoscopy and catheter ablation. The accurate maneuvering of the manipulator in 3D to reach different target locations is demonstrated in two clinically relevant phantoms of a bifurcating artery and a heart.

In future work, the design of the manipulator will be improved to achieve higher range of motion ($> 90^\circ$). Fabrication of complex shape profiles of flexures will be explored using wire EDM, electrochemical etching and laser cutting methods. Redesigning using a combination of segments of the manipulators connected by magnets with different polarities will be investigated. The dexterity and maneuverability will be improved by incorporating additional translation and rotational DoFs to the manipulator during insertion. The positioning and steering accuracy will be addressed by improving the shape sensing of the manipulator. Multiple FBG sensors will be embedded more securely along the length of the manipulator, and helical core fibers will be used to account for twist [314]. Control of the manipulator in tandem with medical imaging techniques and human-in-the-loop operation strategies will be explored. Further testing will be carried out in *ex-vivo* animal studies.

II

Variable Stiffness Mechanisms

Preface

Variable stiffness mechanisms are part of a specialized area of research within robotics that is receiving critical attention in recent years. The idea of stiffness control in continuum manipulators provides an opportunity to harness the best attributes of both soft and rigid bodied manipulators. While rigidity provides stability, precision, and load bearing capacity, softness enhances flexibility and mobility for safe interactions with the environment. Literature research suggests variable stiffness mechanisms based on antagonistic actuation, smart materials like shape memory alloys (SMAs) and shape memory polymers (SMPs), grannular jamming, among others. Although each of these mechanisms has certain advantages over another when it comes to miniaturization and response time, a careful consideration in terms of actuation stimuli is necessary in designing variable stiffness manipulators. This part of the dissertation will propose two approaches in which variable stiffness mechanisms can benefit specific surgical functions.

Chapter 5 introduces a magnetically-actuated variable stiffness robot (VSR) with a sliding nitinol backbone. The synchronized retraction of the backbone within the soft body of the VSR under magnetic actuation leads to high deformation coiling action with a stiffness change factor of 765 and a maximum deformation angle of 400°. The VSR is demonstrated to grasp various objects in closed-loop using camera-based tracking as feedback. Chapter 6 presents a new deployable variable stiffness manipulator (VSM) based on SMP springs. The VSM exhibits variable stiffness and variable bending curvatures at variable operating lengths. The shape locking ability of the VSM has potential to act as a stabilizer in the deployment of surgical tools. Applications of the VSM in endoscopy, biopsy and laser surgery are demonstrated in combination with robotic magnetic actuation.

5

A Magnetically-actuated Coiling Soft Robot with Variable Stiffness

Note: *The following chapter is adapted from the article "A Magnetically-actuated Coiling Soft Robot with Variable Stiffness" by P. Lloyd**, ***T. L. Thomas****, *V. Kalpathy Venkiteswaran, G. Pittiglio, J. H. Chandler, P. Valdastri and S. Misra, under review in "IEEE Robotics and Automation Letters", special issue on "Small-Scale Robots in the Medical Context, From Modeling and Fabrication to Clinical Applications", October 2022.*
The chapter has been reformatted in terms of figures to fit this doctoral thesis. No changes to the technical contents of this peer-reviewed manuscript have been made.

Authors' Contributions: *P. Lloyd and G. Pittiglio conceived the robot design. P. Lloyd performed the design analysis and fabricated the robot. T. L. Thomas carried out the experiments in PaCMag, developed the image processing algorithm, performed the closed-loop control analysis and interpreted the results. P. Lloyd contributed to the experiments and interpreted the results. V. Kalpathy Venkiteswaran aided in the experiments, analysis and interpretation of the results. G. Pittiglio and J. H. Chandler provided critical feedback. P. Valdastri and S. Misra supervised the overall project. P. Lloyd and T. L. Thomas prepared the manuscript with input from all the authors.*

---

*contributed equally to the work

Abstract

Soft and flexible magnetic robots have gained significant attention in the past decade. These robots are fabricated using magnetically-active elastomers, are capable of large deformations, and are actuated remotely thus allowing for small robot size. This combination of properties is appealing to the minimally invasive surgical community, potentially allowing navigation to regions of the anatomy previously deemed inaccessible. Due to the low forces involved, one particular challenge is functionalizing such magnetic devices. To address this limitation we introduce a variable stiffness robot controlled by remote magnetic actuation, capable of grasping objects of varying sizes. We demonstrate a controlled and reversible high deformation coiling action induced via a transient homogeneous magnetic field and a synchronized sliding nitinol backbone. Our soft magnetic coiling grasper is visually tracked and controlled in closed-loop during three experimental demonstrations. We exhibit a maximum coiling deformation angle of 400°.

5.1 Introduction

Soft magnetic robots, due to an inherent reduction in traumatic anatomical forces, display the potential to supersede traditional mechanically-actuated surgical catheters [315] [316] [317]. The ability of these robots to maneuver through delicate and critical anatomy in a minimally invasive manner is key to improving the feasibility and success of many treatments [13]. Magnetic actuation allows devices to be composed of softer materials as forces and torques can be applied directly to embedded magnetic material as opposed to lengthwise force transmission [290] [40]. Furthermore, this class of rapid and clinically safe actuation eliminates the need for on-board power transmission systems (such as electrical or pneumatic) allowing easy miniaturization [318].

In order to introduce shape-programmability, magnetically-hard particles with high coercivity can be incorporated into mechanically soft materials capable of large deformations [319] [320] [321]. This system is capable of creating complex time-varying shapes at small scales as magnetic field control inputs can be specified in magnitude, direction and spatial gradient [322]. Magnetic soft continuum structures can also be fabricated with a continuous lengthwise magnetization profile thus generating spatially resolved

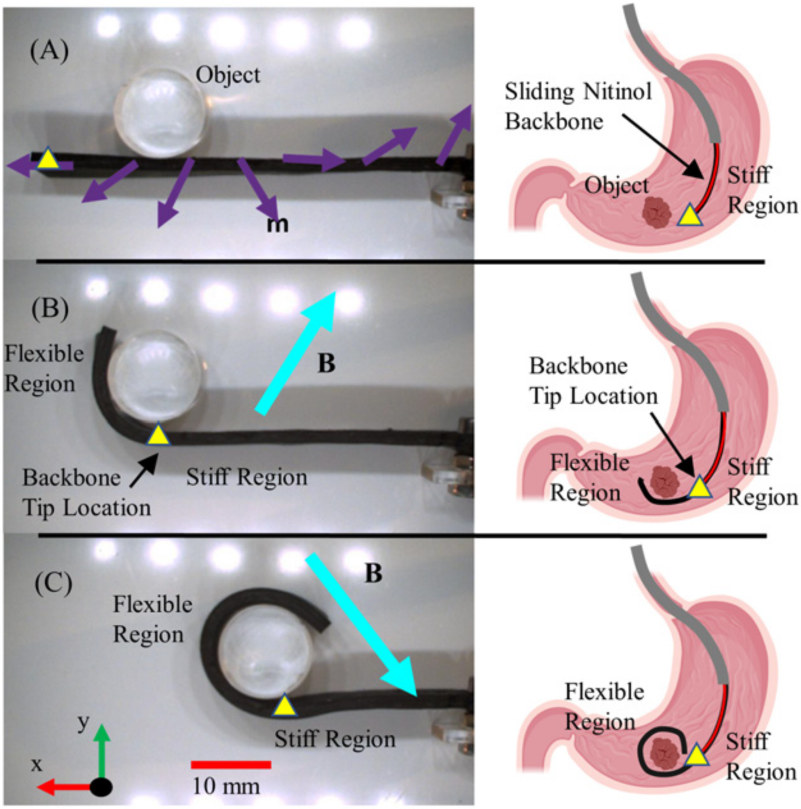

Figure 5.1: Three representative instances taken from the Supplementary Video (left) shown alongside a clinically relevant application - grasping for removal of an excised stomach tumour (right). (A) The sliding nitinol backbone is fully inserted (tip of backbone shown as yellow triangle on the left and red overlay on the right) - the stiff region will not respond to actuation. Magnetization (**m**) is shown here by purple arrows. (B) The wire-frame is partially retracted allowing deformation of the "Flexible Region". This is actuated via a homogeneous magnetic field (**B**) shown as the turquoise arrows. The "Stiff Region" retains its backbone support. (C) The wire-frame is further retracted as the applied field is rotated. This grasping pose would be unachievable without the sliding nitinol backbone.

deformations [322]. A range of applications have been demonstrated using this approach [318] including, amongst other applications, autonomous navigating catheters [40], cilia-like shape forming structures [322], untethered swimmers [321], shape forming catheters [323] [324], and untethered grippers [325].

Softness represents a clear advantage for medical tools [326], however, this can also be problematic when it comes to performing functional tasks. As such, variable stiffness becomes a highly desirable feature such as the magnetic catheter with conductive shape memory polymer demonstrated in [327]. There are many approaches to achieve stiffening, most commonly; geometric changes such as modifying the cross-sectional profile, elastic changes such as phase transition or jamming and antagonistic actuation [328]. The typical motive for stiffening in continuum robots, however, is to shape-lock after actuation [329].

In this proof-of-concept work, we employ material variable stiffness in the form of a sliding nitinol backbone which offers a stiffness change factor of close to 800. This movement is synchronistically controlled within a closed-loop with a time-varying actuating field (Fig. 5.1) for the novel purpose of constraining some proximal length of our robot against deformation whilst we actuate the remaining distal length (Fig. 5.2). This allows us to apply otherwise unstable combinations of magnetization and actuating field to achieve a forward time marching deformation, fully dependent on the previous pose. Consequentially, we generate a higher strain energy equilibrium and achieve circular deformations greater than one full revolution.

We have applied this concept to the demonstrative example of coiling for cargo grasping or delivery. There is a clinical appetite for soft, miniaturizable retrieval and delivery systems for biopsy or therapeutic use [330] [331] [332], and this innovation moves us towards the development of variable stiffness for greater deformation potential under magnetic actuation.

The significant contribution of this work is the closed-loop actuation of a potentially unstable magnetic robot with variable stiffness. Synchronized actuation and variable stiffness combine to achieve stable, large deformation shape forming. To prove the necessity of the inclusion of the sliding nitinol backbone, we also demonstrate the unsuccessful actuation of the robot without the inclusion of stiffening wires. This system is implemented in an 80 mm long, 10 mm x 2 mm cross-section tongue-like robot which grasps

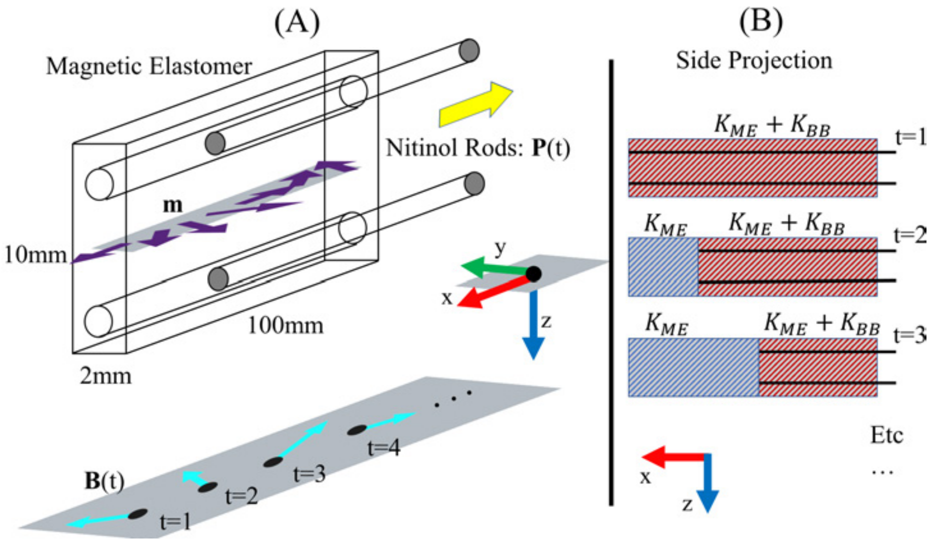

Figure 5.2: Schematic of the underlying design and actuation strategy. (A) The elastomer is magnetized (**m**), shown as purple arrows, in the x-y plane (shown in grey) in a spatially sinusoidal fashion along the length of the x-axis. A temporally sinusoidal actuating field (**B**(t), turquoise arrows) is applied (also in the x-y plane), as the nitinol rod backbone is withdrawn (**P**(t), yellow arrow). (B) This controlled augmentation of the unconstrained, and therefore lower stiffness, length of the VSR allows higher strain energy states to be achieved. K_{ME} and K_{BB} are the bending stiffness of the magnetic elastomer and the nitinol backbone, respectively.

and releases arbitrary objects via coiling.

5.2 The Variable Stiffness Robot

In this section, we detail the analytical design principles, the fabrication technique and the dual material characterization of our tongue-like, variable stiffness robot (VSR).

5.2.1 Analytical Design - Elastic Torque

We represent the flexible, unsupported region of the VSR as a serial chain of rigid links connected by planar (1 Degree of Freedom) rotational joints as a simplification of [333] and [334]. Any desired shape can be represented as a vector of joint angles $\mathbf{q}$ where the length of $\mathbf{q}$ is determined by the granularity of discretization (individual link length l) and the unconstrained length of the VSR, itself a function of time ($L = L(t)$). Elastic joint torque is given as

$$\boldsymbol{\tau}_{elas} = \frac{K\mathbf{q}}{l}, \tag{5.1}$$

where l is the virtual link length and K is the bending stiffness which can be approximately defined as:

$$K = E_{ME}I_{ME} + E_{BB}I_{BB}, \tag{5.2}$$

with E_{ME} and I_{ME} as the Young's modulus and the second moment of area for bending of the rectangular cross-section magnetic elastomer, and E_{BB} and I_{BB} are those of the circular cross-section backbone, respectively (See Fig. 5.2)

$$I_{ME} = \frac{wh^3}{12}, \tag{5.3}$$

$$I_{BB} = \frac{n\pi}{4}r^4, \tag{5.4}$$

with w as the elastomer width, h as the elastomer height, r as the radius of the support rods, and n as the number of support rods. When the nitinol backbone is withdrawn $E_{BB} = 0$ and the mechanical stiffness drops dramatically.

5.2.2 Analytical Design - Magnetic Torque

A magnetic dipole with moment $\mathbf{m}$ in a homogeneous field $\mathbf{B}$(t) will experience a resultant magnetic torque proportional to applied field strength

$$\boldsymbol{\tau}_{mag}(t) = \mathbf{m} \times \mathbf{B}(t), \tag{5.5}$$

where $\mathbf{B}$(t), $\mathbf{m}$, $\boldsymbol{\tau}_{mag}(t) \in \mathbb{R}^3$ (If $\mathbf{B}$ and $\mathbf{m}$ are constrained to the x-y plane then the cross product becomes *effectively* scalar). The body torque acting on any discretized segment (virtual link) of the VSR as a consequence of the interaction of the actuating magnetic field, and the *deformed* magnetization of that region of doped elastomer will produce deformation, and therefore be counteracted by the elastic properties of the material.

5.2.3 Analytical Design - Torque Balance

Assuming gravity to be zero, we can balance the elastic torque at any given virtual joint (i, in a VSR of N virtual joints) with the aggregation of magnetic torques on every distal virtual link in the VSR at any given time step

$$\tau_{i,elas} = \sum_{n=i}^{N} \boldsymbol{\tau}_{n,mag}. \tag{5.6}$$

As illustrated in Fig. 5.3, we can define our desired shape as some proportion of a circle. The joint array q for a full circle of deformation becomes N equal joints of $\frac{360}{N}^{\circ}$, where q increases in length by one entry with each time step from $t = 0$ to $t = N$. Anything proximal to the joint of interest will be constrained by the backbone and is assumed to be rigid (See Section 5.2.5).

Inverting the aggregation of (5.6) over all time steps would give non-unique solutions for $\mathbf{m}$ and $\mathbf{B}$ - the necessary combination of fields and magnetizations can be rotated about z whilst still producing feasible outputs. By implementing constraints (which in practice, aid stability) namely, the distal magnetization must be axial and all segment magnetizations must be within 60° of all their neighboring magnetizations, a unique solution exists for any set of joint angle arrays. This solution was determined using the Genetic Algorithm (GA, Global Optimization Toolbox, Matlab version R2021b) to generate discretized magnetization profiles and time-stepping actuating fields. This was solved in the previous work of [324], hence has not been elaborated further.

As can be observed in Fig. 5.2 and Fig. 5.3, these resultant magnetizations and actuating fields are sinusoidal in nature. The magnetization sinusoid running spatially along the long (x) axis of the robot and the actuating field sinusoid rotating as a function of time.

The driving variable here is the *bending radius* (r) and is defined as the radius of the circle which is formed by the array of equal desired joint angles, so, taking q_{des} as a scalar from the joint angle array and with l as

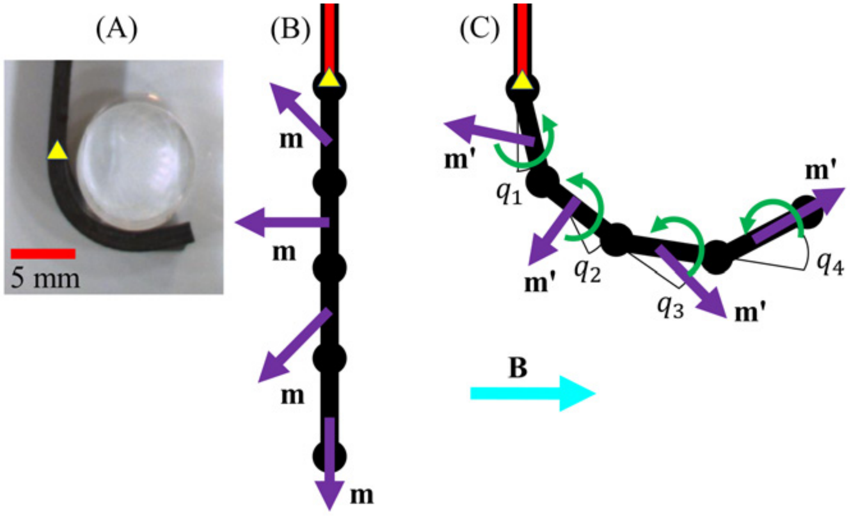

Figure 5.3: (A) A representative pose of the VSR with the tip location of the sliding nitinol backbone indicated by the yellow triangle and the backbone supported region shown as red overlay. (B) Illustratively discretized into four rigid links with referential magnetizations ($\mathbf{m}$) shown as purple arrows. (C) Deformed magnetization ($\mathbf{m'}$) shown again as purple arrows, resultant magnetic torques as green arrows, applied field ($\mathbf{B}$) as turquoise arrow and deformed joint angles as q_i, $i \in [1,4]$.

the virtual link length gives

$$r = \frac{l}{2\sin\left(q_{des}\right)}. \tag{5.7}$$

Consequentially, defining position along the robot length from the tip as S, the magnetization ($\mathbf{m}$) at any point along the robot is defined as

$$\mathbf{m} = |\mathbf{m}|\mathrm{rot}_z(\frac{S}{\pi r}180°)\hat{\mathbf{x}}, \tag{5.8}$$

with $\hat{\mathbf{x}}$ the unit vector in the x direction, and $\mathrm{rot}_z(\cdot) \in SO(3)$ the rotation matrix about the z-axis. The resultant rotational speed of the actuating field is a function of the speed of retraction of the backbone.

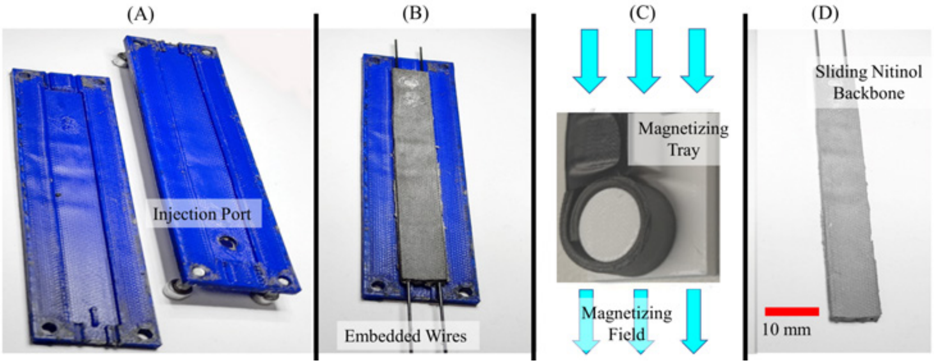

Figure 5.4: The key steps in the process of fabrication. (A) A mold is 3D printed in Polylactic acid. The injection port can be seen here. (B) 0.75 mm diameter nitinol wires are embedded lengthways and doped silicone is injected and cured. (C) The specimen is demolded, wrapped around a magnetizing tray (shown in grey) of specific bending radius and exposed to a saturating magnetizing field, shown here as turquoise arrows. (D) 0.5 mm diameter nitinol wires are inserted to act as the sliding backbone.

5.2.4 Fabrication

The manual fabrication process is outlined in Fig. 5.4 and is based on [323]. A split mold was 3D printed (RS-F2-GPGR-04, Formlabs, USA) into which 0.75 mm diameter nitinol wires are embedded, and the arrangement is bolted and glued shut. The elastomer (Ecoflex-0030, Smooth-On Inc, USA) was mixed with neodymium-iron-boron (NdFeB) microparticles with an average diameter of 5 µm (MQFP-B+, Magnequench GmbH, Germany) in a 1:1 mass ratio giving a saturated remnance of 120 mT [335]. This composite was mixed and degassed in a high vacuum mixer (ARV-310, THINKYMIXER, Japan) at 1400 rpm, 20.0 kPa for 90 seconds. The mixture was injected into the mold and cured at room temperature for four hours. Upon demolding, the 0.75 mm diameter nitinol rods are removed.

The specimens were then secured in a circular 3D printed magnetizing mold before being subjected to a saturating uniform field of 4.644 T (ASC IM-10-30, ASC Scientific, USA). The bending radius of the circle about which the specimen is wrapped during magnetization is described in Section 5.2.3 and discussed in Section 5.5. For Sample 1 this parameter was 7.5

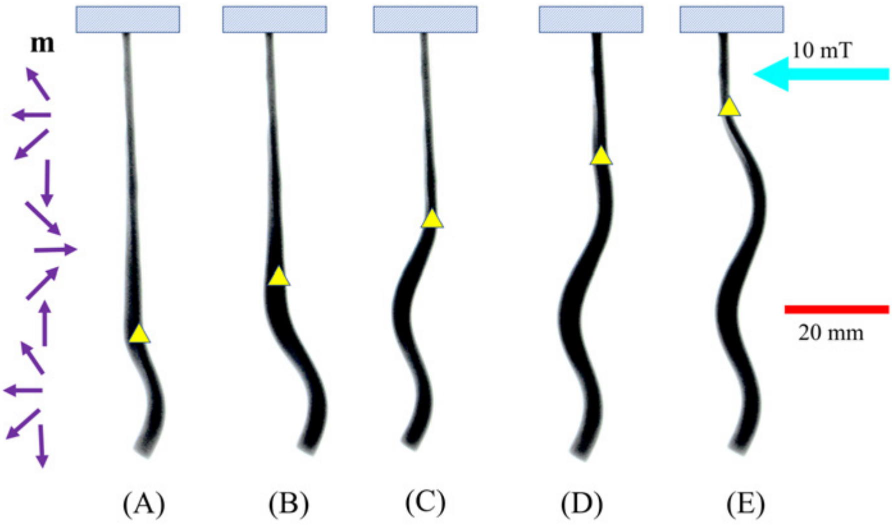

Figure 5.5: The variable stiffness robot (VSR), magnetized according to the purple arrows (**m**) and constrained at the base (blue rectangles), is shown under static one-dimensional magnetic actuation (turquoise arrow) for various insertions of sliding nitinol backbone signified here by yellow triangles. (A) Distal 20 mm unconstrained. (B) Distal 30 mm unconstrained. (C) Distal 40 mm unconstrained. (D) Distal 50 mm unconstrained. (E) Distal 60 mm unconstrained. Due to the stiffness change factor, deformation can only occur in the unconstrained region of the VSR. This shows the lowest energy state of the sinusoidally magnetized VSR.

mm and for Sample 2 it was 5 mm.

Finally, the holes from which the 0.75 mm diameter rods were removed are filled with free sliding 0.5 mm diameter nitinol backbone rods.

5.2.5 Variable Stiffness Characterization

Using Ecoflex-0030 (Smooth-On Inc, USA) doped at 100% by weight gives $E_{ME} = 100$ kPa [335]. $E_{BB} = 50$ GPa [336] and from (5.3) and (5.4) with $w = 2$ mm, $h = 10$ mm, $r = 0.25$ mm and n = 2 gives the bending stiffness of the nitinol backbone (K_{BB}) and the magnetic elastomer (K_{ME}) as

$$K_{BB} = 3 \times 10^{-4}\ \text{Nm}^2,$$

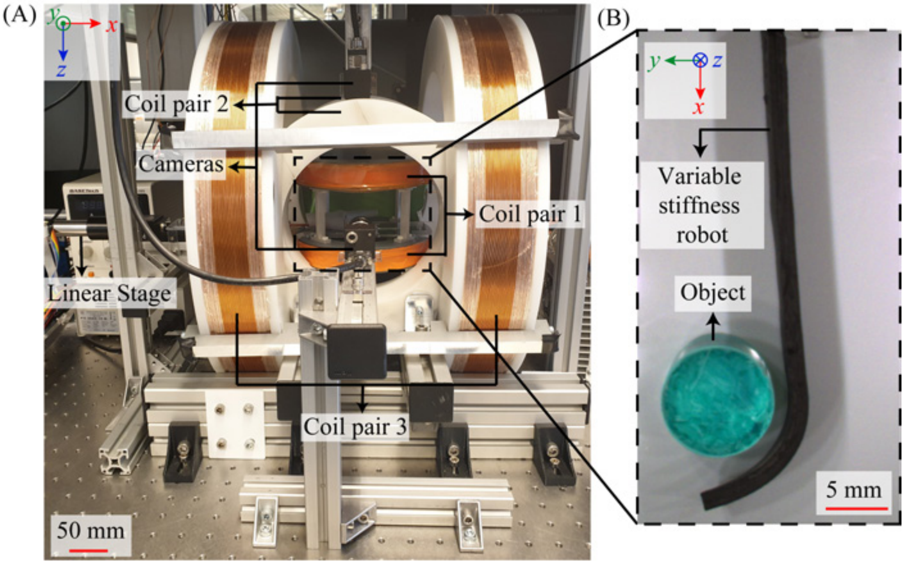

Figure 5.6: The actuation system showing (A) PaCMag - 3D electromagnetic coil setup and the linear stage. (B) Top view of the variable stiffness robot grasping an object in the workspace.

$$K_{ME} = 7 \times 10^{-7}\ \mathrm{Nm}^2.$$

This gives an analytical stiffness change factor of 765. In practice, no amount of actuating field could be imparted in order to generate a measurable bending deformation in the backbone supported region of the VSR. Fig. 5.5 shows the VSR in a static actuating field with incrementally adjusted support positions - the point at which the backbone reaches is marked with a yellow triangle. This clearly demonstrates the absence of bending in any of the proximal, supported regions. Furthermore, Fig. 5.5 shows the lowest energy state of the sinusoidally magnetized VSR. Without forcing the robot into the coiled higher energy state using correctly coupled backbone retraction *and* time-varying applied fields we cannot achieve the large deformations with which we functionalize the system. The Supplementary Video: S1 also illustrates the failure of the VSR to coil around an object and uncoil when the actuating field is applied sinusoidally but the sliding nitinol backbone is absent.

5.3 Controlled Actuation

In this section, we demonstrate a proof-of-concept functionalization of our VSR. By synchronizing the withdrawal of the backbone support with the rotation of the actuating field we force the VSR to coil into a higher energy state equilibrium. We use this coiling action to grasp various objects.

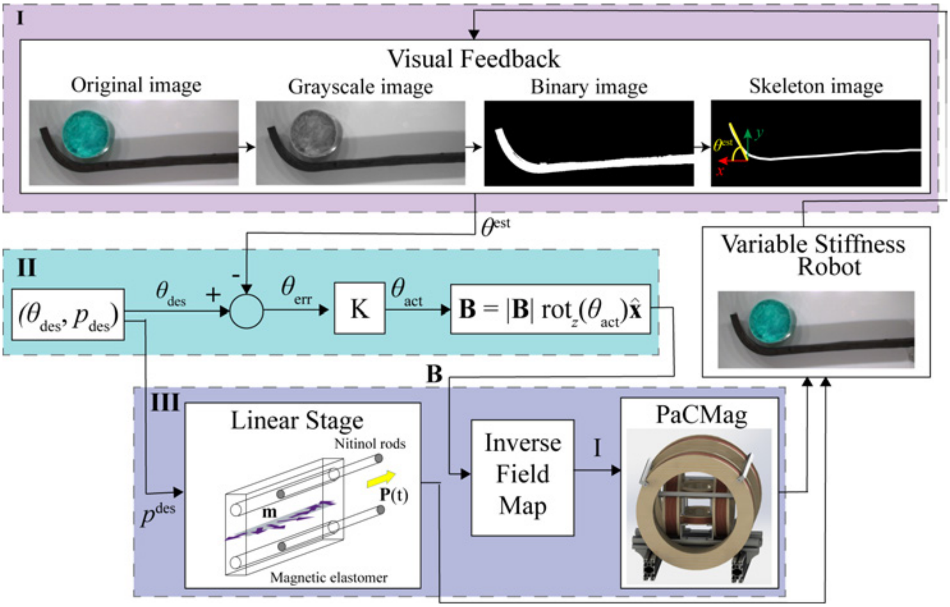

Figure 5.7: Closed-loop control of the variable stiffness robot (VSR) summarized in three blocks: (I) The tip angle (θ_{est}) of the VSR is estimated from the camera and sent as feedback to the controller. (II) A proportional control calculates the magnetic field ($\mathbf{B}$) and its angle (θ_{act}) to be applied from the error (θ_{err}) between the desired (θ_{des}) and estimated (θ_{est}) tip angles. (III) PaCMag applies the magnetic field by computing the required current (I) from the inverse field map. The linear stage moves the nitinol backbone to a position (p_{des}) updated based on the current desired tip angle (θ_{des}).

5.3.1 Actuation Systems

A 3-D electromagnetic coil setup (PaCMag) is used with a cylindrical workspace of equal radius and height of 65 mm as shown in Fig. 5.6 [337]. It has three coil pairs which can generate linearly independent uniform magnetic fields up to 55 mT. Experiments are conducted by supporting the VSR horizontally in the workspace of PaCMag and a linear stage (LX20, Misumi Group Inc., Tokyo, Japan) fixed at the base controls the movement of the nitinol backbone. A camera situated at the top captures the motion of the VSR.

5.3.2 Visual Sensory Feedback

An image processing algorithm is developed in OpenCV to track the tip angles of the VSR in 2D using camera images. Firstly, the original image is converted to a grayscale image and a threshold operation is performed to obtain a binary image of the VSR. Secondly, a skeletonization algorithm is performed on the binary image to extract the shape of the VSR. The tip of the VSR is then identified as the end point of the skeleton. Lastly, the slope of the end segment is calculated to find the tip angle of the VSR, this is used as feedback for the closed-loop controller.

5.3.3 Calculation of Actuating Field

We implemented a linear proportional controller with manually optimized gain parameters. The one dimensional error function is derived as the difference between the estimated tip angle ($\theta_{\text{est}} \in \mathbb{R}^1$) from Section 5.3.2 and the desired tip angle ($\theta_{\text{des}} \in \mathbb{R}^1$). This desired tip angle is predefined as a vector assembled from a circle discretized into small increments, for example, $\theta_{\text{des}} = [10, 24, 38, ..., 206, 220]^\circ$. The actuating field ($\mathbf{B} \in \mathbb{R}^3$) is set to a constant magnitude ($|\mathbf{B}| = 20$ mT) and the control variable is the angle of the applied field (θ_{act}) relative to the x-axis (see Fig. 5.7).

$$\mathbf{B} = |\mathbf{B}|\text{rot}_z(\theta_{\text{act}})\hat{\mathbf{x}}. \tag{5.9}$$

The applied field angle at time (t) is updated according to the error function ($\theta_{err} = \theta_{\text{des}} - \theta_{\text{est}}$) until the tolerance ($\theta_{err} < 5^\circ$) is attained as shown below,

$$\theta_{\text{act}}(t) = \text{K}_\text{P}\theta_{\text{err}}(t) + \theta_{\text{act}}(t-1), \tag{5.10}$$

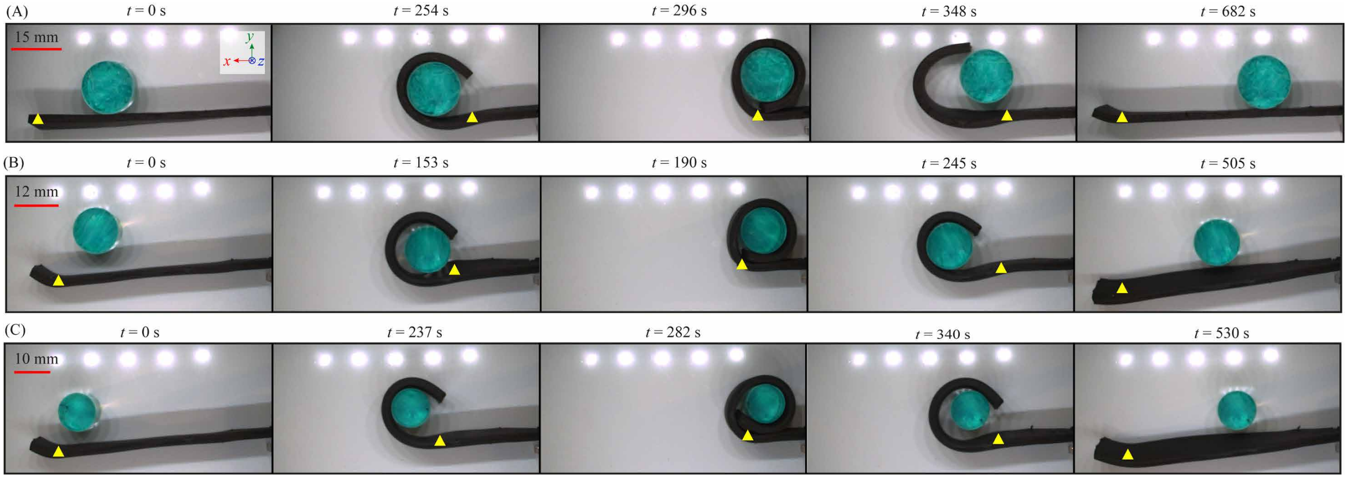

Figure 5.8: Closed-loop control demonstration of grasping and releasing objects placed at arbitrary locations and shown at different time instants (t) for three cases: (A) Sample 1 with 15 mm diameter object. (B) Sample 2 with 12 mm object. (C) Sample 2 with 10 mm object. The four stages of the experiment occur between the successive time snippets in the following order: grasping phase; coiling action; uncoiling action; releasing phase. The yellow triangle represents the tip position of the nitinol backbone. Please refer to the Supplementary Video: S3-S5 for the complete demonstration.

where K_P is the proportional gain. The system then retracts the nitinol backbone one increment before advancing to the next desired tip angle.

5.3.4 Calculation of Retracting Stage Position

The time-varying position of the nitinol backbone $\big(P(t)\big)$ is defined as: $P(t) = L - p_{\text{des}}(t)$, where L is the total robot length and the incremental position $(p_{\text{des}}(t))$ is linearly correlated to the desired angle of deformation $(\theta_{\text{des}}(t))$ via the bending radius (r, the radius the VSR coils about during actuation). Due to the limitation on positioning repeatability of the linear stage, $p_{des}(t)$ is set to a minimum step size of 2.5 mm. The VSR grasps the object placed in the coiling plane as PaCMag applies the magnetic field and the linear stage retracts the nitinol backbone until the set maximum desired tip angle ($\theta_{\text{des}}^{\text{max}} = 220°$) is reached. Beyond this angle as the tip closes the circle, it is not possible to track the tip angle. Hence, the subsequent coiling action is performed by automatically incrementing θ_{des} to complete the grasp. This whole system can also be run in reverse to uncoil the VSR and release the entrapped object. Fig. 5.7 illustrates the complete closed-loop control system.

5.4 Results

The two VSR samples 1 (7.5 mm bending radius) and 2 (5 mm bending radius) are used to demonstrate the grasping and releasing of printed cylindrical objects in closed-loop as shown in Fig. 5.8. Three objects of diameters 15, 12 and 10 mm are placed at various locations facing the coiling side of the VSR. The VSR, initially in its straight configuration, wraps around the object to grasp it, coils further to move the object along, then releases the object and uncoils itself to return to its original configuration (Refer to the Supplementary Video: S3-S5 for the complete demonstration). Fig. 5.9 shows the plots of applied magnetic field (B_x, B_y), resultant field angle (θ_{act}), position of the nitinol backbone (P), desired tip angle (θ_{des}), and estimated tip angle (θ_{est}). These variables are plotted for sample 1 grasping and releasing the 15 mm object (Fig. 5.8 A). The overall control frequency across the three experiments is 1 Hz. The PaCMag coils maintained closed-loop control of the VSR via the visual tip tracking system throughout the “Grasping” and “Releasing” phases of the demonstration

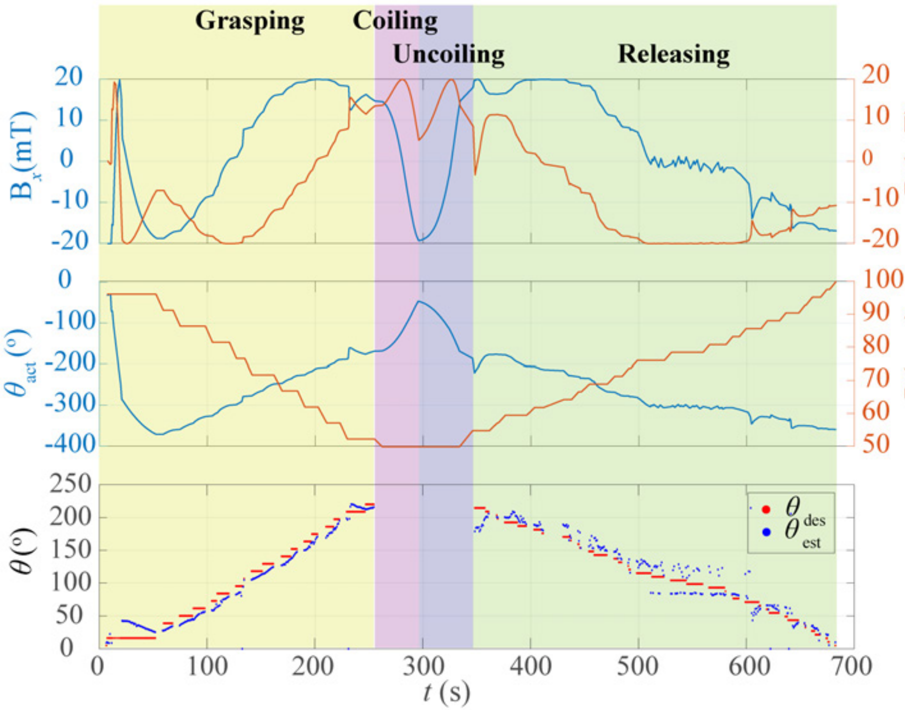

Figure 5.9: Results of closed-loop control experiment of Sample 1 grasping and releasing 15 mm object. Plots show the applied magnetic field (B$_x$, B$_y$) and its orientation (θ_{act}), position of the nitinol backbone (P), the desired (θ_{des}) and estimated (θ_{est}) tip angles of the VSR during the experiment time (t). The four stages of the experiment occur as follows: grasping phase (t = 0-254 s); coiling action (t = 255-296 s); uncoiling action (t = 297-348 s); releasing phase (t = 349-682 s).

(Fig. 5.9). Visual contact with the tip was lost during the “Coiling” and “Uncoiling” phases as discussed in Section 5.3.3. Here the controller was operating in open-loop. The observed maximum coiling deformation angle owing to the decreasing size of the objects in the three experiments were 360^o, 375^o and 400^o, respectively.

5.5 Discussions and Future Work

In this work, we have demonstrated the grasping and releasing under closed-loop control of various diameter cylinders using a magnetically-actuated variable stiffness continuum robot. In doing so we have addressed the non-trivial problem of controlling large (up to 400°) deformations which under magnetic actuation are inherently unstable. Please see the Supplementary Video: S1 for the demonstration of a failed grasping and releasing experiment of the VSR without the nitinol backbone. We have introduced the concept of a synchronized sliding nitinol backbone with an applied actuating field and proved its feasibility within our VSR to grasp and release various objects. We have also shown that the VSR is able to coil itself into higher energy state equilibrium without relying on anatomical contact forces or interaction with external environment [338]. Supplementary Video: S2 shows the coiling of the VSR in free space without the influence of any external object.

In order to simplify the demonstration of our feasibility study, we performed our experiments entirely in the horizontal plane (Fig. 5.8). The VSR is supported in the vertical direction on a smooth acrylic plate thus negating the effects of gravity. Although there are no theoretical issues with the consideration and incorporation of the gravitational force, these simplifications were made on purely practical grounds. Any future study should look to both consider gravity and to control the VSR in unconstrained three dimensional space.

A further simplification worthy of mention pertains to the visual tracking algorithm. Our system locates the tip of the VSR and derives the tip angle to use as a control input. When the VSR wraps into a full circle the tip ceases to be visible, rendering this method of tracking impossible. Any further study should therefore encode a system for tracking the position and size of the circle after a certain deformation angle is achieved. Further ahead, and for a more clinically relevant demonstration, visual tracking is not possible inside the human body so some non-visual sensing method (e.g. medical imaging or strain sensing) should be incorporated.

The bending radius is an interesting parameter worthy of mention here. The radius of the circle around which the robot is magnetized has a profound impact on the achievable radii of the wrapped robot under actuation. If this bending radius is too small the elastic torque will overpower the magnetic torque and the robot will snap open. This can be mitigated to a limited degree with a larger applied field magnitude. Furthermore, if the retraction of the nitinol backbone is not correctly synchronized with the rotation of the applied magnetic field, the actuation descends into the imbalances shown in Fig. 5.5 and the Supplementary Video. Consequentially, the timing of the retraction of the sliding nitinol backbone is a function of the bending radius (the magnetization) and is enabled by having sufficient magnitude of applied field.

The most obvious limitation of this design is that the backbone is always, when present, straight and the base upon which the VSR is mounted is static. As magnetic actuation is an inherently small scale technology with its most likely applications in minimally invasive surgery (and similar) these constraints limit the current clinical relevance of the design. In order to navigate to any area of interest we should be soft, compliant and mobile. These limitations are by no means definitive however, and the imminent next step is to develop miniaturizable backbones with compliant behavior, either fluidically actuated or with phase changing materials. Further to this we must also develop a mobile mounting system, such as a manual endoscope to operate. We also anticipate developing more reliable and miniaturizable automated fabrication techniques. This will allow us to shrink the prototype and potentially incorporate more complex and interesting variable stiffness features.

5.6 Conclusion

This chapter presents a proof-of-concept of a tongue-like, magnetic variable stiffness coiling robot. This system exploits variable lengthwise mechanical properties to achieve high deformation equilibrium in a way which has not previously been shown. We have demonstrated a closed-loop control strategy to grasp and release objects of varying sizes by synchronizing the sliding nitinol backbone of the robot with the actuating magnetic field. With this contribution, we have demonstrated the currently untapped potential of functionalizing variable stiffness magnetically-actuated robots for higher energy state deformations. The variable stiffness grasping robot has potential as a surgical tool for applications in biopsy and grasping.

6

A Magnetically-actuated Variable Stiffness Manipulator based on Deployable Shape Memory Polymer Springs

Note: *The following chapter is adapted from the article "A Magnetically-actuated Variable Stiffness Manipulator based on Deployable Shape Memory Polymer Springs" by* ***T.L. Thomas****, J. Bos, J. J. Huaroto, V. Kalpathy Venkiteswaran, and S. Misra, accepted for publication in "Advanced Intelligent Systems", special issue of "Soft Robotics Across Scales: Fundamentals and Applications", February 2023 (In Press).*
The chapter has been reformatted in terms of figures to fit this doctoral thesis. No changes to the technical contents of this peer-reviewed manuscript have been made.

Authors' Contributions: *T. L. Thomas and V. Kalpathy Venkiteswaran conceived the manipulator design. T. L. Thomas performed the stiffness characterization and thermal analysis, fabricated the manipulator, carried out the experiments, and interpreted the results. J. Bos conducted the thermal actuation experiments and contributed to the thermal analysis. J. J. Huaroto designed the test setup for laser light. V. Kalpathy Venkiteswaran contributed to the planning of experiments, analysis, and interpretation of the results. S. Misra contributed to the planning of robotic magnetic actuation experiments and supervised the project. T. L. Thomas wrote the manuscript in consultation with all the authors.*

6. A Magnetically-actuated Variable Stiffness Manipulator based on Deployable Shape Memory Polymer Springs

Abstract

Continuum manipulators have found several applications in surgical interventions like endoscopy, laparoscopy, and as end-effectors for surgical robots. Continuum manipulators coupled with magnetic actuation can be precisely maneuvered inside the human body. Recently, variable stiffness manipulators (VSMs) have been introduced for enhanced dexterity and safe navigation. This study presents a new design of a magnetically-actuated VSM based on shape memory polymer (SMP) springs. The VSM has a silicone backbone enclosed within a spring made of SMP that can change in length with stiffness change that is triggered by Joule heating. The stiffness and thermal characteristics of the VSM are studied using analytical models and experiments. Subsequently, a one-segment VSM and a two-segment VSM having outer diameters of 9 mm and 10 mm and lengths of 15 mm and 25 mm, respectively, capable of extending to four times their length are designed. The VSM can be deployed in a compact form and extended to achieve variable bending curvatures in soft and rigid states, which can facilitate instrument insertion and reduce operation invasiveness. Potential clinical applications are demonstrated by incorporating miniature camera, biopsy tool, and laser optical fiber in the working channel of the VSM and coupled with robotic magnetic actuation.

6.1 Introduction

The past few years have seen a rapid growth in the application of continuum manipulators in diverse fields ranging from space and deep-sea explorations to minimally invasive surgical interventions [339]. The design of continuum manipulators inspired from nature emulates the flexibility of the body of a snake, the tentacles of an octopus, among others. Such manipulators composed of elastic components with finitely many degrees of freedom can adapt their shape and operate in confined spaces [13]. A great deal of previous research in continuum manipulators has focused on tendon-driven manipulators, concentric tube manipulators, and multibackbone manipulators [53]. Although such manipulators with extrinsic actuation embody high flexibility, they are affected by friction and backlash caused by cables, torsion and snapping behaviour of concentric tube designs [48], [224]. Continuum manipulators based on compliant mechanisms have several advantages as they are monolithic in nature which lead to easy fabrication, and with the elimination of friction, backlash and noise, there is no need for lubrication [110]. However, these mechanisms are affected by fatigue and the input-output relationship is perturbed by energy storage [74].

Minimally invasive surgery (MIS) is an increasingly important application of interest within the field of continuum manipulators [48]. MIS requires only small incisions to perform the surgery on the patient, reduces the operating time and leads to fast recovery. Continuum manipulators can improve MIS by reaching difficult-to-access surgical sites with high dexterity and accuracy. With the rapid advances in the field of robot-assisted surgery, continuum manipulators are increasingly being used as end-effectors for dexterous manipulation of the surgical tools inside the human body, and complement the capabilities of the surgeon. There is a growing trend towards the design of soft continuum manipulators, which can adapt and be gently maneuvered in a constrained environment in the vicinity of various objects [340]. For example, Kim *et al.* demonstrated a ferromagnetic soft continuum robot that can be steered through complex phantom vasculature, while growing hydrogel skin on its surface that significantly reduces friction [40]. Magnetically-actuated soft manipulators have great potential in creating miniaturized designs made by embedding ferromagnetic particles in soft polymer composites or incorporating small permanent magnets, which can then be controlled remotely with the application of external magnetic fields [341], [342]. While soft manipulators have proven good maneuverability, rigidity is essential for higher motion accuracy and to exert forces [228]. Both rigidity and softness are desirable attributes for surgical functions which is useful for instance, during deployment of laparoscopy tools, and performing biopsy.

Variable stiffness in surgical manipulators has been gaining significant attention in recent years. Several studies have investigated different mechanisms to achieve variable stiffness such as granular/particle jamming, antagonistic arrangement of actuators, and stimuli-responsive stiffness-tunable materials [64]. A variable stiffness mechanism based on fiber jamming transition was introduced in the STIFF-FLOP soft manipulator to provide stability to its distal module by making it rigid, however miniaturization of this technology proved to be challenging [343]. A lightweight re-configurable stiffness-changing skin based on layer jamming was created and adopted as on-demand joints for a continuum manipulator enabling dynamic adjustment of the operating workspace [344]. Cable-driven actuators [67] and fluidic actuators [345] are commonly used in antagonistic methods, but are limited by low range of stiffness variation and controllability when it comes to MIS [346].

Stiffness-tunable materials such as low melting point alloys (LMPAs), shape memory alloys (SMAs), and shape memory polymers (SMPs) can attain significant stiffness change [27], [28], [47], [347], [348]. Despite the toxic nature of LMPA, owing to its transition speed, it has been used in the multi-segment designs of a cable-driven continuum manipulator for MIS application [347], and magnetic variable stiffness catheters for applications in cardiac ablation and robotic ophthalmic surgery [47], [68]. SMAs have high power to weight ratio, are bio-compatible, easy to miniaturize, and can be activated using Joule heating [349]. Therefore, SMA wires in the form of springs, strips, and wavy patterns have been used in the design of continuum manipulators for actuation and variable stiffness [28], [350], [351]. However, SMAs exhibit relatively lower range of stiffness change than SMPs, a limitation that could be solved by combining with a thermoplastic [352]. SMPs are versatile due to their compatibility with 3D printing and multi-material fabrication. Material synthesis enables developing multi SMP, that is, SMP with two or more transition temperatures, manifesting improved mechanical properties and recoverability [353], [354]. Recently, SMP was used in the design of magnetic variable stiffness catheters in which graphite, neodymium and carbon black particles were incorporated in the SMP composite to improve the electrical and thermal conductive properties [69], [348].

This work presents a new design of a magnetically-actuated variable stiffness manipulator (VSM) based on SMPs. The VSM is composed of a silicone lumen enveloped by a helix-shaped spring made of SMP and a permanent magnet attached to its tip. The SMP spring with an embedded resistive wire is fabricated by following a novel process of re-training the SMP to alter its primary shape. The working principle of the VSM relies on phase change property of SMP for shape fixity in conjunction with magnetic fields for actuation. The VSM demonstrates shape fixity or shape locking capability, that is, the shape of the VSM can be fixed during magnetic actuation to resist external forces. Moreover, the VSM made of an extensible SMP spring can attain a compact form in its compressed form and operate in various configurations of extendable lengths. The modularity of the VSM as a two-segment VSM (with a central working channel to accommodate laparoscopic tools) is also demonstrated to achieve different bending curvatures with selective shape locking capability. The major contributions of this work are: (i) Design and fabrication of a deployable and modular VSM that is magnetically-actuated and exhibits variable stiffness with variable working length. (ii) Shape locking capability of VSM that has potential to facilitate insertion and act as a stabilizer while deploying laparoscopic tools. (iii) Stiffness and thermal characterization of VSM using analytical models and experiments. (iv) Clinical feasibility demonstration for applications in endoscopy, biopsy and laser surgery using robot-assisted magnetic actuation.

6.2 Results and Discussion

6.2.1 Design

The VSM has a backbone made of a silicone tube enclosed within a spring made of SMP and a permanent ring magnet attached to its tip. The SMP spring is embedded with a resistive wire to heat the SMP by passing current. The SMP spring in rigid phase is initially in a compressed state resulting in a minimum length of the VSM, and it can be moved to a target location in its compact form. When the SMP is activated by heating, it transitions to the soft phase and by pushing the silicone tube, the VSM is extended in length. The orientation of the VSM tip with magnet is controlled with the application of a bending moment resulting from external magnetic fields. The VSM can be deflected to extend or bend while the SMP is in soft phase, and its shape can be fixed when the SMP transitions to rigid phase. A two-segment design of the VSM can be formed using two SMP springs in series enclosing a two segment concentric tube backbone of silicone (Fig. 6.1a). Various bending configurations can be achieved with selective activation, bending and extension of the VSM segments (Fig. 6.1b). The stiffness change of the SMP when transitioning between the soft and rigid phases enables fixing the shape of the VSM (Fig. 6.1c), which is controlled under magnetic actuation.

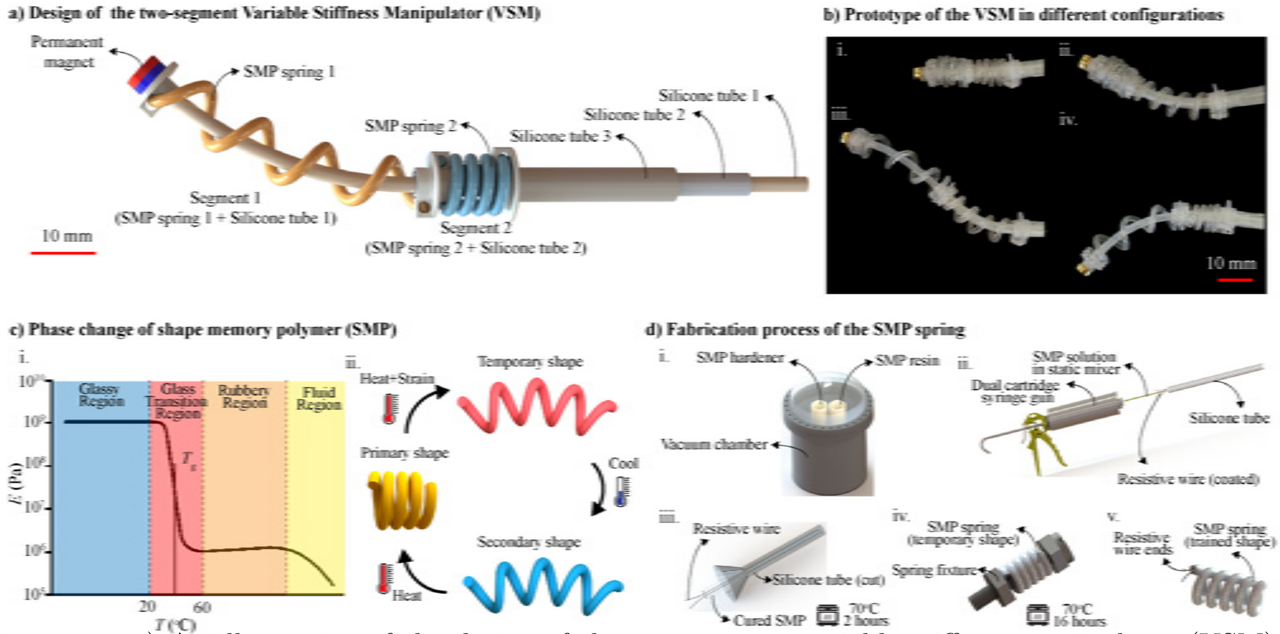

Figure 6.1: a) An illustration of the design of the two-segment variable stiffness manipulator (VSM). b) Fabricated prototype of the VSM in different bending and extension configurations. c) Phase change of shape memory polymer (SMP): i. Plot of elastic modulus (E) versus temperature (T) of the SMP with glass transition temperature (T_g), adapted from [355]. ii. Shape memory effect illustrated for a SMP spring. d) Fabrication process of the SMP spring: i. Vacuum drying of the SMP resin and hardener for 2 hours. ii. Injection of the mixed SMP solution into a silicone tube with a coated resistive wire. iii. Curing of the silicone mold in an oven at 70°C for 2 hours and demolding the cured SMP from the silicone mold. iv. Fixing the SMP wire into a temporary shape of the spring and training the SMP spring in the oven 2 cycles of 70°C for 16 hours. v. The trained SMP spring.

6.2.2 Fabrication Method

The variable stiffness manipulator (VSM) is fabricated by assembling the silicone tube, shape memory polymer (SMP) spring and permanent magnet using flexible clamps made by 3D printing (Form 2, stereolithography printer, USA) as seen in Fig. 6.1a. Off-the-shelf silicone tubes (Technirub International B.V., Netherlands) and N48 neodymium ring magnets (Neomagnete, Germany) of outer diameter = 4 mm, inner diameter = 1.5 mm, and height = 1 mm are used. The SMP spring is made by first making a SMP wire having a 0.12 mm nichrome wire as the embedded resistive wire. The nichrome wire is coated with a urethane lacquer (KONTAKT 255 Urethane 71, Belgium) for insulation. The coated nichrome wire is inserted forming a loop routed inside a silicone tube of inner diameter equal to the spring wire diameter, to obtain two connection points for the current supply. The nichrome wires running though the length of the silicone tube form an electrical circuit loop, with two ends of the nichrome wire leaving one end of the silicone tube. A potting type SMP, MP3510 (SMP Technologies Inc., Japan) which is available in two parts: resin and hardener, is used in this design. Equal amounts of resin and hardener are taken in a dual cartridge syringe gun (Adhesive Dispensing Ltd., UK) and dried using a 1 stage vacuum pump for 2 hours. The resin and hardener are then mixed using a 1:1 ratio mixer nozzle and the solution is injected into the prepared silicone tube mold. The mold is immediately transferred to an oven to cure at 70°C for 2 hours. The cured SMP wire is demolded by cutting out the silicone tube. The SMP spring is obtained by re-training the SMP wire to change its primary shape to a spring shape. This is done by fixing it into a temporary shape of a spring, and heating the SMP wire above its glass transition temperature for a prolonged period of time. This is a process synonymous to annealing where the molecular disturbance due to residual strain is eliminated. A few studies have investigated the different re-training conditions of the primary shape [356], [357]. The following training cycles are tested in an oven: 4 hours at 70°C + 16 hours at 95°C; 16 hours at 70°C; 4 hours at 95°C. It is found that two cycles of 16 hours at 70°C works the best to obtain the SMP spring. The complete process of fabricating the SMP spring is illustrated in Fig. 6.1d. Therefore, in this way the SMP spring with two nichrome wires at one end is obtained. Lastly, the two nichrome wires are covered by a teflon liner of diameter

0.6 mm (Zeus Company Inc., US) and filled with silicone rubber (Ecoflex™ 00-10, Smooth On Inc., US), while leaving two short ends of the nichrome wire for electrical connection.

6.2.3 Stiffness Characterization

The shape fixity of the VSM, that is, the ability of the VSM to retain the temporary shape upon removal of mechanical deformation is crucial for the design. This is achieved by designing the VSM to have high stiffness in the glass phase of SMP when it becomes rigid, and low stiffness in the rubber phase of SMP when it becomes soft. As inferred from Fig. 1c, the elastic modulus of the SMP in glass phase ($E_g = 1000$ MPa) drops by three orders of magnitude when transitioning to rubber phase ($E_r = 1$ MPa). Hence, maximizing the bending rigidity of the SMP spring in glass phase is prioritized. The SMP spring can be modelled as a cantilever beam with bending rigidity (β) given by [358]

$$\beta = \frac{Eld^4}{64nr(2+\nu)}, \tag{6.1}$$

where E and ν are the elastic modulus and Poisson's ratio of SMP at a given phase, respectively; d, l, r, and n are the diameter of the spring wire, length, mean coil radius, and number of active coils of the spring, respectively. The lateral deflection (θ) of the VSM caused by a pure bending moment (M) is given by

$$\theta = \frac{ML}{(\beta + E_\mathrm{s} I_\mathrm{s})}, \tag{6.2}$$

where E_s and I_s are the elastic modulus and area moment of inertia of the silicone tube, and L is the length of the VSM. The lateral deflection of the VSM as a function of mean coil radius and spring wire diameter is shown in Fig. 6.2a. For high stiffness, that is, high bending rigidity given by (6.1), 3 mm mean coil radius and 2 mm spring wire diameter are chosen considering the fabrication limitations. The number of active coils of the SMP spring and length of the VSM are determined by analysing the resulting bending rigidity of the VSM composed of the SMP spring and silicone tube. To retain the shape fixity for a given length of VSM, the bending rigidity of the SMP spring (β) should be dominant over that of the silicone tube ($E_s I_s$). The suitable design region can be ascertained from Fig. 6.2b, for lengths after the intersection of the plot lines of SMP spring and silicone tube.

Three VSMs with different combinations of length, number of active coils, size of silicone tubes, and magnets are designed. The lateral deflection of the VSMs in glass and rubber phases are analysed with the application of a bending moment resulting from the magnetic fields (Fig. 6.2d and 2e, Supplementary Video: S1). Experiments are conducted in compressed and different extended lengths of the VSMs (Fig. 6.2f). The theoretical model agrees better with the experimental results for small deflections ($< 10°$) in glass phase than for large deflections in rubber phase. This can be attributed to the ambiguity in the elastic modulus of the SMP as it transitions from the glass transition range to the fully rubber region and the geometric non-linearities due to large deflection.

Based on the results, VSM-2 and VSM-3 having 4.5 and 5.5 active coils are chosen over VSM-1 having 3.5 active coils as the final designs as these demonstrate less deflection in glass phase (Fig. 6.2c). VSM-2 and VSM-3 have compressed lengths of 13 mm and 15 mm, and an extended working lengths of 50 mm and 70 mm, respectively. For demonstration of VSM functions, a one-segment VSM is fabricated using VSM-3 design and a two-segment VSM is fabricated using a combination of two VSM-2 designs. Both the one-segment and the two-segment VSM designs in their respective fully extended lengths are capable of bending up to an angle of 180° in rubber phase while using a magnetic field of 70 mT. The different shapes of the two-segment VSM are captured by selectively heating each of the segments, extending to various lengths and deflecting to various bending curvatures with the application of magnetic fields of 40 mT (Fig. 6.2g).

6.2.4 Thermal Actuation

The variable stiffness in the VSM is activated by means of Joule heating. The SMP used in the design has a glass transition temperature of 35°C, below which it is in glass phase and at 60°C it reaches the rubber phase. The SMP spring wire is embedded with a nichrome wire of diameter 0.12 mm running through the cross section of the SMP spring wire twice, with the two ends of the nichrome wire leaving the end of the SMP spring wire to connect to a power supply. The cross section of the SMP spring wire is composed of two circular sections of the nichrome wire (running in two

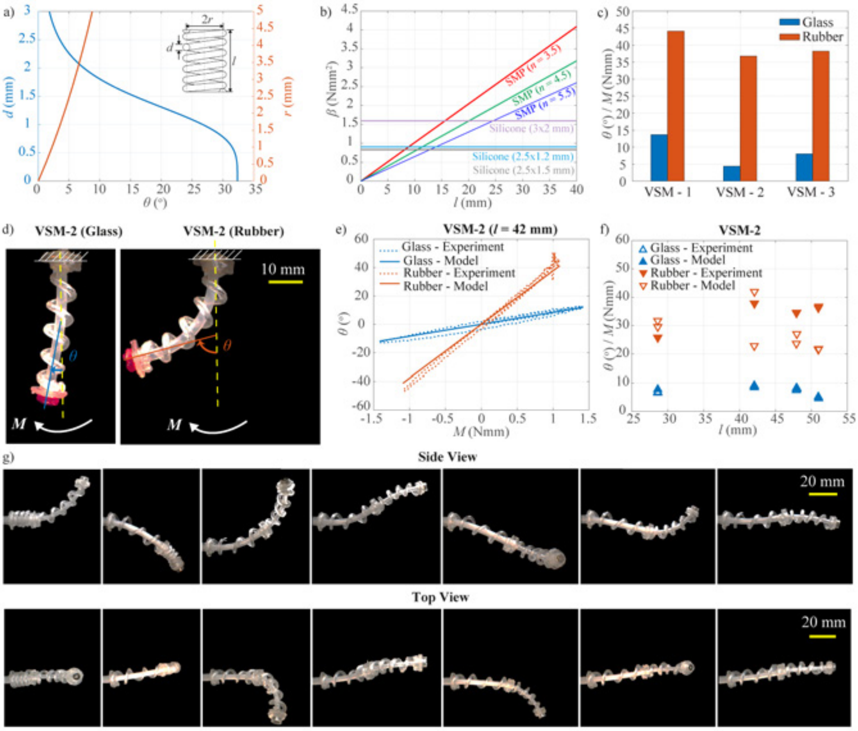

Figure 6.2: a) Effect of wire diameter (d) and mean coil radius (r) of the spring on its lateral deflection (θ). b) Bending rigidity (β) for different lengths of the SMP springs with n active coils and silicone ($D_o \times D_i$) tubes of outer diameter (D_o) and inner diameter (D_i). c) The degree of lateral deflection (θ) over the bending moment (M) in glass and rubber phases for three designs of variable stiffness manipulator (VSM): VSM-1 (n = 3.5, l = 35 mm, D_o = 2.5 mm, D_i = 1.2 mm); VSM-2 (n = 4.5, l = 51 mm, D_o = 3 mm, D_i = 2 mm); VSM-3 (n = 5.5, l = 45 mm, D_o = 2.5 mm, D_i = 1.5 mm). d) θ of VSM-2 in glass and rubber phases for the same magnetic bending moment ($\boldsymbol{M}$) generated by external magnetic fields. e) θ versus M relationship calculated by the cantilever beam model and measured by the experiments with VSM-2 of length (l = 42 mm). f) The degree of θ over M in glass and rubber phases for VSM-2 design with different working lengths (l). g) Different bending shapes of the two-segment VSM design at varying lengths with the application of magnetic fields captured as side and top views.

directions) surrounded by the SMP layer. The overall design can be approximated by a cross section composed of single section of nichrome wire having an effective radius of two wires and surrounded by the SMP layer (Fig. 3b). As current flows through the nichrome wire, the temperature of the surrounding SMP increases. Assuming a cylindrical coordinate system with the center of the cross section as origin and temperature varies along the radial direction, the rise in temperature is modelled using the one-dimensional transient heat transfer equation [359] given by

$$\frac{\partial T}{\partial t} = a_o \left(\frac{\partial T}{\partial r} \frac{1}{r} + \frac{\partial^2 T}{\partial r^2} \right), \tag{6.3}$$

with an initial condition:

$$T(r,0) = T_0, \quad (r_1 \leq r \leq r_2) \tag{6.4}$$

and the boundary conditions:

$$I^2 R = 2\pi r \lambda_0 \frac{\partial T}{\partial r}, \quad (r = r_1) \tag{6.5}$$

$$\lambda_0 \frac{\partial T}{\partial r} = h(T - T_0), \quad (r = r_2) \tag{6.6}$$

Here T and T_0 are the temperatures of the SMP layer and the ambient temperature, respectively; t is the time, r_1 is the effective radius of the two nichrome wires, r_2 is the radius of the SMP layer, and r is any point radius in the SMP layer. The thermal diffusivity of nichrome is given by $a_0 = \lambda_0/(\rho_0 c)$, where λ_0, ρ_0, and c are the thermal conductivity, density and specific heat capacity of nichrome, respectively. i, R, h are the current, the resistance of the nichrome wire, and the surface heat transfer coefficient of the SMP with air, respectively.

The heating and cooling behaviour of the VSM upon actuation are analysed by measuring the temperature using an infrared camera. The straight SMP wire before training, the SMP spring, and the VSM are tested. Temperatures are measured between the transition from glass to rubber phase, and vice versa, with the application of currents in the range 0.1 - 0.3 A. The thermal camera images (Supplementary Video: S2), temperatures of the samples measured by the infrared camera, and the temperatures calculated by the heat transfer model (equation 6.3) are shown in Fig. 6.3.

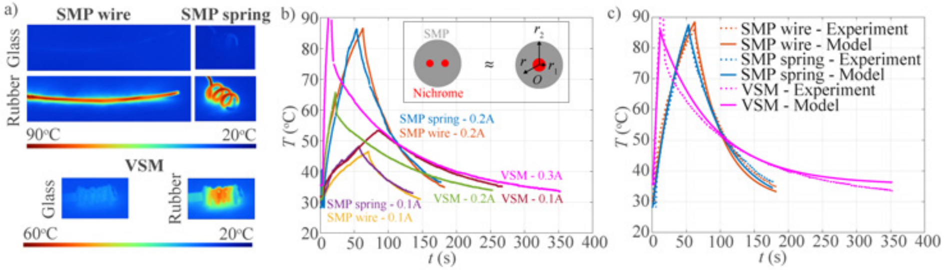

Figure 6.3: a) Thermal camera images showing the glass and rubber phases of the shape memory polymer (SMP) wire, SMP spring and the variable stiffness manipulator (VSM). b) The temperatures (T) measured by the thermal camera over time (t) at applied currents of 0.1 A, 0.2 A, and 0.3 A. The inset depicts the cross section of the samples composed of SMP (gray) and nichrome (red), and the approximation of the two nichrome wire parts as a single part for the heat transfer model. A cylindrical coordinate system is fixed with origin (O) at the center of the cross section, r_1 is the effective radius of nichrome and r_2 is the radius of SMP, and r is any point radius in the SMP layer. (c) The temperatures estimated by the heat transfer model and measured by the thermal camera for the SMP wire at 0.2 A, SMP spring at 0.2 A and the VSM at 0.3 A.

Results show a good agreement between the model estimated and experimentally measured temperatures. It takes 20 s to thermally actuate the VSM and reach rubber phase (60°C) while using a current of 0.2 A, and 230 s to cool the VSM and reach glass phase (30°C) at room temperature.

It is to be noted that this work is a proof-of-concept study using a polyurethane SMP with phase change that occurs between 35°C and 60°C. This temperature range can be challenging for clinical applications as the human body temperature is typically 36-37°C, and prolonged exposure to higher temperatures can cause thermal damage to tissue [360]. In the experiments here, the cooling time is long owing to the natural convection cooling process of the VSM that takes place in air. It can be reduced if operating in fluid or with the inclusion of an active cooling element [47]. Moreover, the development and usage of SMPs with phase transition taking place within a smaller range of temperatures while exhibiting a wider range of stiffness change can reduce cooling time, and in turn can improve the response time of the VSM [361]–[363].

6.2.5 Applications

Potential clinical applications of the VSM as a steerable surgical manipulator are demonstrated with one-segment and two-segment designs. A permanent magnet attached to the end-effector of a robotic arm is programmed to generate the required magnetic field to control the VSM. The one-segment VSM is used to demonstrate endoscopy and biopsy procedure in a stomach phantom having polyps. Stomach polyps are abnormal tissue growth found in the inner lining of the stomach, which maybe cause no external symptoms can sometimes become cancerous if left untreated [364]. The polyps are detected during an endoscopy procedure in which a long flexible tube equipped with a miniature camera at the end is inserted via the mouth, through the esophagus, and into the stomach for visual examination. A polyp can be removed for inspection by inserting a biopsy forceps or snare.

In the first experiment, a miniature camera (0.91 mm in diameter) is integrated in the working channel of the one-segment VSM and tested in a stomach phantom. The one-segment VSM is inserted through the esophagus in its compressed form while in glass phase phase, and upon entering the stomach the VSM is extended in length by activating the SMP to rubber phase. The VSM is deflected in rubber phase with the application of magnetic fields using the robot arm while manually controlling its length to scan the volume of the stomach and detect the three polyps. Fig. 6.4a depicts the endoscopy procedure carried out by the one-segment VSM and the view through the miniature camera of the polyps inside the stomach (Supplementary Video: S3). In the second experiment, a cold snare polypectomy tool is integrated in the working channel of the one-segment VSM. As shown in Fig. 6.4b, the one-segment VSM is inserted to reach the polyp similar to the first experiment. Thereafter, the VSM is locked in position using the magnetic field while the SMP transitions to glass phase, and the snare is deployed to grasp the polyp. The polyp is resected by retracting the snare, and the SMP is activated to rubber phase. Thereafter, the VSM is retracted back to its compressed form for subsequent withdrawal through the esophagus (Supplementary Video: S4).

The maneuverability and shape fixity of the two-segment VSM is demon-

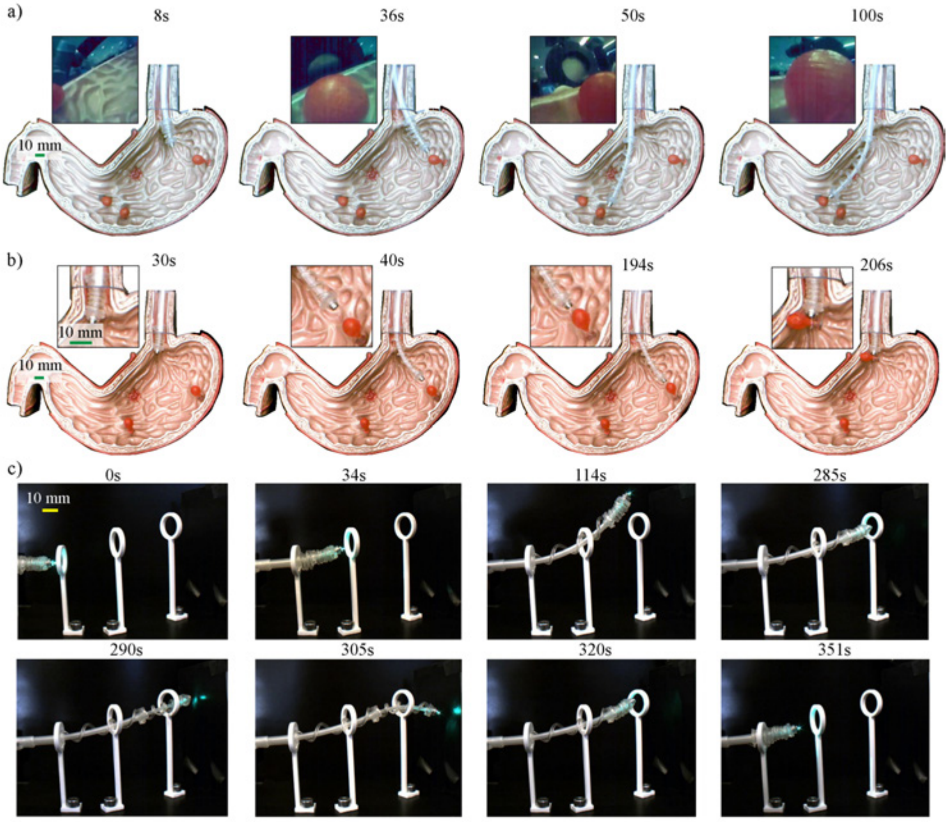

Figure 6.4: Demonstration of endoscopy, biopsy and laser ablation applications of the variable stiffness manipulator (VSM): a) One-segment VSM integrated with a miniature camera guided inside a stomach phantom using robotic magnetic actuation to detect the three polyps. The inset shows the miniature camera view. b) One-segment VSM integrated with a cold snare removes one of the polyps in the inner lining of the stomach. The inset shows a magnified view of the VSM. c) Two-segment VSM integrated with an optical fiber carrying laser light is steered to navigate through three rings oriented in 3D space.

strated by navigating it through three rings distinctly oriented in 3D (Supplementary Video: S5). An optical fiber is integrated in the working channel of the VSM to transmit laser light. As shown in Fig. 6.4c, The VSM enters the first ring in its compact form, in which both the distal and proximal segments known as segments 1 and 2, respectively as indicated in Fig. 6.1a, are in fully compressed states while in glass phase. The SMP spring in segment 2 is activated by heating, as it transitions to rubber phase the VSM is deflected with the application of magnetic field to align the tip with the second ring. Subsequently, segment 2 is extended in length by pushing silicone tube 2 to pass through the second ring, and the VSM is deflected again to align the tip to the third ring. Thereafter, segment 2 is cooled to transition the SMP to glass phase, consequently locking the shape of the VSM. Thereon, segment 1 is activated by heating, and with the transition to rubber phase it is extended in length by pushing silicone tube 1 to pass through the third ring. While in the current phase of glass segment 2 and rubber segment 1, the tip of the VSM is further deflected by bending segment 1 to point the laser beam on a black screen located in the vicinity. The VSM is retracted back through the three rings following the whole process in reverse order. This demonstration shows the uncoupled actuation, bending, and shape locking capability of the two-segment VSM while navigating a restricted environment and transporting laser beam as a potential application for laser surgery.

The focus of this work is in maximizing the shape fixity of the VSM by designing SMP spring with optimal dimensions, which has proven to be effective in the above demonstrations. It is worth mentioning that a very small deflection or bounce back of the SMP segment might occur as it becomes rigid. The amount of bounce back depends on broadly three factors: shape fixity of SMP material, fabrication process, and overall design [365], [366]. For the VSM design proposed here, the silicone tube and integrated laparoscopic tools will also contribute to this effect. Therefore, it is challenging to estimate the exact amount of bounce back of the VSM owing to the convoluted factors of SMP fixity and design-dependency. However, it is safe to say that the bounce back is minimal and does not significantly affect manipulation, especially under controlled magnetic actuation as shown in the the biopsy and the laser surgery demonstrations (Supplementary Video: S4-S5). For future clinical translation, commercially-available systems such as Stereotaxis Niobe magnetic navigation system (Stereotaxis, USA) and Aeon Phocus (Aeon Scientific AG, Switzerland) can be used for the magnetic actuation of the VSM [39], [367]. Furthermore, the biocompatibility of polyurethane SMPs has been reported in other work [368]; however, the biocompatibility of the overall design needs to be evaluated.

6.3 Experimental Section

6.3.1 Stiffness Characterization

The three VSMs designed for the characterization experiments have the following number of active coils (n), inner (D_i) and outer diameters (D_o) of silicone tube, and thickness (t), inner (d_i) and outer diameters (d_o) of ring magnets: n = 3.5, 4.5, 5.5; D_o (mm) = 2.5, 3, 2.5; D_i (mm) = 1.2, 2, 1.5; t (mm) = 1, 2, 2; d_o (mm) = 4, 4, 6; d_i (mm) = 1.5, 1.5, 2; corresponding to VSM-1, VSM-2, VSM-3, respectively.

6.3.2 Magnetic Actuation

The stiffness characterization experiments are conducted in an electromagnetic coil setup (PaCMag), which can generate a maximum magnetic field of 55 mT [337]. The VSM is suspended in the cylindrical workspace (equal radius and height of 65 mm) and magnetic fields (B = 30 mT and 40 mT) are applied to deflect the manipulator. The resulting bending moment ($\boldsymbol{M}$) acting on the VSM is given by, $\boldsymbol{M} = \boldsymbol{\mu} \times \mathbf{B}$, where $\boldsymbol{\mu}$ is the dipole moment of the magnet attached to the VSM. Thirteen experiments each in glass and rubber phases, are conducted for the three VSMs at various extended lengths and at different radial orientations of the SMP spring. Each experiment is repeated twice for bending in either direction. The deflection (θ) of the VSM is measured by a camera (FLIR Blackfly S USB3 camera, USA) which tracks the tip of the VSM.

6.3.3 Thermal Actuation

The heating and cooling behaviour of a SMP wire of length 15 cm, SMP spring with 3.5 active coils and VSM-1 are analysed. Each of the samples is composed of a 0.12 mm diameter nichrome wire (resistivity $\rho = 98\ \Omega$/m) of length 60 cm. The thermal actuation of the three samples is done by connecting the lead wires of the SMP to a power supply (TSX3510 - Precision DC Bench Power Supply, UK). Seven measurements of the temperature are taken using an infrared camera (Fluke Ti400 Infrared Camera, Washington, USA) while the samples are heated with currents 0.1, 0.2 and 0.3 A, and cooled at room temperature (≈ 27°C). The measured data is processed using the Fluke Connect software.

6.3.4 Applications

The one-segment VSM and two-segment VSM designs used for the demonstrations are made of one segment having 5.5 coils and two segments having 4.5 coils, respectively. Magnetic field is generated by moving a N45 neodymium disc magnet (diameter = 70 mm and height = 35 mm), which is connected to the end effector of a robot (UR5, Universal Robots, Denmark). The trajectory of the robot carrying the magnet is planned and programmed for each of the experiments. The magnet is held at a distance of 50-100 mm away from the VSM during the experiments resulting in the generation of 20-70 mT magnetic fields. For endoscopy and biopsy demonstrations, a miniature camera of diameter 0.91 mm (MD-B1000-120-01, Misumi Electronic Corporation, Taiwan) and a Diamond Cut™ Cold Snare of diameter 10 mm (Micro-Tech Endoscopy, China) are used. Experiments are performed in an anatomical model of the stomach (193 mm × 30 mm × 156 mm), and 3D printed elastic dome-shaped polyps of size 8 mm are glued on different locations. For laser application, a 0.2 NA 50/125 graded index multimode optical fiber (Plasma Optical Fibre B.V., Netherlands) is integrated to the VSM. A diode-pumped solid-state laser (37-028, Edmund Optics, USA) and an objective lens 5X (M Plan Apo, Mitutoyo, Japan) are used to couple and transmit the laser light through the fiber. The three rings of inner diameters 15 mm with centers at heights of 50 mm, 60 mm, and 70 mm are 3D printed and are positioned with spacings of 25 mm and 35 mm.

6.4 Conclusions

A new design of a magnetically-actuated VSM with a silicone backbone and enclosed within deployable SMP springs is presented in this work. Variable stiffness is attained with phase change and expansion of the SMP springs. The SMP springs with embedded resistive wires are fabricated using a novel process of re-training the primary shape of SMP. The optimal dimensions of the SMP springs are determined by analysing the bending characteristics of three VSM samples of different design parameters under magnetic actuation. Additionally, the thermal characteristics of the VSM are analysed using 1D transient heat transfer model and infrared camera images. The coated resistive wires for Joule heating are seamlessly integrated in the VSM and proven to generate uniform thermal actuation of the SMP. As a result of preliminary design evaluations, a one-segment VSM of outer diameter 9 mm, inner diameter 2 mm, with a working length in the range 15-70 mm, and a two-segment VSM of outer diameter 10 mm, inner diameter 1 mm, with a working length in the range 25-100 mm are developed. Thus, both the VSMs are capable of increasing their respective lengths by 4 times from their fully compressed forms to their fully extended forms. The one-segment VSM is integrated with a miniature camera and a clinically-used endoscopic cold snare to demonstrate endoscopy and biopsy applications in a stomach phantom with gastric polyps. The two-segment VSM integrated with an optical fiber for laser light delivery is maneuvered to follow a sequential arrangement of three distinctly oriented rings in 3D.

The proposed concept of deployable VSM demonstrates the ability to independently actuate and bend the two segments of the VSM to form variable curvatures across varying lengths of the VSM. The variable working length of the VSM can be useful in inserting the VSM and steering to reach the target surgical site with less likelihood of deviation of the VSM from its intended path, and subsequent expansion of the VSM enhances the range of motion and reach. Additionally, the entire shape of the VSM can be fixed which is an effective way of stabilizing the VSM while deploying laparoscopic tools through its working channel. The novel design has potential to develop a new class of smart surgical manipulators with controllable stiffness that can enhance instrument maneuverability to reach difficult-to-access surgical sites safely.

Acknowledgment

I would like to thank Prof. G. K. Ananthasuresh for his advice in conceiving the VSM design concept, and Mr. Gideon Geurtsen for his help in stiffness characterization. I am grateful to Mr. Rob Struik for assisting in the experiments using robotic magnetic actuation. I would also like to thank Dr. Jose Alfredo Alvarez-Chavez and Dr. Daniel Jauregui-Vazquez for their assistance in building the optical fiber setup using laser light.

III

Concluding Remarks

7

Discussion

This doctoral dissertation contributes to the rapidly expanding field of continuum manipulators for minimally invasive surgery (MIS) by designing surgical manipulators based on compliant mechanisms (CMs) and variable stiffness mechanisms. A magnetically-actuated flexure-based continuum manipulator is developed using the concept of CMs. The localization and steering accuracy of the manipulator are evaluated using rigid-link modelling and embedded sensing. The variable stiffness of manipulators for achieving high coiling deformation and deployable shape locking are investigated following two approaches based on mechanical sliding backbone constraint and shape memory effect, respectively. his dissertation has provided a deeper insight into our understanding of the design, modeling, sensing, and control aspects of surgical continuum manipulators. This chapter consolidates the significant findings that have emerged from this work, provides suggestions for improvement, and recommendations for future research directions.

7.1 Conclusions

7.1.1 Part I: Compliant Mechanisms

The first three research questions (**RQ. 1-3**) are investigated in this part. In order to answer **RQ. 1** on how CMs improve various surgical interventions, the utility of CMs in surgical interventions is assessed in **Chapter 2**. The applications of CMs in the design of surgical devices are examined focusing on five key aspects: (i) Conceptual design and synthesis, (ii) analysis, (iii) materials, (iv) manufacturing, and (v) actuation. An exhaustive account of all the methods pertaining to each of the aspects is formulated, shedding light on their applications, pros and cons. To the best of our knowledge, this study is the first comprehensive investigation of the surgical applications of CMs. In this survey, we identified 103 studies that report the use of CMs in the development of surgical devices. Accordingly, the surgical applications of CMs are broadly classified into five major groups: (i) Grasping and cutting, (ii) reachability and steerability, (iii) transmission, (iv) sensing, and (v) implants and deployable devices. The review highlights the advantages of CMs over typical rigid body mechanisms, with innovative monolithic designs eliminating friction, wear, or backlash, and attaining high precision and repeatability. However, the analysis of CMs undertaken here has exposed some of the drawbacks of CMs related to fatigue, stress concentrations, output efficiency, modeling methods, and biocompatibility as a surgical device. This new understanding should help to improve design of safe, dexterous, and cutting-edge surgical devices for MIS.

The aforementioned review of the surgical application of CMs has shown that CMs have been predominantly dedicated to enhance the range of motion and steerability of surgical instruments. Thereby, it consequently leads us to **RQ. 2**, can a compliant surgical manipulator be designed for precise motion using magnetic actuation. Having established the significance of CMs in the design of continuum manipulators, **Chapter 3** moves on to develop a new design of a compliant continuum manipulator which is magnetically-actuated. This work presents a monolithic metallic manipulator having an outer diameter of 3 mm and an inner working channel of 2 mm diameter, and attached with a permanent magnet at its tip. The manipulator is fabricated by making a series of cuts along the length of a titanium tube forming flexures. Each flexure acts as an elastic rotational joint that enables the bending of the manipulator with the application of an external force or moment. The novel notched-tube pattern of flexures results in built-in mechanical motion constraints that keeps the stresses within limits. A design framework based on cantilever beam modeling is provided to design a single-axis and a two-axis bending design of the manipulator.

In the first proof-of-concept study, three single-axis bending designs of the manipulator are analysed under magnetic actuation using Helmholtz coils. The mean errors between the theoretical model and the experiments in estimating the in-plane position and orientation of the tip, and the whole shape of the manipulators are reported as 1.9 mm, 5.1°, and 1.2 mm, respectively across all three designs. The accurate maneuvering of the manipulator along a path of known curvature is demonstrated in a gelatin phantom which mimics the stiffness characteristics of human tissue, and visualized in real-time using ultrasound (US) imaging. These experiments confirm the potential of the manipulator as a steerable surgical manipulator. Compliant design coupled with magnetic actuation eliminates force transmission mechanisms leading to miniaturized design of manipulators that can be controlled without any contact using external magnetic fields.

A follow-up study with a two-axis bending design of the manipulator of outer diameter 3 mm with an inner working channel of 1 mm diameter was carried out to address **RQ. 3**. The question on improving the localization of surgical manipulators using compliant design and sending modalities is rasied here. **Chapter 4** proceeds to describe in detail a quasi-static model based on rigid link modeling to study the 3D motion characteristics of the manipulator under magnetic actuation. For this purpose, a magnetic actuation setup - PaCMag consisting of three pairs of electromagnetic coils to generate magnetic fields in 3D with a cylindrical workspace of equal radius and height of 65 mm is developed. Additionally, PaCMag is equipped with two cameras forming a stereo vision system to capture the 3D shape of the manipulator in the workspace which serves as ground truth. Static experiments report an overall mean error in whole shape estimation of the manipulator between the model and the ground truth of 1.7 mm and 4.8 mm when suspended vertically and horizontally in the workspace, respectively.

In order to complement the shape estimation of the manipulator by quasi-static model, a multi-core optical fiber inscribed with fiber Bragg grating (FBG) sensors is integrated in the working channel of the manipulator. This is the first work to demonstrate an improved shape sensing method for the manipulator that unifies the FBG sensor data with quasi-static model using an observer-based sensor fusion algorithm based on Kalman state estimators. The proposed fusion algorithm does not require external imaging like cameras or ultrasound imaging to estimate the tip pose of the manipulator. A closed-loop control strategy to trace a square and a straight line trajectories with the tip of the manipulator is demonstrated with an average error in tip position of 4.1 mm between the desired and estimated positions. Furthermore, the visualization and steering capabilities of the manipulator under magnetic actuation are demonstrated in clinically relevant phantoms of a bifurcating artery and a heart with the integration of a miniature camera.

7.1.2 Part II: Variable Stiffness Mechanisms

In Part I of this thesis, we focused on CMs to design continuum manipulators for enhanced steering and shape sensing. Delving into the concept of variable stiffness mechanism for achieving specific functions with surgical manipulators raised in **RQ. 4**, two different variable stiffness manipulator designs are explored. **Chapter 5** introduces a magnetic variable stiffness robot (VSR) for cargo grasping or delivery. A stiffness change factor of 765 is attained with a 80 mm long, 10 mm×2 mm cross section VSR made of silicone doped with ferromagnetic particles and embedded with a sliding nitinol backbone. The ability of the VSR to grasp objects of varying sizes in closed-loop with feedback from visual tracking is demonstrated by synchronizing the movement of the sliding nitinol backbone with the actuating magnetic field generated by PaCMag. The results support the necessity of including a sliding backbone design as evident from the unsuccessful actuation of the VSR without the backbone. A maximum coiling deformation angle of 400° is achieved by the VSR which is otherwise not possible. The high deformation coiling action of the magnetically-actuated VSR can be advantageous for surgical applications related to grasping or biopsy. It is also shown that the reversible coiling action does not depend on the anatomical contact forces or the influence of the external environment.

Chapter 6 presents a novel design of a deployable variable stiffness manipulator (VSM) which exhibits variable stiffness with variable working length. The VSM has a concentric tube design with two nested concentric silicone tubes as the backbone, enveloped by two extensible springs made of shape memory polymers (SMPs), and with a permanent magnet at the tip. The stiffness of the VSM is changed by phase change in the SMP induced by Joule heating of nichrome wires, and the shape of the VSM is controlled by application of magnetic fields. The stiffness and thermal characteristics of three one-segment VSM designs are experimentally validated using a cantilever beam model and a transient heat transfer model, respectively.

As a result, one-segment and two-segment designs of VSM having outer diameters of 9 mm and 10 mm, respectively and working lengths in the range of 15-70 mm and 25-100 mm, respectively are developed. Potential clinical applications of endoscopy, biopsy and laser ablation are demonstrated by incorporating surgical tools like miniature camera, cold snare and optical fiber in the working channel of the VSM. Experiments are conducted by steering the VSM in a stomach phantom and a 3D obstacle course consisting of rings, guided by the magnetic fields produced by a permanent magnet attached to the end-effector of a robot arm. The VSM is designed to be inserted in its compact form to reach target site with less risk of undergoing any deviations from the planned path. The subsequent expansion of the VSM with stiffness control enhances the range of motion and attain complex curvatures. Moreover, the shape locking ability of the VSM provides stability to deploy surgical tools through the working channel and perform surgical tasks.

7.2 Future Work

This thesis lays the groundwork for future research into the development of continuum manipulators for surgical interventions which is discussed in three parts as follows.

7.2.1 Design and Fabrication

In Part I, a monolithic flexure-based continuum manipulator design with built-in mechanical motion constraints is presented. Although the novel notch pattern with mechanical constraints is designed to limit the stresses in the flexures, it also limits the range of motion. A major drawback of this design is that the maximum deflection angle is limited to 57°. This is due to the contact between the adjacent wall of the tube taking place before the flexures even make contact with the adjoining wall. There is, therefore, a definite need to redesign the topology of the notches in order to increase the range of motion ($> 90°$). A “tip-first-bending” design in which the heights of the cuts are varied so that the distal notches bend before the proximal notch, can increase the bending angle of the manipulator [116]. Asymmetric notch topologies reportedly attain more tight bending curvatures compared to symmetric notch topologies like our design, as the former can fold into themselves during articulation [44]. A varied combination of different notch topologies is worth investigating in future manipulator designs.

The fabrication of the monolithic compliant manipulator using electric discharge machining (EDM) of a titanium tube proved to be effective. However, plastic deformation was observed in single-axis bending design which was overcome in the two-axis bending design by increasing the wall thickness of the tube. An alternative to consider when scaling down the design is to reduce the stress concentrations in the flexures by rounding the corners using different diameters of the EDM wire. The fatigue life of the manipulator also needs further investigation to determine its safety in surgical applications.

In Part II, two variable stiffness mechanisms are developed for grasping and shape fixing purposes. The magnetically-actuated VSR with sliding nitinol backbone demonstrates successful grasping of objects in-plane supported horizontally by an acrlyic plate. Due to the rectangular cross-section of the VSR, twisting of the VSR with retraction and insertion of the backbone was problematic. This can be addressed by using braided reinforcement in the design of the VSR [369]. The deployable VSM based on SMP springs demonstrates a higher range of motion over the compliant manipulator. However, the miniaturization of the VSM proved to be challenging owing to the fabrication limitations and the stiffness properties of the used SMP. Hence, it is suggested to use a different SMP having a wide range of elastic modulus to make it very rigid in glass phase and soft in rubber phase [361].

7.2.2 Modeling and Sensing

A quasi-static model based on rigid link modeling is developed for the compliant manipulator. Static experiment results show that the whole shape estimation of the manipulator is more accurate when vertically suspending the manipulator compared to horizontal suspension. Although the discrepancy is attributed to the direction of gravity, a better stiffness approximation of the flexures would help us to establish a greater degree of accuracy on this matter. A further study could examine the deformations characteristics of a single flexure at micro-scale using a universal testing machine and corroborate with finite element analysis. Furthermore, it is noted that FBG sensors integrated to improve shape estimation also resulted in errors. This can be addressed by increasing the number and distribution of the FBGs along the length of the manipulator, in addition to securely embedding them on the manipulator. Previous work on FBGs also supports the use of helical core fibers for improving twist measurements [314].

The stiffness characterization of the VSM is done using a cantilever beam model which works well for small deflections ($< 10°$) while SMP is in glass phase. An essential next step would be to apply large deflection theory to assess the large deflections of the VSM. It is also important to fully understand the implications of the thermomechanical behavior of SMPs by implementing a 3D SMP constitutive model in geometrically nonlinear finite element software [370].

7.2.3 Actuation and Control

Magnetic actuation forms the basis for all the manipulators developed in this thesis. Most of the experiments are conducted in the magnetic actuation setup - PaCMag, which has produced fruitful results in expanding our understanding of the steering capability of the manipulators in a small workspace. However, PaCMag did not allow us to evaluate the full potential of the manipulators in a clinically-relevant setting. PaCMag posed limitations on the magnetic fields it can generate, on incorporating a mobile insertion setup and the heat generated by the coils affects the phase change of SMP. A natural progression to circumvent these issues led us to opt for robot-assisted magnetic actuation for the clinical application experiments with the VSM. Further experimental investigations into the steerability of the manipulators using systems like ARMM and DeltaMag, which use mobile electromagnetic coils should be considered [371], [372].

Two closed-loop strategies to trace different trajectories with the compliant manipulator and grasp various objects with the VSR are demonstrated. Both the strategies rely on tip orientation information as feedback to compensate for model inaccuracy during control. Adaptive and learning-based control methods can be considered to improve the accuracy [373], [374]. It is also important to improve the accuracy of the feedback for better results, motion models and disturbance observers can be used in this regard [375], [376].

7.3 Outlook

The results of this dissertation have shown that there is abundant room for further progress in the research on continuum manipulators for MIS. The findings drawn from CMs and variable stiffness mechanisms contribute in several ways to the development of the next generation of cutting-edge surgical manipulators. Building on the concept of CM with mechanical motion constraints, there is a scope of designing active flexures and active constraints. For instance, a manipulator can be designed using 3-DOF compliant joints limited by SMP-based mechanical constraints. This will allow the possibility to control the range of motion of the compliant joint by varying the stiffness of the constraint. Another interesting prospect is in designing active notch-tubed manipulators, which is based on a SMA tube like nitinol composed of flexures. By locally activating the shape memory property of specific flexures of the manipulator, complex bending curvatures can be attained. Hence, the CMs joining forces with the shape memory materials opens up new opportunities to create active compliant continuum manipulators.

The novel concept of deployable VSM is one of the more significant findings to emerge from our research on SMPs. The insights gained support the idea of designing a deployable and modular multi-segment manipulator with selective actuation, bending and extension capabilities. Origami-inspired foldable structures can be explored to miniaturize the manipulator, facilitate the insertion process in surgery and reduce patient discomfort. Future research on SMPs with a wide range of stiffness change while maintaining a lower range of transition temperatures would strengthen the applications of SMPs. Further investigation on incorporating electrical and thermal conductive properties in SMP composite, and multi-material 3D printing of SMP and conductive elastomer thermoplastic polyurethane is strongly recommended. Moreover, SMP-based manipulators can be strategically adapted to work using SMPs activated by other external stimuli such as light-induced SMP, electro-active SMP and magnetically-induced SMP depending on the application [377]. The use of such stimuli in addition to magnetic actuation can supplement the degrees of actuation of the manipulator.

For the localization of the manipulators, combining shape reconstruction based on modeling and sensors with medical imaging modalities like magnetic resonance imaging (MRI), US imaging or endoscopy camera is the imminent next step towards clinical practice [378]–[380]. A greater focus on human-in-the-loop operation strategies with shared control using teleoperation devices, and hybrid force/stiffness control considering the tissue-tool interactions could produce interesting findings that account more for surgical applications [52], [381]. Taken together, these recommendations promote experimentation using robotic magnetic actuation. Considerably more work will need to be done to determine a MIS workflow that integrates a mounting and insertion setup for the manipulator, robotic positioning of mobile electromagnets to generate the required magnetic fields, and test-bed to accommodate the subject. These developments can further expedite the improvement of existing commercial systems. For example, cardiac ablation is performed using a 4 mm flexible catheter (NaviStar-RMT, Biosense Webster, Inc., USA) integrated with small permanent magnets, controlled using the Niobe magnetic navigation system (uniform magnetic field: 80 mT) and a motor drive (Cardiodrive, Stereotaxis, Inc., USA) [38].

A number of important implications for future clinical translation has resulted from this dissertation. It is foremost essential to investigate the bio-compatibility of the manipulators. The interaction of the manipulators inside human body in the presence of blood and tissue needs to be studied. Further experiments using a broad range of soft tissue phantoms, animal tissue, and human cadaver could shed more light on the capabilities of the manipulators. Subsequently, a decision has to be made whether the manipulators could be used as a disposable surgical instrument and what surgical procedures can be targeted. The manipulators also have to meet the Medical Device Regulation (EU) 2017/745 of the European Union, in which they undergo a clinical evaluation and obtain CE-marking [382]. We envision that the designed manipulators could serve as end-effectors for robotic surgical systems like the Da Vinci tools. The compliant manipulator of 3 mm diameter is comparable to the 2 - 3.33 mm Magnellan robotic catheters [312]. Depending on the application, the bending angle of steerable catheters can be between 45°and 180°(SwiftNINJA Steerable Microcatheter by Merit Medical Systems, USA), up to 270°(Artisan Extend Control Catheter by Hansen Medical, USA) or even 360°in some cases. Endoscopes generally have insertion tube outer diameters in the range 2.6 – 13.7 mm, instrument channel internal diameters in the range 1.2 – 4.2 mm, and working lengths in the range 270 – 2500 mm. It is therefore suggested that designs like the VSR and VSM could be useful as a soft grasper for biopsy applications, and for stable deployment of surgical tools in endoscopy and laparoscopy applications.

While these studies suggest a lot of promise, significantly additional work needs to be done to clinically investigate the design viability, the benefits over existing standard treatment and the regulatory requirements to make it a reality. The empirical findings of this doctoral research have unraveled avenues for a new class of smart surgical manipulators which can reduce operation invasiveness to efficiently and safely operate in difficult-to-access surgical sites.

Bibliography

[1] R. Hargest, “Five thousand years of minimal access surgery: 3000 BC to 1850: early instruments for viewing body cavities,” *Journal of the Royal Society of Medicine*, vol. 113, no. 12, pp. 491–496, 2020.

[2] K. Natarajan, “Surgical instruments and endoscopes of Susruta, the sage surgeon of ancient India,” *Indian Journal of Surgery*, vol. 70, no. 5, pp. 219–223, 2008.

[3] S. A. Antoniou, G. A. Antoniou, A. I. Antoniou, and F.-A. Granderath, “Past, present, and future of minimally invasive abdominal surgery,” *JSLS: Journal of the Society of Laparoendoscopic Surgeons*, vol. 19, no. 3, 2015.

[4] S. S. Amr and A. Tbakhi, “Abu al qasim al zahrawi (albucasis): pioneer of modern surgery,” *Annals of Saudi medicine*, vol. 27, no. 3, pp. 220–221, 2007.

[5] H. R. Turner, *Science in medieval Islam: an illustrated introduction.* University of Texas Press, 2010.

[6] D. K. Nakayama, “The minimally invasive operations that transformed surgery,” *American College of Surgeons*, 2017.

[7] D. Bernard, “The origins of minimally invasive surgery,” *Outpatient Surg*, pp. 6–7, 2006.

[8] B. F. Overholt, “Colonoscopy: a review,” *Gastroenterology*, vol. 68, no. 5, pp. 1308–1320, 1975.

[9] G. S. Litynski, “Kurt Semm and the fight against skepticism: endoscopic hemostasis, laparoscopic appendectomy, and Semm’s impact on the “laparoscopic revolution”,” *JSLS: Journal of the Society of Laparoendoscopic Surgeons*, vol. 2, no. 3, p. 309, 1998.

[10] S. D. S. Peter and G. W. Holcomb III, *History of minimally invasive surgery.* Philadelphia: Elsevier Health Sciences, 2008.

[11] H.-H. Liu, L.-J. Li, B. Shi, C.-W. Xu, and E. Luo, "Robotic surgical systems in maxillofacial surgery: a review," *International journal of oral science*, vol. 9, no. 2, pp. 63–73, 2017.

[12] T. Lane, "A short history of robotic surgery," *The Annals of The Royal College of Surgeons of England*, vol. 100, no. 6_sup, pp. 5–7, 2018.

[13] J. Burgner-Kahrs, D. C. Rucker, and H. Choset, "Continuum robots for medical applications: A survey," *IEEE Transactions on Robotics*, vol. 31, no. 6, pp. 1261–1280, 2015.

[14] A. Bajo, L. M. Dharamsi, J. L. Netterville, C. G. Garrett, and N. Simaan, "Robotic-assisted micro-surgery of the throat: The trans-nasal approach," in *2013 IEEE International Conference on Robotics and Automation*, 2013, pp. 232–238.

[15] J. Burgner, D. C. Rucker, H. B. Gilbert, P. J. Swaney, P. T. Russell, K. D. Weaver, and R. J. Webster, "A telerobotic system for transnasal surgery," *IEEE/ASME Transactions on Mechatronics*, vol. 19, no. 3, pp. 996–1006, 2013.

[16] A. Bajo, R. E. Goldman, L. Wang, D. Fowler, and N. Simaan, "Integration and preliminary evaluation of an insertable robotic effectors platform for single port access surgery," in *2012 IEEE International Conference on Robotics and Automation*, 2012, pp. 3381–3387.

[17] Hansen Medical Inc., accessed January 2023, "Artisan catheter," https://www.medicalexpo.com/prod/hansen-medical/product-99069-639810.html.

[18] ——, "Artisan catheter," https://www.dicardiology.com/content/auris-surgical-robotics-agrees-acquire-hansen-medical.

[19] J. Burgner, P. J. Swaney, R. A. Lathrop, K. D. Weaver, and R. J. Webster, "Debulking from within: a robotic steerable cannula for intracerebral hemorrhage evacuation," *IEEE Transactions on Biomedical Engineering*, vol. 60, no. 9, pp. 2567–2575, 2013.

[20] H. Yu, J.-H. Shen, K. M. Joos, and N. Simaan, "Design, calibration and preliminary testing of a robotic telemanipulator for oct guided

retinal surgery," in *2013 IEEE International Conference on Robotics and Automation*, 2013, pp. 225–231.

[21] C. Bedell, J. Lock, A. Gosline, and P. E. Dupont, "Design optimization of concentric tube robots based on task and anatomical constraints," in *2011 IEEE International Conference on Robotics and Automation*, 2011, pp. 398–403.

[22] R. J. Hendrick, S. D. Herrell, and R. J. Webster, "A multi-arm hand-held robotic system for transurethral laser prostate surgery," in *2014 IEEE International Conference on Robotics and Automation (ICRA)*, 2014, pp. 2850–2855.

[23] R. E. Goldman, A. Bajo, L. S. MacLachlan, R. Pickens, S. D. Herrell, and N. Simaan, "Design and performance evaluation of a minimally invasive telerobotic platform for transurethral surveillance and intervention," *IEEE Transactions on Biomedical Engineering*, vol. 60, no. 4, pp. 918–925, 2012.

[24] G. Robinson and J. Davies, "Continuum robots - a state of the art," in *Proceedings 1999 IEEE International Conference on Robotics and Automation (Cat. No.99CH36288C)*, vol. 4, 1999, pp. 2849–2854 vol.4.

[25] Y. Hao, S. Zhang, B. Fang, F. Sun, H. Liu, and H. Li, "A review of smart materials for the boost of soft actuators, soft sensors, and robotics applications," *Chinese Journal of Mechanical Engineering*, vol. 35, no. 1, pp. 1–16, 2022.

[26] C. Chautems, A. Tonazzini, D. Floreano, and B. J. Nelson, "A variable stiffness catheter controlled with an external magnetic field," in *2017 IEEE/RSJ International Conference on Intelligent Robots and Systems (IROS)*, 2017, pp. 181–186.

[27] Y. Zhong, L. Hu, and Y. Xu, "Recent advances in design and actuation of continuum robots for medical applications," in *Actuators*, vol. 9, no. 4. MDPI, 2020, p. 142.

[28] C. Yang, S. Geng, I. Walker, D. T. Branson, J. Liu, J. S. Dai, and R. Kang, "Geometric constraint-based modeling and analysis of a novel continuum robot with shape memory alloy initiated variable

stiffness," *The International Journal of Robotics Research*, vol. 39, no. 14, pp. 1620–1634, 2020.

[29] N. G. Cheng, M. B. Lobovsky, S. J. Keating, A. M. Setapen, K. I. Gero, A. E. Hosoi, and K. D. Iagnemma, "Design and analysis of a robust, low-cost, highly articulated manipulator enabled by jamming of granular media," in *2012 IEEE International Conference on Robotics and Automation*, 2012, pp. 4328–4333.

[30] M. Yalcintas and H. Dai, "Magnetorheological and electrorheological materials in adaptive structures and their performance comparison," *Smart Materials and Structures*, vol. 8, no. 5, p. 560, 1999.

[31] R. Zhao, Y. Yao, and Y. Luo, "Development of a variable stiffness over tube based on low-melting-point-alloy for endoscopic surgery," *Journal of Medical Devices*, vol. 10, no. 2, 2016.

[32] A. Firouzeh, S. S. M. Salehian, A. Billard, and J. Paik, "An under actuated robotic arm with adjustable stiffness shape memory polymer joints," in *2015 IEEE International Conference on Robotics and Automation (ICRA)*, 2015, pp. 2536–2543.

[33] M. Henke, J. Sorber, and G. Gerlach, "Multi-layer beam with variable stiffness based on electroactive polymers," in *Electroactive Polymer Actuators and Devices (EAPAD) 2012*, vol. 8340. SPIE, 2012, pp. 412–424.

[34] Y. Yang, Y. Li, and Y. Chen, "Principles and methods for stiffness modulation in soft robot design and development," *Bio-Design and Manufacturing*, vol. 1, no. 1, pp. 14–25, 2018.

[35] J. Hughes, U. Culha, F. Giardina, F. Guenther, A. Rosendo, and F. Iida, "Soft manipulators and grippers: a review," *Frontiers in Robotics and AI*, vol. 3, p. 69, 2016.

[36] L. Wang, D. Zheng, P. Harker, A. B. Patel, C. F. Guo, and X. Zhao, "Evolutionary design of magnetic soft continuum robots," *Proceedings of the National Academy of Sciences*, vol. 118, no. 21, p. e2021922118, 2021.

[37] C. Heunis, J. Sikorski, and S. Misra, “Flexible instruments for endovascular interventions: Improved magnetic steering, actuation, and image-guided surgical instruments,” *IEEE Robotics & Automation Magazine*, vol. 25, no. 3, pp. 71–82, 2018.

[38] C. Pappone, G. Vicedomini, F. Manguso, F. Gugliotta, P. Mazzone, S. Gulletta, N. Sora, S. Sala, A. Marzi, G. Augello *et al.*, “Robotic magnetic navigation for atrial fibrillation ablation,” *Journal of the American College of Cardiology*, vol. 47, no. 7, pp. 1390–1400, 2006.

[39] F. Carpi and C. Pappone, “Stereotaxis niobe® magnetic navigation system for endocardial catheter ablation and gastrointestinal capsule endoscopy,” *Expert Review of Medical Devices*, vol. 6, no. 5, pp. 487–498, 2009.

[40] Y. Kim, G. A. Parada, S. Liu, and X. Zhao, “Ferromagnetic soft continuum robots,” *Science Robotics*, vol. 4, no. 33, p. eaax7329, 2019.

[41] Stereotaxis, Inc., accessed January 2023, “Stereotaxis niobe robotic magnetic navigation system,” https://www.stereotaxis.com/products/.

[42] AEON Scientific AG, accessed January 2023, “Aeon phocus,” http://www.eu-robotics-sme.org/aeon-scientific-ag/.

[43] Magnetecs Corporation, accessed January 2023, “Catheter guidance control and imaging (cgci) system,” https://www.magnetecs.com/news.php?id=67.

[44] K. W. Eastwood, P. Francis, H. Azimian, A. Swarup, T. Looi, J. M. Drake, and H. E. Naguib, “Design of a contact-aided compliant notched-tube joint for surgical manipulation in confined workspaces,” *Journal of Mechanisms and Robotics*, vol. 10, no. 1, p. 015001, 2018.

[45] T. Kato, I. Okumura, S.-E. Song, A. J. Golby, and N. Hata, “Tendon-driven continuum robot for endoscopic surgery: Preclinical development and validation of a tension propagation model,” *IEEE/ASME Transactions on Mechatronics*, vol. 20, no. 5, pp. 2252–2263, 2014.

[46] M. D. Kutzer, S. M. Segreti, C. Y. Brown, M. Armand, R. H. Taylor, and S. C. Mears, “Design of a new cable-driven manipulator with a large open lumen: Preliminary applications in the minimally-invasive removal of osteolysis,” in *2011 IEEE International Conference on Robotics and Automation*, 2011, pp. 2913–2920.

[47] C. Chautems, A. Tonazzini, Q. Boehler, S. H. Jeong, D. Floreano, and B. J. Nelson, “Magnetic continuum device with variable stiffness for minimally invasive surgery,” *Advanced Intelligent Systems*, vol. 2, no. 6, p. 1900086, 2020.

[48] T. da Veiga, J. H. Chandler, P. Lloyd, G. Pittiglio, N. J. Wilkinson, A. K. Hoshiar, R. A. Harris, and P. Valdastri, “Challenges of continuum robots in clinical context: a review,” *Progress in Biomedical Engineering*, vol. 2, no. 3, p. 032003, 2020.

[49] R. J. Webster III and B. A. Jones, “Design and kinematic modeling of constant curvature continuum robots: A review,” *The International Journal of Robotics Research*, vol. 29, no. 13, pp. 1661–1683, 2010.

[50] D. Trivedi, A. Lotfi, and C. D. Rahn, “Geometrically exact models for soft robotic manipulators,” *IEEE Transactions on Robotics*, vol. 24, no. 4, pp. 773–780, 2008.

[51] T. Greigarn and M. C. Çavuşoğlu, “Pseudo-rigid-body model and kinematic analysis of mri-actuated catheters,” in *2015 IEEE International Conference on Robotics and Automation (ICRA)*, 2015, pp. 2236–2243.

[52] A. Bajo and N. Simaan, “Hybrid motion/force control of multi-backbone continuum robots,” *The International Journal of Robotics Research*, vol. 35, no. 4, pp. 422–434, 2016.

[53] M. T. Chikhaoui and J. Burgner-Kahrs, “Control of continuum robots for medical applications: State of the art,” in *ACTUATOR 2018; 16th International Conference on New Actuators*. VDE, 2018, pp. 1–11.

[54] L. Wu, S. Song, K. Wu, C. M. Lim, and H. Ren, “Development of a compact continuum tubular robotic system for nasopharyngeal biopsy,” *Medical & Biological Engineering & Computing*, vol. 55, no. 3, pp. 403–417, 2017.

[55] F. Khan, A. Donder, S. Galvan, F. R. y Baena, and S. Misra, “Pose measurement of flexible medical instruments using fiber bragg gratings in multi-core fiber,” *IEEE Sensors Journal*, vol. 20, no. 18, pp. 10 955–10 962, 2020.

[56] A. Vandini, C. Bergeles, F.-Y. Lin, and G.-Z. Yang, “Vision-based intraoperative shape sensing of concentric tube robots,” in *2015 IEEE/RSJ International Conference on Intelligent Robots and Systems (IROS)*, 2015, pp. 2603–2610.

[57] C. Shi, X. Luo, P. Qi, T. Li, S. Song, Z. Najdovski, T. Fukuda, and H. Ren, “Shape sensing techniques for continuum robots in minimally invasive surgery: A survey,” *IEEE Transactions on Biomedical Engineering*, vol. 64, no. 8, pp. 1665–1678, 2016.

[58] F. Khan, A. Denasi, D. Barrera, J. Madrigal, S. Sales, and S. Misra, “Multi-core optical fibers with bragg gratings as shape sensor for flexible medical instruments,” *IEEE Sensors Journal*, vol. 19, no. 14, pp. 5878–5884, 2019.

[59] A. Bajo and N. Simaan, “Kinematics-based detection and localization of contacts along multisegment continuum robots,” *IEEE Transactions on Robotics*, vol. 28, no. 2, pp. 291–302, 2011.

[60] G. J. Vrooijink, M. Abayazid, and S. Misra, “Real-time three-dimensional flexible needle tracking using two-dimensional ultrasound,” in *2013 IEEE International Conference on Robotics and Automation*, 2013, pp. 1688–1693.

[61] S. Jagtap, B. Deshmukh, and S. Pardeshi, “Applications of compliant mechanism in today’s world–a review,” in *Journal of Physics: Conference Series*, vol. 1969, no. 1. IOP Publishing, 2021, p. 012013.

[62] S. Li and G. Hao, “Current trends and prospects in compliant continuum robots: A survey,” in *Actuators*, vol. 10, no. 7. MDPI, 2021, p. 145.

[63] F. Jelínek, E. A. Arkenbout, P. W. Henselmans, R. Pessers, and P. Breedveld, “Classification of joints used in steerable instruments for minimally invasive surgery—a review of the state of the art,” *Journal of Medical Devices*, vol. 9, no. 1, 2015.

[64] W. Dou, G. Zhong, J. Cao, Z. Shi, B. Peng, and L. Jiang, “Soft robotic manipulators: Designs, actuation, stiffness tuning, and sensing,” *Advanced Materials Technologies*, vol. 6, no. 9, p. 2100018, 2021.

[65] Y.-J. Kim, S. Cheng, S. Kim, and K. Iagnemma, “A novel layer jamming mechanism with tunable stiffness capability for minimally invasive surgery,” *IEEE Transactions on Robotics*, vol. 29, no. 4, pp. 1031–1042, 2013.

[66] T. Wang, J. Zhang, Y. Li, J. Hong, and M. Y. Wang, “Electrostatic layer jamming variable stiffness for soft robotics,” *IEEE/ASME Transactions on Mechatronics*, vol. 24, no. 2, pp. 424–433, 2019.

[67] K. Althoefer, “Antagonistic actuation and stiffness control in soft inflatable robots,” *Nature Reviews Materials*, vol. 3, no. 6, pp. 76–77, 2018.

[68] J. Lussi, M. Mattmann, S. Sevim, F. Grigis, C. De Marco, C. Chautems, S. Pané, J. Puigmartí-Luis, Q. Boehler, and B. J. Nelson, “A submillimeter continuous variable stiffness catheter for compliance control,” *Advanced Science*, vol. 8, no. 18, p. 2101290, 2021.

[69] Y. Piskarev, J. Shintake, C. Chautems, J. Lussi, Q. Boehler, B. J. Nelson, and D. Floreano, “A variable stiffness magnetic catheter made of a conductive phase-change polymer for minimally invasive surgery,” *Advanced Functional Materials*, p. 2107662, 2022.

[70] L. L. Howell, *Compliant mechanisms.* John Wiley & Sons, 2001.

[71] D. A. Bloom, E. J. McGuire, and J. Lapides, “A brief history of urethral catheterization,” *The Journal of Urology*, vol. 151, no. 2, pp. 317–325, 1994.

[72] R. Fowler, L. Howell, and S. Magleby, “Compliant space mechanisms: a new frontier for compliant mechanisms,” *Mechanical Sciences*, vol. 2, no. 2, pp. 205–215, 2011.

[73] L. L. Howell, S. P. Magleby, B. M. Olsen, and J. Wiley, *Handbook of Compliant Mechanisms.* Wiley Online Library, 2013.

[74] L. L. Howell, “Compliant mechanisms,” in *21st Century Kinematics.* Springer, 2013, pp. 189–216.

[75] J. A. Gallego and J. Herder, “Synthesis methods in compliant mechanisms: An overview,” in *ASME 2009 International Design Engineering Technical Conferences and Computers and Information in Engineering Conference*, 2009, pp. 193–214.

[76] S. Kota, K.-J. Lu, Z. Kreiner, B. Trease, J. Arenas, and J. Geiger, “Design and application of compliant mechanisms for surgical tools,” *Journal of Biomechanical Engineering*, vol. 127, no. 6, pp. 981–989, 2005.

[77] K. Entsfellner, I. Kuru, T. Maier, J. D. Gumprecht, and T. Lüth, “First 3D printed medical robot for ENT surgery - Application specific manufacturing of laser sintered disposable manipulators,” in *2014 IEEE/RSJ International Conference on Intelligent Robots and Systems (IROS)*, 2014, pp. 4278–4283.

[78] C.-C. Lan and J.-Y. Wang, “Design of adjustable constant-force forceps for robot-assisted surgical manipulation,” in *2011 IEEE International Conference on Robotics and Automation (ICRA)*, 2011, pp. 386–391.

[79] L. Li and Z. J. Chew, “Microactuators: Design and technology,” in *Smart Sensors and MEMS.* Elsevier, 2018, pp. 313–354.

[80] N. Lobontiu, *System dynamics for engineering students: Concepts and applications.* Academic Press, 2017.

[81] J. B. Gafford, S. B. Kesner, R. J. Wood, and C. J. Walsh, “Microsurgical Devices by Pop-Up Book MEMS,” in *ASME 2013 International Design Engineering Technical Conferences and Computers and Information in Engineering Conference*, 2013.

[82] S. Russo, T. Ranzani, J. Gafford, C. J. Walsh, and R. J. Wood, “Soft pop-up mechanisms for micro surgical tools: Design and characterization of compliant millimeter-scale articulated structures,” in *2016 IEEE International Conference on Robotics and Automation (ICRA)*, 2016, pp. 750–757.

[83] R. Gassert, R. Moser, E. Burdet, and H. Bleuler, "MRI/fMRI-compatible robotic system with force feedback for interaction with human motion," *IEEE/ASME Transactions on Mechatronics*, vol. 11, no. 2, pp. 216–224, 2006.

[84] M. B. Hong and Y.-H. Jo, "Design and evaluation of 2-DOF compliant forceps with force-sensing capability for minimally invasive robot surgery," *IEEE Transactions on Robotics*, vol. 28, no. 4, pp. 932–941, 2012.

[85] P. A. Halverson, "Modeling, design, and testing of contact-aided compliant mechanisms in spinal arthroplasty," *PhD Thesis. Brigham Young University-Provo*, 2010.

[86] K. A. James and H. Waisman, "Layout design of a bi-stable cardiovascular stent using topology optimization," *Computer Methods in Applied Mechanics and Engineering*, vol. 305, pp. 869–890, 2016.

[87] M. Johnson, Y. Chen, S. Hovet, S. Xu, B. Wood, H. Ren, J. Tokuda, and Z. T. H. Tse, "Fabricating biomedical origami: A state-of-the-art review," *International journal of computer assisted radiology and surgery*, vol. 12, no. 11, pp. 2023–2032, 2017.

[88] J. A. Gallego and J. Herder, "Classification for literature on compliant mechanisms: a design methodology based approach," in *ASME 2009 International Design Engineering Technical Conferences and Computers and Information in Engineering Conference*, 2009, pp. 289–297.

[89] S. Hegde and G. K. Ananthasuresh, "Design of Single-Input-Single-Output Compliant Mechanisms for Practical Applications Using Selection Maps," *Journal of Mechanical Design*, vol. 132, no. 8, 2010.

[90] ——, "A Spring-mass-lever Model, Stiffness and Inertia Maps for Single-input, Single-output Compliant Mechanisms," *Mechanism and Machine Theory*, vol. 58, pp. 101–119, 2012.

[91] K. Amellal, C. Tzoganakis, A. Penlidis, and G. L. Rempel, "Injection molding of medical plastics: a review," *Advances in Polymer Technology: Journal of the Polymer Processing Institute*, vol. 13, no. 4, pp. 315–322, 1994.

[92] M. I. Frecker, G. K. Ananthasuresh, S. Nishiwaki, N. Kikuchi, and S. Kota, "Topological Synthesis of Compliant Mechanisms Using Multi-Criteria Optimization," *Journal of Mechanical Design*, vol. 119, no. 2, pp. 238–245, 06 1997.

[93] O. Sigmund, "On the design of compliant mechanisms using topology optimization," *Journal of Structural Mechanics*, vol. 25, no. 4, pp. 493–524, 1997.

[94] A. Saxena and G. K. Ananthasuresh, "On an optimal property of compliant topologies," *Structural and Multidisciplinary Optimization*, vol. 19, no. 1, pp. 36–49, 2000.

[95] D. J. de Lange, M. Langelaar, and J. L. Herder, "Towards the design of a statically balanced compliant laparoscopic grasper using topology optimization," in *ASME 2008 International Design Engineering Technical Conferences and Computers and Information in Engineering Conference*, 2008, pp. 293–305.

[96] U.-X. Tan, B. Yang, R. Gullapalli, and J. P. Desai, "Triaxial MRI-compatible fiber-optic force sensor," *IEEE Transactions on Robotics*, vol. 27, no. 1, pp. 65–74, 2010.

[97] T. Guimarães, S. Oliveira, and M. Duarte, "Application of the topological optimization technique to the stents cells design for angioplasty," *Journal of the Brazilian Society of Mechanical Sciences and Engineering*, vol. 30, no. 3, pp. 261–268, 2008.

[98] Y. Sun, Y. Liu, L. Xu, and T. C. Lueth, "Design of a disposable compliant medical forceps using topology optimization techniques," in *2019 IEEE International Conference on Robotics and Biomimetics (ROBIO)*, 2019, pp. 924–929.

[99] C. J. Kim, Y.-M. Moon, and S. Kota, "A building block approach to the conceptual synthesis of compliant mechanisms utilizing compliance and stiffness ellipsoids," *Journal of Mechanical Design*, vol. 130, no. 2, 2008.

[100] G. Krishnan, C. Kim, and S. Kota, "An intrinsic geometric framework for the building block synthesis of single point compliant mechanisms," *Journal of Mechanisms and Robotics*, vol. 3, no. 1, 2011.

[101] K. Hoetmer, J. L. Herder, and C. J. Kim, “A building block approach for the design of statically balanced compliant mechanisms,” in *ASME 2009 International Design Engineering Technical Conferences and Computers and Information in Engineering Conference*, 2009, pp. 313–323.

[102] A. Lamers, J. A. G. Sánchez, and J. L. Herder, “Design of a statically balanced fully compliant grasper,” *Mechanism and Machine Theory*, vol. 92, pp. 230–239, 2015.

[103] J. B. Hopkins and M. L. Culpepper, “Synthesis of multi-degree of freedom, parallel flexure system concepts via Freedom and Constraint Topology (FACT)–Part I: Principles,” *Precision Engineering*, vol. 34, no. 2, pp. 259–270, 2010.

[104] ——, “Synthesis of multi-degree of freedom, parallel flexure system concepts via freedom and constraint topology (FACT)– Part II: Practice,” *Precision Engineering*, vol. 34, no. 2, pp. 271–278, 2010.

[105] H.-J. Su, D. V. Dorozhkin, and J. M. Vance, “A screw theory approach for the conceptual design of flexible joints for compliant mechanisms,” *Journal of Mechanisms and Robotics*, vol. 1, no. 4, 2009.

[106] L. L. Howell and A. Midha, “Parametric Deflection Approximations for End-Loaded, Large-Deflection Beams in Compliant Mechanisms,” *Journal of Mechanical Design*, vol. 117, no. 1, pp. 156–165, 03 1995.

[107] H.-J. Su, “A pseudorigid-body 3r model for determining large deflection of cantilever beams subject to tip loads,” *Journal of Mechanisms and Robotics*, vol. 1, no. 2, 2009.

[108] V. K. Venkiteswaran and H.-J. Su, “Pseudo-rigid-body models for circular beams under combined tip loads,” *Mechanism and Machine Theory*, vol. 106, pp. 80–93, 2016.

[109] N. Tolou and J. L. Herder, “Concept and modeling of a statically balanced compliant laparoscopic grasper,” in *ASME 2009 International Design Engineering Technical Conferences and Computers and Information in Engineering Conference*, 2009, pp. 163–170.

[110] T. L. Thomas, V. K. Venkiteswaran, G. K. Ananthasuresh, and S. Misra, “A Monolithic Compliant Continuum Manipulator: A Proof-of-Concept Study,” *Journal of Mechanisms and Robotics*, vol. 12, no. 6, 05 2020, 061006.

[111] G. S. Baichapur, H. Gugale, A. Maheshwari, S. D. Bhargav, and G. K. Ananthasuresh, “A Vision-based Micro-Newton Static Force Sensor using a Displacement-amplifying Compliant Mechanism (DaCM),” *Mechanics Based Design of Structures and Machines*, vol. 42, no. 2, pp. 193–210, 2014.

[112] S. Khan and G. K. Ananthasuresh, “Improving the sensitivity and bandwidth of in-plane capacitive micro-accelerometers using compliant mechanical amplifiers,” *Journal of Microelectromechanical Systems*, vol. 23, no. 4, pp. 871–887, 2014.

[113] ——, “A Micromachined Wideband In-plane Single-axis Capacitive Accelerometer with a Displacement-amplifying Compliant Mechanism,” *Mechanics Based Design of Structures and Machines*, vol. 42, no. 3, pp. 355–370, 2014.

[114] S. D. Bhargav, S. Chakravarthy, and G. K. Ananthasuresh, “A compliant end-effector to passively limit the force in tele-operated tissue-cutting,” *Journal of Medical Devices*, vol. 6, no. 4, 2012.

[115] S. Coemert, M. F. Traeger, E. C. Graf, and T. C. Lueth, “Suitability evaluation of various manufacturing technologies for the development of surgical snake-like manipulators from metals based on flexure hinges,” *Procedia CIRP*, vol. 65, pp. 1–6, 2017.

[116] P. J. Swaney, P. A. York, H. B. Gilbert, J. Burgner-Kahrs, and R. J. Webster, “Design, fabrication, and testing of a needle-sized wrist for surgical instruments,” *Journal of Medical Devices*, vol. 11, no. 1, 2017.

[117] J.-w. Suh, K.-y. Kim, J.-w. Jeong, and J.-j. Lee, “Design considerations for a hyper-redundant pulleyless rolling joint with elastic fixtures,” *IEEE/ASME Transactions on Mechatronics*, vol. 20, no. 6, pp. 2841–2852, 2015.

[118] D. Chapuis, R. Gassert, L. Sache, E. Burdet, and H. Bleuler, "Design of a simple MRI/fMRI compatible force/torque sensor," in *2004 IEEE/RSJ International Conference on Intelligent Robots and Systems (IROS)*, vol. 3, 2004, pp. 2593–2599.

[119] R. Gassert, D. Chapuis, H. Bleuler, and E. Burdet, "Sensors for applications in magnetic resonance environments," *IEEE/ASME Transactions On Mechatronics*, vol. 13, no. 3, pp. 335–344, 2008.

[120] A. Disch, T. Lutze, D. Schauer, C. Mueller, and H. Reinecke, "Innovative polymer-based shaft instruments for minimally invasive surgery," *Minimally Invasive Therapy & Allied Technologies*, vol. 17, no. 5, pp. 275–284, 2008.

[121] Y. Haga, Y. Muyari, S. Goto, T. Matsunaga, and M. Esashi, "Development of minimally invasive medical tools using laser processing on cylindrical substrates," *Electrical Engineering in Japan*, vol. 176, no. 1, pp. 65–74, 2011.

[122] F. Dewaele, A. F. Kalmar, F. De Ryck, N. Lumen, L. Williams, E. Baert, H. Vereecke, J. P. Kalala Okito, C. Mabilde, B. Blanckaert *et al.*, "A novel design for steerable instruments based on laser-cut nitinol," *Surgical Innovation*, vol. 21, no. 3, pp. 303–311, 2014.

[123] H. Fischer, B. Vogel, W. Pfleging, and H. Besser, "Flexible distal tip made of nitinol (niti) for a steerable endoscopic camera system," *Materials Science and Engineering: A*, vol. 273, pp. 780–783, 1999.

[124] R. Gassert, L. Dovat, O. Lambercy, Y. Ruffieux, D. Chapuis, G. Ganesh, E. Burdet, and H. Bleuler, "A 2-DOF fMRI compatible haptic interface to investigate the neural control of arm movements," in *Proceedings 2006 IEEE International Conference on Robotics and Automation (ICRA)*, 2006, pp. 3825–3831.

[125] M. Scharvogel and W. Winkelmueller, "Metal injection molding of titanium for medical and aerospace applications," *JOM*, vol. 63, no. 2, pp. 94–96, 2011.

[126] V. Goodship, *Practical Guide to Injection Moulding.* Smithers Rapra, 2004.

[127] W. Bejgerowski, J. W. Gerdes, S. K. Gupta, and H. A. Bruck, “Design and fabrication of miniature compliant hinges for multi-material compliant mechanisms,” *The International Journal of Advanced Manufacturing Technology*, vol. 57, no. 5-8, p. 437, 2011.

[128] W. Theisen and A. Schuermann, “Electro discharge machining of nickel–titanium shape memory alloys,” *Materials Science and Engineering: A*, vol. 378, no. 1-2, pp. 200–204, 2004.

[129] C. Prakash, H. K. Kansal, B. Pabla, S. Puri, and A. Aggarwal, “Electric discharge machining–a potential choice for surface modification of metallic implants for orthopedic applications: A review,” *Proceedings of the Institution of Mechanical Engineers, Part B: Journal of Engineering Manufacture*, vol. 230, no. 2, pp. 331–353, 2016.

[130] W. Sieklicki, M. Zoppi, and R. Molfino, “Superelastic compliant mechanisms for needlescopic surgical wrists,” in *2009 ASME/IFToMM International Conference on Reconfigurable Mechanisms and Robots*, 2009, pp. 392–399.

[131] M. N. M. Zubir and B. Shirinzadeh, “Development of a high precision flexure-based microgripper,” *Precision Engineering*, vol. 33, no. 4, pp. 362–370, 2009.

[132] A. Gao, R. J. Murphy, H. Liu, I. I. Iordachita, and M. Armand, “Mechanical model of dexterous continuum manipulators with compliant joints and tendon/external force interactions,” *IEEE/ASME Transactions on Mechatronics*, vol. 22, no. 1, pp. 465–475, 2016.

[133] M. Doria and L. Birglen, “Design of an underactuated compliant gripper for surgery using nitinol,” *Journal of Medical Devices*, vol. 3, no. 1, 2009.

[134] J. Peirs, J. Clijnen, D. Reynaerts, H. Van Brussel, P. Herijgers, B. Corteville, and S. Boone, “A micro optical force sensor for force feedback during minimally invasive robotic surgery,” *Sensors and Actuators A: Physical*, vol. 115, no. 2-3, pp. 447–455, 2004.

[135] F. Alambeigi, M. Bakhtiarinejad, A. Azizi, R. Hegeman, I. Iordachita, H. Khanuja, and M. Armand, “Inroads toward robot-assisted

internal fixation of bone fractures using a bendable medical screw and the curved drilling technique," in *2018 7th IEEE International Conference on Biomedical Robotics and Biomechatronics (BioRob)*, 2018, pp. 595–600.

[136] S. Coemert, A. Gao, J. P. Carey, M. F. Traeger, R. H. Taylor, T. C. Lueth, and M. Armand, "Development of a snake-like dexterous manipulator for skull base surgery," in *2016 38th Annual International Conference of the IEEE Engineering in Medicine and Biology Society (EMBC)*, 2016, pp. 5087–5090.

[137] J. Peirs, H. Van Brussel, D. Reynaerts, and G. De Gersem, "A flexible distal tip with two degrees of freedom for enhanced dexterity in endoscopic robot surgery," in *Proceedings of the 13th Micromechanics Europe Workshop*, 2002, pp. 271–274.

[138] T. Yoneyama, T. Watanabe, H. Kagawa, J. Hamada, Y. Hayashi, and M. Nakada, "Force detecting gripper and flexible micro manipulator for neurosurgery," in *2011 Annual International Conference of the IEEE Engineering in Medicine and Biology Society*, 2011, pp. 6695–6699.

[139] J. B. Gafford, S. B. Kesner, R. J. Wood, and C. J. Walsh, "Force-sensing surgical grasper enabled by pop-up book MEMS," in *2013 IEEE/RSJ International Conference on Intelligent Robots and Systems (IROS)*, 2013, pp. 2552–2558.

[140] R. K. Pathak, A. R. Kumar, and G. K. Ananthasuresh, "Simulations and experiments in punching spring-steel devices with sub-millimeter features," *Journal of Manufacturing Processes*, vol. 15, no. 1, pp. 108–114, 2013.

[141] Stratasys Ltd., "Biocompatible," accessed August 2020, https://www.stratasys.com/materials/search/biocompatible.

[142] K. Chandrasekaran and A. Thondiyath, "Design of a two degree-of-freedom compliant tool tip for a handheld powered surgical tool," *Journal of Medical Devices*, vol. 11, no. 1, p. 014502, 2017.

[143] K. Chandrasekaran, A. Sathuluri, and A. Thondiyath, "MagNex—Expendable robotic surgical tooltip," in *2017 IEEE International Conference on Robotics and Automation (ICRA)*, 2017, pp. 4221–4226.

[144] P. Polygerinos, L. D. Seneviratne, R. Razavi, T. Schaeffter, and K. Althoefer, "Triaxial catheter-tip force sensor for mri-guided cardiac procedures," *IEEE/ASME Transactions on mechatronics*, vol. 18, no. 1, pp. 386–396, 2012.

[145] S. B. Kesner and R. D. Howe, "Design principles for rapid prototyping forces sensors using 3-D printing," *IEEE/ASME Transactions on mechatronics*, vol. 16, no. 5, pp. 866–870, 2011.

[146] N. Liu, C. Bergeles, and G.-Z. Yang, "Design and analysis of a wire-driven flexible manipulator for bronchoscopic interventions," in *2016 IEEE International Conference on Robotics and Automation (ICRA)*, 2016, pp. 4058–4063.

[147] U.-X. Tan, W. T. Latt, C. Y. Shee, and W. T. Ang, "A low-cost flexure-based handheld mechanism for micromanipulation," *IEEE/ASME Transactions on Mechatronics*, vol. 16, no. 4, pp. 773–778, 2010.

[148] I. Ebert-Uphoff, C. M. Gosselin, D. W. Rosen, and T. Laliberte, "Rapid prototyping for robotics," *Cutting Edge Robotics*, pp. 17–46, 2005.

[149] D. Y. Choi and C. N. Riviere, "Flexure-based manipulator for active handheld microsurgical instrument," in *2005 IEEE Engineering in Medicine and Biology 27th Annual Conference*, 2006, pp. 2325–2328.

[150] C. L. Grames, J. D. Tanner, B. D. Jensen, S. P. Magleby, J. R. Steger, and L. L. Howell, "A meso-scale rolling-contact gripping mechanism for robotic surgery," in *ASME 2015 International Design Engineering Technical Conferences and Computers and Information in Engineering Conference*, 2015.

[151] K. Tan, C. Chua, K. Leong, C. Cheah, W. Gui, W. Tan, and F. Wiria, "Selective laser sintering of biocompatible polymers for

applications in tissue engineering," *Bio-medical Materials and Engineering*, vol. 15, no. 1, 2, pp. 113–124, 2005.

[152] Y. Sun, Y. Liu, and T. C. Lueth, "Fe-analysis of bio-inspired compliant mechanisms in matlab for medical applications," in *2019 IEEE International Conference on Cyborg and Bionic Systems (CBS)*, 2019, pp. 54–59.

[153] Y. S. Krieger, D. B. Roppenecker, I. Kuru, and T. C. Lueth, "Multi-arm snake-like robot," in *2017 IEEE International Conference on Robotics and Automation (ICRA)*, 2017, pp. 2490–2495.

[154] C. Y. Yap, C. K. Chua, Z. L. Dong, Z. H. Liu, D. Q. Zhang, L. E. Loh, and S. L. Sing, "Review of selective laser melting: Materials and applications," *Applied Physics Reviews*, vol. 2, no. 4, p. 041101, 2015.

[155] Y. Hu, L. Zhang, W. Li, and G.-Z. Yang, "Design and Fabrication of a 3-D Printed Metallic Flexible Joint for Snake-Like Surgical Robot," *IEEE Robotics and Automation Letters*, vol. 4, no. 2, pp. 1557–1563, 2019.

[156] D. J. Abbott, C. Becke, R. I. Rothstein, and W. J. Peine, "Design of an endoluminal NOTES robotic system," in *2007 IEEE/RSJ International Conference on Intelligent Robots and Systems (IROS)*, 2007, pp. 410–416.

[157] P. Breedveld, J. Sheltes, E. M. Blom, and J. E. Verheij, "A new, easily miniaturized steerable endoscope," *IEEE Engineering in Medicine and Biology Magazine*, vol. 24, no. 6, pp. 40–47, 2005.

[158] P. J. Johnson, C. M. R. Serrano, M. Castro, R. Kuenzler, H. Choset, S. Tully, and U. Duvvuri, "Demonstration of transoral surgery in cadaveric specimens with the medrobotics flex system," *The Laryngoscope*, vol. 123, no. 5, pp. 1168–1172, 2013.

[159] H. M. Le, T. N. Do, and S. J. Phee, "A survey on actuators-driven surgical robots," *Sensors and Actuators A: Physical*, vol. 247, pp. 323–354, 2016.

[160] Y. Sun, Y. Liu, L. Xu, Y. Zou, A. Faragasso, and T. C. Lueth, "Automatic design of compliant surgical forceps with adaptive grasping

functions," *IEEE Robotics and Automation Letters*, vol. 5, no. 2, pp. 1095–1102, 2020.

[161] N. Morgan, "Medical shape memory alloy applications—the market and its products," *Materials Science and Engineering: A*, vol. 378, no. 1-2, pp. 16–23, 2004.

[162] D. Tarniţă, D. Tarniţă, N. Bîzdoacă, I. Mîndrilă, and M. Vasilescu, "Properties and medical applications of shape memory alloys," *Rom J Morphol Embryol*, vol. 50, no. 1, pp. 15–21, 2009.

[163] M. Salerno, K. Zhang, A. Menciassi, and J. S. Dai, "A novel 4-DOF origami grasper with an SMA-actuation system for minimally invasive surgery," *IEEE Transactions on Robotics*, vol. 32, no. 3, pp. 484–498, 2016.

[164] K. Kuribayashi, K. Tsuchiya, Z. You, D. Tomus, M. Umemoto, T. Ito, and M. Sasaki, "Self-deployable origami stent grafts as a biomedical application of Ni-rich TiNi shape memory alloy foil," *Materials Science and Engineering: A*, vol. 419, no. 1-2, pp. 131–137, 2006.

[165] A. J. Taylor, T. Slutzky, L. Feuerman, H. Ren, J. Tokuda, K. Nilsson, and Z. T. H. Tse, "MR-Conditional SMA-Based Origami Joint," *IEEE/ASME Transactions on Mechatronics*, vol. 24, no. 2, pp. 883–888, 2019.

[166] Y. Nakamura, A. Matsui, T. Saito, and K. Yoshimoto, "Shape-memory-alloy active forceps for laparoscopic surgery," in *Proceedings of 1995 IEEE International Conference on Robotics and Automation (ICRA)*, vol. 3, 1995, pp. 2320–2327.

[167] M. Zoppi, W. Sieklicki, and R. Molfino, "Design of a microrobotic wrist for needle laparoscopic surgery," *Journal of Mechanical Design*, vol. 130, no. 10, 2008.

[168] H. C. Liaw, B. Shirinzadeh, and J. Smith, "Robust adaptive motion tracking control of piezoelectric actuation systems for micro/nano manipulation," in *Proceedings 2007 IEEE International Conference on Robotics and Automation (ICRA)*, 2007, pp. 1110–1115.

[169] Y. Haddab, N. Chaillet, and A. Bourjault, “A microgripper using smart piezoelectric actuators,” in *Proceedings of 2000 IEEE/RSJ International Conference on Intelligent Robots and Systems (IROS)*, vol. 1, 2000, pp. 659–664.

[170] Q. Xu and K. K. Tan, *Advanced control of piezoelectric micro-/nano-positioning systems.* Springer, 2016.

[171] S. Krucinski, I. Vesely, M. Dokainish, and G. Campbell, “Numerical simulation of leaflet flexure in bioprosthetic valves mounted on rigid and expansile stents,” *Journal of Biomechanics*, vol. 26, no. 8, pp. 929–943, 1993.

[172] S. Yim and M. Sitti, “Design and analysis of a magnetically actuated and compliant capsule endoscopic robot,” in *2011 IEEE International Conference on Robotics and Automation (ICRA)*, 2011, pp. 4810–4815.

[173] M. Simi, N. Tolou, P. Valdastri, J. Herder, A. Menciassi, and P. Dario, “Modeling of a compliant joint in a magnetic levitation system for an endoscopic camera,” *Mechanical Sciences*, vol. 3, no. 1, 2012.

[174] C. Forbrigger, A. Lim, O. Onaizah, S. Salmanipour, T. Looi, J. Drake, and E. D. Diller, “Cable-less, magnetically driven forceps for minimally invasive surgery,” *IEEE Robotics and Automation Letters*, vol. 4, no. 2, pp. 1202–1207, 2019.

[175] A. De Greef, P. Lambert, and A. Delchambre, “Towards flexible medical instruments: Review of flexible fluidic actuators,” *Precision Engineering*, vol. 33, no. 4, pp. 311–321, 2009.

[176] J. Jovanova, A. Nastevska, M. Frecker, and M. E. Aguirre, “Analysis of a functionally graded compliant mechanism surgical grasper,” in *2018 International Conference on Reconfigurable Mechanisms and Robots (ReMAR)*, 2018, pp. 1–8.

[177] M. Aguirre, Á. T. Steinórsson, T. Horeman, and J. Herder, “Technology demonstrator for compliant statically balanced surgical graspers,” *Journal of Medical Devices*, vol. 9, no. 2, p. 020926, 2015.

[178] O. Piccin, N. Kumar, L. Meylheuc, L. Barbé, and B. Bayle, "Design, development and preliminary assessment of grasping devices for robotized medical applications," in *ASME 2012 International Design Engineering Technical Conferences and Computers and Information in Engineering Conference*, 2012, pp. 65–73.

[179] J. A. Cronin, M. I. Frecker, and A. Mathew, "Design of a compliant endoscopic suturing instrument," *Journal of Medical Devices*, vol. 2, no. 2, p. 025002, 2008.

[180] M. E. Aguirre and M. Frecker, "Design innovation size and shape optimization of a 1.0 mm multifunctional forceps-scissors surgical instrument," *Journal of Medical Devices*, vol. 2, no. 1, p. 015001, 2008.

[181] M. I. Frecker, K. M. Powell, and R. Haluck, "Design of a multifunctional compliant instrument for minimally invasive surgery," *Journal of Biomechanical Engineering*, vol. 127, no. 6, pp. 990–993, 2005.

[182] J. Arata, Y. Fujisawa, R. Nakadate, K. Kiguchi, K. Harada, M. Mitsuishi, and M. Hashizume, "Compliant four degree-of-freedom manipulator with locally deformable elastic elements for minimally invasive surgery," in *2019 International Conference on Robotics and Automation (ICRA)*, 2019, pp. 2663–2669.

[183] S. Awtar, T. T. Trutna, J. M. Nielsen, R. Abani, and J. Geiger, "Flexdex™: a minimally invasive surgical tool with enhanced dexterity and intuitive control," *Journal of Medical Devices*, vol. 4, no. 3, 2010.

[184] A. Gao, Y. Zhou, L. Cao, Z. Wang, and H. Liu, "Fiber bragg grating-based triaxial force sensor with parallel flexure hinges," *IEEE Transactions on Industrial Electronics*, vol. 65, no. 10, pp. 8215–8223, 2018.

[185] M. Turkseven and J. Ueda, "Analysis of an MRI compatible force sensor for sensitivity and precision," *IEEE Sensors Journal*, vol. 13, no. 2, pp. 476–486, 2012.

[186] T. Martin, U. Gengenbach, H. Guth, P. Ruther, O. Paul, and G. Bretthauer, "Silicon linkage with novel compliant mechanism for piezoelectric actuation of an intraocular implant," *Sensors and Actuators A: Physical*, vol. 188, pp. 335–341, 2012.

[187] H. C. Herrmann, N. Mankame, and G. K. Ananthasuresh, "Percutaneous heart valve," November 2009, US Patent 7,621,948.

[188] M. I. Frecker, R. Dziedzic, and R. Haluck, "Design of multifunctional compliant mechanisms for minimally invasive surgery," *Minimally Invasive Therapy & Allied Technologies*, vol. 11, no. 5-6, pp. 311–319, 2002.

[189] M. E. Aguirre and M. Frecker, "Design of a 1.0 mm multifunctional forceps-scissors instrument for minimally invasive surgery," in *ASME 2006 International Design Engineering Technical Conferences and Computers and Information in Engineering Conference*, 2006, pp. 557–563.

[190] L. George B and R. Bharanidaran, "A novel design of compliant forceps with serpentine flexures," *Australian Journal of Mechanical Engineering*, pp. 1–8, 2020.

[191] H. O'Hanley, M. Rosario, Y. Chen, A. Maertens, J. Walton, and J. Rosen, "Design and Testing of a Three Fingered Flexural Laparoscopic Grasper," *Journal of Medical Devices*, vol. 5, no. 2, 2011, p. 027508.

[192] M. E. Aguirre and M. Frecker, "Design and optimization of hybrid compliant narrow-gauge surgical forceps," in *ASME 2010 Conference on Smart Materials, Adaptive Structures and Intelligent Systems*, 2010, pp. 779–788.

[193] M. Aguirre, G. Hayes, R. Meirom, M. I. Frecker, C. Muhlstein, and J. H. Adair, "Optimal design and fabrication of narrow-gauge compliant forceps," *Journal of Mechanical Design*, vol. 133, no. 8, 2011.

[194] M. E. Aguirre and M. Frecker, "Design of a multi-contact-aided compliant mechanism," in *ASME 2011 International Design Engineering Technical Conferences and Computers and Information in Engineering Conference*, 2011, pp. 255–259.

[195] S. Canfield, B. Edinger, M. I. Frecker, and G. H. Koopmann, "Design of a piezoelectric inchworm actuator and compliant end effector for minimally invasive surgery," in *Smart Structures and Materials 1999:*

Smart Structures and Integrated Systems, vol. 3668. International Society for Optics and Photonics, 1999, pp. 835–843.

[196] S. Shuib, R. Yusoff, A. Hassan, M. Ridzwan, and M. Ibrahim, "A disposable compliant-forceps for hiv patients," *Journalof Medical Science*, vol. 7, no. 4, pp. 591–596, 2007.

[197] B. Gonenc, J. Handa, P. Gehlbach, R. H. Taylor, and I. Iordachita, "Design of 3-DOF force sensing micro-forceps for robot assisted vitreoretinal surgery," in *2013 35th Annual International Conference of the IEEE Engineering in Medicine and Biology Society (EMBC)*, 2013, pp. 5686–5689.

[198] M. Yang, K. M. Culkar, K. Powell, M. I. Frecker, and J. D. Zahn, "Design and fabrication of a UV-LIGA compliant micrograsper for ophthalmic surgery," in *ASME 2004 International Mechanical Engineering Congress and Exposition*, 2004, pp. 159–164.

[199] M. Goldfarb and N. Celanovic, "A flexure-based gripper for small-scale manipulation," *Robotica*, vol. 17, no. 2, pp. 181–187, 1999.

[200] G. Ramu and G. K. Ananthasuresh, "A flexure-based deployable stereo vision mechanism and temperature and force sensors for laparoscopic tools," in *Proceedings of the 14th National Conference on Machines and Mechanisms (NaCoMM)*, 2009.

[201] J. Peirs, D. Reynaerts, H. Van Brussel, G. De Gersem, and H.-W. Tang, "Design of an advanced tool guiding system for robotic surgery," in *2003 IEEE International Conference on Robotics and Automation (ICRA)*, vol. 2, 2003, pp. 2651–2656.

[202] Y. Kanada, T. Yoneyama, T. Watanabe, H. Kagawa, N. Sugiyama, K. Tanaka, and T. Hanyu, "Force feedback manipulating system for neurosurgery," *Procedia CIRP*, vol. 5, pp. 133–136, 2013.

[203] T. Kato, I. Okumura, H. Kose, K. Takagi, and N. Hata, "Extended kinematic mapping of tendon-driven continuum robot for neuroendoscopy," in *2014 IEEE/RSJ International Conference on Intelligent Robots and Systems (IROS)*, 2014, pp. 1997–2002.

[204] D. Wei, Y. Wenlong, H. Dawei, and D. Zhijiang, “Modeling of flexible arm with triangular notches for applications in single port access abdominal surgery,” in *2012 IEEE International Conference on Robotics and Biomimetics (ROBIO)*, 2012, pp. 588–593.

[205] Y. Wenlong, D. Wei, and D. Zhijiang, “Mechanics-based kinematic modeling of a continuum manipulator,” in *2013 IEEE/RSJ International Conference on Intelligent Robots and Systems (IROS)*, 2013, pp. 5052–5058.

[206] Z. Du, W. Yang, and W. Dong, “Kinematics modeling of a notched continuum manipulator,” *Journal of Mechanisms and Robotics*, vol. 7, no. 4, 2015.

[207] ——, “Kinematics modeling and performance optimization of a kinematic-mechanics coupled continuum manipulator,” *Mechatronics*, vol. 31, pp. 196–204, 2015.

[208] P. A. York, P. J. Swaney, H. B. Gilbert, and R. J. Webster, “A wrist for needle-sized surgical robots,” in *2015 IEEE International Conference on Robotics and Automation (ICRA)*, 2015, pp. 1776–1781.

[209] K. W. Eastwood, H. Azimian, B. Carrillo, T. Looi, H. E. Naguib, and J. M. Drake, “Kinetostatic design of asymmetric notch joints for surgical robots,” in *2016 IEEE/RSJ International Conference on Intelligent Robots and Systems (IROS)*, 2016, pp. 2381–2387.

[210] W. P. Liu, B. C. Lucas, K. Guerin, and E. Plaku, “Sensor and sampling-based motion planning for minimally invasive robotic exploration of osteolytic lesions,” in *2011 IEEE/RSJ International Conference on Intelligent Robots and Systems (IROS)*, 2011, pp. 1346–1352.

[211] R. J. Murphy, M. S. Moses, M. D. Kutzer, G. S. Chirikjian, and M. Armand, “Constrained workspace generation for snake-like manipulators with applications to minimally invasive surgery,” in *2013 IEEE International Conference on Robotics and Automation (ICRA)*, 2013, pp. 5341–5347.

[212] R. J. Murphy, M. D. Kutzer, S. M. Segreti, B. C. Lucas, and M. Armand, "Design and kinematic characterization of a surgical manipulator with a focus on treating osteolysis," *Robotica*, vol. 32, no. 6, pp. 835–850, 2014.

[213] M. S. Moses, R. J. Murphy, M. D. Kutzer, and M. Armand, "Modeling cable and guide channel interaction in a high-strength cable-driven continuum manipulator," *IEEE/ASME Transactions on Mechatronics*, vol. 20, no. 6, pp. 2876–2889, 2015.

[214] F. Alambeigi, R. J. Murphy, E. Basafa, R. H. Taylor, and M. Armand, "Control of the coupled motion of a 6 DoF robotic arm and a continuum manipulator for the treatment of pelvis osteolysis," in *2014 36th Annual International Conference of the IEEE Engineering in Medicine and Biology Society*, 2014, pp. 6521–6525.

[215] P. Wilkening, F. Alambeigi, R. J. Murphy, R. H. Taylor, and M. Armand, "Development and experimental evaluation of concurrent control of a robotic arm and continuum manipulator for osteolytic lesion treatment," *IEEE Robotics and Automation Letters*, vol. 2, no. 3, pp. 1625–1631, 2017.

[216] H. Liu, A. Farvardin, R. Grupp, R. J. Murphy, R. H. Taylor, I. Iordachita, and M. Armand, "Shape tracking of a dexterous continuum manipulator utilizing two large deflection shape sensors," *IEEE Sensors Journal*, vol. 15, no. 10, pp. 5494–5503, 2015.

[217] A. Gao, J. P. Carey, R. J. Murphy, I. Iordachita, R. H. Taylor, and M. Armand, "Progress toward robotic surgery of the lateral skull base: Integration of a dexterous continuum manipulator and flexible ring curette," in *2016 IEEE International Conference on Robotics and Automation (ICRA)*, 2016, pp. 4429–4435.

[218] S. Coemert, F. Alambeigi, A. Deguet, J. Carey, M. Armand, T. Lueth, and R. Taylor, "Integration of a snake-like dexterous manipulator for head and neck surgery with the da vinci research kit," in *Proc. Hamlyn Symp. Med. Robot.*, 2016, pp. 58–59.

[219] F. Alambeigi, Y. Wang, R. J. Murphy, I. Iordachita, and M. Armand, "Toward robot-assisted hard osteolytic lesion treatment using a con-

tinuum manipulator," in *2016 38th Annual International Conference of the IEEE Engineering in Medicine and Biology Society (EMBC)*, 2016, pp. 5103–5106.

[220] F. Alambeigi, S. Sefati, R. J. Murphy, I. Iordachita, and M. Armand, "Design and characterization of a debriding tool in robot-assisted treatment of osteolysis," in *2016 IEEE International Conference on Robotics and Automation (ICRA)*, 2016, pp. 5664–5669.

[221] F. Alambeigi, Y. Wang, S. Sefati, C. Gao, R. J. Murphy, I. Iordachita, R. H. Taylor, H. Khanuja, and M. Armand, "A curved-drilling approach in core decompression of the femoral head osteonecrosis using a continuum manipulator," *IEEE Robotics and Automation Letters*, vol. 2, no. 3, pp. 1480–1487, 2017.

[222] F. Alambeigi, M. Bakhtiarinejad, S. Sefati, R. Hegeman, I. Iordachita, H. Khanuja, and M. Armand, "On the use of a continuum manipulator and a bendable medical screw for minimally invasive interventions in orthopedic surgery," *IEEE Transactions on Medical Robotics and Bionics*, vol. 1, no. 1, pp. 14–21, 2019.

[223] P. E. Dupont, J. Lock, B. Itkowitz, and E. Butler, "Design and control of concentric-tube robots," *IEEE Transactions on Robotics*, vol. 26, no. 2, pp. 209–225, 2009.

[224] H. B. Gilbert, D. C. Rucker, and R. J. Webster III, "Concentric tube robots: The state of the art and future directions," in *Robotics Research*. Springer, 2016, pp. 253–269.

[225] H. Alfalahi, F. Renda, and C. Stefanini, "Concentric tube robots for minimally invasive surgery: Current applications and future opportunities," *IEEE Transactions on Medical Robotics and Bionics*, vol. 2, no. 3, pp. 410–424, 2020.

[226] J. Liu, B. Hall, M. Frecker, and E. W. Reutzel, "Compliant articulation structure using superelastic nitinol," *Smart Materials and Structures*, vol. 22, no. 9, p. 094018, 2013.

[227] J. Arata, S. Kogiso, M. Sakaguchi, R. Nakadate, S. Oguri, M. Uemura, C. Byunghyun, T. Akahoshi, T. Ikeda, and M. Hashizume,

"Articulated minimally invasive surgical instrument based on compliant mechanism," *International Journal of Computer Assisted Radiology and Surgery*, vol. 10, no. 11, pp. 1837–1843, 2015.

[228] Z. Wu, D. Bandara, K. Kiguchi, and J. Arata, "Design Strategy for a Surgical Manipulator based on a Compliant Mechanism: Rigidity and Range of Motion: Finding the Optimized Balance," in *2019 IEEE International Conference on Robotics and Biomimetics (ROBIO)*, 2019, pp. 2220–2224.

[229] B. W. Hanks, M. Frecker, and M. Moyer, "Design of a compliant endoscopic ultrasound-guided radiofrequency ablation probe," in *ASME 2016 International Design Engineering Technical Conferences and Computers and Information in Engineering Conference*, 2016.

[230] B. Hanks, M. Frecker, and M. Moyer, "Optimization of a compliant endoscopic radiofrequency ablation electrode," in *ASME 2017 International Design Engineering Technical Conferences and Computers and Information in Engineering Conference*, 2017.

[231] G. J. Tuijthof, J. L. Herder, C. N. van Dijk, and P. V. Pistecky, "A compliant instrument for arthroscopic joint fusion," in *ASME 2004 International Design Engineering Technical Conferences and Computers and Information in Engineering Conference*, 2004, pp. 397–405.

[232] T. Y. Nai, G. J. M. Tuijthof, and J. L. Herder, "Design of a compliant steerable arthroscopic punch," *Journal of Medical Devices*, vol. 4, p. 027525, 2010.

[233] T. Y. Nai, J. L. Herder, and G. J. Tuijthof, "Steerable mechanical joint for high load transmission in minimally invasive instruments," *Journal of Medical Devices*, vol. 5, no. 3, p. 034503, 2011.

[234] P. J. Swaney, J. Burgner, H. B. Gilbert, and R. J. Webster, "A flexure-based steerable needle: high curvature with reduced tissue damage," *IEEE Transactions on Biomedical Engineering*, vol. 60, no. 4, pp. 906–909, 2012.

[235] B. A. Salamon and A. Midha, "An Introduction to Mechanical Advantage in Compliant Mechanisms," *Journal of Mechanical Design*, vol. 120, no. 2, pp. 311–315, 06 1998.

[236] J. Herder and F. Van Den Berg, "Statically balanced compliant mechanisms (SBCM's), an example and prospects," in *Proceedings of the 26th ASME DETC Biennial, Mechanisms and Robotics Conference*, 2000.

[237] J. Drenth and J. L. Herder, "Numerical optimization of the design of a laparoscopic grasper, statically balanced with normal springs," in *ASME 2004 International Design Engineering Technical Conferences and Computers and Information in Engineering Conference*, 2004, pp. 923–933.

[238] K. M. Powell and M. I. Frecker, "Method for optimization of a nonlinear static balance mechanism with application to ophthalmic surgical forceps," in *ASME 2005 International Design Engineering Technical Conferences and Computers and Information in Engineering Conference*, 2005, pp. 441–447.

[239] K. Hoetmer, G. Woo, C. Kim, and J. Herder, "Negative stiffness building blocks for statically balanced compliant mechanisms: design and testing," *Journal of Mechanisms and Robotics*, vol. 2, no. 4, 2010.

[240] J. Lassooij, N. Tolou, G. Tortora, S. Caccavaro, A. Menciassi, and J. Herder, "A statically balanced and bi-stable compliant end effector combined with a laparoscopic 2DoF robotic arm," *Mechanical Sciences*, vol. 3, no. 2, pp. 85–93, 2012.

[241] A. Stapel and J. L. Herder, "Feasibility study of a fully compliant statically balanced laparoscopic grasper," in *ASME 2004 International Design Engineering Technical Conferences and Computers and Information in Engineering Conference*, 2004, pp. 635–643.

[242] A. N. Reddy, N. Maheshwari, D. K. Sahu, and G. K. Ananthasuresh, "Miniature compliant grippers with vision-based force sensing," *IEEE Transactions on Robotics*, vol. 26, no. 5, pp. 867–877, 2010.

[243] P. J. Berkelman, L. L. Whitcomb, R. H. Taylor, and P. Jensen, "A miniature microsurgical instrument tip force sensor for enhanced force feedback during robot-assisted manipulation," *IEEE Transactions on Robotics and Automation*, vol. 19, no. 5, pp. 917–921, 2003.

[244] U. Seibold, B. Kubler, and G. Hirzinger, "Prototype of instrument for minimally invasive surgery with 6-axis force sensing capability," in *Proceedings of the 2005 IEEE International Conference on Robotics and Automation (ICRA)*, 2005, pp. 496–501.

[245] M. Tada and T. Kanade, "An MR-compatible optical force sensor for human function modeling," in *International Conference on Medical Image Computing and Computer-Assisted Intervention.* Springer, 2004, pp. 129–136.

[246] T. Tokuno, M. Tada, and K. Umeda, "High-precision MRI-compatible force sensor with parallel plate structure," in *2008 2nd IEEE RAS & EMBS International Conference on Biomedical Robotics and Biomechatronics*, 2008, pp. 33–38.

[247] P. Puangmali, K. Althoefer, and L. D. Seneviratne, "Novel design of a 3-axis optical fiber force sensor for applications in magnetic resonance environments," in *2009 IEEE International Conference on Robotics and Automation (ICRA)*, 2009, pp. 3682–3687.

[248] H. Su and G. S. Fischer, "A 3-axis optical force/torque sensor for prostate needle placement in magnetic resonance imaging environments," in *2009 IEEE International Conference on Technologies for Practical Robot Applications*, 2009, pp. 5–9.

[249] S. K. Fifanski, J. L. Rivera Gutiérrez, M. Clogenson, C. Baur, A. Bertholds, P. Llosas, and S. Henein, "Flexure-based multi-degrees-of-freedom in-vivo force sensors for medical instruments," *Proceedings of Euspen 2016*, vol. 1, no. CONF, pp. 333–334, 2016.

[250] N. Kumar, O. Piccin, L. Meylheuc, L. Barbé, and B. Bayle, "Design, development and preliminary assessment of a force sensor for robotized medical applications," in *2014 IEEE/ASME International Conference on Advanced Intelligent Mechatronics*, 2014, pp. 1368–1374.

[251] G. Krishnan and G. K. Ananthasuresh, "Evaluation and design of displacement-amplifying compliant mechanisms for sensor applications," *Journal of Mechanical Design*, vol. 130, no. 10, 2008.

[252] M. Turkseven and J. Ueda, "Design of an MRI compatible haptic interface," in *2011 IEEE/RSJ International Conference on Intelligent Robots and Systems (IROS)*, 2011, pp. 2139–2144.

[253] S. Chakravarthy, M. V. Balakuntala, A. M. Rao, R. K. Thakur, and G. K. Ananthasuresh, "Development of an integrated haptic system for simulating upper gastrointestinal endoscopy," *Mechatronics*, vol. 56, pp. 115–131, 2018.

[254] E. Stratton, L. Howell, and A. Bowden, "Force-displacement model of the FlexSuRe™ spinal implant," in *ASME 2010 International Design Engineering Technical Conferences and Computers and Information in Engineering Conference*, 2010, pp. 37–46.

[255] Y. Chen, T. T. Zion, W. Wang, R. Y. Kwong, W. G. Stevenson, and E. J. Schmidt, "Intra-cardiac MR imaging & MR-tracking catheter for improved MR-guided EP," *Journal of Cardiovascular Magnetic Resonance*, vol. 17, no. 1, pp. 1–2, 2015.

[256] B. J. Edmondson, L. A. Bowen, C. L. Grames, S. P. Magleby, L. L. Howell, and T. C. Bateman, "Oriceps: Origami-inspired forceps," in *ASME 2013 conference on Smart Materials, Adaptive Structures and Intelligent Systems*, 2013.

[257] P. S. Gollnick, S. P. Magleby, and L. L. Howell, "An introduction to multilayer lamina emergent mechanisms," *Journal of Mechanical Design*, vol. 133, no. 8, 2011.

[258] Medgadget Inc., 10 March 2016, "Origami used to miniaturize, improve surgical tools, medical implants," accessed August 2020, https://www.medgadget.com/2016/03/origami-used-to-miniaturize-improve-surgical-tools-medical-implants.html.

[259] F. Bobbert, S. Janbaz, T. van Manen, Y. Li, and A. Zadpoor, "Russian doll deployable meta-implants: Fusion of kirigami, origami, and multi-stability," *Materials & Design*, p. 108624, 2020.

[260] T. G. Nelson, R. J. Lang, S. P. Magleby, and L. L. Howell, "Curved-folding-inspired deployable compliant rolling-contact element (D-CORE)," *Mechanism and Machine Theory*, vol. 96, pp. 225–238, 2016.

[261] L. Tang, Y. Chen, and X. He, "Multi-material compliant mechanism design and haptic evaluation," *Virtual and Physical Prototyping*, vol. 2, no. 3, pp. 155–160, 2007.

[262] R. M. Gouker, S. K. Gupta, H. A. Bruck, and T. Holzschuh, "Manufacturing of multi-material compliant mechanisms using multi-material molding," *The International Journal of Advanced Manufacturing Technology*, vol. 30, no. 11-12, pp. 1049–1075, 2006.

[263] D. E. Vogtmann, S. K. Gupta, and S. Bergbreiter, "Multi-material compliant mechanisms for mobile millirobots," in *2011 IEEE International Conference on Robotics and Automation (ICRA)*, 2011, pp. 3169–3174.

[264] C. Conlan-Smith, A. Bhattacharyya, and K. A. James, "Optimal design of compliant mechanisms using functionally graded materials," *Structural and Multidisciplinary Optimization*, vol. 57, no. 1, pp. 197–212, 2018.

[265] S. Akbari, A. H. Sakhaei, K. Kowsari, B. Yang, A. Serjouei, Z. Yuanfang, and Q. Ge, "Enhanced multimaterial 4d printing with active hinges," *Smart Materials and Structures*, vol. 27, no. 6, p. 065027, 2018.

[266] D. Rus and M. T. Tolley, "Design, fabrication and control of soft robots," *Nature*, vol. 521, no. 7553, pp. 467–475, 2015.

[267] J. Joo, S. Kota, and N. Kikuchi, "Large deformation behavior of compliant mechanisms," in *ASME 2001 Design Engineering Technical Conference and Computers and Information in Engineering Conference*, vol. 1, no. 2001, 2001, pp. 9–12.

[268] A. Saxena and G. K. Ananthasuresh, "Topology synthesis of compliant mechanisms for nonlinear force-deflection and curved path specifications," *Journal of Mechanical Design*, vol. 123, no. 1, pp. 33–42, 2001.

[269] J. Joo and S. Kota, "Topological synthesis of compliant mechanisms using nonlinear beam elements," *Mechanics Based Design of Structures and Machines*, vol. 32, no. 1, pp. 17–38, 2004.

[270] D. Jung and H. C. Gea, "Compliant mechanism design with nonlinear materials using topology optimization," *International Journal of Mechanics and materials in Design*, vol. 1, no. 2, pp. 157–171, 2004.

[271] G. Hao, J. Yu, and H. Li, "A brief review on nonlinear modeling methods and applications of compliant mechanisms," *Frontiers of Mechanical Engineering*, vol. 11, no. 2, pp. 119–128, 2016.

[272] S. Kota, "Compliant systems using monolithic mechanisms," *Smart Materials Bulletin*, vol. 2001, no. 3, pp. 7–10, 2001.

[273] M. C. Yip, S. G. Yuen, and R. D. Howe, "A robust uniaxial force sensor for minimally invasive surgery," *IEEE Transactions on Biomedical Engineering*, vol. 57, no. 5, pp. 1008–1011, 2010.

[274] G. S. Chirikjian and J. W. Burdick, "A hyper-redundant manipulator," *IEEE Robotics & Automation Magazine*, vol. 1, no. 4, pp. 22–29, 1994.

[275] V. Vitiello, S.-L. Lee, T. P. Cundy, and G.-Z. Yang, "Emerging robotic platforms for minimally invasive surgery," *IEEE Reviews in Biomedical Engineering*, vol. 6, pp. 111–126, 2012.

[276] C. Bergeles and G.-Z. Yang, "From passive tool holders to microsurgeons: safer, smaller, smarter surgical robots," *IEEE Transactions on Biomedical Engineering*, vol. 61, no. 5, pp. 1565–1576, 2013.

[277] P. Berthet-Rayne, G. Gras, K. Leibrandt, P. Wisanuvej, A. Schmitz, C. A. Seneci, and G.-Z. Yang, "The i 2 snake robotic platform for endoscopic surgery," *Annals of Biomedical Engineering*, vol. 46, no. 10, pp. 1663–1675, 2018.

[278] W. Saliba, J. E. Cummings, S. Oh, Y. Zhang, T. N. Mazgalev, R. A. Schweikert, J. D. Burkhardt, and A. Natale, "Novel robotic catheter

remote control system: feasibility and safety of transseptal puncture and endocardial catheter navigation," *Journal of Cardiovascular Electrophysiology*, vol. 17, no. 10, pp. 1102–1105, 2006.

[279] D. Thomas, E. P. Scholz, P. A. Schweizer, H. A. Katus, and R. Becker, "Initial experience with robotic navigation for catheter ablation of paroxysmal and persistent atrial fibrillation," *Journal of Electrocardiology*, vol. 45, no. 2, pp. 95–101, 2012.

[280] I. Pantos, G. Patatoukas, D. G. Katritsis, and E. Efstathopoulos, "Patient radiation doses in interventional cardiology procedures," *Current Cardiology Reviews*, vol. 5, no. 1, pp. 1–11, 2009.

[281] A. M. Kim, M. Turakhia, J. Lu, N. Badhwar, B. K. Lee, R. J. Lee, G. M. Marcus, Z. H. Tseng, M. Scheinman, and J. E. Olgin, "Impact of remote magnetic catheter navigation on ablation fluoroscopy and procedure time," *Pacing and Clinical Electrophysiology*, vol. 31, no. 11, pp. 1399–1404, 2008.

[282] J. A. Gallego and J. Herder, "Synthesis methods in compliant mechanisms: An overview," in *International Design Engineering Technical Conferences and Computers and Information in Engineering Conference*, vol. 49040, 2009, pp. 193–214.

[283] N. Lobontiu, *Compliant mechanisms: design of flexure hinges.* CRC press, 2002.

[284] L. Yin and G. K. Ananthasuresh, "Design of distributed compliant mechanisms," *Mechanics based design of structures and machines*, vol. 31, no. 2, pp. 151–179, 2003.

[285] Y.-J. Kim, S. Cheng, S. Kim, and K. Iagnemma, "Design of a tubular snake-like manipulator with stiffening capability by layer jamming," in *2012 IEEE/RSJ International Conference on Intelligent Robots and Systems*, 2012, pp. 4251–4256.

[286] F. Leong, N. Garbin, C. Di Natali, A. Mohammadi, D. Thiruchelvam, D. Oetomo, and P. Valdastri, "Magnetic surgical instruments for robotic abdominal surgery," *IEEE Reviews in Biomedical Engineering*, vol. 9, pp. 66–78, 2016.

[287] S. Ernst, F. Ouyang, C. Linder, K. Hertting, F. Stahl, J. Chun, H. Hachiya, D. Bansch, M. Antz, and K.-H. Kuck, "Initial experience with remote catheter ablation using a novel magnetic navigation system: magnetic remote catheter ablation," *Circulation*, vol. 109, no. 12, pp. 1472–1475, 2004.

[288] A. Arya, R. Zaker-Shahrak, P. Sommer, A. Bollmann, U. Wetzel, T. Gaspar, S. Richter, D. Husser, C. Piorkowski, and G. Hindricks, "Catheter ablation of atrial fibrillation using remote magnetic catheter navigation: a case–control study," *Europace*, vol. 13, no. 1, pp. 45–50, 2011.

[289] D. R. Davis, A. S. Tang, M. H. Gollob, R. Lemery, M. S. Green, and D. H. Birnie, "Remote magnetic navigation-assisted catheter ablation enhances catheter stability and ablation success with lower catheter temperatures," *Pacing and Clinical Electrophysiology*, vol. 31, no. 7, pp. 893–898, 2008.

[290] J. Edelmann, A. J. Petruska, and B. J. Nelson, "Magnetic control of continuum devices," *The International Journal of Robotics Research*, vol. 36, no. 1, pp. 68–85, 2017.

[291] K. J. Boskma, S. Scheggi, and S. Misra, "Closed-loop control of a magnetically-actuated catheter using two-dimensional ultrasound images," in *2016 6th IEEE International Conference on Biomedical Robotics and Biomechatronics (BioRob)*, 2016, pp. 61–66.

[292] V. N. Le, N. H. Nguyen, K. Alameh, R. Weerasooriya, and P. Pratten, "Accurate modeling and positioning of a magnetically controlled catheter tip," *Medical Physics*, vol. 43, no. 2, pp. 650–663, 2016.

[293] V. K. Venkiteswaran, J. Sikorski, and S. Misra, "Shape and contact force estimation of continuum manipulators using pseudo rigid body models," *Mechanism and Machine Theory*, vol. 139, pp. 34–45, 2019.

[294] T. Liu, N. Lombard Poirot, T. Greigarn, and M. Cenk Çavuşoğlu, "Design of a magnetic resonance imaging guided magnetically actuated steerable catheter," *Journal of Medical Devices*, vol. 11, no. 2, 2017.

[295] J. Sikorski, E. S. Rutting, and S. Misra, “Grasping using magnetically-actuated tentacle catheter: A proof-of-concept study,” in *2018 7th IEEE International Conference on Biomedical Robotics and Biomechatronics (BioRob)*, 2018, pp. 609–614.

[296] V. K. Venkiteswaran, L. F. P. Samaniego, J. Sikorski, and S. Misra, “Bio-inspired terrestrial motion of magnetic soft millirobots,” *IEEE Robotics and Automation Letters*, vol. 4, no. 2, pp. 1753–1759, 2019.

[297] ASM Aerospace Specification Metals Inc., “Titanium grade-2,” accessed March 2020, http://asm.matweb.com/search/SpecificMaterial.asp?bassnum=MTU020.

[298] T. L. Thomas, V. Kalpathy Venkiteswaran, G. K. Ananthasuresh, and S. Misra, “Surgical Applications of Compliant Mechanisms: A Review,” *Journal of Mechanisms and Robotics*, vol. 13, no. 2, 01 2021, 020801.

[299] D. Trivedi, A. Lotfi, and C. D. Rahn, “Geometrically exact dynamic models for soft robotic manipulators,” in *IEEE/RSJ International Conference on Intelligent Robots and Systems*, San Diego, CA, USA, Nov. 2007, pp. 1497–1502.

[300] T. Greigarn, R. Jackson, T. Liu, and M. C. Çavuşoğlu, “Experimental validation of the pseudo-rigid-body model of the mri-actuated catheter,” in *2017 IEEE International Conference on Robotics and Automation (ICRA)*, Singapore, Jun. 2017, pp. 3600–3605.

[301] B. S. Peters, P. R. Armijo, C. Krause, S. A. Choudhury, and D. Oleynikov, “Review of emerging surgical robotic technology,” *Surgical Endoscopy*, vol. 32, no. 4, pp. 1636–1655, 2018.

[302] L. B. Kratchman, T. L. Bruns, J. J. Abbott, and R. J. Webster, “Guiding elastic rods with a robot-manipulated magnet for medical applications,” *IEEE Transactions on Robotics*, vol. 33, no. 1, pp. 227–233, 2016.

[303] Y.-L. Park, S. Elayaperumal, B. Daniel, S. C. Ryu, M. Shin, J. Savall, R. J. Black, B. Moslehi, and M. R. Cutkosky, “Real-time estimation of 3-d needle shape and deflection for mri-guided interventions,”

IEEE/ASME Transactions On Mechatronics, vol. 15, no. 6, pp. 906–915, 2010.

[304] R. J. Roesthuis, M. Kemp, J. J. van den Dobbelsteen, and S. Misra, "Three-dimensional needle shape reconstruction using an array of fiber bragg grating sensors," *IEEE/ASME Transactions on Mechatronics*, vol. 19, no. 4, pp. 1115–1126, 2013.

[305] O. Al-Ahmad, M. Ourak, J. Van Roosbroeck, J. Vlekken, and E. Vander Poorten, "Improved fbg-based shape sensing methods for vascular catheterization treatment," *IEEE Robotics and Automation Letters*, vol. 5, no. 3, pp. 4687–4694, 2020.

[306] J. Sikorski, A. Denasi, G. Bucchi, S. Scheggi, and S. Misra, "Vision-based 3-d control of magnetically actuated catheter using bigmag—an array of mobile electromagnetic coils," *IEEE/ASME Transactions on Mechatronics*, vol. 24, no. 2, pp. 505–516, 2019.

[307] A. Denasi, F. Khan, K. J. Boskma, M. Kaya, C. Hennersperger, R. Göbl, M. Tirindelli, N. Navab, and S. Misra, "An observer-based fusion method using multicore optical shape sensors and ultrasound images for magnetically-actuated catheters," in *IEEE International Conference on Robotics and Automation (ICRA)*, Brisbane, QLD, Australia, May 2018, pp. 50–57.

[308] J. P. Den Hartog, *Advanced strength of materials.* Dover Publications, Inc., New York, USA, 1987.

[309] M. Richter, V. K. Venkiteswaran, and S. Misra, "Multi-point orientation control of discretely-magnetized continuum manipulators," *IEEE Robotics and Automation Letters*, vol. 6, no. 2, pp. 3607–3614, 2021.

[310] N. Shahriari, W. Heerink, T. Van Katwijk, E. Hekman, M. Oudkerk, and S. Misra, "Computed tomography (ct)-compatible remote center of motion needle steering robot: Fusing ct images and electromagnetic sensor data," *Medical Engineering & Physics*, vol. 45, pp. 71–77, 2017.

[311] M. Kaya, A. Denasi, S. Scheggi, E. Agbahca, C. Yoon, D. H. Gracias, and S. Misra, "A multi-rate state observer for visual tracking of

magnetic micro-agents using 2d slow medical imaging modalities," in *2018 IEEE/RSJ International Conference on Intelligent Robots and Systems (IROS)*, Madrid, Spain, October 2018, pp. 1–8.

[312] X. Hu, A. Chen, Y. Luo, C. Zhang, and E. Zhang, "Steerable catheters for minimally invasive surgery: a review and future directions," *Computer Assisted Surgery*, vol. 23, no. 1, pp. 21–41, 2018.

[313] F. H. Wittkampf, E. F. Wever, R. Derksen, H. Ramanna, R. N. Hauer, and E. O. R. de Medina, "Accuracy of the localisa system in catheter ablation procedures," *Journal of Electrocardiology*, vol. 32, pp. 7–12, 1999.

[314] F. Khan, D. Barrera, S. Sales, and S. Misra, "Curvature, twist and pose measurements using fiber bragg gratings in multi-core fiber: A comparative study between helical and straight core fibers," *Sensors and Actuators A: Physical*, vol. 317, p. 112442, 2021.

[315] P. E. Dupont, B. J. Nelson, M. Goldfarb, B. Hannaford, A. Menciassi, M. K. O'Malley, N. Simaan, P. Valdastri, and G.-Z. Yang, "A decade retrospective of medical robotics research from 2010 to 2020," *Science Robotics*, vol. 6, no. 60, 2021.

[316] R. V. Martinez, J. L. Branch, C. R. Fish, L. Jin, R. F. Shepherd, R. M. D. Nunes, Z. Suo, and G. M. Whitesides, "Robotic tentacles with three-dimensional mobility based on flexible elastomers," *Advanced materials*, vol. 25, no. 2, pp. 205–212, 2013.

[317] J. C. Norton, P. R. Slawinski, H. S. Lay, J. W. Martin, B. F. Cox, G. Cummins, M. P. Desmulliez, R. E. Clutton, K. L. Obstein, S. Cochran, and P. Valdastri, "Intelligent magnetic manipulation for gastrointestinal ultrasound," *Science Robotics*, vol. 4, no. 31, pp. 1–14, 2019.

[318] T. da Veiga, J. H. Chandler, P. Lloyd, G. Pittiglio, N. J. Wilkinson, A. K. Hoshiar, R. A. Harris, and P. Valdastri, "Challenges of continuum robots in clinical context: a review," *Progress in Biomedical Engineering*, vol. 2, no. 3, Aug 2020.

[319] R. Zhao, Y. Kim, S. A. Chester, P. Sharma, and X. Zhao, "Mechanics of hard-magnetic soft materials," *Journal of the Mechanics and Physics of Solids*, vol. 124, pp. 244–263, 2019.

[320] Y. Kim and X. Zhao, "Magnetic soft materials and robots," *Chemical Reviews*, vol. 122, no. 5, pp. 5317–5364, 2022.

[321] E. Diller, J. Zhuang, G. Zhan Lum, M. R. Edwards, and M. Sitti, "Continuously distributed magnetization profile for millimeter-scale elastomeric undulatory swimming," *Applied Physics Letters*, vol. 104, no. 17, p. 174101, 2014.

[322] G. Z. Lum, Z. Ye, X. Dong, H. Marvi, O. Erin, W. Hu, and M. Sitti, "Shape-programmable magnetic soft matter," *Proceedings of the National Academy of Sciences*, vol. 113, no. 41, pp. E6007–E6015, 2016.

[323] G. Pittiglio, P. Lloyd, T. da Veiga, O. Onaizah, C. Pompili, J. Chandler, and P. Valdastri, "Patient-specific magnetic catheters for atraumatic autonomous endoscopy," *Soft Robotics*, 2022.

[324] P. Lloyd, O. Onaizah, G. Pittiglio, D. K. Vithanage, J. H. Chandler, and P. Valdastri, "Magnetic soft continuum robots with braided reinforcement," *IEEE Robotics and Automation Letters*, vol. 7, no. 4, pp. 9770–9777, 2022.

[325] J. Zhang, O. Onaizah, K. Middleton, L. You, and E. Diller, "Reliable grasping of three-dimensional untethered mobile magnetic microgripper for autonomous pick-and-place," *IEEE Robotics and Automation Letters*, vol. 2, no. 2, pp. 835–840, 2017.

[326] T. L. Thomas, V. Kalpathy Venkiteswaran, G. K. Ananthasuresh, and S. Misra, "Surgical Applications of Compliant Mechanisms: A Review," *Journal of Mechanisms and Robotics*, vol. 13, no. 2, 01 2021.

[327] Y. Piskarev, J. Shintake, C. Chautems, J. Lussi, Q. Boehler, B. Nelson, and D. Floreano, "A variable stiffness magnetic catheter made of a conductive phase-change polymer for minimally invasive surgery," *Advanced Functional Materials*, vol. 32, 05 2022.

[328] L. Blanc, A. Delchambre, and P. Lambert, “Flexible medical devices: Review of controllable stiffness solutions,” *Actuators*, vol. 6, no. 3, 2017.

[329] M. Manti, V. Cacucciolo, and M. Cianchetti, “Stiffening in soft robotics: A review of the state of the art,” *IEEE Robotics and Automation Magazine*, vol. 23, no. 3, pp. 93–106, 2016.

[330] Y. Dong, L. Wang, N. Xia, Z. Yang, C. Zhang, C. Pan, D. Jin, J. Zhang, C. Majidi, and L. Zhang, “Untethered small-scale magnetic soft robot with programmable magnetization and integrated multifunctional modules,” *Science Advances*, vol. 8, no. 25, 2022.

[331] S. Miyashita, S. Guitron, K. Yoshida, S. Li, D. D. Damian, and D. Rus, “Ingestible, controllable, and degradable origami robot for patching stomach wounds,” in *2016 IEEE International Conference on Robotics and Automation (ICRA)*, 2016, pp. 909–916.

[332] T. Xu, J. Zhang, M. Salehizadeh, O. Onaizah, and E. Diller, “Millimeter-scale flexible robots with programmable three-dimensional magnetization and motions,” *Science Robotics*, vol. 4, no. 29, 2019.

[333] V. Kalpathy Venkiteswaran, J. Sikorski, and S. Misra, “Shape and contact force estimation of continuum manipulators using pseudo rigid body models,” *Mechanism and Machine Theory*, vol. 139, pp. 34–45, 2019.

[334] P. Lloyd, G. Pittiglio, J. H. Chandler, and P. Valdastri, “Optimal design of soft continuum magnetic robots under follow-the-leader shape forming actuation,” in *2020 International Symposium on Medical Robotics (ISMR)*, 2020, pp. 111–117.

[335] T. Da Veiga, J. H. Chandler, G. Pittiglio, P. Lloyd, M. Holdar, O. Onaizah, A. Alazmani, and P. Valdastri, “Material characterization for magnetic soft robots,” in *IEEE 4th International Conference on Soft Robotics (RoboSoft)*, 2021, pp. 335–342.

[336] P. Lee, Y. Chen, J. Hu, and C. Chang, “Comparison of mechanical stability of elastic titanium, nickel-titanium, and stainless steel nails

used in the fixation of diaphyseal long bone fractures," *Materials*, vol. 11, pp. 1–11, 11 2018.

[337] T. L. Thomas, J. Sikorski, G. K. Ananthasuresh, V. K. Venkiteswaran, and S. Misra, "Design, sensing, and control of a magnetic compliant continuum manipulator," *IEEE Transactions on Medical Robotics and Bionics*, vol. 4, no. 4, pp. 910–921, 2022.

[338] T. L. Bruns, K. E. Riojas, D. S. Ropella, M. S. Cavilla, A. J. Petruska, M. H. Freeman, R. F. Labadie, J. J. Abbott, and R. J. Webster, "Magnetically steered robotic insertion of cochlear-implant electrode arrays: System integration and first-in-cadaver results," *IEEE Robotics and Automation letters*, vol. 5, no. 2, pp. 2240–2247, 2020.

[339] I. D. Walker, H. Choset, and G. S. Chirikjian, "Snake-like and continuum robots," in *Springer handbook of robotics.* Springer, 2016, pp. 481–498.

[340] X. Chen, X. Zhang, Y. Huang, L. Cao, and J. Liu, "A review of soft manipulator research, applications, and opportunities," *Journal of Field Robotics*, vol. 39, no. 3, pp. 281–311, 2022.

[341] S. Wu, W. Hu, Q. Ze, M. Sitti, and R. Zhao, "Multifunctional magnetic soft composites: A review," *Multifunctional Materials*, vol. 3, no. 4, p. 042003, 2020.

[342] M. Richter, M. Kaya, J. Sikorski, L. Abelmann, V. K. Venkiteswaran, and S. Misra, "Magnetic soft helical manipulators with local dipole interactions for flexibility and forces," *Soft Robotics*, 2023.

[343] M. Brancadoro, M. Manti, F. Grani, S. Tognarelli, A. Menciassi, and M. Cianchetti, "Toward a variable stiffness surgical manipulator based on fiber jamming transition," *Frontiers in Robotics and AI*, vol. 6, p. 12, 2019.

[344] D. S. Shah, E. J. Yang, M. C. Yuen, E. C. Huang, and R. Kramer-Bottiglio, "Jamming skins that control system rigidity from the surface," *Advanced Functional Materials*, vol. 31, no. 1, p. 2006915, 2021.

[345] M. E. Giannaccini, C. Xiang, A. Atyabi, T. Theodoridis, S. Nefti-Meziani, and S. Davis, "Novel design of a soft lightweight pneumatic

continuum robot arm with decoupled variable stiffness and positioning," *Soft Robotics*, vol. 5, pp. 54 – 70, 2018.

[346] J. Zhu, L. Lyu, Y. Xu, H. Liang, X. Zhang, H. Ding, and Z. Wu, "Intelligent soft surgical robots for next-generation minimally invasive surgery," *Advanced Intelligent Systems*, vol. 3, no. 5, p. 2100011, 2021.

[347] F. Alambeigi, R. Seifabadi, and M. Armand, "A continuum manipulator with phase changing alloy," in *2016 IEEE International Conference on Robotics and Automation (ICRA)*, 2016, pp. 758–764.

[348] M. Mattmann, C. De Marco, F. Briatico, S. Tagliabue, A. Colusso, X.-Z. Chen, J. Lussi, C. Chautems, S. Pané, and B. Nelson, "Thermoset shape memory polymer variable stiffness 4d robotic catheters," *Advanced Science*, vol. 9, no. 1, p. 2103277, 2022.

[349] H. Jeon, Q. N. Le, S. Jeong, S. Jang, H. Jung, H. Chang, H. J. Pandya, and Y. Kim, "Towards a snake-like flexible robot with variable stiffness using an sma spring-based friction change mechanism," *IEEE Robotics and Automation Letters*, vol. 7, no. 3, pp. 6582–6589, 2022.

[350] Y. Cao, F. Ju, L. Zhang, D. Bai, F. Qi, and B. Chen, "A novel variable-stiffness flexible manipulator actuated by shape memory alloy for minimally invasive surgery," *Proceedings of the Institution of Mechanical Engineers, Part H: Journal of Engineering in Medicine*, vol. 232, no. 11, pp. 1098–1110, 2018.

[351] S. Jiang, B. Chen, F. Qi, Y. Cao, F. Ju, D. Bai, and Y. Wang, "A variable-stiffness continuum manipulators by an sma-based sheath in minimally invasive surgery," *The International Journal of Medical Robotics and Computer Assisted Surgery*, vol. 16, no. 2, p. e2081, 2020.

[352] M. C. Yuen, R. A. Bilodeau, and R. K. Kramer, "Active variable stiffness fibers for multifunctional robotic fabrics," *IEEE Robotics and Automation Letters*, vol. 1, no. 2, pp. 708–715, 2016.

[353] A. Lendlein and O. E. Gould, "Reprogrammable recovery and actuation behaviour of shape-memory polymers," *Nature Reviews Materials*, vol. 4, no. 2, pp. 116–133, 2019.

[354] K. Wang, Y.-G. Jia, C. Zhao, and X. Zhu, "Multiple and two-way reversible shape memory polymers: Design strategies and applications," *Progress in Materials Science*, vol. 105, p. 100572, 2019.

[355] SMP Technologies Inc., accessed December 2022, "Elastic modulus and temperature plot of shape memory polymers," http://www.smptechno.com/index_en.html.

[356] H. Tobushi, D. Shimada, S. Hayashi, and M. Endo, "Shape fixity and shape recovery of polyurethane shape-memory polymer foams," *Proceedings of the Institution of Mechanical Engineers, Part L: Journal of Materials: Design and Applications*, vol. 217, no. 2, pp. 135–143, 2003.

[357] W. Small IV, T. S. Wilson, W. J. Benett, J. M. Loge, and D. J. Maitland, "Laser-activated shape memory polymer intravascular thrombectomy device," *Optics Express*, vol. 13, no. 20, pp. 8204–8213, 2005.

[358] A. M. Wahl, *Mechanical Springs.* Penton Publishing Company, Cleveland, Ohio, 1944.

[359] X.-j. Li, J. Yang, B.-q. Yan, and X. Zheng, "Insulated cable temperature calculation and numerical simulation," in *MATEC Web of Conferences*, vol. 175. EDP Sciences, 2018, p. 03014.

[360] P. S. Yarmolenko, E. J. Moon, C. Landon, A. Manzoor, D. W. Hochman, B. L. Viglianti, and M. W. Dewhirst, "Thresholds for thermal damage to normal tissues: an update," *International Journal of Hyperthermia*, vol. 27, no. 4, pp. 320–343, 2011.

[361] M. D. Hager, S. Bode, C. Weber, and U. S. Schubert, "Shape memory polymers: Past, present and future developments," *Progress in Polymer Science*, vol. 49, pp. 3–33, 2015.

[362] H. Koerner, R. J. Strong, M. L. Smith, D. H. Wang, L.-S. Tan, K. M. Lee, T. J. White, and R. A. Vaia, "Polymer design for high temperature shape memory: Low crosslink density polyimides," *Polymer*, vol. 54, no. 1, pp. 391–402, 2013.

[363] A. Alteheld, Y. Feng, S. Kelch, and A. Lendlein, "Biodegradable, amorphous copolyester-urethane networks having shape-memory properties," *Angewandte Chemie International Edition*, vol. 44, no. 8, pp. 1188–1192, 2005.

[364] M. Hallissey, W. Allum, A. Jewkes, D. Ellis, and J. Fielding, "Early detection of gastric cancer." *British Medical Journal*, vol. 301, no. 6751, pp. 513–515, 1990.

[365] J. Delaey, P. Dubruel, and S. Van Vlierberghe, "Shape-memory polymers for biomedical applications," *Advanced Functional Materials*, vol. 30, no. 44, p. 1909047, 2020.

[366] G. Baer, T. Wilson, D. Matthews, and D. Maitland, "Shape-memory behavior of thermally stimulated polyurethane for medical applications," *Journal of Applied Polymer Science*, vol. 103, no. 6, pp. 3882–3892, 2007.

[367] C. Chautems, S. Lyttle, Q. Boehler, and B. J. Nelson, "Design and evaluation of a steerable magnetic sheath for cardiac ablations," *IEEE Robotics and Automation Letters*, vol. 3, no. 3, pp. 2123–2128, 2018.

[368] W. Small IV, P. Singhal, T. S. Wilson, and D. J. Maitland, "Biomedical applications of thermally activated shape memory polymers," *Journal of Materials Chemistry*, vol. 20, no. 17, pp. 3356–3366, 2010.

[369] P. Lloyd, O. Onaizah, G. Pittiglio, D. K. Vithanage, J. H. Chandler, and P. Valdastri, "Magnetic soft continuum robots with braided reinforcement," *IEEE Robotics and Automation Letters*, vol. 7, no. 4, pp. 9770–9777, 2022.

[370] Y. Feng, M. Bodaghi, and W. Liao, "Numerical/experimental assessment of 3d-printed shape-memory polymeric beams," *Journal of Applied Polymer Science*, vol. 136, no. 16, p. 47422, 2019.

[371] J. Sikorski, C. M. Heunis, F. Franco, and S. Misra, "The armm system: An optimized mobile electromagnetic coil for non-linear actuation of flexible surgical instruments," *IEEE Transactions on Magnetics*, vol. 55, no. 9, pp. 1–9, 2019.

[372] L. Yang, X. Du, E. Yu, D. Jin, and L. Zhang, "Deltamag: An electromagnetic manipulation system with parallel mobile coils," in *2019 International Conference on Robotics and Automation (ICRA)*, 2019, pp. 9814–9820.

[373] C. Kim, S. C. Ryu, and P. E. Dupont, "Real-time adaptive kinematic model estimation of concentric tube robots," in *2015 IEEE/RSJ International Conference on Intelligent Robots and Systems (IROS)*, 2015, pp. 3214–3219.

[374] T. George Thuruthel, E. Falotico, M. Manti, A. Pratesi, M. Cianchetti, and C. Laschi, "Learning closed loop kinematic controllers for continuum manipulators in unstructured environments," *Soft Robotics*, vol. 4, no. 3, pp. 285–296, 2017.

[375] Y. Fei and H. Xu, "Modeling and motion control of a soft robot," *IEEE Transactions on Industrial Electronics*, vol. 64, no. 2, pp. 1737–1742, 2016.

[376] O. Kaya, M. C. Yildirim, N. Kuzuluk, E. Cicek, O. Bebek, E. Oztop, and B. Ugurlu, "Environmental force estimation for a robotic hand: Compliant contact detection," in *2015 IEEE-RAS 15th International Conference on Humanoid Robots (Humanoids)*, 2015, pp. 791–796.

[377] M. Behl and A. Lendlein, "Shape-memory polymers," *Materials today*, vol. 10, no. 4, pp. 20–28, 2007.

[378] O. Erin, D. Antonelli, M. E. Tiryaki, and M. Sitti, "Towards 5-dof control of an untethered magnetic millirobot via mri gradient coils," in *2020 IEEE International Conference on Robotics and Automation (ICRA)*, 2020, pp. 6551–6557.

[379] A. J. A. de Oliveira, J. Batista, S. Misra, and V. K. Venkiteswaran, "Ultrasound tracking and closed-loop control of a magnetically-actuated biomimetic soft robot," in *2022 IEEE/RSJ International Conference on Intelligent Robots and Systems (IROS)*, 2022, pp. 3422–3428.

[380] A. Vandini, A. Salerno, C. J. Payne, and G.-Z. Yang, "Vision-based motion control of a flexible robot for surgical applications," in *2014*

IEEE International Conference on Robotics and Automation (ICRA), 2014, pp. 6205–6211.

[381] C. Pacchierotti, M. Abayazid, S. Misra, and D. Prattichizzo, "Teleoperation of steerable flexible needles by combining kinesthetic and vibratory feedback," *IEEE Transactions on Haptics*, vol. 7, no. 4, pp. 551–556, 2014.

[382] REGULATION (EU) 2017/745 OF THE EUROPEAN PARLIAMENT AND OF THE COUNCIL, accessed March 2023, "Regulations," https://eur-lex.europa.eu/legal-content/EN/TXT/PDF/?uri=CELEX:32017R0745.

[383] R. M. Murray, Z. Li, and S. S. Sastry, *A mathematical introduction to robotic manipulation.* CRC press, Florida, USA, 1994.

IV

Appendices

A

Supplementary information for Magnetic Compliant Continuum Manipulator

A.1 Load Capacity

The distal force-bearing capacity of the manipulator is calculated in this section by considering three different loading conditions during bending, extension and compression.

A.1.1 Bending bearing load

In this case, the manipulator is subjected to bending. If we consider the sectional view of one segment of the manipulator as shown in Fig. A.1, one half of the rigid tube is approximated to have a semi-cylindrical cross-section. When the manipulator is bent to its maximum, each section is subjected to a force (F_{bend}) at its end due to contact with the next segment. The bending bearing load will be the maximum value of F_{bend} before failure. For the semi-cylindrical cross-section, the centroid ($\bar{y}$) and second moment of area (I) are given by,

$$\bar{y} = \frac{\int_0^R y dA}{\int_0^R dA}, \tag{A.1}$$

$$I = \int_0^R y^2 dA, \tag{A.2}$$

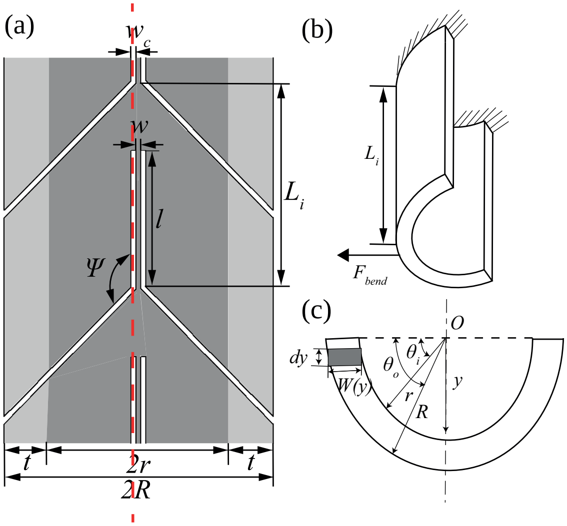

Figure A.1: (a) Section view of one segment of the manipulator with a cut made perpendicular to its plane along the red line (b) One half of the cut section of the segment (c) Semi-cylindrical cross-section of the cut segment.

where $dA = W(y)dy = (R\cos\theta_o - r\cos\theta_i)dy$; $\sin\theta_o = y/R$; $\sin\theta_i = y/r$; R = 1.5 mm; r = 1 mm. Substituting these values to (A.1) and (A.2) gives,

$$\bar{y} = \frac{\left(\int_0^R yR\sqrt{1-\frac{y^2}{R^2}} - \int_0^r yr\sqrt{1-\frac{y^2}{r^2}}\right)dy}{\left(\int_0^R R\sqrt{1-\frac{y^2}{R^2}} - \int_0^r r\sqrt{1-\frac{y^2}{r^2}}\right)dy} = \frac{4(R^2+Rr+r^2)}{3\pi(R+r)}, \quad (A.3)$$

$$I = \int_0^R y^2 R\sqrt{1-\frac{y^2}{R^2}}dy - \int_0^r y^2 r\sqrt{1-\frac{y^2}{r^2}}dy = \frac{\pi(R^4-r^4)}{16}. \quad (A.4)$$

The bending bearing load is given by,

$$F_{bend} = \frac{\sigma_y I}{L_i \bar{y}}. \quad (A.5)$$

where σ_y = 345 MPa, is the yield strength of titanium. Substituting other parameters, we get the bending loads for the three designs as follows: F^A_{bend} = 151.67 N; F^B_{bend} = 151.67 N; F^C_{bend} = 206.83 N.

A.1.2 Extension bearing load

In this case, the manipulator is subjected to an extension load which is carried by the flexures. Therefore, the extension bearing load is given by,

$$F_{ext} = \sigma_y A. \tag{A.6}$$

Where $A = 2wt = 2w(R - r)$, is the cross sectional area of the two flexures in a segment. Substituting other parameters, we get the extension bearing loads for the three designs as follows: F^A_{ext} = 13.80 N; F^B_{ext} = 22.42 N; F^C_{ext} = 10.35 N.

A.1.3 Compression bearing load

In this case, the manipulator is under compression and the critical load to be calculated is the buckling load (P_{cr}) which is given by the Euler's formula as

$$F_{comp} = P_{cr} = \frac{\pi^2 EI}{l^2} = \frac{\pi^2 E w^3 t}{12 l^2}. \tag{A.7}$$

Substituting other parameters, we get the compression bearing loads for the three designs as follows: F^A_{comp} = 2.45 N; F^B_{comp} = 10.54 N; F^C_{comp} = 1.92 N.

A.2 Spatial Manipulator Jacobian Calculation

This section presents the procedure to calculate the spatial manipulator Jacobian for the rigid-body model of the manipulator described in Section III-A. Each spherical joint (i) undergoes three angular deformations: β_i, γ_i and α_i. Assuming the transformation matrix ($\mathbf{T}_i^{i+1}$) from joint (i) to joint ($i+1$) is defined as

$$\mathbf{T}_i^{i+1} = \begin{bmatrix} \mathrm{c}_{\beta_i}\mathrm{c}_{\gamma_i} & \mathrm{s}_{\alpha_i}\mathrm{s}_{\beta_i} - \mathrm{c}_{\alpha_i}\mathrm{c}_{\beta_i}\mathrm{s}_{\gamma_i} & \mathrm{c}_{\alpha_i}\mathrm{s}_{\beta_i} + \mathrm{c}_{\beta_i}\mathrm{s}_{\alpha_i}\mathrm{s}_{\gamma_i} & l_i\mathrm{c}_{\beta_i}\mathrm{c}_{\gamma_i} \\ \mathrm{s}_{\gamma_i} & \mathrm{c}_{\alpha_i}\mathrm{c}_{\gamma_i} & -\mathrm{c}_{\gamma_i}\mathrm{s}_{\alpha_i} & l_i\mathrm{s}_{\gamma_i} \\ -\mathrm{c}_{\gamma_i}\mathrm{s}_{\beta_i} & \mathrm{c}_{\beta_i}\mathrm{s}_{\alpha_i} + \mathrm{c}_{\alpha_i}\mathrm{s}_{\beta_i}\mathrm{s}_{\gamma_i} & \mathrm{c}_{\alpha_i}\mathrm{c}_{\beta_i} - \mathrm{s}_{\alpha_i}\mathrm{s}_{\beta_i}\mathrm{s}_{\gamma_i} & -l_i\mathrm{c}_{\gamma_i}\mathrm{s}_{\beta_i} \\ 0 & 0 & 0 & 1 \end{bmatrix}^T, \tag{A.8}$$

where c_* and s_* represent the cosine and sine of angle (*). Note that the first link (l_1) is rigidly attached to the base frame at point ($\mathbf{r}_1$), hence $\beta_1 = \gamma_1 = \alpha_1 = 0$. The position coordinates of each joint (i) are computed as

$$\begin{bmatrix} \mathbf{r}_i \\ 1 \end{bmatrix} = \prod_{j=1}^{i-1} \mathbf{T}_j^{j+1} . \begin{bmatrix} \mathbf{r}_1 \\ 1 \end{bmatrix}^T, \tag{A.9}$$

The position vector ($p_* \in \mathbb{R}^3$) and the rotation axis ($\omega_* \in \mathbb{R}^3$) of spherical joint ($i$) are given by

$$\mathbf{p}_{\beta_i} = \begin{bmatrix} l_{i-1} & 0 & 0 \end{bmatrix}^T, \mathbf{p}_{\gamma_i} = \begin{bmatrix} 0 & 0 & 0 \end{bmatrix}^T, \mathbf{p}_{\alpha_i} = \begin{bmatrix} 0 & 0 & 0 \end{bmatrix}^T. \quad \text{(A.10)}$$

$$\boldsymbol{\omega}_{\beta_i} = \begin{bmatrix} 0 & 1 & 0 \end{bmatrix}^T, \boldsymbol{\omega}_{\gamma_i} = \begin{bmatrix} 0 & 0 & 1 \end{bmatrix}^T, \boldsymbol{\omega}_{\alpha_i} = \begin{bmatrix} 1 & 0 & 0 \end{bmatrix}^T. \quad \text{(A.11)}$$

The geometric twist between two successive DoFs is calculated using the above equations as follows

$$\boldsymbol{\xi}_{\beta_i} = \begin{bmatrix} \mathbf{p}_{\beta_i} \times \boldsymbol{\omega}_{\beta_i} \\ \boldsymbol{\omega}_{\beta_i} \end{bmatrix}^T = \begin{bmatrix} 0 & 0 & l_{i-1} & 0 & 1 & 0 \end{bmatrix}^T, \quad \text{(A.12a)}$$

$$\boldsymbol{\xi}_{\gamma_i} = \begin{bmatrix} \mathbf{p}_{\gamma_i} \times \boldsymbol{\omega}_{\gamma_i} \\ \boldsymbol{\omega}_{\gamma_i} \end{bmatrix}^T = \begin{bmatrix} 0 & 0 & 0 & 0 & 0 & 1 \end{bmatrix}^T, \quad \text{(A.12b)}$$

$$\boldsymbol{\xi}_{\alpha_i} = \begin{bmatrix} \mathbf{p}_{\alpha_i} \times \boldsymbol{\omega}_{\alpha_i} \\ \boldsymbol{\omega}_{\alpha_i} \end{bmatrix}^T = \begin{bmatrix} 0 & 0 & 0 & 1 & 0 & 0 \end{bmatrix}^T. \quad \text{(A.12c)}$$

The spatial manipulator Jacobian ($\mathbf{J}_{\boldsymbol{\Theta}} \in \mathbb{R}^{6\times 6}$) is computed using the set of angles ($\boldsymbol{\Theta} \in \mathbb{S}^6$) that describe the configuration of the rigid-body model as follows

$$\boldsymbol{\Theta} = \begin{bmatrix} \beta_2 & \gamma_2 & \alpha_2 & \beta_3 & \gamma_3 & \alpha_3 \end{bmatrix}^T, \quad \text{(A.13)}$$

$$\mathbf{J}_{\boldsymbol{\Theta}} = \begin{bmatrix} \boldsymbol{\xi}'_{\beta_2} & \boldsymbol{\xi}'_{\gamma_2} & \boldsymbol{\xi}'_{\alpha_2} & \boldsymbol{\xi}'_{\beta_3} & \boldsymbol{\xi}'_{\gamma_3} & \boldsymbol{\xi}'_{\alpha_3} \end{bmatrix}, \quad \text{(A.14)}$$

with

$$\boldsymbol{\xi}'_{\beta_i} = \mathrm{Ad}\left(\mathbf{T}_1^2 \dots \mathbf{T}_{i-2}^{i-1}\big|_{l_{i-1}=0}\right) \boldsymbol{\xi}_{\beta_i}, \quad \text{(A.15a)}$$

$$\boldsymbol{\xi}'_{\gamma_i} = \mathrm{Ad}\left(\mathbf{T}_1^2 \dots \mathbf{T}_{i-1}^{i}\big|_{l_i=0,\gamma_i=0}\right) \boldsymbol{\xi}_{\gamma_i}, \quad \text{(A.15b)}$$

$$\boldsymbol{\xi}'_{\alpha_i} = \mathrm{Ad}\left(\mathbf{T}_1^2 \dots \mathbf{T}_{i-1}^{i}\big|_{l_i=0,\alpha_i=0}\right) \boldsymbol{\xi}_{\alpha_i}, \quad \text{(A.15c)}$$

where $\mathrm{Ad}(\mathbf{T})$ is the adjoint transformation of transformation matrix $\mathbf{T}$. The details of the above derivation can be found in [383].

A.3 Observer-based Fusion Derivation

A simplified kinematics-based model is developed with a disturbance term. Furthermore, it is assumed that the dynamics of the manipulator can be approximated by a linear time-invariant model. More information on the formulation of the system dynamics and the disturbance dynamics can be found in the work by Denasi *et al.* [307]. The Kalman filter uses the model with a suitable update term to estimate state variables that cannot be measured. The Kalman filter has two phases at each sampling loop: prediction and update. Prediction is applied on the augmented system dynamics, where the system is observable. The state estimate is obtained using the discretized system dynamics as follows

$$\hat{\mathbf{x}}_{k+1|k} = \mathbf{A}_d \hat{\mathbf{x}}_{k|k} + \mathbf{B}_d \mathbf{u}(k) \ , \tag{A.16}$$

where $\hat{\mathbf{x}}_{k|k}$ is the estimate of $\hat{\mathbf{x}}$ at time instant k given observations up to and including at time k. $\mathbf{u}(k)$ is the control input, $\mathbf{A}_d$ and $\mathbf{B}_d$ are the discretized terms of the augmented system. The predicted estimate of the error covariance matrix is given by

$$\mathbf{P}_{k+1|k} = cov\big(\mathbf{x}_{k+1} - \hat{\mathbf{x}}_{k+1|k}\big) = \mathbf{A}_d \mathbf{P}_{k|k} \mathbf{A}_d^T + \mathbf{Q} \ , \tag{A.17}$$

where $\mathbf{Q} \in \mathbb{R}^{3(n_d+n_p)\times 3(n_d+n_p)}$ is the covariance matrix of the process noise in the three coordinate axes, n_d and n_p are the order of the plant and disturbance dynamics, respectively. In the update phase, the state estimate is corrected with an innovation term involving the measurements.

$$\hat{\mathbf{x}}_{k+1|k+1} = \hat{\mathbf{x}}_{k+1|k} + \mathbf{K}_{k+1}\big[\mathbf{y}(k) - \mathbf{C}_d \hat{\mathbf{x}}_{k+1|k}\big] \ , \tag{A.18}$$

where $\mathbf{y}(k)$ is the measurement data from the model and FBG sensors at time k and $\mathbf{K}_{k+1}$ is the optimal Kalman gain calculated as

$$\mathbf{K}_{k+1|k+1} = \mathbf{P}_{k+1|k}\big[\mathbf{C}_d \mathbf{P}_{k+1|k} \mathbf{C}_d^T + \mathbf{R}\big]^{-1} \ , \tag{A.19}$$

Here, $\mathbf{R} \in \mathbb{R}^{l\times l}$ is the covariance matrix of the measurement noise and $l = 6$ represents the number of the measurement data from the sensors. Finally, the estimate of the error covariance is updated as follows

$$\mathbf{P}_{k+1|k+1} = \big[\mathbf{I}_{(n_d+n_p)} - \mathbf{K}_{k+1}\mathbf{C}_d\big]\mathbf{P}_{k+1|k} \ , \tag{A.20}$$

where $\mathbf{I}_{(n_d+n_p)}$ is the identity matrix and $\mathbf{C}_d$ belongs to the disturbance dynamics measurement. Therefore, the estimated pose of the manipulator is obtained from the fused position ($\mathbf{p}^{\text{est}} \in \mathbb{R}^3$) and orientation ($\boldsymbol{\theta}^{\text{est}} \in \mathbb{S}^3$) computed using (A.18).

B

Supplementary information for Variable Stiffness Manipulator

B.1 Stiffness Characterization

The three designs of VSM are tested in an electromagnetic setup (PaCMag) which consists of three pairs electromagnetic coils oriented orthogonal with respect to one another to generate a maximum magnetic field of 55 mT in three dimensions [337]. The VSMs are suspended vertically in the workspace of PaCMag and subjected to magnetic actuation rotating about the $\mathbf{y}$ axis. A camera tracks the motion of the VSM as shown in Fig. B.1. The resulting bending moment ($\boldsymbol{M} \in \mathbb{R}^3$) on the VSM due to the applied magnetic field ($\mathbf{B} \in \mathbb{R}^3$) is given by

$$\boldsymbol{M} = \boldsymbol{\mu} \times \mathbf{B} = |\boldsymbol{\mu}|\mathbf{R}_{\mathbf{y}}(\theta)\hat{\mathbf{z}} \times \mathbf{B}, \tag{B.1}$$

where $\boldsymbol{\mu} \in \mathbb{R}^3$ and $\theta \in \mathbb{S}$ are the dipole moment of the magnet attached to the VSM and the lateral deflection of the VSM, respectively, and $\mathbf{R}_{\mathbf{y}}(\theta) \in SO(3)$ is the rotation matrix about the $\mathbf{y}$ axis. The lateral deflection of the VSM is calculated using

$$\theta = \frac{ML}{(\beta + E_{\mathrm{s}}I_{\mathrm{s}})}, \tag{B.2}$$

where E_{s} and I_{s} are the elastic modulus and area moment of inertia of the silicone tube, respectively, L is the length of the VSM, and β is the bending rigidity of the SMP spring.

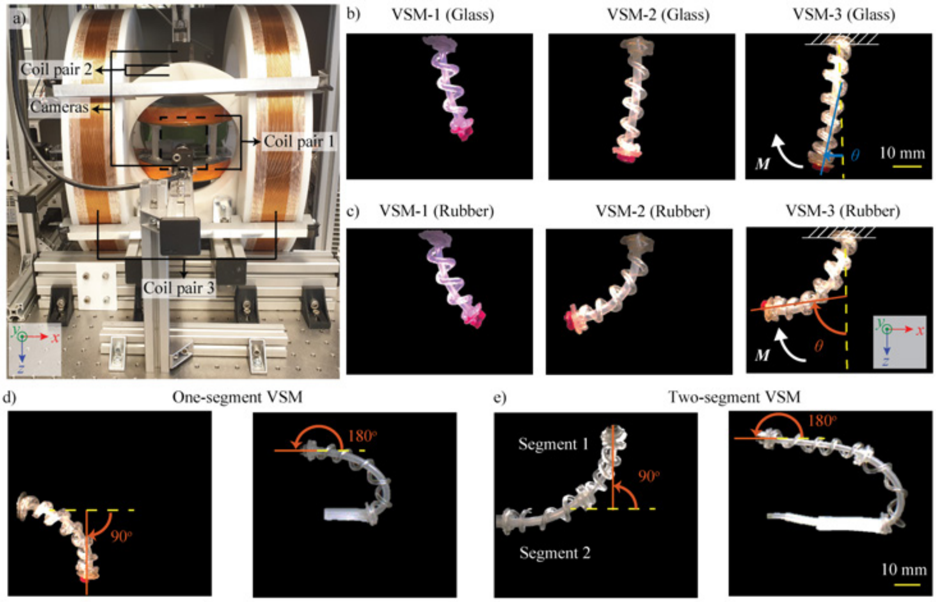

Figure B.1: Experimental setup for the stiffness characterization of one-segment variable stiffness manipulator (VSM): a) The electromagnetic setup (PaCMag) used for magnetic actuation of the VSM. The dashed rectangle represents the workspace where the three designs of VSM are suspended vertically and deflected using magnetic field of 40 mT in b) glass phase and c) rubber phase. Maximum bending angle in rubber phase observed using PaCMag and a handheld permanent magnet for: d) one-segment VSM and e) two-segment VSM.

The bending of the one-segment VSM and the two-segment VSM in their fully extended lengths in rubber phase are tested in PaCMag and using a handheld permanent magnet (N45 neodymium disc magnet of diameter = 70 mm and height = 35 mm). Both the designs can bend up to an angle of 90° when using a magnetic field of 40 mT in PaCMag. However, a higher bending angle of 180° is also possible for both the designs when using the handheld permanent magnet with a magnetic field strength of 70 mT. These bending angles can be observed in Fig. B.1d and B.1e.

B.2 DiAPLEX Shape Memory Polymer

In this work, a DiAPLEX SMP, MP3510 (SMP Technologies Inc., Japan) with a glass transition temperature (T_g) of 35°C is used. The differential scanning calorimetry (DSC) and dynamic mechanical analysis (DMA) for MP3510 cured in one step for 4h at 80°C have been reported in the work by Baer *et al.* [366]. Two heating/cooling cycles were used for DSC measurements. The shear storage modulus (G'), shear loss modulus (G''), and the ratio of loss to storage modulus ($\tan\delta$) were plotted as a function of temperature; glass transition temperature (T_g) was determined from the $\tan\delta$ peak, and the glassy and rubbery moduli of elasticity were obtained from the G'curve. The results reported are as follows: T_g by DSC first heat = 31.3°C; T_g by DSC second heat = 25.2°C; T_g by $\tan\delta$ = 46.1°C; Glassy plateau modulus = 520 MPa; Rubbery plateau modulus = 1.2 MPa.

In order to achieve shape fixity, the SMP spring is designed for high stiffness in the glass phase of SMP and low stiffness in the rubber phase of SMP. It is worth mentioning here that the shape fixity will also depend on the shape fixity rate of the SMP. The shape fixity rate (R_f) quantifies the extent to which a SMP material can retain its temporary shape in stress-free conditions and is given by [365],

$$R_f(N) = \frac{\varepsilon_u(N) - \varepsilon_p(N-1)}{\varepsilon_m - \varepsilon_p(N-1)}, \tag{B.3}$$

where $\varepsilon_u(N)$ is the strain present in the stress-free state after unloading the sample in the N^{th} cycle, ε_m is the maximum strain applied to the sample in %, and $\varepsilon_p(N-1)$ is the residual strain in the permanent shape after $(N-1)$ cycles. A few studies have investigated the shape fixity rate of the DiAPLEX SMP. Baer *et al.* reported the shape fixity between 96% and 99.5% for MP5510 which has a glass transition temperature of 55°C, and noted that high elastic modulus in glass phase correlates with high shape fixity [366]. The shape fixity rate of MP3510 used in this work is not known, and there is uncertainty in the stiffness value of the SMP as the glass elastic modulus is temperature-dependent. The focus of this work is on designing the SMP spring with optimal dimensions for maximizing the shape fixity as discussed in Section B.1.

B.3 Applications

The demonstration of endoscopy, biopsy, and laser surgery applications using the one-segment and two-segment VSMs are conducted in the experimental setup shown in Fig. B.2. The insertion and elongation of the VSM is done by pushing/pulling the silicone backbone by hand as needed. A robot arm (UR5, Universal Robots, Denmark) attached with a permanent magnet is used for the magnetic actuation of the VSM. For the demonstration, the trajectory of the robot is pre-planned to generate the required magnetic fields for deflecting the VSM. This is done by programming different waypoints to move and orient the robot end-effector carrying the magnet to specific locations in the workspace.

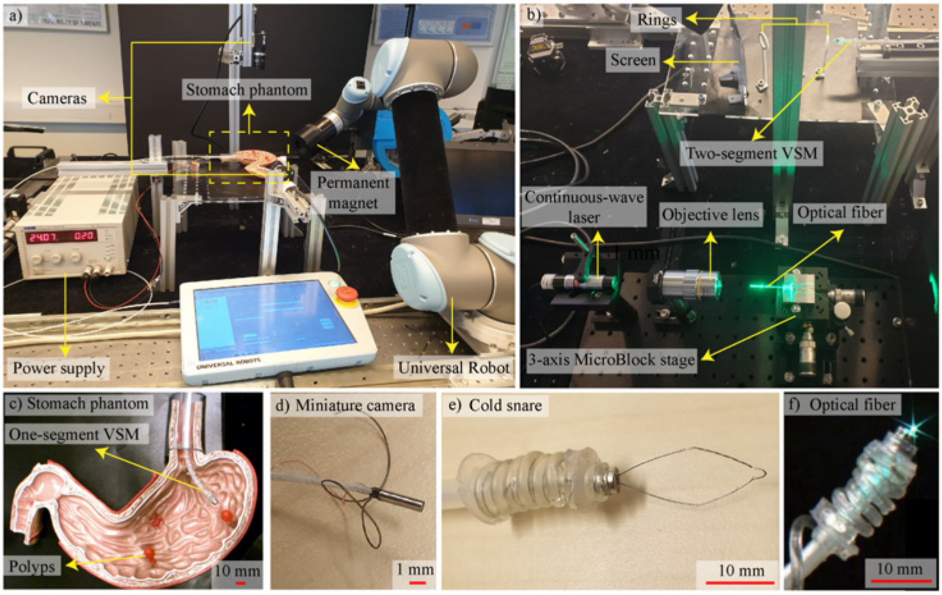

Figure B.2: Experimental setup for the demonstration of endoscopy, biopsy, and laser surgery applications of the variable stiffness manipulator (VSM): a) One-segment VSM inserted in a stomach phantom with the guidance of a permanent magnet attached to the end-effect of a robot. b) Test setup for transmitting laser light though an optical fiber. Two-segment VSM integrated with the optical fiber is steered to navigate through three rings oriented in 3D. c) Top view of the stomach phantom with polyps. d) 0.91 mm miniature camera used for the endoscopy demonstration. e) Diamond Cut™ cold snare used for the biopsy demonstration. f) Optical fiber used for the laser surgery demonstration.

Acknowledgements

I am incredibly grateful for the support of so many wonderful people I was fortunate of meeting during my 4.5 years of doctoral journey. First and foremost, I express my deepest gratitude to my supervisor and promoter, **Prof. Sarthak Misra**. Thank you for believing in me and accepting me as your doctoral student. You have been an essential driving factor in inspiring me always to push my limits and strive for excellence. I always feel reassured knowing your quick response to my messages, regardless of the time of the day or your location in the world. I have learnt so much from you about good scientific practices in writing and presentation. Your guidance has been instrumental in improving my skills in managing time and projects and effectively collaborating with others. I also appreciate your trust and understanding during both good and difficult times.

The next most crucial person behind my doctoral research is my co-supervisor, **Dr. Venkat Kalpathy Venkiteswaran**. Without your unwavering support and mentorship, I would not have made it this far. From brainstorming new research directions to debugging technical issues, you have always been available to provide your valuable inputs. I'm grateful for your infinite patience in guiding me through the depth and breadth of research and improving my writing. Your critical and constructive feedback has transformed me from a novice, muddled engineer to a proficient, analytical researcher. Thank you for listening and encouraging me during challenging times. Your kindness and friendship have been a constant source of motivation both inside and outside of work. I'm also thankful to an honorary co-supervisor, **Prof. G. K. Ananthasuresh**, with whom I worked with for most of my Ph.D. Despite being geographically distant, you fully comprehended my work, providing insightful inputs that significantly enhanced the quality of my research outcomes. Your thought-provoking questions challenged me to think more deeply and creatively about my research. Your scientific expertise inspires me, and I am privileged to have you on my doctoral examination committee.

I'm happy to have been part of the Surgical Robotics Lab (SRL) and worked alongside some of the most talented Roboticists. **Jakub:** You were the human-form encyclopedia of SRL who could solve anything and every-

thing. Thank you for helping me set up many things in PaCMag countless times, which was the essential foundation for all my projects. Your persistence and knowledge are something I always look up to. **The Mert:** I'm overwhelmed by your generosity in helping me in any way possible. You have been my go-to person for procuring all kinds of lab equipment, and your inputs on my thesis were beneficial. And special thanks to your constant supply of sweet treats from your magical drawer, a.k.a. mini AH. **Christoff:** You have been supportive since I started my Ph.D., being the first person to welcome me to SRL in person. Thanks for being a good mentor and sharing your wisdom in tackling many technical and personal challenges of doing a Ph.D. **Sumit:** Although our research topics never crossed paths, your feedback and suggestions on my projects have been helpful and encouraging. You and Christoff were my most amusing pair of office mates, with your non-stop banter brightening my humdrum routine work. **Michiel:** Your technical know-how and clever ideas have boosted my experiments and added a new dimension to the results. It was equally enriching working with you as RMA TAs. **Juan:** It was fun collaborating with you on the laser experiments, and your ideas added refreshing elements to the VSM paper. **Yu-Hsiang:** Your friendly and approachable persona made our discussions about lab experiments or Asian cuisines all the more enjoyable. **Rob:** You have a big hand, literally and metaphorically, in the success of my final year experiments. You are a remarkable asset to our lab with your proactiveness and resourcefulness. **Islam:** Although I did not get to work in your forte of Microrobotics, our impromptu interactions were always heart-warming. **Franco:** It was a pleasure getting to know you in a short frame of time. **Chen:** The awesome stunts you pull off with your soft robots in PaCMag amazes me every time. **Chuang:** Thanks for your ready-to-help attitude and friendly demeanor, uplifting all our conversations. **Zihan:** Your company has been amusing, and I really enjoyed the trip with you and Chuang to Veluwe. **Fouzia:** I had a great time with you at the dinner parties and significantly more fun with your amazing collection of games. **Federico:** You were the smart yet most hilarious colleague I had the pleasure of knowing. **Guilherme:** You were an incredible Control expert. Your memories have become the foundation that brought SRL even closer together. **Foad:** As I recount our trip to the Stepcraft CNC machine workshop, you were always courteous. **Filip:** Thanks for your advice on cameras and image processing. **Edwin:** Thank you for helping me assemble the enormous coils of PaCMag. **Luigi:** You were a fun and easygoing person to talk to in my new office. **Hugo:** Though I could not keep up with you while biking, we had good times at the fitness circuit. **Mina:** You were good company when working late hours. I also had a great time with **Zhengya, Yiyang, Kaixuan, Zhouye, Guilia, Morteza, Jesus, Alaa, Abbas, Fianna, Abhishek, Uthvag, Danica, Ritwick, Rithwick, Onno, Bruno**, and the other former members of SRL.

I'm thankful to a few important people who laid the groundwork for me in the first two years of my Ph.D. **Dr. David Barrera:** Thank you for making and repairing the FBG fibers for us and patiently answering all my queries. **Prof. Dr. Paul Jutte:** Thank you for showing me the radiofrequency ablation procedure first-hand and demonstrating the ablation experiments on animal tissues. I'm honored to have you on my doctoral examination committee. **Dr. Yuri Blaauw:** Thank you for showing me the catheter ablation treatment first-hand. I would like to thank **Mark Jansen** from Jansen Precision Technology for fabricating the compliant continuum manipulator designs, **Henk Waaijer** from TCO for PaCMag coils winding, and **Gerard Oude Meijers** from TCO for fabricating the mechanical components of PaCMag. I owe my progress in the crucial second half of my Ph.D. to a few fantastic people for their fruitful collaborations. **Welmoed:** You are a bright and ambitious learner, and I'm proud to have supervised you as my first BSc student. **Jasper:** It was just as rewarding to supervise you as my first MSc student. Your thorough literature review helped me understand SMPs, a new research territory I was about to explore. **Gideon:** You were proactive and went above and beyond to complete your BSc assignment, which was very useful for our final VSM design. **Jonathan:** It was a testing time for the both of us while working on your BSc assignment, but I'm happy we managed to pull through with great results. I appreciate all your help with the fabrication and thermal experiments. **Dr. Jose Alfredo Alvarez-Chavez** and **Dr. Daniel Jauregui-Vazquez:** Thank you for explaining the basics of fiber optics in layman's terms and helping me with the laser experiments. **Pete:** Your enthusiasm is infectious and helped me achieve the goals of our collaborative project. I appreciate your dedication and couldn't have asked for a better partner. **Giovanni:** Working with you was an absolute pleasure. **Prof. Pietro Valdastri:** Thank you for supporting and encouraging us in making the VSR project possible. I would also like to thank the **European Research Council** and **Netherlands Organization for Scientific Research** for funding and supporting my Ph.D. research.

I'm grateful to some amazing people from the Department of Biomechanical Engineering (BE) at UT. **Jeanine:** Thank you for promptly helping me set up meetings, send packages, print documents, arrange farewells, etc. I also appreciate you personally checking up on me and my well-being. You are the social glue that binds SRL together. **Lianne** and **Yolanda:** Thank you for the warm smiles and cheerful conversations, and together with Jeanine taking care of the treasured BE's Room of Requirement [Harry Potter reference]. **Quint:** Thank you for all your advice and help with 3D printing and laser cutting. **Wouter**: Thank you for ordering the SMA samples for me and helping me with mechanical components. **Nikolai**: Thank you for taking care of the software installations, especially EtherCAT. I would also like to thank **Michiel, Gert Jan,** and **Martijn** for their technical support. **Prasanna:** From exchanging ideas for our respective Ph.D. research to making travel plans to use up our accrued holidays, it was nice having light-hearted banter with you. **Deepti:** I enjoyed exploring the picturesque landscapes of Austria to the hilarious moments we shared taking and retaking photos of you and Prasanna. **Zeynab:** It was a delight to have you as my office mate, and I enjoyed your sense of humor and company. **Pardis:** You were the other best addition to our office. Thank you for being a great listener during the intense final year of my Ph.D., which helped me stay motivated. **Nick:** Thanks for your inputs on 3D printing SMPs which gave me a better understanding of the fabrication possibilities. **Dr. Ali Sadeghi:** Thank you for your advice on SMPs and tips on improving the fabrication process. I also want to extend my thanks to **Ir. Edsko Hekman, Dr. Jeroen Rouwkema, Prof. Herman van der Kooij, Prof. Jutta Arens, Prof. Gabrielle Tuijthof, Prof. Bart Koopman, Dr. Frank Halfwerk, Dr. Rai MacLean, Dr. Izad Tamadon, Nanja, Vasileios, Allan, Jiena, Saivimal, Zahra, Ana, Ander, Mahdi, Alex, Alejandro, Aurora, Rafael, Donatella, Federica, Xinyu**, and the other members of BE for a pleasant time that we shared in various occasions.

I would like to express my heartfelt appreciation to a few fabulous friends for their unwavering support. **Arputha:** Thank you for adopting me as your younger sister. You made me feel at home after I moved to the Netherlands, and your home-cooked meals have always been the perfect remedy for my homesickness. **Shantal:** I appreciate your exceptional listening skills. Whether it's about venting about a rough day or discussing any personal challenges, I'm happy to have you as a friend to turn to. **Shweta:** I feel lucky to have met you at the Ph.D. introductory workshop, which marked the beginning of our friendship, and introduced me to many great individuals. Thank you for believing in my abilities more than myself, and for all the pep talks that always help me regain my confidence. **Prachi:** I'm grateful for your caring nature and encouragement. Also, thank you for teaching me how to swim confidently in the sometimes tumultuous waters of life. **Shreyasi:** I appreciate your thoughtfulness, and I always enjoy our insightful discussions about baking. **Marek:** In addition to our shared interest in making cocktails, I appreciate your level-headed perspective on things. **Shivam:** Thank you for bringing in the fun and positive energy. **Sabari:** Thank you for your moral support and for cheering me up during difficult times. **Jeanette:** I enjoyed our long and meaningful conversations about both our Ph.D. and personal lives, which was always uplifting. Thank you for helping me adjust to living in the Netherlands. **Mukesh:** Your one-of-a-kind quirky sense of humor never fails to lift my spirits. I'm grateful for the other friendships I made during my Ph.D., particularly with **Ameya, Dona, Nitha, Francis, Castro, Ata, Kenia,** and **Cristina**. I'm also thankful to my long-term friends who have supported me from afar, **Haritha, Surya, Kritica, Niranjhana, Tarun,** and **Tanay**. I would also like to express my immense gratitude to two amazing trainers, **Denisa** and **Heidy**, for keeping me healthy and active through fitness and swimming.

As I type these final words of my doctoral dissertation, my heart swells with gratitude for my family's love and support. My brother, **Theophilus** has been the perfect role model, guiding me beyond my comfort zone, and reminding me that sky is truly the limit. Without his constant prodding and boundless encouragement, I may have settled for less than what I'm capable of. I must also express my gratitude to my sister-in-law, **Konkona**. She has been the yin to my brother's yang, keeping me grounded with her calming and uplifting presence. Above all, I owe everything I am today to my parents, **Lilly Pushpam** and **Thomas**. Leaving my home country and moving to the Netherlands has not been easy, especially for my mother. I admire her strength and trust in me, and everything she has done to make my transition as smooth as possible. My father has always been my biggest cheerleader in this rigorous academic journey, constantly pushing me to aim higher and dream bigger. I am excited to see where the future takes me and to continue making my family proud.

About the Author

Theodosia Lourdes Thomas was born on 11th February 1996 in Gobichettipalayam, India. She received a bachelor's degree in Engineering Design and a master's degree in Biomedical Design from the Indian Institute of Technology (IIT) Madras, Chennai, India, in 2018. She was a recipient of the prestigious Eaton Excellence Award, a scholarship recognizing exceptional women engineering students in leading engineering institutions in India. During the course of her studies, she completed industry internships at ABB India Research and Development Center, Bengaluru, and at Philips Healthcare Innovation Center, Pune. In June 2018, she was selected to attend the International Honors Program: Biomedical Engineering Frontiers in Health Care, conducted by the Taipei Medical University, Taiwan.

In October 2018, she commenced her doctoral studies in the Surgical Robotics Laboratory at the University of Twente, under the supervision of Prof. Dr. Sarthak Misra and Dr. Venkatasubramanian Kalpathy Venkiteswaran. Her doctoral research centered on the design and control of magnetically-actuated continuum manipulators for applications in minimally invasive surgery. She developed flexible manipulator designs based on compliant mechanisms, soft polymers, and phase-change polymers. Her work also led to the creation of PaCMag, an electromagnetic test setup for the magnetic actuation of continuum manipulators and soft robots. While her research endeavors resulted in this doctoral dissertation, she also served as a teaching assistant for the Robotics for Medical Applications course and supervised one master's and three bachelor's students. Beyond her academic pursuits, she enjoys experimenting with different plant-based ingredients to bake delicious treats.